Alma Mater Studiorum - Università di Bologna

DOTTORATO DI RICERCA IN

INGEGNERIA ELETTRONICA, INFORMATICA E
DELLE TELECOMUNICAZIONI

Ciclo XXIV

Settore Concorsuale di afferenza: 09/F1 - Campi Elettromagnetici
Settore Scientifico disciplinare: ING-INF/02 - Campi Elettromagnetici

Fiber-Optic Technologies for Wireline and Wireless In-building Networks

Presentata da:
Ing. Davide Visani

Relatore:
Prof. Ing. Giovanni Tartarini

Tutore:
Chiar.mo Prof. Ing. Paolo Bassi

Coordinatore Dottorato:
Chiar.mo Prof. Ing. Luca Benini

Esame finale anno 2012

Typeset using LaTeX.

Abstract

This doctoral dissertation aims to establish fiber-optic technologies overcoming the limiting issues of data communications in indoor environments. Specific applications are broadband mobile distribution in different in-building scenarios and high-speed digital transmission over short-range wired optical systems.

Two key enabling technologies are considered: Radio over Fiber (RoF) techniques over standard silica fibers for distributed antenna systems (DASs) and plastic optical fibers (POFs) for short-range communications.

The combination of RoF and DAS, which allows to shift the complex electronic processing from the antenna base station towards a central office, has already been recognized as a cost-effective solution for the radio coverage of hostile propagation environments and scenarios with a high traffic demand. However, the RoF technology is mainly limited to large locations, such as stadiums, conference centers and university campi. The application of RoF technologies to in-building scenarios needs to be deeply investigated in conjunction with the exploitation of the available fiber infrastructures based either on single or multi mode fibers.

POF is a well-known medium for short-range data communication with two main advantages: the large-core size together with robustness and flexibility, and the low cost mainly due to the use of silicon transceivers. Extensive research activities on gigabit transmission over POF for home networking have been performed in recent years. However, the ultimate exploitation of

POF for higher data rates and transport of wireless signals needs still to be investigated.

The objectives of this thesis are related to the application of RoF and POF technologies in different in-building scenarios.

On one hand, a theoretical and experimental analysis combined with demonstration activities has been performed on cost-effective RoF systems for the distribution of mobile signals over silica single and multi mode fibers.

On the other hand, digital signal processing techniques to overcome the bandwidth limitation of POF have been investigated. In particular, discrete multitone (DMT) modulation and novel constellation formats have been studied with the purpose to maximize the transmission throughput of a POF link. Moreover, the exploitation of POF for wireless signal distribution has also been investigated.

The main achievements of the work included in this dissertation can be summarized as follows:

- Theoretical and experimental characterization of distortion effects on a radio multi-standard transmission over state-of-the-art intensity-modulated direct-detection (IM–DD) RoF links over silica singlemode fiber with directly modulated laser diodes (LDs). This activity was pursued through modeling and measurements with third generation (3G) mobile signals.

- Extensive modeling on modal noise impact both on linear and nonlinear characteristics of IM–DD RoF links over silica multimode fiber with directly modulated LDs. The theoretical activity was validated with experimental results leading to the definition of link design rules for an optimum choice of the transmitter, receiver and launching technique.

- Successful transmission of Long Term Evolution (LTE) mobile signals on the resulting optimized RoF system over silica multimode fiber employing a Fabry-Perot LD, central launch technique and a photodiode

with a built-in ball lens. The performances were well compliant with standard requirements up to 525 m of multimode fiber.

- Theoretical investigation and experimental demonstration of multi-gigabit transmission over IM–DD POF links. An uncoded net bit-rate of 5.15 Gbit/s was obtained on a 50 m long IM–DD POF link employing an eye-safe transmitter, a silicon photodiode, and DMT modulation with bit and power loading algorithm.

- Insertion of 3×2^N quadrature amplitude modulation (QAM) in the constellations set of the DMT bit and power loading algorithm for maximum capacity attainment in IM–DD POF links. An uncoded net bit-rate of 5.4 Gbit/s was obtained on a 50 m long IM–DD POF link employing an eye-safe transmitter and a silicon avalanche photodiode.

- Experimental validation of the simultaneous transmission of a multi-gigabit baseband signal based on DMT and a radio frequency signal based on ultra wideband (UWB) technology over a 50 m long IM–DD POF link. An uncoded net bit-rate of 2 Gbit/s was obtained with DMT, while a data stream of 200 Mbit/s was transported with the UWB radio signal.

Contents

Introduction

"Broadband access for everyone, everywhere". This is one popular motto of the information and communications technology (ICT) community since the rising of broadband wireline and wireless technologies. The possibility to use broadband services wherever you are (everywhere) and at an affordable price (everyone) was an added benefit provided by wireless broadband technologies since the first introduction of the third generation (3G) mobile network. For this reason, telecom operators have put considerable efforts in the last decade on wireline last-mile solutions and wireless coverage. Although wireline and wireless access technologies are considered as competitors, they have one thing in common: they are mostly deployed outdoor. However, the majority of the broadband traffic is generated inside premises by devices using wireless connections, such as smartphones and tablets, or using wireline connections, such as desktop PCs and data centers. Until now, the industry did not put a large emphasis on planning for in-building deployments capable of supporting new broadband telecommunication services, such as new video-based services and advanced Internet applications. But, this is expected to become soon a basic necessity.

The chances that telecom operators will solve every in-building wireline and wireless coverage issue are very slim. Hence, technical solutions are highly case-dependent and mainly based on a compromise between present service requirements, future-proofness and cost. In this framework, fiber-optic technologies are typically considered an answer to the request to be

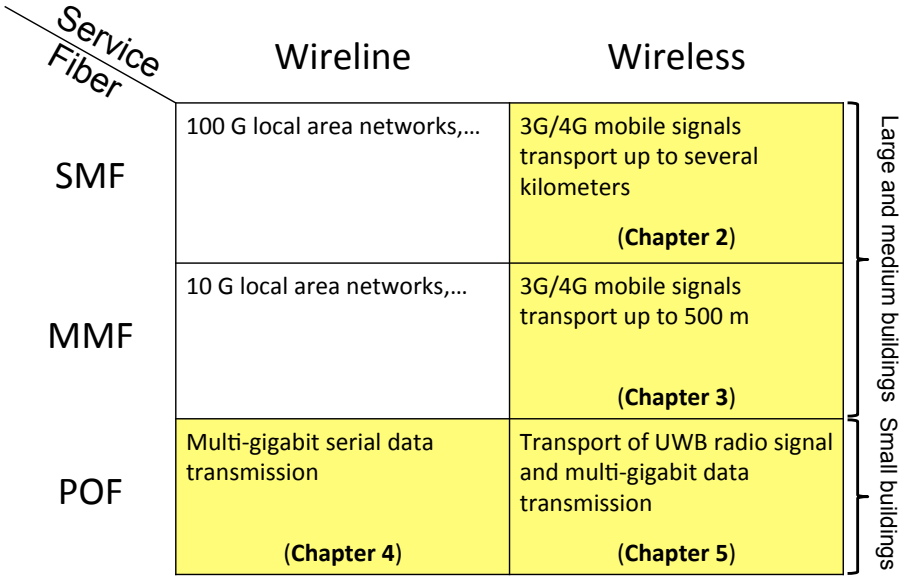

Figure 1: Summary of the topics investigated (yellow cells) in this thesis

future-proof and to comply with present services for wireline networks. But, are they convenient in every scenario? Are they still a need now that wireless technologies are driving the market?

This thesis aims to give some answers investigating fiber-optic technologies which enable broadband wireline and wireless connectivity for in-building networks. As fiber technologies both silica fibers, singlemode (SMF) and multimode (MMF), and plastic optical fibers (POFs) are considered for different in-building application areas. Indeed, silica fibers are suitable for large and medium building deployment, while large diameter plastic optical fibers are considered for small buildings, such as home networks.

The solutions enabling wireline and wireless broadband connectivity are presented at a physical and transmission level. Fig. 1 summarizes my contributions (colored cells) within the application areas of silica and plastic fibers for wireline and wireless broadband services in an in-building scenario. For broadband wireline connectivity, multi-gigabit serial data transmission with discrete multitone modulation on large core plastic optical fiber is stud-

ied for small building deployment. For in-building wireless connectivity, two main categories are investigated. For large and medium building deployment, radio over fiber techniques for fiber distributed antenna systems employing silica fibers are studied as an enabling technology for the efficient distribution of 3G and fourth generation (4G) mobile services. For small buildings, the feasibility of a converged optical infrastructure based on plastic optical fiber supporting wireless signal transport and multi-gigabit baseband data transmission is inquired.

The thesis is organized in five chapters.

Chapter 1 gives an overview of the optical properties of silica fibers and large diameter plastic optical fibers. Hence, the application of these fiber media to the distribution of wireline and wireless communication technologies is depicted and referred to the in-building application scenario.

Chapter 2 presents a numerical model for the evaluation of the transmission performance of real radio signals in radio over fiber links employing directly modulated lasers and singlemode fiber. Transmission experiments are also shown and compared with the simulated results.

Chapter 3 reports the modeling and experimental activity on radio over fiber links employing directly modulated lasers and multimode fiber. The developed model describes the impact of modal noise on linear and non-linear characteristics of the link. The experimental results are used to confirm the model prediction and to design a radio over multimode fiber link with good characteristics. Finally, transmission experiments are shown.

Chapter 4 presents the research activity on multi-gigabit transmission over large diameter plastic optical fibers. A model for the estimation of the channel capacity is derived. Multi-gigabit transmission experiments employing discrete multitone modulation with bit-loading are presented. Finally, constellation formats transporting a fractional number of bits per symbol are introduced and applied to transmission experiments with discrete multitone modulation and bit-loading.

Chapter 5 reports the experimental activity on the simultaneous transmission of an ultra wideband radio signal and a multi-gigabit data stream based on discrete multitone modulation.

Finally, the achieved results are summarized with a unified approach in the **Conclusions** section.

The work presented in this thesis is the outcome of my Ph.D. research activity at the "Dipartimento di Elettronica, Informatica e Sistemistica" (DEIS) of the University of Bologna within the European FP7 project 212352 ICT "Architectures for fLexible Photonic Home and Access networks" (ALPHA). Part of this work was performed in collaboration with Commscope Italy S.r.l. Part of this work is a result of a research period at the COBRA Research Institute of the Eindhoven University of Technology, The Netherlands.

Chapter 1

Technologies for in-building networks

In this chapter an overview of fiber-optic technologies and solutions for in-building networks are presented. An in-building network can be defined as a communication system which connects devices and users inside a premise with each other and with the external networks, i.e. access and/or mobile networks.

In section 1.1 classification and main properties of optical fibers based on silica and Poly(methyl methacrylate) (PMMA) will be illustrated.

In section 1.2 and 1.3 the appropriate fiber-optic technology for large/medium buildings and small buildings is discussed. Section 1.2 refers to the distribution of wireline services, in particular referred to high-speed local area and home networks. Section 1.3 describes the distribution of wireless services, with emphasis on in-building radio coverage with current and emerging wireless standards. In this dissertation, I considered separately wireline and wireless services since the proposed solutions needs to meet different service requirements.

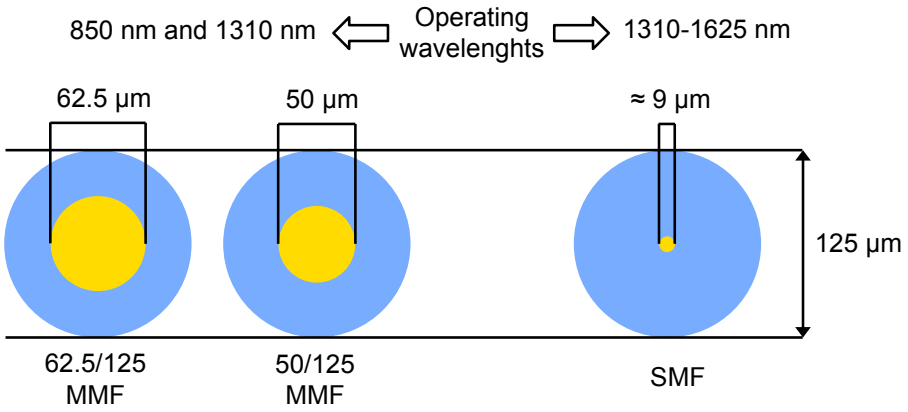

Figure 1.1: Schematic drawing of multimode and singlemode fibers

1.1 Fiber technologies

1.1.1 Silica optical fiber

Silica optical fiber is by definition the optical fiber for data communication. It consists of two silica-based materials: a higher refractive index core and a lower refractive index cladding. As summarized in Fig. 1.1 there are two main types of silica optical fiber: multimode and singlemode fiber. Multimode fiber (MMF) for data communications has a core diameter of 62.5 or 50 μm, a cladding diameter of 125 μm, and is used in the 850 nm and 1310 nm spectral windows. Singlemode fiber (SMF) has a narrow core diameter of about 9 μm, a cladding diameter of 125 μm, and is used between 1310 and 1625 nm. I will not consider in this work other silica-based optical fibers such as plastic and hard polymer clad silica fibers, where a silica core is surrounded by a thin plastic polymer material [1], or photonic crystal fibers, in which the light is guided by a reduced effective index of the cladding or by a photonic bandgap effect [2].

SMF is based on a step-index (SI) profile meaning that there is an abrupt index change at the core-cladding surface, while core and cladding have a uniform refractive index as shown in Fig. 1.2. Due to the small core diameter SMF supports only one mode, or more correctly two orthogonal polariza-

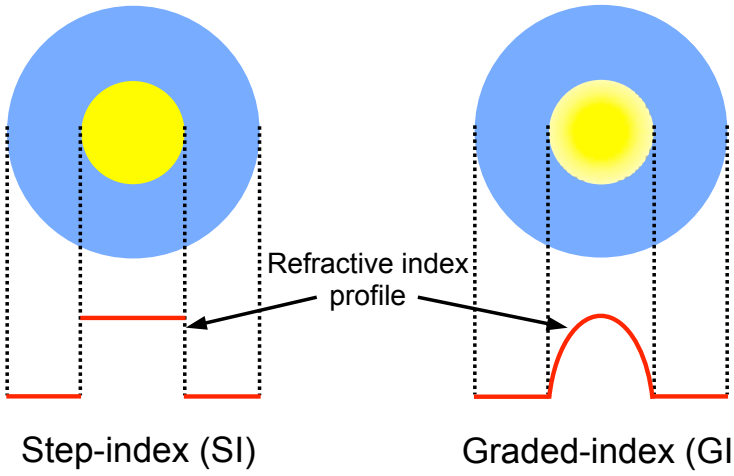

Figure 1.2: Schematic drawing of step-index and graded-index profiles

tion modes whose different propagation properties are revealed after long transmission distances [3]. SMF is standardized under several international standards. One of the most known is the ITU–T G.652 recommendation of the International Telecommunication Union (ITU) [4]. The typical optical attenuation is 0.2 dB/km at 1550 nm and 0.35 dB/km at 1310 nm which, together with the availability of optical amplifiers, allows for long-haul transmission [5]. The bandwidth (BW) per distance product of SMF systems is typically limited by the modulating signal bandwidth of the transmitter (TX) and the receiver (RX) in short-range transmission and by the effects of chromatic dispersion, polarization mode dispersion and non-linearity in medium and long-haul transmission [3].

MMF for data communication is designed with a graded-index (GI) profile where the refractive index decreases gradually from the center of the core to the cladding as shown in Fig. 1.2. Since MMF core diameter is more than five times larger than SMF core diameter, MMF supports a large number of guided modes. This characteristic produces a strong BW limitation of MMF compared to SMF. Indeed, because of an effect similar to multi-path propagation in a radio channel, the BW of MMF systems is typically limited by modal dispersion. Chromatic dispersion, polarization mode dispersion and

non-linear effects are also present in MMF systems, but their contributions are typically negligible with respect to modal dispersion. To minimize modal dispersion an accurate design of the GI profile is employed. However, modal dispersion compensation depends in an critical manner on the refractive index profile and so modal dispersion can be minimized just for a small interval of operating wavelengths [6].

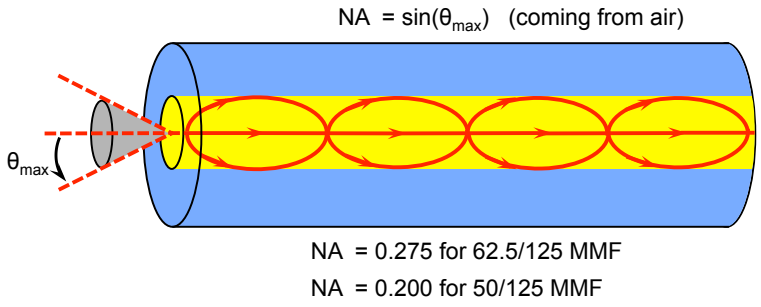

(a) Multimode fiber

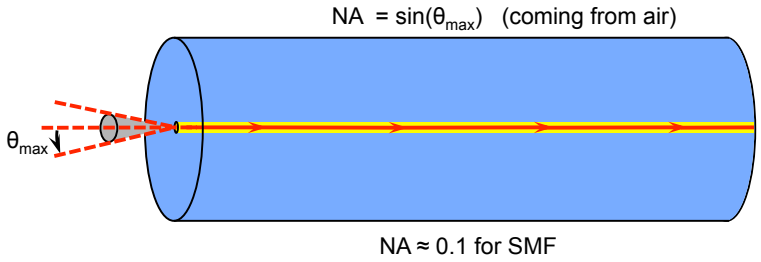

(b) Singlemode fiber

Figure 1.3: Schematic drawing of numerical aperture of multimode (a) and singlemode (b) fibers

MMF is standardized under ISO/IEC 11801 standards and ITU–T G.651.1 (only 50/125 MMF) [7, 8], but also the TIA–492AAAx classification is often used [9]. The maximum optical attenuation should comply with the values of 3.5 dB/km at 850 nm and 1 dB/km at 1310 nm, while the numerical aperture (NA) is set to 0.2 for 50/125 MMF and 0.275 for 62.5/125 MMF. Fig. 1.3 shows graphically the meaning of the numerical aperture which is related to the half-angle θ_{max} of the maximum cone of light that can enter or

OM designation	Core diameter (μm)	OFL BW 850 nm ($MHz \cdot km$)	OFL BW 1310 nm ($MHz \cdot km$)	EMB 850 nm ($MHz \cdot km$)
OM1	62.5	200	500	N/A
OM2	50	500	500	N/A
OM3	50	1500	500	2000
OM4	50	3500	500	4700

Table 1.1: ISO/IEC 11801 OM designation

exit the fiber. In the same figure the NA of MMF is also compared to a typical value of 0.1 for SMF. However, the NA is not standardized for SMF in [4]. The higher NA of MMF at 850 nm allows the possibility to use relatively low-cost optical components and light sources such as silicon light emitting diodes (LEDs) and vertical cavity surface emitting lasers (VCSELs).

Tab. 1.1 shows the identification of current MMFs for data communication as outlined in the ISO/IEC 11801 international cabling standard [8]. OM1 and OM2 fibers are, respectively, 62.5/125 and 50/125 MMFs. They are intended for use with LED sources at speeds of 10 or 100 Mbit/s. Their standard performances are specified by the minimum overfilled launch (OFL) BW that is the measured bandwidth when a light source with approximately uniform power emission in all directions and NA larger than the MMF NA illuminates the fiber. This case corresponds to the excitation of all the MMF modes with comparable power levels and hence to the worst case in terms of modal dispersion.

OM3 and OM4 fibers are 50/125 MMFs and are laser-optimized, or optimized for use with VCSEL light sources. OM3 and OM4 fibers are designed to get the most performance out of VCSELs compared to LEDs. For this reason, in Tab. 1.1 the effective modal bandwidth (EMB) is specified together with the OFL BW. OM3 and OM4 MMFs with laser sources are intended for 1 and 10 Gbit/s transmission, and even higher data rate. OM1 and OM2 cables can also be applied for shorter reach 1 Gb/s networks.

1.1.2 PMMA-based plastic optical fiber

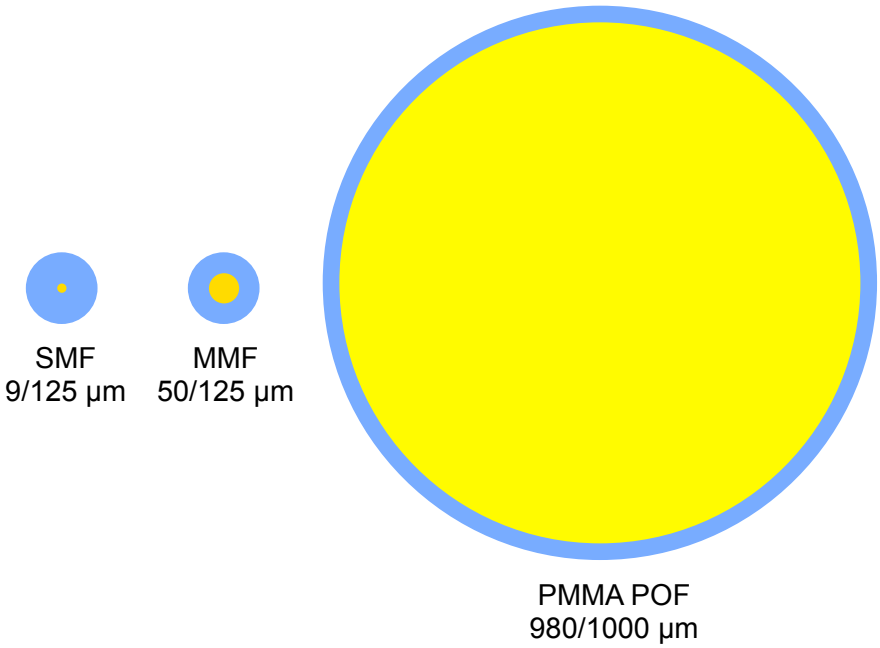

Figure 1.4: Comparison of the fiber core diameters for (left-to-right) SMF, 50/125 MMF and 1 mm diameter PMMA SI–POF

An optical fiber based on silica is also called a glass optical fiber (GOF). Due to the intrinsic nature of glass materials the size of the core of GOF cannot overcome approximately 200 μm without incurring in mechanical stiffness. However, other materials can be employed to manufacture optical fibers. Utilizing polymer, or plastic, materials it is possible to obtain plastic optical fibers (POFs). POFs can have a large core diameter of 0.5 and 1 mm keeping flexibility and mechanical resistance [10]. This leads to a simpler termination, splicing, connectorization, and coupling between a light source and the fiber compared to GOF.

Among polymer materials, Poly(methyl methacrylate) (PMMA) is the most popular and used material for POFs. Fig. 1.4 shows a comparison between the cross section of SMF, 50/125 MMF and 1 mm diameter PMMA SI–POF. As suggested in the figure, a PMMA based SI–POF has a core

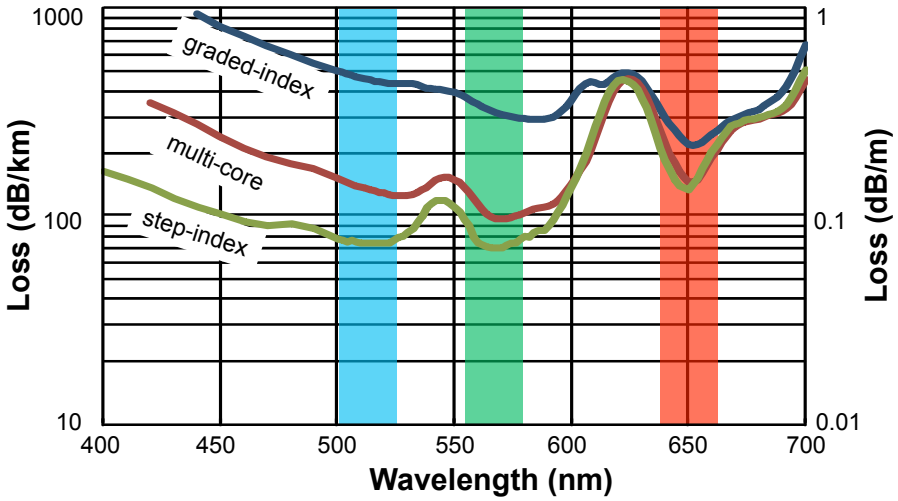

Figure 1.5: Spectral attenuation for 1 mm diameter PMMA SI–POF, GI–POF and MC–POF

diameter of 980 μm and a cladding thickness of 20 μm to obtain an overall fiber diameter of 1000 μm. The refractive index difference between core and cladding is kept at higher values compared to GOF [11]. This index profile determines a NA of 0.5. However, all the positive features of PMMA–POF are paid with a small bandwidth and a large attenuation. Indeed, the optical attenuation of PMMA SI–POF is typically above 100 dB/km and regards the visible wavelength region (see Fig. 1.5), while the bandwidth is limited to 50 MHz after 100 m. Consequently, PMMA SI–POF is intended for use with visible light LED and resonant cavity (RC) LEDs in short-range datacom applications, such as automotive and short-range communications. Other non datacom applications are sensor, illumination and industrial automation.

To overcome the bandwidth limitation of SI–POF, GI–POF with a graded-index profile can be manufactured. This fiber can increase the bandwidth of more than 20 times. This type of fiber is suitable to enable multi-gigabit transmission and is intended to be used with RC–LEDs, edge-emitting lasers and VCSELs. Due to the manufacturing process, some of the benefits of POF such as small bending radius and large coupling tolerance are decreased

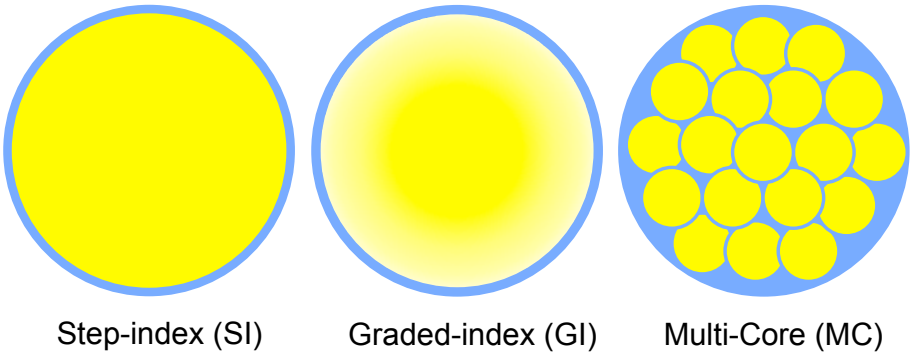

Figure 1.6: Schematic drawing for the cross section of (left-to-right) 1 mm diameter PMMA SI–POF, GI–POF and MC–POF

caused by the lower NA of 0.25 compared to SI–POF. Moreover, the attenuation of GI–POF is increased approximately at 200 dB/km in the visible region as can be observed from Fig. 1.5. Another disadvantage is the small operating temperature range between −30 and +60 °C, which avoids the use of this fiber for automotive applications. Nevertheless, GI–POF is a promising candidate for providing multi-gigabit communication networks in consumer applications.

Another type of 1 mm diameter POF which is worthy to be discussed is the multi-core (MC)–POF. The design of MC–POF was based on the consideration that keeping fixed the NA while reducing the fiber core, the ratio between fiber core diameter and bending radius diminishes, hence reducing the impact of a small bending radius. However, the use of smaller diameter fibers lose the ease of handling which is typical of 1 mm diameter POF. Hence, Asahi developed a MC fiber where many cores (19 to over 1000) are manufactured together is such a way that they fill a round cross-section of 1 mm diameter. Fig. 1.6 shows a schematic drawing of a 19 core 1 mm diameter MC–POF compared with a SI–POF and a GI–POF. Note that the the single fiber cores are not perfect circles since during the manufacturing process the fibers are placed together at high temperatures meaning that their shapes are changed.

MC–POF can reduce the bending radius down to 1 mm, which is much

Fiber type	Loss at 650 nm (dB/km)	BW-length product ($MHz \cdot km$)	NA	Bending radius (mm)
SI–POF	< 160	5	0.5	20
GI–POF	< 200	> 100	0.25	25
MC–POF	< 160	> 20	0.6	1-3

Table 1.2: Characteristics of some 1 mm diameter PMMA POF

less than 20 mm for SI–POF and 25 mm for GI–POF. The optical attenuation of MC–POF is similar to the one of SI–POF as shown in Fig. 1.5. Due to a NA of 0.6 and to the step-index profile of each fiber core MC–POF should have bandwidth properties similar to SI–POF. However, the measured values are actually higher than the one of SI–POF. This fact has been explained by means of mode coupling and mode-selective attenuation [11].

Tab. 1.2 summarizes the main optical properties of SI–POF, GI–POF and MC–POF. I underline that 1 mm diameter SI–POF is at present the only standardized cable for indoor applications under A4a category in IEC 60793-2-40 standard [12]. GI–POF and MC–POF are not yet standardized, hence limiting their widespread availability and causing higher prices due the lack of a volume market.

1.2 Wireline communication technologies

At present, most of the services offered to an in-building device or user are completely or partially transported by a wired network. Some example of current services are VoIP, IPTV, Internet related applications, like large file-sharing, high-definition video streaming. The current wired technologies are mostly based on copper cables, such as twisted-pair, Category 5 (Cat-5), coaxial, and power-lines. With Cat-5 technology a throughput of 100 Mbit/s (officially 100 BASE-TX, known as Fast-Ethernet) is possible up to 100 m under any operating condition [13]. Also Gigabit Ethernet (1000BASE-T) is possible on Cat-5 up to 100 m [14], but under controlled operating condition, e.g. limited bending condition and electromagnetic interference. Higher

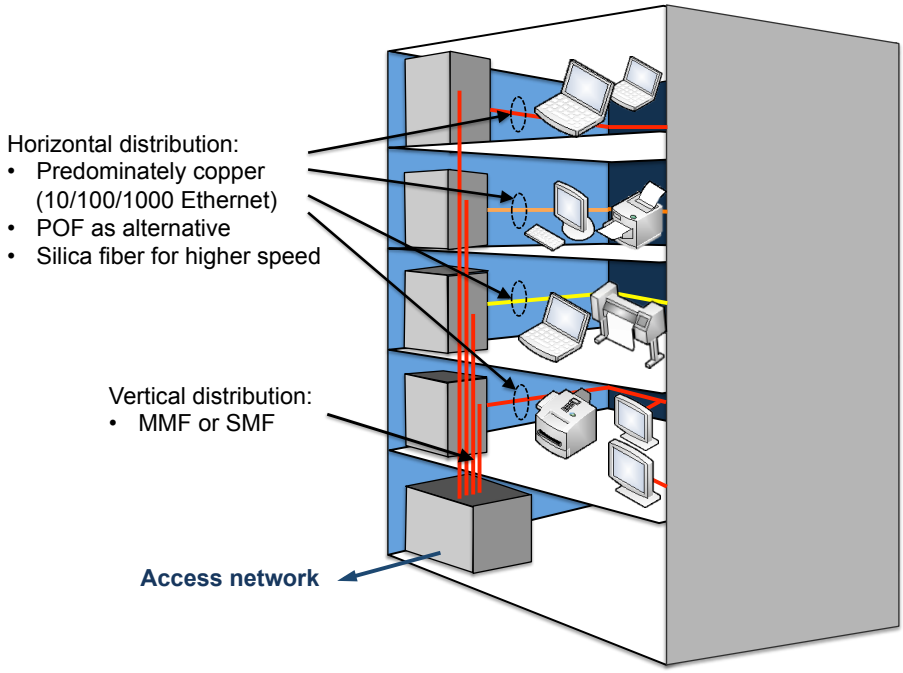

Figure 1.7: Large and medium buildings wireline network

speeds are instead not feasible with Cat-5 and requires higher-quality cables (Category 6 or better) [15]. In the framework of this limitation for copper wires, fiber-optic cables show their advantages. Indeed, SMF is a future-proof transmission medium, whose bandwidth per length product can be considered unlimited for in-building application, and limited just by the current transceiver technology. Anyway, SMF–based in-building networks have a cost which is not suitable for every scenario. For this reason, I divide the deployment choice among fiber-optic cables on the network size, i.e. usually the building size.

1.2.1 Large and medium in-building networks

For large and medium building networks I consider a telecommunication network deployed over several floors and rooms. Some examples of a large building are a shopping mall, a large corporate building, and a sport-center,

while medium buildings are a medium corporate building, a full-service hotel, and a school. The wired coverage of these scenarios with fiber-optic solutions is currently implemented as shown in Fig. 1.7.

The vertical distribution from the bottom to the top of the building is performed with silica SMF or MMF due to the large amount of data which needs to be delivered. For horizontal, or floor, distribution copper technologies are currently employed, mostly Cat-5 and Cat-6. This is due to the lower amount of data to be distributed, typically 100/1000 Mbit/s, and to the short requested range, typically around 100 m. As an optical alternative to copper solutions, standard POF can be employed as it will be described in section 1.2.2. For future-proof deployment or when the requested data rate or range increases, silica fiber gains attraction.

Although SMF has a fundamental larger bandwidth compared to MMF, there is still an increasing interest to install silica MMF in an indoor scenario. This is not due to a lower fiber cost per unit length, since from this point of view there is no advantage to choose MMF. However, there are other aspects, rather than fiber cost, which are more favorable for MMF than for SMF:

- SMF has a much smaller core diameter, and hence needs very accurate tools for splicing and connectorizing, plus highly-skilled installers. Thus, splicing and connectorizing of MMF is cheaper

- Due to its small core diameter, a SMF connection is more vulnerable for contamination by dust and scratches, as may happen easily in detachable connections in in-building networks. The larger core size of MMF significantly relaxes these contamination problems

- For wavelengths below 1 μm, silicon photodetectors may be used, which offer the advantage of co-integration with the electronic circuitry in a single silicon-based receiver integrated circuit. This enables really low-cost receiver modules and reduced power consumption. However, a standard SMF is no longer single-mode at wavelengths below its cut-off wavelength, typically around 1.2 μm. On the other hand, silica

	SMF	MMF
Information carrying capacity	×	
Distance supported	×	
Fiber price	×	
Transceiver and connector price		×
Ease of handling		×
Transceiver power consumption		×

Table 1.3: Comparison of the advantages of SMF and MMF for in-building networks

MMF operates fine at wavelengths in the 850 nm near infra-red region

In addition to this green-field installation advantages, silica MMF is already installed in many premises and thus it can be used as a basis for a network upgrade. Related to the previous list, Tab. 1.3 summarizes the main advantages of using SMF or MMF solutions.

The main application of optical fibers for in-building networks is local area network (LAN) using Ethernet technology. The advantage of MMF depends on the capability to deliver a high data-rate inside the premise. This capability depends on the size of the building and the desired data rate. Fig. 1.8 shows graphically the maximum reachable distance and data rate of OMx MMFs with 850 nm sources and of SMF. While it is possible to achieve 100 Mbit/s, i.e. Fast-Ethernet, with OM1 MMF and better up to 2 km, Gigabit Ethernet (1000 Mbit/s) is limited to 300 m with OM1 MMF, and reaches 600 m with OM2 MMF and 1 km with OM3 MMF and better. These distances are compatible with almost every building size, and for this reason MMFs are widespread employed for in-building Gigabit Ethernet. Moreover, most of the same Gigabit links can successfully be upgraded to 10 Gbit/s speed with a distance limitation of 300 m with OM3 MMF and 550 m with OM4 MMF. At present OM3 and OM4 MMFs are becoming the most popular choices for in-building networks. 40 and 100 Gbit/s networks are also possible within a distance of 150 m, while for longer distances SMF should be considered.

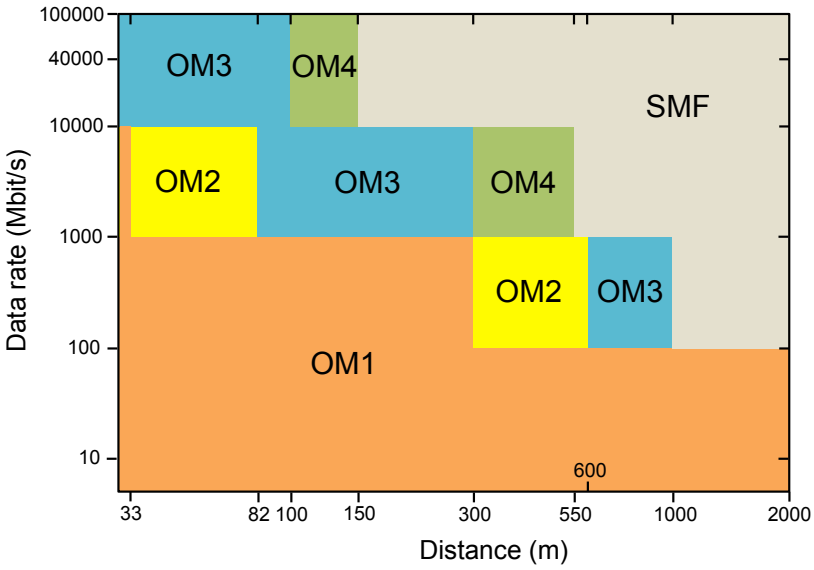

Figure 1.8: Fiber choices depending on requested data rate and distance with OMx MMF using 850 nm sources and with SMF

These technical considerations conclude that MMF can be considered a future-proof solution for medium building networks. For data rate above 100 Gbit/s and for large buildings networks SMF should be instead considered.

1.2.2 Home and small in-building networks

For small building networks I refer to a telecommunication network deployed over the premise of a small enterprise or a family house with maximum three floors and three rooms per floor.

Small in-building networks are more cost-sensitive than large and medium in-building networks because fewer users are sharing equipment and installation costs. Particularly, in home area networks (HANs) there is no sharing of costs at all. Furthermore, the installation costs typically exceed the equipment costs per user. Therefore, the focus on home and small in-building networks should be on keeping installation costs at a minimum level. While

for some small building networks silica MMF can be still considered as a good tradeoff between performance and cost, a fiber-optic solution with a potential lower cost need to be considered for home networks.

On this basis, POF is an interesting solution to be applied in low-cost short-range optical communication systems. Indeed, 1 mm diameter POF has interesting characteristics for small networks compared to silica fibers:

- Easy coupling with sources and no strict needs for connectors
- Use of cheap visible light sources such as LED
- Robustness against mechanical stress and bending

All these positive features of POF have as counterpart its limited bandwidth compared to silica fibers. However, the real competitors of POF in small in-building networks are copper technologies, e.g. Cat-5. POF solutions are already commercially available for Fast-Ethernet (100 Mbit/s) within a distance of 100 m. This is the same data-rate and distance target of Cat-5 solutions. With respect to Cat-5, POF cable has diameter of 2.2 mm which offers multiple ways to be installed. Moreover, it can be installed separately or in combination with other cables such as power-line, twisted-pair and coaxial cabling due to electromagnetic immunity (EMI). The easy of handling and the use of visible light makes POF an attractive candidate for do-it-yourself installation, meaning that there is no mandatory need for professional installation.

Research studies have demonstrated the possibility to increase the performance of standard SI–POF to 1 Gbit/s up to 75 m [16, 17]. Higher data-rates have been demonstrated utilizing GI–POF or MC–POF [18].

The possibility to have a gigabit or more optical backbone in a small building scenario is crucial to distribute all the residential or office services in a single infrastructure. Currently, a plethora of delivery methods and cable media are employed for different kinds of wireline services; e.g., coaxial cabling for video broadcast, Cat-5 cabling for LAN, twisted pair cable for wired telephony and internet access. Such multiple network infrastructure

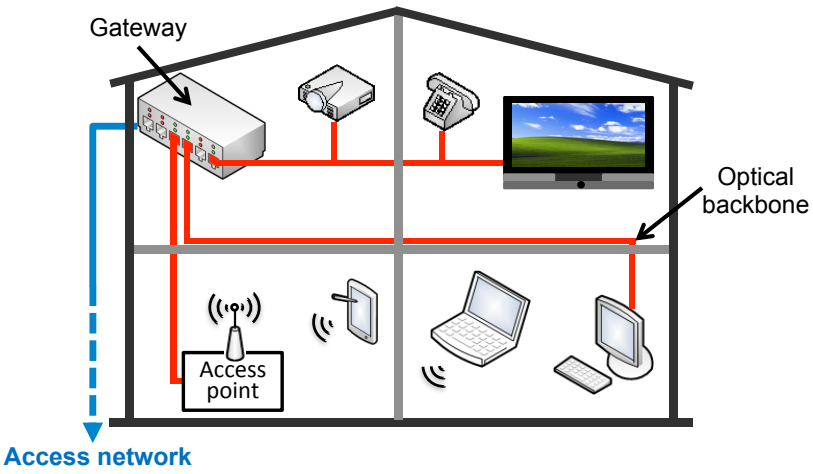

Figure 1.9: Optical backbone for home and small in-building networks

leads to a complicated consumer experience and high service and maintenance costs. To provide a simplified and easily upgradable small building network, a single common backbone infrastructure is required, as shown in Fig. 1.9. High-speed wireline services are delivered to the home via fiber-to-the-home (FTTH) or other technologies until the point of the gateway. Then, the wireline services are distributed among the rooms through the optical backbone. For this reason, the maximum data rate transferable over a low-cost do-it-yourself POF network needs to be carefully investigated.

1.3 Wireless communication technologies

Wireless communications have experienced an ever-growing development and commercial fortune in the last decade. Every day office and residential users surf on the Internet through a wireless connection. In this thesis, with wireless technologies I refer to radio and microwave transmission techniques for personal communications. However, short-range wireless systems can also exploit light as the information carrier, in particular visible light [19] or infra-red light [20]. Fig. 1.10 shows a graphical list of current and emerging wireless technologies present in an in-building scenario related to their data

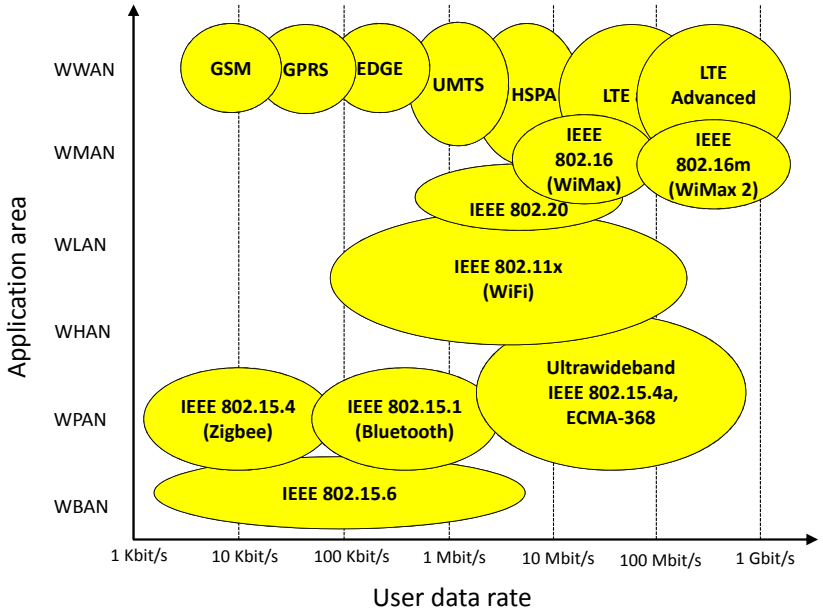

Figure 1.10: Current and emerging wireless communication systems

range and application area.

Among all these wireless technologies the most widespread ones for data communication within a building fall into these categories:

- Wireless local area network (WLAN)
- Wireless personal area network (WPAN)
- Mobile/cellular networks

WLAN technologies are intended for use within a range of tens meters. At present the majority of WLAN technologies is based on devices having the certification label Wireless Fidelity (WiFi), i.e. that comply with the IEEE 802.11x specifications [21]. WiFi networks have achieved high popularity in the in-building market as a cost-effective and easy to install solution both for business and residential access to the wired infrastructure connected to the access network. The IEEE 802.11x standards operate in the 2.4 and 5 GHz windows of the industrial, scientific and medical (ISM) bands for unlicensed

use and guarantee throughput of 11 Mbit/s (802.11b), 54 Mbit/s (802.11a/g) and 320 Mbit/s (802.11n) up to tens meters. There is also an active research activity towards the 1 Gbit/s performance.

WPAN technologies are intended to interconnect devices around an individual person's area, and thus their range is typically below 10 m. The most known WPAN technologies are Bluetooth, Zigbee and ultra wideband (UWB) technologies. All these technologies are also considered for wireless body area network (WBAN), which are intended to connect wearable devices within a range of few meters. UWB technologies have also application in wireless home area network (WHAN), such as high-definition video streaming or gaming, which is a special case of WLAN for residential use.

In contrast with WLAN and WPAN technologies which are wireless fixed systems, mobile networks are intended to guarantee voice and data communications between users in mobility. For this reason, a mobile network is deployed by a mobile operator which requests a fee to its subscribers. Current widespread mobile networks are based on the following technologies: Global System for Mobile communications (GSM), Universal Mobile Telecommunications System (UMTS), Long Term Evolution (LTE) which use the licensed radio frequency (RF) bands, such as the ones around 800-900, 1800-1900 and 2100 MHz [22]. These technologies are typically considered as wireless wide area networks (WWANs), since they are used to cover a wide geographical area. However, they are not only limited to WWANs. For example high speed packet access (HSPA) was mainly deployed in metro areas. In this framework, also wireless metropolitan area network (WMAN) technologies, such as Worldwide Interoperability for Microwave Access (WiMAX), are starting to support mobile users. Indeed, next-generation LTE–Advanced and WiMAX 2 (IEEE 802.16m), identified as WirelessMAN–Advanced, are both included in IMT-Advanced technologies of International Mobile Telecommunications (IMT) [23], i.e. 4G mobile technologies, offering up to 100 Mbit/s to users with high mobility and up to 1 Gbit/s to relatively fixed users. Since in-building users are relatively fixed, the next-future challenge will be to be really able to deliver 1 Gbit/s per user in an indoor scenario.

Differently from WPAN and WLAN technologies whose equipment is in

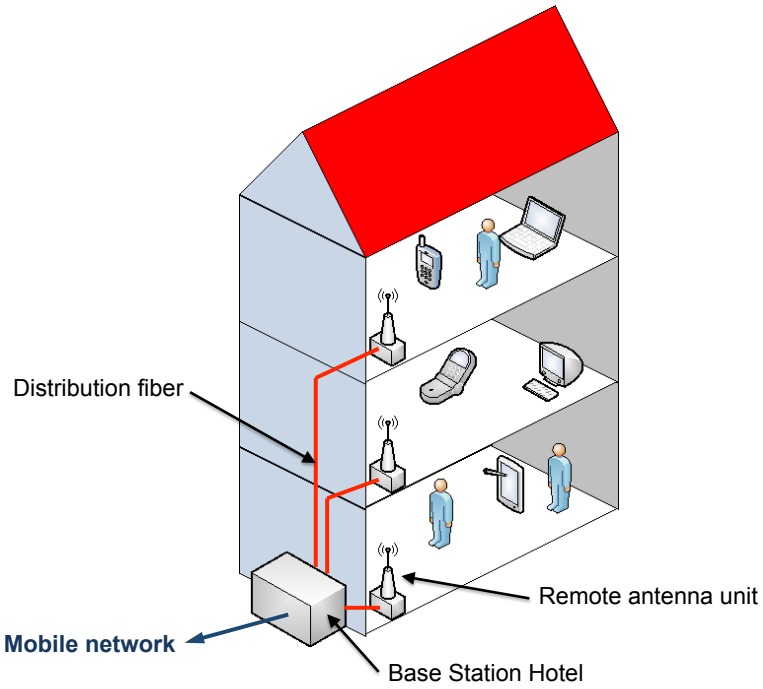

Figure 1.11: F–DAS for in-building wireless coverage

the building, mobile/cellular networks reach the in-building users through the premise walls. Therefore, the indoor radio coverage can result to be irregular and poor or the data rate offered to be very low. A solution to this issue is to guarantee a proper radio coverage in the building with the extension of the mobile network inside the premise. However, this approach can become soon complex or expensive when it is applied to a real scenario because it requires the deployment of several base stations and of radio equipment for each mobile operator and service. In this outline, the appliance of distributed antenna systems can simplify the radio coverage within a premise.

A distributed antenna system (DAS) is a network of spatially separated antennas fed by coaxial cable, Cat-5 or fiber from a central office, or base station hotel, where all the base stations of the operators and their services are located. While it is possible to implement a DAS by using copper technologies, the superior characteristics of optical fibers have focused a lot of

effort in the implementation of fiber DASs (F–DASs) [24]. Fig. 1.11 shows an in-building F–DASs infrastructure. The base station hotel collects all the wireless technologies and services of the telecom operators which are distributed to the remote antenna units through optical links.

A F–DAS typically exploits the radio over fiber (RoF) technology, which consists in the transport of the radio signal over a fiber-optic link [25]. RoF systems can be classified into three categories depending on the way the radio signal is transported on the fiber-optic link:

- the **RF-over-fiber** technique carries the radio signal in its original band by modulating the light in an analog way. It guarantees complete transparency and it is the approach typically used for all the radio signals up to 10 GHz [26].

- the **IF-over-fiber** technique carries a down-converted version of the original radio signal, which modulates the light in an analog way. Then, the IF version of the radio signal is up-converted by electrical or optical means at the remote antenna unit before being radiated into the air [27]. This approach is typically used for the transport of high frequency radio signals, such as at 60 GHz [28, 29] and at 75–100 GHz [30].

- the **Digitized RF-over-fiber** technique carries the radio signal in a digital way. The radio signal is digitized according to the Nyquist pass-band sampling theorem and its samples are transported by a digital fiber-optic link [31]. This approach allows to employ the widespread digital fiber links, but it is currently able to transport few narrow-band radio carriers and with a higher cost compared to the RF-over-fiber technique [32].

Since WLAN, WPAN and mobile/cellular systems use radio frequencies below 5 GHz, the most convenient radio over fiber approach is constituted by the RF-over-Fiber technique. The broadband capability of F–DAS based on RF-over-Fiber technology allows the simultaneous transport of several mobile/cellular systems and also of radio signal compliant with WLAN and

WPAN standards. Moreover, due to the transparency to the radio format, it provides future-proof upgradability.

However, it is important to underline that a F–DAS is not in principle a low-cost system, hence the effective convenience of its implementation will depend on the scenario where it is considered to be applied. For this reason, as it was done in section 1.2, I differentiate the two cases of large-medium and small in-building networks.

1.3.1 Large and medium in-building networks

Large and medium buildings are a case of in-building networks where there can be a need for a multi-operator and multi-service wireless distribution system. Indeed, a shopping mall or a corporate building is a scenario where a large number of low-mobility users ask to access the radio resources simultaneously. Therefore, a F–DAS can be the solution to provide a good radio coverage while keeping the cost per operator/service under control due to the shared nature of a F–DAS infrastructure.

In large and medium in-building networks the wireless coverage through F–DAS should be implemented by RF-over-fiber techniques. The capability of multi-band and multi-operator is certainly of primary importance in large and medium premises, together with a future-proofness of the implemented network.

For this reason, as described in section 1.2.1, silica fibers are considered as the proper transmission medium for the implementation of large and medium in-building F–DASs. Moreover, also in this case both silica SMF and MMF are good candidates depending on the application. In particular, SMF is a mandatory choice for a new installation in large premises, while new silica MMF can be used in medium buildings and existing MMF can be exploited in both scenarios.

Several RF-over-fiber techniques can be employed for RF signals distribution in combination with silica fibers. I differentiate them into three main categories:

- Intensity modulation techniques

- Phase or frequency modulation techniques
- Hybrid phase/frequency and intensity modulation techniques

Intensity modulation techniques are the simplest method to deliver a RF signal and are realized via a direct or external modulation of a laser [33]. The transmitter intensity modulation is usually connected with a receiver direct detection achieved by a single photodiode [34], thus constituting an intensity modulation – direct detection (IM–DD) system.

The IM–DD technique is applied to the great majority of current commercial F–DAS systems for cellular signal distribution. Indeed, IM–DD systems are able to deliver radio signals up to about 4–5 GHz for some hundreds of meters of MMF and for tens kilometers of SMF [35, 36]. Strong limitations come for higher radio frequencies or longer fiber link lengths due to modal dispersion for MMF or chromatic dispersion for SMF [37, 38].

Phase or frequency modulation techniques consist in the modulation of the phase/frequency of the light emitted by a laser [39]. The receiver can be realized via a coherent scheme [40] or a phase to intensity modulation converter scheme, realized by a dispersive medium [41], an optical frequency discriminator [42] or an interferometric detection scheme [43, 44].

The main advantage of this technique with respect to intensity modulated systems is the possibility to achieve a higher broadband RF link gain and a lower noise, hence enhancing the dynamic-range of the analog optical link [45]. Phase or frequency modulation techniques are yet at a research stage and are not applied to commercial F–DAS systems, but they could turn interesting in the future if the complexity and cost of the system will reduce.

Hybrid phase/frequency and intensity modulation techniques apply simultaneously an intensity and a phase/frequency modulation to the light emitted by a laser. This scheme can be used to obtain particular modulation format such as optical single sideband (SSB) modulation [46, 47]. The receiver can be based on several schemes depending on the modulation scheme used. To demodulate the SSB signal a direct detection scheme is typically employed [48].

The advantage of an hybrid phase/frequency and intensity modulation

with respect to the previous two modulation schemes is not general. For optical SSB the advantage is a major resilience to chromatic dispersion [46]. As for phase/frequency modulation, hybrid modulation is presently not applied to commercial F–DAS systems due to cost-issues and complexity.

Since the length of an in-building RF-over-fiber link does not exceed few kilometers of length in large premises, and few hundreds of meters in medium premises, the IM–DD technique is still an attractive solution for the distribution of current and emerging WLAN, WPAN and cellular mobile signals which are all below 3 GHz.

1.3.2 Home and small in-building networks

Contrary to large and medium premises, home and small in-building networks do not require to support a multi-operators multi-services wireless distribution. Indeed, home or small office costumer pays a fee to just one telecom operator. For this scenario several mobile operators have studied the possibility to provide their customers with a femto-cell, or femto-node, which is a simple, small and light cellular base station able to support 4-8 mobile users within a small office or a home environment, and connect to the mobile network via the access network (e.g. a digital subscriber line (DSL) connection) [49]. Moreover, also other types of technologies, such as WiFi, do not require more than one or two access points to cover all the home or small office network.

In this scenario a separate in-building F–DAS becomes then unnecessary. However, the possibility of using a fiber-optic infrastructure also for the transport of wireless services to enhance the radio coverage can still be convenient and attractive. Fig. 1.12 shows the scenario I am referring to. All the home or small building services coming from the access network, the satellite and wireless networks are centralized to the building gateway. These services are then distributed to the different rooms through a converged optical backbone. The in-building users can have access to the different services via a wireline or a wireless connection. Note that with respect to the scenario presented in Fig. 1.9 where a wireless connection was enabled through

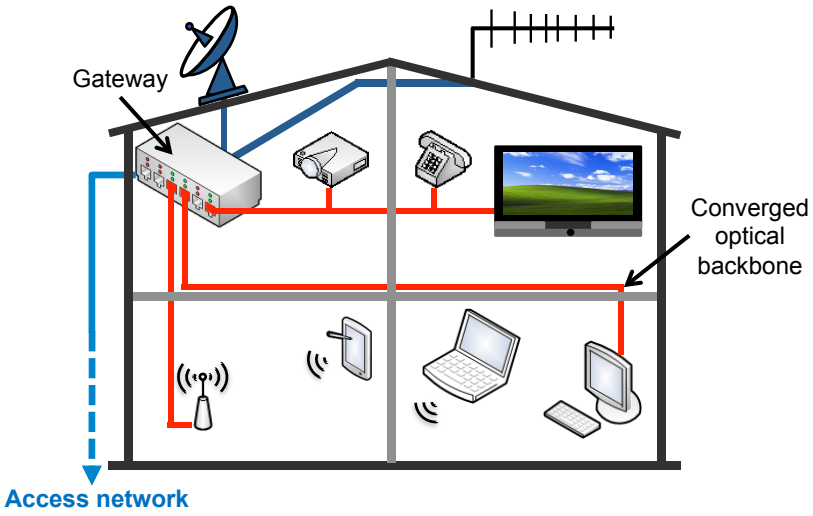

Figure 1.12: Converged optical backbone for home and small in-building networks

a separate wireless access point, in Fig. 1.12 wireline and wireless services are together delivered in the optical backbone and a simple RF front-end is used to "tap" and irradiate the wireless services.

As stated in section 1.2.2, 1 mm diameter POF can be employed to implement a low-cost optical backbone for wireline services. The possibility to use 1 mm diameter POF to transport broadband wireless signal has been demonstrated in [50]. However, the capability to support a converged scenario needs still to be proved.

1.4 Summary

Fiber optic technologies and techniques for in-building networks have been presented in this chapter. Section 1.1 described optical fibers based on silica and polymer materials intended for indoor applications. For silica fiber, the characteristics and classification of standardized single and multimode fibers were reported, while for polymer fiber, plastic optical fibers based on PMMA materials with a diameter of 1 mm were introduced. In particular,

the standard POF, and 1 mm diameter PMMA POFs with a graded-index or a multi-core profile were described.

Sections 1.2 and 1.3 presented the application of these fiber technologies to in-building networks. Single and multimode silica fibers find appropriate applications in large and medium building networks. For wireline services distribution multimode fiber can reach 10 Gbit/s transmission up to 600 m, while for 40 and 100 Gbit/s multimode fiber is limited to 150 m. For longer distances and higher data rates single mode fiber should be considered. For wireless services distribution the fiber distributed antenna system was introduced as an enabling technology to enhance the radio coverage. An overview of the state-of-the-art techniques was reported, and the cost-effectiveness of the IM–DD RF-over-fiber technique for in-building networks has been underlined. My contribution on the potential achievement of this last technique in conjunction with current optical components will be pointed out in chapter 2 and 3 of this dissertation with reference to single and multimode fibers, respectively.

For small building networks, such as small office and home scenarios, the benefits of employing 1 mm diameter PMMA POFs were discussed. Indeed, small building networks are very cost-sensitive due to the absence of cost sharing. For this reason, silica fiber solutions are not widespread applicable, while copper solutions, e.g. Cat-5, and power line communications are typically utilized. However, with respect to copper solutions plastic optical fibers have the advantage to be thinner and to be able to share electrical wiring ducts. Commercial POF products support 100 Mbit/s transmission up to 100 m, while prototypes have been reported for 1 Gbit/s transmission up to 75 m on standard step-index POF. Only recently, multi-gigabit transmission over 1 mm diameter PMMA POFs was demonstrated. In chapter 4 my research activity on multigigabit POF solutions will be described.

The possibility to exploit POF for a converged wireline and wireless optical backbone in small-building scenarios has been discussed in subsection 1.3.2. With reference to this challenge, chapter 5 will report my contribution on converged short-range communications over 1 mm diameter PMMA POF.

Chapter 2

RoF systems over SMF for in-building F–DAS

In this chapter studies on state-of-the-art F–DAS links employing SMF and directly modulated distributed feed-back (DFB) lasers are reported. An efficient and accurate model evaluating the performance of the transmission of real radio signals in these links is presented. Finally, transmission experiments employing UMTS and WiMAX signals will be presented and compared with simulated results.

2.1 Developed theoretical model

In this section I present the modeling of the different components of our system. The scope of this activity is to obtain a numerical model which is able to calculate some important link performance parameters while keeping the simulation time and the complexity under control.

This chapter is based on the results published in P1., P9., and P14.

2.1.1 Directly modulated laser

2.1.1.1 Intensity modulation and transmitter non-linearities

An intensity modulation produced by the direct modulation of a laser diode gives rise to an optical power $P(t)$ that can be written as,

$$P(t) = P_0 + \eta_{TX} i(t) + \alpha_2 i^2(t) + \alpha_3 i^3(t) \tag{2.1}$$

where P_0 is the optical power, $i(t)$ is the electrical modulating current, η_{TX} is the conversion efficiency of the laser diode, α_2 and α_3 are the undesired non-linear coefficients of the second and third order [51].

The electrical modulating current $i(t)$ is a radio signal. It can be written as a generic pass-band signal, i.e. a carrier modulated in amplitude and in phase. An equivalent representation is to consider it as a sum of two orthogonal carriers modulated in amplitude at the same frequency, mathematically cos(.) and sin(.) functions of the same argument,

$$i(t) = I_{RF} \left[I(t) \cos\left(2\pi f_c t\right) - Q(t) \sin\left(2\pi f_c t\right) \right] = I_{RF} s(t) \tag{2.2}$$

where I_{RF} and f_c are the amplitude and the frequency of the carrier, respectively. $I(t)$ and $Q(t)$ are the in-phase and in-quadrature components, which contain the signal information.

In (2.2) I introduce the normalized modulating signal $s(t)$. There are two possible normalization choices. The first one is to normalize $s(t)$ to its maximum value, i.e. $\max(|s(t)|) = 1$. This is the common choice when considering digital baseband transmission, where the peak-to-peak electrical voltage or current is of primary importance, and it can measured via an oscilloscope. The second choice is to normalize the mean square value of $s(t)$ to get the same value of a sinusoidal tone, i.e. $\langle s^2(t) \rangle = 1/2$. Here, I took this second choice since I consider the analog transmission of a radio signal, where the main parameter under study is the electrical power, which is typically measured by a spectrum analyzer.

Using (2.2) in (2.1) it is,

$$\begin{aligned} P(t) &= P_0 \left[1 + \frac{\eta_{TX} I_{RF}}{P_0} s(t) + \frac{\alpha_2 I_{RF}^2}{P_0} s^2(t) + \frac{\alpha_3 I_{RF}^3}{P_0} s^3(t)\right] = \\ &= P_0 \left[1 + m_I s(t) + a_2 m_I^2 s^2(t) + a_3 m_I^3 s^3(t)\right] \end{aligned} \tag{2.3}$$

In (2.3) I introduce the optical modulation index (OMI), $m_I = \eta_{TX} I_{RF}/P_0$. Similarly, I define the second and third order coefficients $a_2 = \alpha_2 P_0/\eta_{TX}^2$ and $a_3 = \alpha_3 P_0^2/\eta_{TX}^3$.

It is possible to generalize (2.3) to the transmission of more than one radio signal,

$$P(t) = P_0 \left[1 + \sum_k m_k s_k(t) + a_2 \left(\sum_k m_k s_k(t)\right)^2 + a_3 \left(\sum_k m_k s_k(t)\right)^3\right] \tag{2.4}$$

where $s_k(t)$ is the k^{th} normalized modulating signal and m_k is its OMI.

Starting from (2.4) and using a two-tone test it is possible to determine experimentally the non-linear coefficients a_2 and a_3. In this case, it is,

$$\begin{aligned} P(t) &= P_0 \left[1 + m\left(\cos(2\pi f_{c,1} t) + \cos(2\pi f_{c,2} t)\right) + \right. \\ &\quad + a_2 m^2 \left(\cos(2\pi f_{c,1} t) + \cos(2\pi f_{c,2} t)\right)^2 + \\ &\quad \left. + a_3 m^3 \left(\cos(2\pi f_{c,1} t) + \cos(2\pi f_{c,2} t)\right)^3\right] \end{aligned} \tag{2.5}$$

To calculate a_2 we look at the ratio between the power of one of the two carriers at $f_{c,1}$ or $f_{c,2}$, identified as C, and the power of the second order intermodulation distorsion (IMD) at $f_{c,1} + f_{c,2}$, identified as $IMD2$,

$$\frac{C}{IMD2} = \frac{1}{a_2^2 m^2} \tag{2.6}$$

Since $C/IMD2$ changes with the input power C_{IN}, I will relate a_2 to the input intercept point of the second order (IIP2) [52], that is a quantity invariant with respect to C_{IN}. Indeed, it is $IIP2 = C/IMD2 + C_{IN}$. Then, it is,

$$a_2 = \frac{P_0}{\eta_{TX}} \sqrt{\frac{R_L}{2 \cdot IIP2}} \tag{2.7}$$

In (2.7) I applied the definition of m_I and $C_{IN} = R_L/2 \cdot I_{RF}^2$, where R_L is the load resistance, typically 50 Ω.

Similarly, it is possible to calculate a_3 from the input intercept point of the third order (IIP3),

$$a_3 = \left(\frac{P_0}{\eta_{TX}}\right)^2 \frac{2R_L}{3 \cdot IIP3} \tag{2.8}$$

2.1.1.2 Frequency chirping

When a laser is directly modulated in intensity it also produces an unwanted frequency and phase modulation, called frequency chirping. The frequency deviation is equal to,

$$\Delta f(t) = \frac{\alpha}{4\pi}\left(\frac{d\left(\ln(P(t)\right)}{dt} + \kappa P(t)\right) \tag{2.9}$$

α is the line-width enhancement factor and κ is the adiabatic frequency chirp scaling factor [53].

Substituting (2.4) in (2.9) and approximating at the first order we have,

$$\Delta f(t) \approx \sum_k m_k \cdot \frac{\alpha}{4\pi}\left(\frac{ds_k(t)}{dt} + \kappa P_0 s_k(t)\right) = \sum_k \Delta f_k(t) \tag{2.10}$$

The derivative of $s_k(t)$ in (2.10) is equal to,

$$\begin{aligned}\frac{ds_k(t)}{dt} &= \left(\frac{dI_k(t)}{dt} - 2\pi f_{c,k} Q_k(t)\right)\cos\left(2\pi f_{c,k} t\right) + \\ &+ \left(\frac{dQ_k(t)}{dt} - 2\pi f_{c,k} I_k(t)\right)\sin\left(2\pi f_{c,k} t\right)\end{aligned} \tag{2.11}$$

Since $s_k(t)$ are pass-band signal, $I_k(t)$ and $Q_k(t)$ are slow varying signals compared to the radio carrier at frequency $f_{c,k}$. Then, applying the slowly varying envelope approximation [54], it is $|dI_k(t)/dt| \ll 2\pi f_{c,k}|Q_k(t)|$ and $|dQ_k(t)/dt| \ll 2\pi f_{c,k}|I_k(t)|$. Thus, (2.11) can be approximated as,

$$\frac{ds_k(t)}{dt} \approx -2\pi f_{c,k}\left(Q_k(t)\cos\left(2\pi f_{c,k} t\right) + I_k(t)\sin\left(2\pi f_{c,k} t\right)\right) \tag{2.12}$$

It is possible to proceed further to get,

$$\begin{aligned}\frac{d^2 s_k(t)}{dt^2} &\approx -(2\pi f_{c,k})^2 \left(I_k(t)\cos\left(2\pi f_{c,k}t\right) - Q_k(t)\sin\left(2\pi f_{c,k}t\right)\right) = \\ &= -(2\pi f_{c,k})^2 s_k(t) \end{aligned} \tag{2.13}$$

From (2.13) we get then,

$$\begin{aligned}\int_{-\infty}^{t} s_k(\tau)d\tau &\approx -\frac{1}{(2\pi f_{c,k})^2}\frac{ds_k(t)}{dt} = \\ &= \frac{1}{2\pi f_{c,k}}\left(Q_k(t)\cos\left(2\pi f_{c,k}t\right) + I_k(t)\sin\left(2\pi f_{c,k}t\right)\right) \end{aligned} \tag{2.14}$$

From this last result we can calculate the phase variation, $\varphi_k(t)$, induced by the frequency deviation $\Delta f_k(t)$.

$$\begin{aligned}\varphi_k(t) &= 2\pi\int_{-\infty}^{t}\Delta f_k(\tau)d\tau = m_k\cdot\frac{\alpha}{2}\left(s_k(t) + \kappa P_0\int_{-\infty}^{t} s_k(\tau)d\tau\right) = \\ &= m_k\cdot\frac{\alpha}{2}\left[\left(I_k(t) + \frac{\kappa P_0}{2\pi f_{c,k}}Q_k(t)\right)\cos\left(2\pi f_{c,k}t\right) - \right. \\ &\quad \left. - \left(Q_k(t) - \frac{\kappa P_0}{2\pi f_{c,k}}I_k(t)\right)\sin\left(2\pi f_{c,k}t\right)\right] \end{aligned} \tag{2.15}$$

To determine experimentally the factors α and κ, I employed the delayed self-homodyne technique [55, 56]. In this method the laser source is directly modulated with a sinusoidal tone, thus generating an intensity and a frequency/phase modulation. To measure the frequency/phase modulation a phase-to-intensity conversion is obtained with an interferometer. In the case of a modulation signal equal to $s(t) = \cos(2\pi f_c t)$ the phase $\varphi(t)$ becomes,

$$\begin{aligned}\varphi(t) &= m\cdot\frac{\alpha}{2}\left[\cos\left(2\pi f_c t\right) + \frac{\kappa P_0}{2\pi f_c}\sin\left(2\pi f_c t\right)\right] = \\ &= m\cdot\frac{\alpha}{2}\sqrt{1+\left(\frac{\kappa P_0}{2\pi f_c}\right)^2}\cdot\sin\left[2\pi f_c t + \arctan\left(\frac{2\pi f_c}{\kappa P_0}\right)\right] = \\ &= p\sin\left[2\pi f_c\left(t-\nu\right)\right] \end{aligned} \tag{2.16}$$

The self-homodyne technique is able to measure the phase index p together with the modulation index m, from which we can recover the intrinsic

characteristic of the laser p/m at several modulation frequency f_c.

$$\frac{p}{m} = \frac{\alpha}{2}\sqrt{1 + \left(\frac{\kappa P_0}{2\pi f_c}\right)^2} \tag{2.17}$$

From the values of p/m determined at different values of the modulation frequency, f_c, it is possible to extrapolate the characteristic quantities α and κ. Since typical values for κ are between 2 and 10 GHz/mW while they are between 4 and 10 mW for P_0, the ratio $\kappa P_0/2\pi f_c \gg 1$ for modulation frequencies well below the resonance frequency of the laser, which is typically ranging from 4 to 10 GHz for laser intended for analog applications below 10 GHz [57]. Equivalently this means that the frequency modulation component (proportional to κ) tends to overcome the phase modulation component. For this reason, it is a common practice to consider a frequency modulation index K_f in (MHz/mA) instead of the phase modulation index p/m. The two quantities are related by,

$$\Delta f(t) = p f_c \cos\left[2\pi f_c\,(t-\nu)\right] = K_f I_{RF} \cos\left[2\pi f_c\,(t-\nu)\right] \tag{2.18}$$

In Fig. 2.1 it is shown a comparison of the values of p/m and K_f versus the modulating frequency f_c for typical values of the quantities α, κ and P_0. It can be observed that the frequency index K_f can be considered almost constant for modulation frequencies typical of mobile radio communications (f_c ranging from 700 to about 2700 MHz), while the phase index p/m strongly varies especially in the radio frequencies region. Indeed, for frequencies well below the resonance frequencies K_f is not so depending on the modulation frequency f_c. In the following the transmitter frequency chirp characteristic will be often referred through its frequency index K_f.

2.1.1.3 Electrical field

With the mathematical model of the laser intensity modulation and frequency chirping it is possible to express the electrical field $E(t)$,

$$\begin{aligned} E(t) &= \sqrt{2ZP(t)} \cdot \exp\left\{\jmath 2\pi \left[f_0 t + \int_{-\infty}^{t} \Delta f(\tau) d\tau\right]\right\} = \\ &= E_{LP}(t) \exp\left\{\jmath 2\pi f_0 t\right\} \end{aligned} \tag{2.19}$$

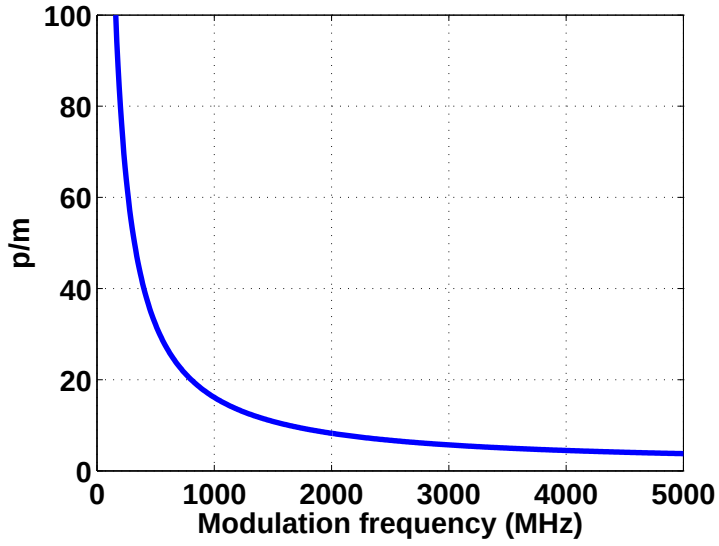

(a)

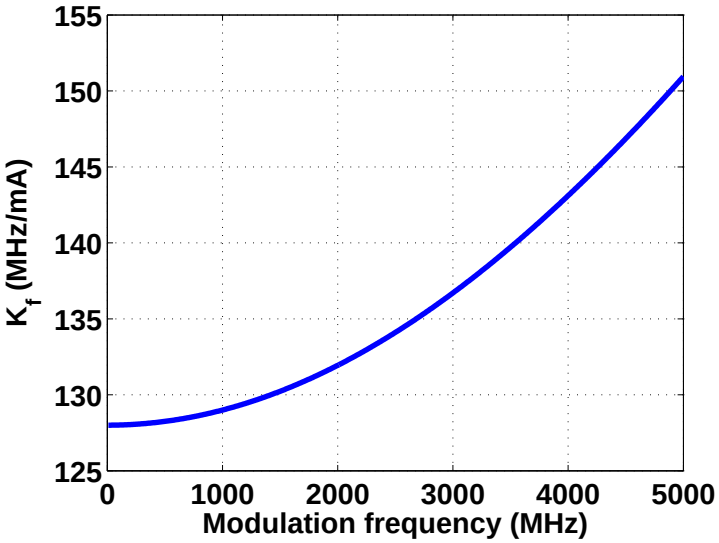

(b)

Figure 2.1: Example of phase modulation index p/m (a) and corresponding frequency index K_f (b)

where Z is the wave impedance [58] and f_0 is the central emission frequency of the laser.

In (2.19) I defined the complex-envelope or equivalent low-pass electrical field $E_{LP}(t)$. Using (2.4), (2.10) and (2.15) it is,

$$E_{LP}(t) = E_0\sqrt{1+\sum_k m_k s_k(t) + a_2\left(\sum_k m_k s_k(t)\right)^2 + a_3\left(\sum_k m_k s_k(t)\right)^3}\cdot \cdot \exp\left\{\jmath\sum_k \varphi_k(t)\right\} \quad (2.20)$$

$E_0 = \sqrt{2ZP_0}$ is the electrical field amplitude, and $\varphi_k(t)$ is the phase modulation generated by the k^{th} modulating signal.

Equations (2.19) and (2.20) allow writing the electrical field generated by the direct modulation of a laser source by a set of radio signals, identified by their in-phase and in-quadrature components and carrier frequencies.

In Fig. 2.2 an example of the application of equation (2.20) is shown. In this case there are two modulating signal centered at $f_{c,1} = 900$ MHz and $f_{c,2} = 1900$ MHz, respectively, and with a bandwidth of 5 MHz each. In Fig. 2.2(a) the ideal spectrum of $E_{LP}(t)$ with only a linear intensity modulation is depicted. In Fig. 2.2(b) the spectrum of $E_{LP}(t)$ is shown when also non-linear intensity modulation and frequency modulation are present. Note that the spectrum of $E_{LP}(t)$ in real situations occupies a larger bandwidth compared to the ideal intensity modulation. This is due primarily to the frequency chirping of the laser source and then to the non-linear behavior of the intensity modulation. In the case shown in Fig. 2.2 the required bandwidth to describe correctly $E_{LP}(t)$ becomes at least 10 times the ideal intensity modulation case. This is reflected in the value of the sample time value that is required for an accurate description of $E_{LP}(t)$.

2.1.2 Singlemode fiber propagation

The propagation model for the single mode fiber assumes that a linear behavior can be adopted. That means that we can consider as negligible the

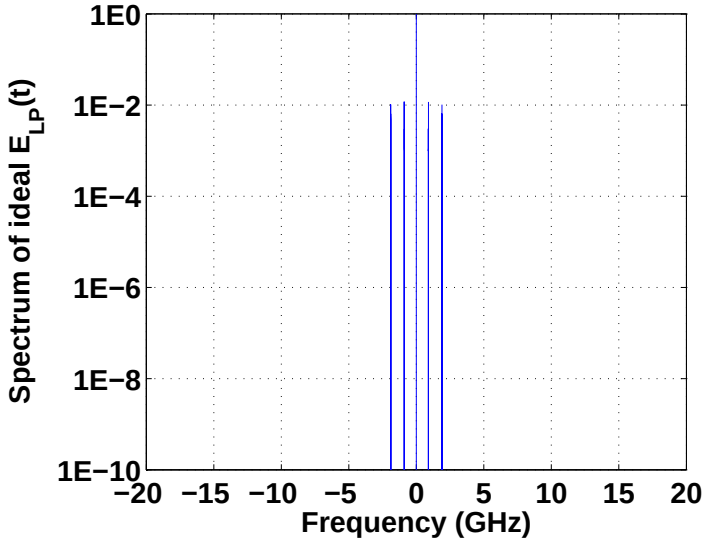

(a)

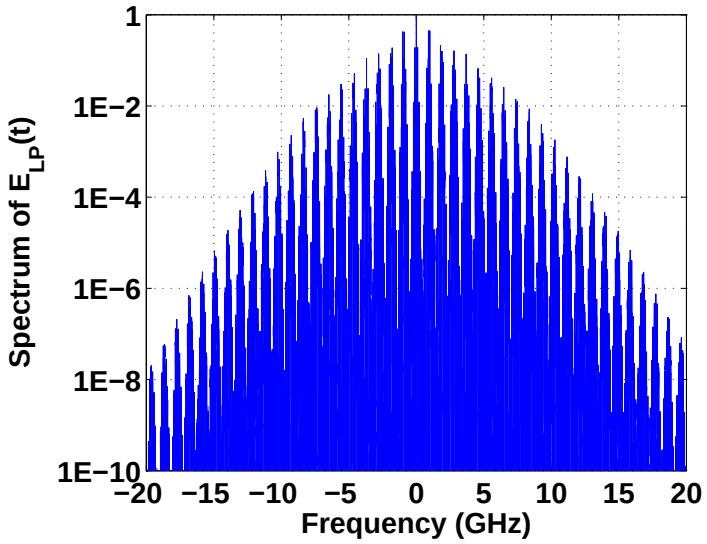

(b)

Figure 2.2: Spectrum of $E_{LP}(t)$ in the case of an ideal intensity modulation (a) and in a real situation (b). The modulating signals are centered at $f_{c,1} = 900$ and $f_{c,2} = 1900$ MHz and with a bandwidth of 5 MHz

effects of the fiber non-linearities, and that an impulse response or a transfer function can be defined [3]. In particular, the transfer function $H(f,z)$ is,

$$H(f,z) = e^{-(\alpha(f)+\jmath\beta(f))z} \tag{2.21}$$

$\alpha(f)$ and $\beta(f)$ are, respectively, the fiber attenuation and propagation coefficient per unit of length. z is the fiber length and f is the optical frequency.

Since this model is applied to a single wavelength source as described in subsection 2.1.1, the transfer function in (2.21) can be approximated around the optical central frequency f_0 of the source by,

$$H(f,z) = e^{-\alpha(f_0)z} \cdot e^{-\jmath\left(\beta(f_0)+\tau_g 2\pi(f-f_0)-\frac{c}{4\pi f_0^2}D(2\pi(f-f_0))^2\right)z} \tag{2.22}$$

where τ_g is the fiber group delay per unit of length, c is the light velocity, and D is the fiber chromatic dispersion in s/m^2.

Since the electrical field in (2.19) is an optical pass-band signal, the optical transfer function $H(f,z)$ in (2.21) can be replaced by an equivalent low-pass transfer function, $H_0(\overline{f},z)$, which is applied to $E_{LP}(t)$ of (2.20). Moreover it is possible to neglect the terms containing $\beta(f_0)$ and τ_g since they simply provide a phase shift to the optical carrier and a time delay to the complex-envelope. It is then,

$$H_0(\overline{f},z) = e^{-\alpha(f_0)z} \cdot e^{\jmath\frac{c}{4\pi f_0^2}D(2\pi\overline{f})^2 z} \tag{2.23}$$

where $\overline{f} = f - f_0$ is the frequency distance from the optical carrier.

The corresponding time impulse response is

$$h_0(t,z) = e^{-\alpha(f_0)z} \cdot \sqrt{\frac{\pi}{\jmath\vartheta}} \cdot e^{\jmath\frac{\pi^2}{\vartheta}t^2} \tag{2.24a}$$

$$\vartheta = D \cdot z \cdot \frac{\pi c}{f_0^2} \tag{2.24b}$$

Theoretically the impulse response in (2.24a) can be employed to describe numerically the fiber propagation. However, the infinite time length of $h_0(t)$ does not allow this approach. For this reason the linear fiber propagation is usually modeled in the frequency domain by multiplying the Fourier

Transform of $E_{LP}(t)$ with the transfer function $H_0(\overline{f}, z)$ and with an inverse Fourier transform of the obtained result. This model is general and correct, but it becomes heavy in term of resources and time for increasing size of the samples which describes $E_{LP}(t)$, i.e. decreasing sample time and/or increasing simulation time. In this framework, a numerical method employing the convolution of a short impulse response with respect to the signal $E_{LP}(t)$ can bring advantages in terms of time simulation and resources needed.

Therefore, I aim to determine an impulse response which, contrary to $h_0(t, z)$, exhibits a finite time length. My starting point is to note that the complex-envelope $E_{LP}(t)$ has a finite double-side bandwidth B. For our aim $H_0(f, z)$ can then also be considered limited to this bandwidth. Therefore it is possible to assume,

$$H_{0,B}(\overline{f}, z) = H_0(\overline{f}, z) \cdot W_B(\overline{f}) \tag{2.25}$$

where $W_B(\overline{f})$ is a window with the property to limit the transfer function bandwidth around B.

Among the infinite choices for this window I choose the following,

$$W\left(\overline{f}\right) = \begin{cases} 1 & \left|\overline{f}\right| \leq B/2 \\ e^{-\left(\frac{|\overline{f}|-B/2}{\Delta\overline{f}}\right)^2} & \left|\overline{f}\right| > B/2 \end{cases} \tag{2.26}$$

where $\Delta\overline{f}$ is a window parameter

The main advantage of this window function is that the impulse response obtained through the inverse Fourier transform of $H_{0,B}(\overline{f}, z)$ can be expressed by an analytical formula. After some calculations it is,

$$h_{0,B}(t, z) = e^{-\alpha(f_0)z} \cdot \left(h_B\left(t, z\right) + h_+\left(t, z\right) + h_-\left(t, z\right)\right) \tag{2.27a}$$

$$\begin{aligned} h_B\left(t, z\right) \;=\; & e^{-\jmath\frac{\pi^2}{\vartheta}t} \cdot \sqrt{\frac{\jmath\pi}{\vartheta}} \left[\frac{1}{2}\mathrm{erf_Z}\left(\sqrt{\frac{\vartheta}{\jmath}}\frac{B}{2} + \frac{\pi}{\sqrt{\jmath\vartheta}}t\right) - \right. \\ & \left. - \frac{1}{2}\mathrm{erf_Z}\left(-\sqrt{\frac{\vartheta}{\jmath}}\frac{B}{2} + \frac{\pi}{\sqrt{\jmath\vartheta}}t\right)\right] \end{aligned} \tag{2.27b}$$

$$h_{\pm}(t,z) = \frac{\sqrt{\pi}\cdot \mathrm{erfc_Z}\left(u_{\pm}(z)\right)}{2\sqrt{\frac{1}{\Delta\overline{f}^2}-\jmath\vartheta}}\cdot \cdot\exp\left[\frac{\left(\pm\jmath\pi t+\frac{B}{2\Delta\overline{f}^2}\right)^2}{\frac{1}{\Delta\overline{f}^2}-\jmath\vartheta}-\frac{B^2}{4\Delta\overline{f}^2}\right] \tag{2.27c}$$

$$u_{\pm}(z) = \frac{B}{2}\cdot\sqrt{\frac{1}{\Delta\overline{f}^2}-\jmath\vartheta}-\frac{\pm\jmath\pi t+\frac{B}{2\Delta\overline{f}^2}}{\sqrt{\frac{1}{\Delta\overline{f}^2}-\jmath\vartheta}} \tag{2.27d}$$

the quantity ϑ is the same as in (2.24b), while $\mathrm{erf_Z}$ and $\mathrm{erfc_Z}$ are the error function and the complementary error function, respectively, evaluated for a complex input argument [59].

Fig. 2.3 shows a comparison between the real and imaginary components of $h_0(t,z)$ and $h_{0,B}(t,z)$. In this example $f_0 = 193.4$ THz, $\alpha(f_0) = 0$ dB/km, $D = 16$ ps/nm/km, $z = 50$ km, $B = 28$ GHz, $\Delta\overline{f} = 3$ GHz.

As depicted in Fig. 2.3, the impulse response $h_{0,B}(t,z)$ is a energy finite function, which goes to zero for increasing time (t). The key to diminish the computation complexity and time with respect to the frequency domain approach is to limit together with the bandwidth also its time-width. To this purpose, the length of $h_{0,B}(t,z)$ can be fixed to that interval whose values are above a relative threshold, th, with respect to the maximum absolute value. Referring to the case considered to obtain Fig. 2.3, taking a threshold $th = 10^{-4}$ the time-width of the impulse response is 1.6 ns for $z = 10$ km and 2.1 ns for $z = 50$ km. Taking a threshold $th = 10^{-3}$ the time-width reduces to 0.75 ns and 0.95 ns for $z = 10$ km and $z = 50$ km, respectively.

From a numerical point of view, the time-width reduction of the impulse response reflects in a faster computation of the convolution of $E_{LP}(t)$ with $h_{0,B}(t,z)$. In relation with the previous numerical example, choosing a sampling time $\Delta t = 1/(2(B+2\Delta\overline{f})) = 25$ ps the impulse response is constituted by 65 and 85 samplings in the case of $z = 10$ km and $z = 50$ km, respectively, for $th = 10^{-4}$. For $th = 10^{-3}$ the samples reduces to 31 and 39. The samples required for $E_{LP}(t)$ depend instead on the simulation time. In the case of

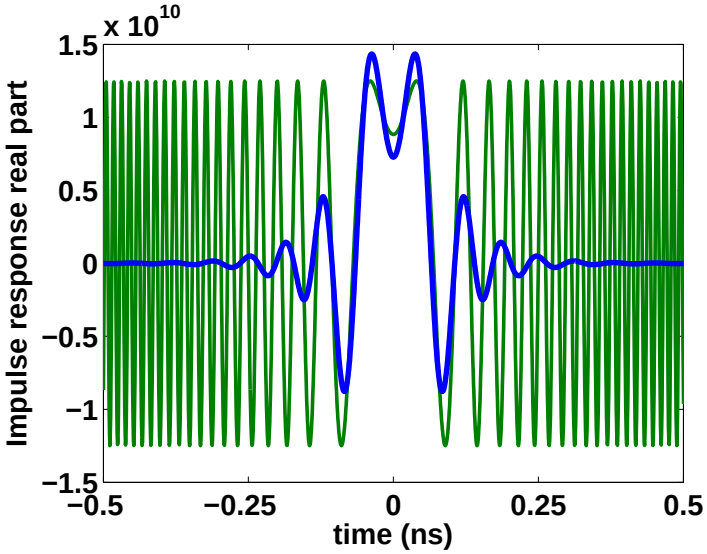

(a) Real component

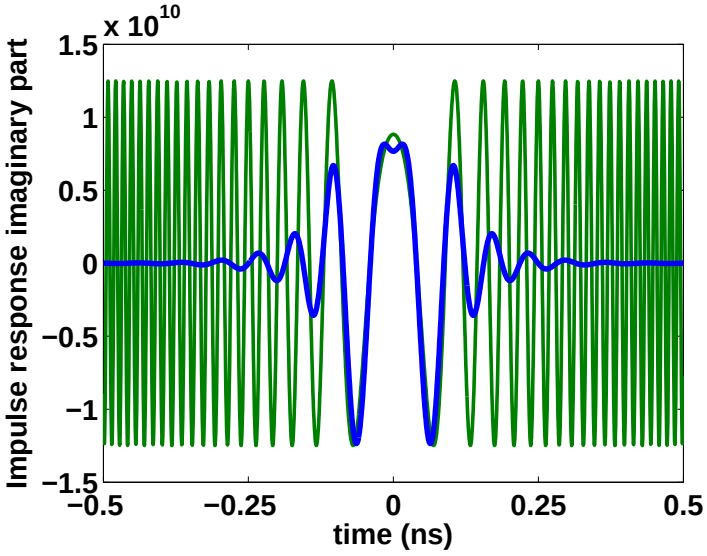

(b) Imaginary component

Figure 2.3: Comparison of the real (a) and imaginary (b) components of an example of the bandwidth unlimited impulse response $h_0(t, z)$ (green) with the corresponding bandwidth limited impulse response $h_{0,B}(t, z)$ (blue)

500 μs of simulated time the samples of $E_{LP}(t)$ are 20 million which is infinitely more than the 30-90 samples required for the impulse response. Thus the numerical convolution between $E_{LP}(t)$ and $h_{0,B}(t,z)$ becomes identical to a filtering of $E_{LP}(t)$ performed by a finite impulse response (FIR) filter with 30-90 taps. This leads to an efficient computation of the convolution algorithm in term of memory resources and simulation time.

2.1.3 Photodiode model

The photodiode model describes the envelope detection performed by the photodiode. If it is able to receive all the spectrum components within the system bandwidth B, then the received current $i_{out}(t)$ can simply be calculated by,

$$i_{out}\left(t,z\right) = \mathrm{R} \cdot \frac{\left|E_{LP}(t) * h_{0,B}(t,z)\right|^2}{2Z} \tag{2.28}$$

where R is the photodiode responsivity and the notation $*$ stands for the convolution operation.

Fig. 2.4 displays numerical results obtained by applying the model described in this section. The input field and the fiber impulse response are the same shown in Fig. 2.2(b) and Fig. 2.3(a)–(b), respectively. In Fig. 2.4(a) the spectrum of the current $i_{out}(t)$ in the case of no fiber propagation is shown. In this case what is shown is the spectrum of $|E_{LP}(t)|^2$, which is due to the linear and non-linear intensity modulation. Fig. 2.4(b) shows the spectrum of the current $i_{out}(t)$ after a fiber length $z = 50$ km. Comparing Fig. 2.4(a) and 2.4(b), it can be observed that higher order harmonics are generated by fiber propagation. For this reason, some important performance parameters need to be taken under consideration to define the signal quality transmission. In the next section experimental results of radio signals transmission on IM–DD links employing singlemode fiber will be shown and compared with the simulation predictions obtained by the application of the model described in this section.

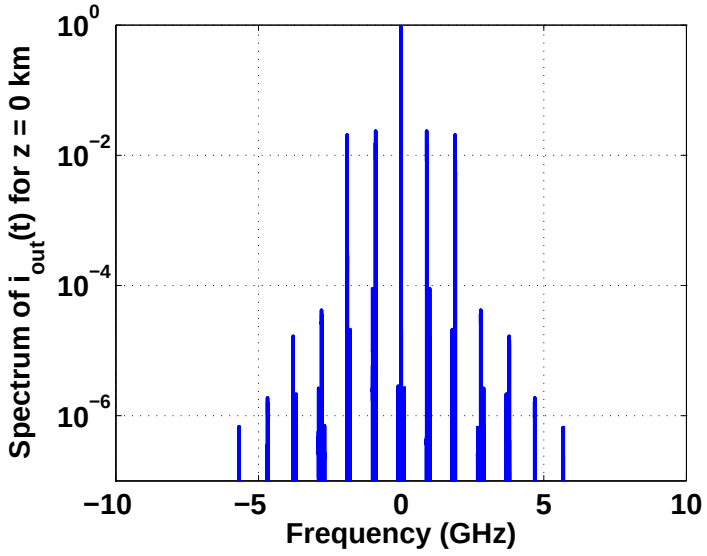

(a) $z = 0$ km

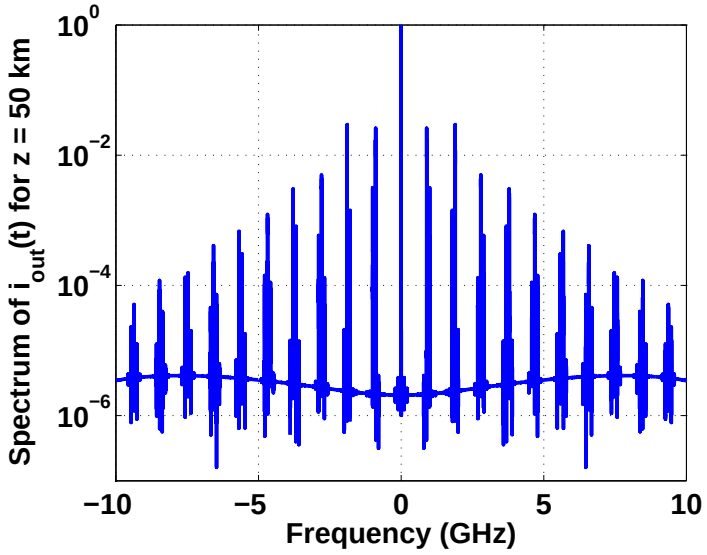

(b) $z = 50$ km

Figure 2.4: Comparison of the spectrum of $i_{out}(t)$ for a fiber length $z = 0$ km (a) and for $z = 50$ km (b)

2.2 Experimental and theoretical results

In this section the experimental activity performed on RoF IM–DD links employing singlemode fiber is presented. The aim of this work was to verify the adjacent channel leakage ratio (ACLR) degradation due to RoF TX, RX and fiber propagation in a dual standard transmission. After the introduction on the experimental setup, experimental results obtained with different RoF TXs will be shown and compared with simulation results obtained with the numerical model described in section 2.1.

2.2.1 Experimental setup

The experimental setup is shown in Fig. 2.5. Two RF signals were combined and transmitted on the RoF IM–DD link. The RF signals were generated by two Agilent N5182A MXG vector signal generators (VSGs) and were compliant with the UMTS and WiMAX standards. The UMTS carrier frequency was fixed in the 2110–2170 MHz downlink (DL) band [60] and the WiMAX carrier frequency in the 2500–2690 MHz DL band [61], which are both IMT-2000 allocated bands. The output power of the two VSGs was kept at a value which gave the highest level of ACLR directly from the instrument. Since this value was below $-10/-5$ dBm, two highly-linear power amplifiers (PAs) were needed to increase the power levels to highest values.

The combination of the two signals was applied to three different RoF TXs based on directly modulated DFB laser diodes (LDs). The emission wavelength, λ_0, of the RoF TXs were around 1550 nm (C band) and the optical power was +10 dBm. The other measured and modeled parameters are listed in Tab. 2.1. The output pig-tail of the RoF TX was connected to an optical variable attenuator, followed by different spans of SMF to reach a total length ranging from few meters to 50 km. All the fiber spans were of standard SMF compliant with ITU-T G.652 recommendation [4]. Therefore, fiber chromatic dispersion was modeled according to the formula in [4],

$$D(\lambda_0) = D_{1550} + S_{1550}(\lambda_0 - 1550) \tag{2.29}$$

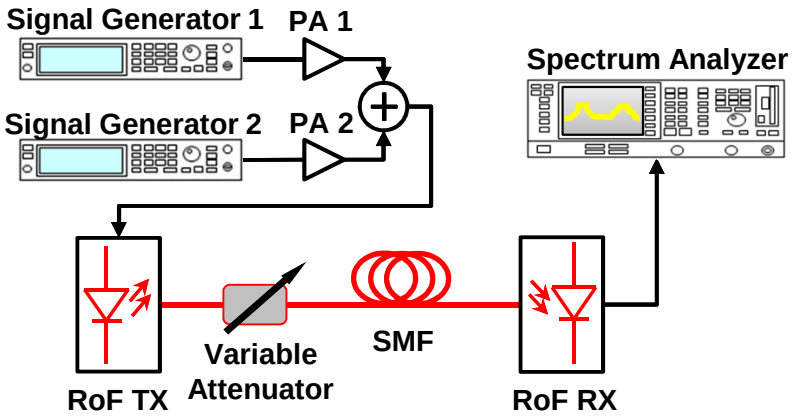

Figure 2.5: Experimental setup employed for the characterization of IM–DD links on SMF

Parameter	*TX1*	*TX2*	*TX3*
λ_0 (nm)	1551.31	1540.11	1547.72
f_0 (THz)	193.25	194.65	193.70
P_0 (mW)	10	10	10
η_{TX} (mW/mA)	0.075	0.084	0.072
IIP2 (dBm)	61.0	47.0	49.0
IIP3 (dBm)	44.0	38.0	40.0
a_2	1.88×10^{-2}	8.41×10^{-2}	7.79×10^{-2}
a_3	2.36×10^{-2}	7.49×10^{-2}	6.43×10^{-2}
α	4.55	3	4
κ (GHz/mW)	4.78	4.08	1.32
K_f (MHz/mA)	135	85	45

Table 2.1: Parameters of RoF TXs used in the experimental activity

D_{1550} is the dispersion coefficient at 1550 nm ($ps/nm \times km$) and S_{1550} is the dispersion slope coefficient at 1550 nm ($ps/nm^2 \times km$). According to the representative value in [4], I set $D_{1550} = 17\ ps/nm \times km$ and $S_{1550} = 0.056\ ps/nm^2 \times km$. The corresponding dispersion values at the three different operating wavelengths of the RoF TXs were 17.07, 16.45, and 16.87 $ps/nm \times km$ for TX1, TX2 and TX3, respectively.

The variable attenuator was used to guarantee the same optical power at the output of the fiber with the aim to set the noise level of the link in all the configurations reported. In particular, the total optical attenuation including optical connectors was set to 13.5 dBm.

Finally, the fiber was connected to a RoF RX based on a InGaAs positive-intrinsic-negative (PIN) photodiode followed by a trans-impedance amplifier (TIA). The electrical output port of the RoF RX was connected to an Agilent N9020A MXA vector signal analyzer (VSA) used to measure the ACLR in the two bands. The RoF RX was modeled by (2.28) assuming that receiver non-linearities were negligible compared to the ones induced by the transmitter and by the optical link. This assumption was well consistent since the received optical power was quite low due to the fixed optical budget of 13.5 dBm. Hence, the TIA worked in his linear region.

To explain graphically the meaning of ACLR, Fig. 2.6 shows an example of ACLR test on a UMTS signal centered at 2140 MHz. The nominal TX-channel bandwidth is 3.84 MHz and the channel spacing is 5 MHz. Therefore, the adjacent channels are centered at 2140 ± 5 MHz, and the alternate channels at 2140 ± 10 MHz. The nominal channel bandwidth is always 3.84 MHz for the adjacent and alternate channels. The ACLR is defined as the ratio between the power in the adjacent channel and the power in the transmitted channel. It is expressed in dB or dBc (dB carrier).

In the same way, the ACLR test for a WiMAX signal set the nominal channel bandwidth to 9.5 MHz with a carrier spacing of 10 MHz. In my case, the signal was centered at 2675 MHz, thus the adjacent channels were centered at 2675 ± 10 MHz.

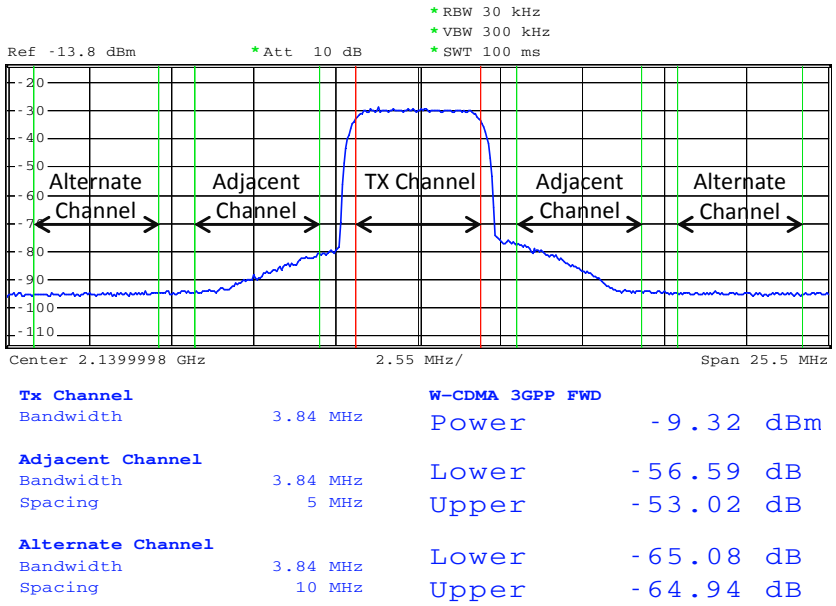

Figure 2.6: Example of ACLR test for an UMTS–compliant signal

2.2.2 Experimental results and comparisons

The purpose of the experimental activity was to study the mutual distortions generated by the simultaneous transmission of the two different radio signals. Hence, the ACLR test was performed for different pairs of modulation indexes of the two signals, namely m_1 and m_2. I chose the three discrete values 0.1, 0.2 and 0.3 for m_1 and m_2 and it was possible to consider all the combinations with $m_1 + m_2 \leq 0.4$ avoiding LD clipping.

From Fig. 2.7 to Fig. 2.9 the most significant results are shown for the three RoF TXs. In subfigures (a) three different curves of ACLR for the UMTS signal are shown versus increasing fiber length. Each curve corresponds to a different value of the modulation index of the WiMAX signal, m_2, varying from 0.1 to 0.3, while the modulation index of the UMTS signal, m_1, was kept at 0.1. Similarly, subfigures (b) show three different curves of ACLR for the WiMAX signal with m_2 constant at 0.1 and m_1 varying from 0.1 to 0.3. The only exception are Fig. 2.9(a) and Fig. 2.9(b) where the only

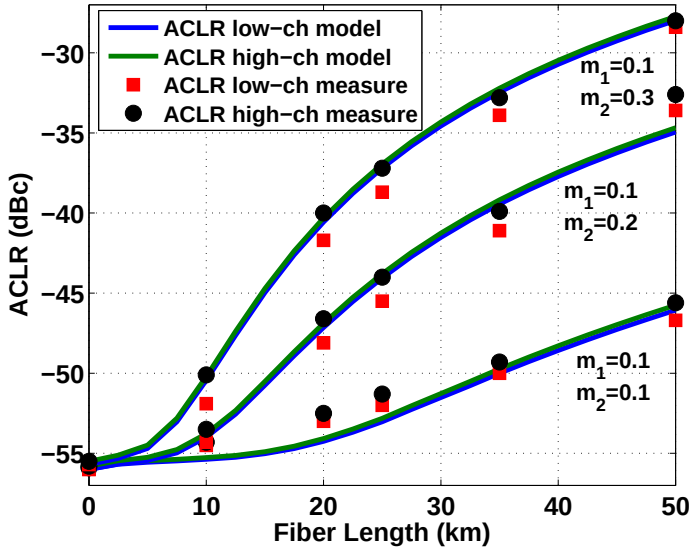

(a) UMTS

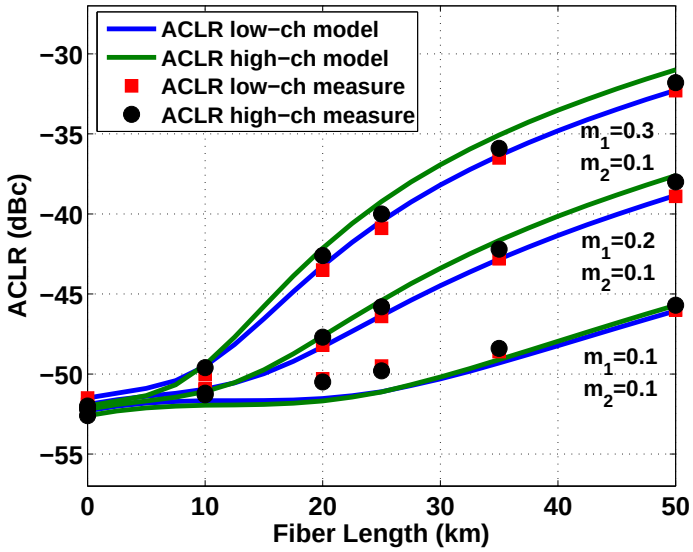

(b) WiMAX

Figure 2.7: Measured and simulated ACLR values for the link employing RoF TX1 in the case of UMTS (a) and WiMAX (b) signals. m_1 and m_2 refer to UMTS and WiMAX, respectively

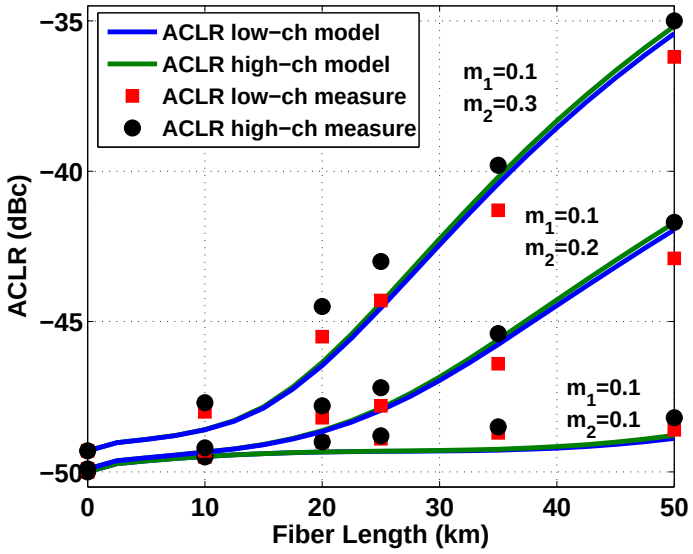

(a) UMTS

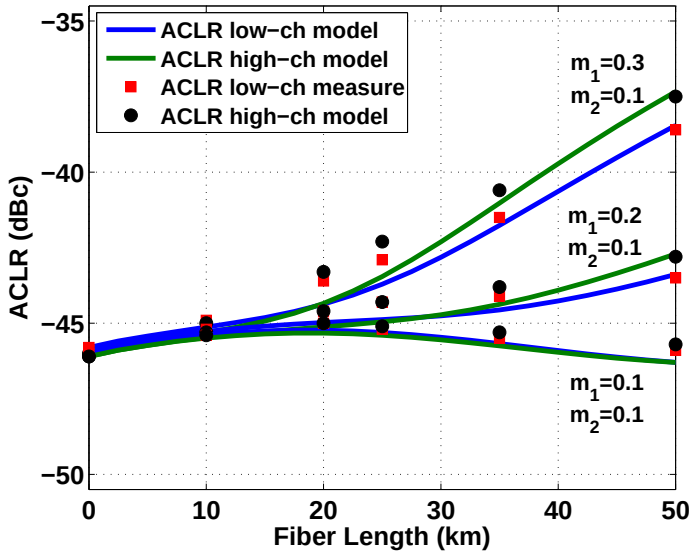

(b) WiMAX

Figure 2.8: Measured and simulated ACLR values for the link employing RoF TX2 in the case of UMTS (a) and WiMAX (b) signals. m_1 and m_2 refer to UMTS and WiMAX, respectively

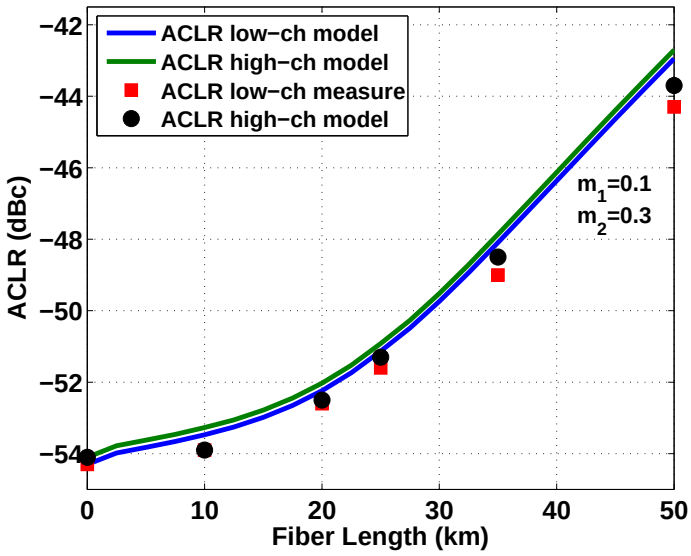

(a) UMTS

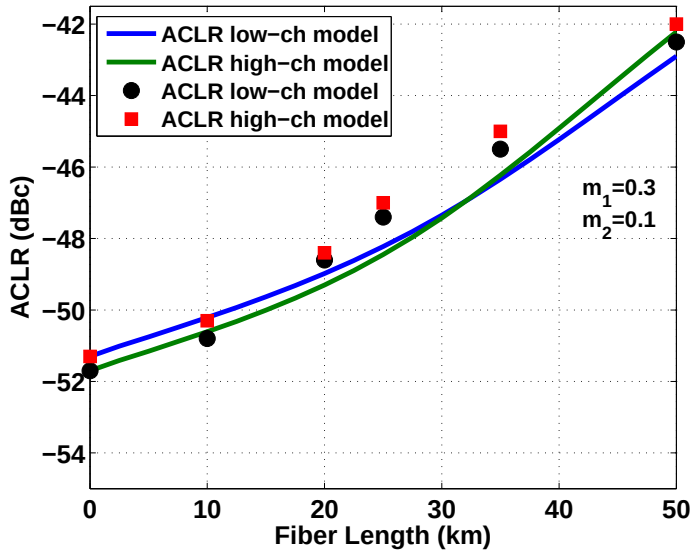

(b) WiMAX

Figure 2.9: Measured and simulated ACLR values for the link employing RoF TX3 in the case of UMTS (a) and WiMAX (b) signals. m_1 and m_2 refer to UMTS and WiMAX, respectively

pairs $m_1 = 0.1$ and $m_2 = 0.3$ (a), $m_1 = 0.3$ and $m_2 = 0.1$ (b) are shown since the other combinations give rise to similar curves that are not reported here for readability of the two graphs.

Note that the ACLR values for short distances differ in the two cases of UMTS and WiMAX signals. This is caused by the different integration bandwidth in the two cases. UMTS nominal bandwidth is fixed to 3.84 MHz and WiMAX nominal bandwidth to 9.5 MHz. Hence, when distortions generated in the adjacent channels caused by the optical link are negligible compared to noise, the power in the adjacent channel increases with integration bandwidth. In this particular case the difference is $10 \times \log_{10}(9.5/3.84) = 3.9$ dB, that is observed in Fig. 2.7, 2.8 and 2.9.

Another behavior for short distances to be observed is that ACLR values are practically independent from m_2 (a) or m_1 (b). This means that the non-linear characteristics of the RoF TX does not produce a considerable cross-effect on ACLR. The only exception is the case $m_1 = 0.1$ and $m_2 = 0.3$ in Fig. 2.8(a). This is due to the worse non-linearity characteristics of RoF TX2 with respect to the other transmitters as shown in Tab. 2.1.

For increasing fiber length the common behavior is the increase of ACLR in every curve in Fig. 2.7, 2.8 and 2.9. The only exception is the curve corresponding to $m_1 = 0.1$ and $m_2 = 0.1$ in Fig. 2.8(b). This peculiar effect is not due to a decrease of the power in the adjacent channel, but to a relative increase of the power in the received TX-channel caused by a phase-to-intensity conversion produced by fiber chromatic dispersion. This is exactly the same reason which produces a higher relative increase of power in the adjacent channels with respect to the TX-channel as can be observed in all the other cases in Fig. 2.7, 2.8 and 2.9. However, when the relative increase of power in the adjacent channel remains under the noise floor the ACLR variations are driven by the relative change of power in the TX-channel. This is the case of the curve corresponding to $m_1 = 0.1$ and $m_2 = 0.1$ in Fig. 2.8(b).

Pointing the attention in all the curves with $m_1 = 0.1$ and $m_2 = 0.3$ in Fig. 2.7(a), 2.8(a), 2.9(a), it is possible to observe that the relative increase of ACLR is higher for RoF TX1 compared to RoF TX2 and for RoF TX2

compared to RoF TX3. This is caused by the higher adiabatic frequency chirp scaling factor κ (or equivalently adiabatic frequency chirp K_f) of RoF TX1 with respect to RoF TX2 and of RoF TX2 with respect to RoF TX3, as summarized in Tab. 2.1. Higher κ (or K_f) also produces higher detrimental interference between the two radio signals as can be observed comparing the curves corresponding to a different pair of m_1 and m_2 in Fig. 2.7, 2.8, 2.9.

From a design point of view, the latter discussion might lead to the conclusion that DFB LDs with low frequency chirp parameters are preferable for multi-standard transmission. However, referred to the in-building scenarios of this thesis the fiber length does not typically exceed few kilometers. With this range limitation all the three RoF TXs are compliant with the -45 dBc and -37 dBc of ACLR upper limit fixed for UMTS and WiMAX standards [62, 61], respectively, because the performance parameters are influenced mainly by the intensity modulation non-linearities. Actually, RoF TX1 gives rise to the best performance in this case. On the contrary, for longer SMF transmission only RoF TX3 is able to be compliant with the specifications up to 40 km.

2.3 Summary

This chapter presented the modeling and experimental activity on state-of-the-art RoF links employing SMF and directly modulated DFB lasers. A numerical model providing accurate results together with a reduced need of simulation time and resources was described in section 2.1. An experimental activity focused on the determination of the ACLR performances of the simultaneous transmission of UMTS and WiMAX signals has been described in section 2.2. A good agreement between experimental and simulation results has been reported. Hence, the developed model has been proven to be a useful tool for the design of SMF IM–DD links. Moreover, the experimental activity pointed out the interactions between the different modulating RF signals and related them to the transmitter properties, among all the frequency chirp parameter K_f. Some criticalities have been underlined for

SMF link exceeding few tens of kilometer, while a general wide feasibility of the studied cost-effective RoF links has been illustrated for short-range ones, which are typically needed in in-building scenarios.

Chapter 3

RoF systems over MMF for in-building F–DAS

In this chapter radio over multi-mode fiber (RoMMF) IM–DD systems employing DFB and fabry-perot (FP) lasers will be deeply studied. A model describing the impact of modal noise on gain, harmonic and intermodulation distortions is derived. The theoretical results will be compared with experimental ones to obtain some link design rules. Finally, transmission experiments employing LTE signals will be presented.

3.1 Developed theoretical model

3.1.1 Electrical field produced by the laser

The starting point of the theoretical model is the electrical field produced by a directly modulated DFB LD. To determine the gain of the link and the harmonic and intermodulation distortions of the system I consider as modulating signal two sinusoidal tones at frequencies $f_{c,1}$ and $f_{c,2}$ with identical OMI, $m_1 = m_2 = m_I$. In this case (2.19) and (2.20) lead to the following

This chapter is based on the results published in P2., P3., P11., P15., and P18.

electrical field $\bar{E}(t)$.

$$\bar{E}(t) = E_0 \cdot \bar{e}(x,y) \cdot \sqrt{1+y(t)} \cdot \exp\left\{\jmath\left[2\pi f_0 t + \psi(t)\right]\right\} \tag{3.1}$$

where

$$\begin{aligned} y(t) \;=\; & m_I\left[\cos\left(2\pi f_{c,1}t\right) + \cos\left(2\pi f_{c,2}t\right)\right] + \\ & + a_2 m_I^2\left[\cos\left(2\pi f_{c,1}t\right) + \cos\left(2\pi f_{c,2}t\right)\right]^2 + \\ & + a_3 m_I^3\left[\cos\left(2\pi f_{c,1}t\right) + \cos\left(2\pi f_{c,2}t\right)\right]^3 \end{aligned} \tag{3.2}$$

and

$$\psi(t) = \frac{K_f I_{RF}}{f_{c,1}} \sin\left(2\pi f_{c,1}\left(t-\nu_1\right)\right) + \frac{K_f I_{RF}}{f_{c,2}} \sin\left(2\pi f_{c,2}\left(t-\nu_2\right)\right) \tag{3.3}$$

The meaning of m, a_2, a_3, K_f, I_{RF} is the same of the laser model in section 2.1. Moreover, $\bar{e}(x,y)$ is the normalized field distribution to be coupled with the MMF, while x and y are the transversal coordinates. To derive (3.3) I used (2.16) and (2.18). The quantities ν_1 and ν_2 are referred to the sinusoidal tones at frequency $f_{c,1}$ and $f_{c,2}$, respectively.

3.1.2 Multimode fiber launch and propagation

The electrical field (3.1) is launched into a MMF. Hence, the modulation is divided onto the N_M different fiber modes [63]. The electrical field at the input of the fiber becomes,

$$\bar{E}_{in}(t) = E_0 \sum_{m=1}^{N_M} A_m \cdot \bar{e}_m(x,y) \cdot \sqrt{1+y(t)} \cdot \exp\left\{\jmath\left[2\pi f_0 t + \psi(t)\right]\right\} \tag{3.4}$$

Referring to the generic propagating mode of subscript m taken within the set of N_M modes: $\bar{e}_m(x,y)$ is the normalized field and A_m is the weight coefficient derived from,

$$A_m = \int_{S_\infty} \bar{e}_m\left(x,y\right) \bullet \bar{e}^*\left(x,y\right) dS \tag{3.5}$$

S_∞ stands for an infinite plane surface, the notation $\bullet$ for scalar product, and the superscipt $*$ for complex conjugation.

In the framework of this activity, I will report experimental results related to three types of launch, i.e. central launch, offset launch and overfilled launch. Central launch is obtained launching the single mode of a SMF in the center of the MMF, while offset launch is obtained launching the single mode of a SMF at a fixed offset from the center of the MMF. Overfilled launch is achieved employing a mode scrambler. Further details will be given in section 3.2.3.

To compare experimental and theoretical results the calculation of the coefficient A_m is required. To this purpose, the normalized electrical field $\bar{e}_m(x, y)$ was calculated through COMSOL Multiphysics®, an electromagnetic mode solver based on the finite element method. The refractive index profile $n(r)$ of a graded-index fiber was approximated by the generally adopted power law equation [63],

$$n(r) = \begin{cases} n_1\sqrt{1 - 2\Delta\left(\frac{r}{a}\right)^\alpha} & |r| \leq a \\ n_2 = n_1\sqrt{1-2\Delta} & |r| > a \end{cases} \tag{3.6}$$

where n_1 is the refractive index at the center of the fiber core, n_2 is the refractive index in the cladding, $\Delta = (n_1^2 - n_2^2)/(2n_1^2)$ is the relative index difference, a is the core radius, and α is the power law profile parameter.

Since the refractive index of core and cladding depends on the wavelength, also the index profile varies with the wavelength. To model the refractive index wavelength dependence a three terms Sellmeier equation is used for core and cladding refractive indexes [63],

$$n_k^2 - 1 = \sum_{i=1}^{3} \frac{A_i^{(k)}\lambda^2}{\lambda^2 - \left(l_i^{(k)}\right)^2} \tag{3.7}$$

where $l_i^{(k)}$ is the i-th resonance wavelength and $A_i^{(k)}$ its coefficient.

With the assumption that the cladding is made of pure SiO_2 and the core of SiO_2 doped with GeO_2 it is possible to determine the coefficients $l_i^{(k)}$ and $A_i^{(k)}$ using the values summarized in Tab. 3.1. For the cladding refractive

	SiO_2	GeO_2
A_1	$0.69616630E+00$	$0.80686642E+00$
l_1 (μm)	$0.68404300E-01$	$0.68972606E-01$
A_2	$0.40794260E+00$	$0.71815848E+00$
l_2 (μm)	$0.11624140E+00$	$0.15396605E+00$
A_3	$0.89747940E+00$	$0.85416831E+00$
l_3 (μm)	$0.98961610E+01$	$0.11841931E+02$

Table 3.1: Sellmeier Coefficients for SiO_2 and for GeO_2 from [64]

index, n_2, only the SiO_2 Sellemeier coefficients will be used. For the core refractive index in the center, n_1, a linear relationship will be used for the determination of the Sellmeier coefficients according to [64],

$$A_i^{(2)} = (1 - X) \cdot A_i^{SiO_2} + X \cdot A_i^{GeO_2} \tag{3.8a}$$

$$l_i^{(2)} = (1 - X) \cdot l_i^{SiO_2} + X \cdot l_i^{GeO_2} \tag{3.8b}$$

where X is the mole fraction of GeO_2.

According to [65], the standard MMF with a core diameter $2a = 50$ μm has $\Delta = 1$ % and $\alpha \approx 2.05$ to be optimum at 850 nm. That is the case of OM2, OM3 and OM4 MMFs which are differentiated by the manufacturing process able to obtain an index profile closer to the optimum one. By forcing $\Delta = 1$ % at 850 nm it is possible to calculate the mole fraction X of GeO_2 in the center of the fiber core. It results $X = 10$ mol%, corresponding to $n_1 = 1.4676$ and $n_2 = 1.4527$ at 850 nm, and $n_1 = 1.4618$ and $n_2 = 1.4469$ at 1310 nm.

The normalized electrical field $\bar{e}_m(x, y)$, the propagation constant β_m and the group delay τ_m of the fiber modes were obtained by solving an eigenvalue problem on the magnetic field [66]. The numerical solution was obtained by using the RF module of COMSOL Multiphysics® on the described geometry [67]. There are 380 propagating modes at 850 nm, and 156 propagating modes at 1310 nm. From $\bar{e}_m(x, y)$ we can determine A_m once $\bar{e}(x, y)$ has been fixed.

In the case of an input electrical field coming from a single mode fiber, $\bar{e}(x, y)$ was determined through the model described above assuming $2a = 9\ \mu m$, step-index profile ($\alpha \to \infty$ in (3.6)), and $X = 6.3$ mol% [68]. Naming $\bar{e}_{SMF}(x, y)$ the normalized electrical field of the SMF centered with respect to the SMF axis, in the case of central launch it is $\bar{e}(x, y) = \bar{e}_{SMF}(x, y)$, while in the case of offset launch it is $\bar{e}(x, y) = \bar{e}_{SMF}(x - x_{offset}, y)$ where x_{offset} is the misalignment between SMF and MMF.

Fig. 3.1 shows the values of A_m^2 at 1310 nm in two cases: central launch from a SMF in Fig. 3.1(a), and offset launch performed with $x_{offset} = 12\ \mu m$ in Fig. 3.1(b). Note that central launch excites few modes, all exhibiting a low mode number, m, (lower order modes), while offset launch excites a larger number of modes, many of which are modes with a high mode number, m, (higher order modes).

The reason to use offset launch is that, since in practice a perfect central launch is not feasible and can be corrupted by modal coupling, offset launch can guarantee a more stable situation compared to central launch. Moreover, Raddatz et al. stated that this technique can enhance the bandwidth of multimode fiber links [69, 70]. Anyway, this is not a general rule. Central and offset launch performance depends on the MMF and other restricted launch techniques can outperform central or offset launches [71, 72].

As mentioned above, with the MMF characterization performed with COMSOL Multiphysics® it was possible also to determine the propagation constant β_m and the group delay τ_m of every mode. In Fig. 3.2 typical values of β_m (a) and τ_m (b) are presented for a graded-index MMF at 1310 nm. Note that β_m in Fig. 3.2(a) has a stair-shape which allows to distinguish between groups of modes with similar propagation constants. The group delays τ_m in Fig. 3.2(b) are instead not exactly aligned on a stair-shape. Anyhow, I do not assemble in this model the modes into groups, but I use the complete set of modes, each one taken separately from the others. Furthermore, chromatic or third-order dispersions of the modes are not considered since this model is applied to short-range MMF link. However, analytical models taking into account chromatic and third-order dispersions have been reported [73, 74].

Starting from (3.4) the electrical field after propagation in a MMF of

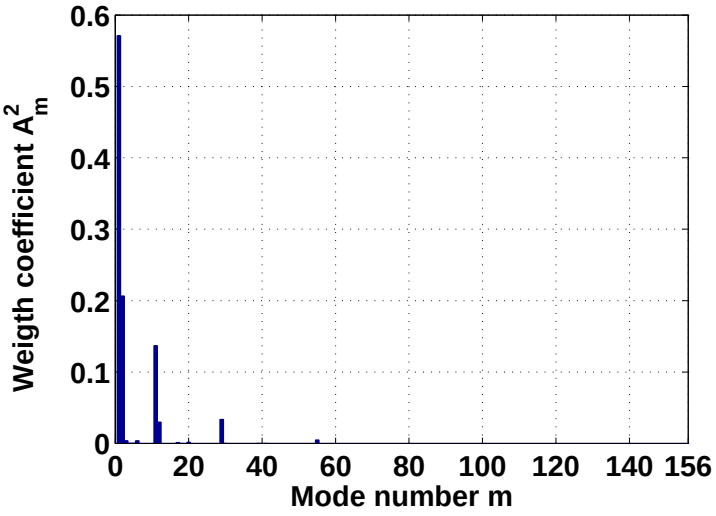

(a) Central launch

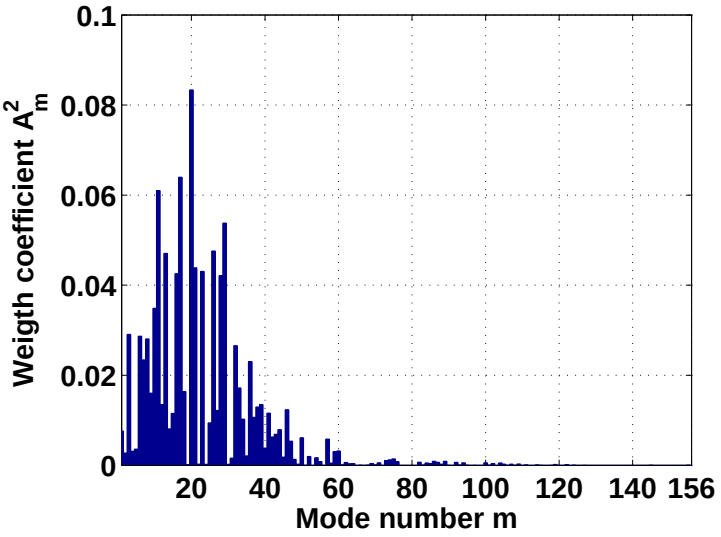

(b) Offset launch

Figure 3.1: Example of typical values of A_m^2 in the case of central launch (a) and offset launch with a displacement of 12 μm (b)

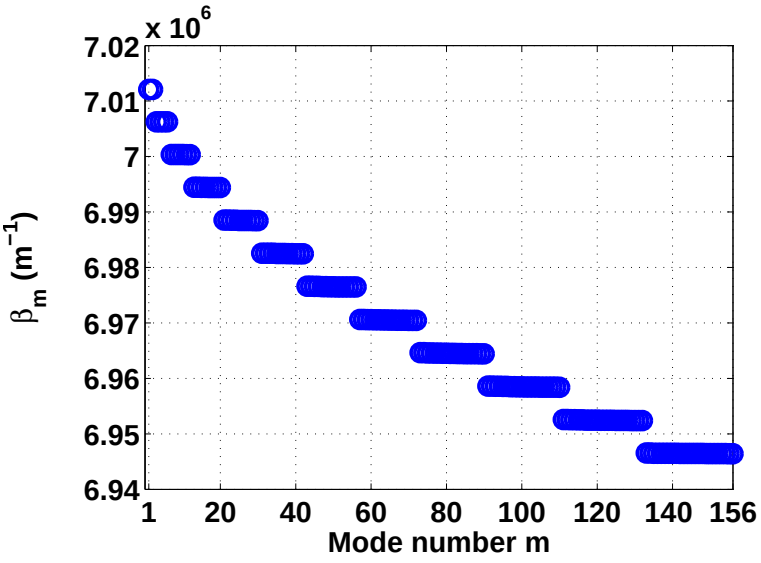

(a)

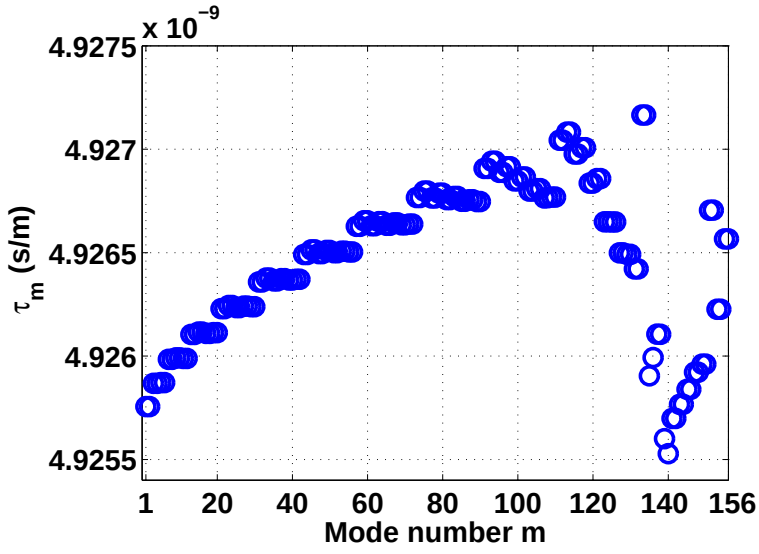

(b)

Figure 3.2: Example of typical values of β_m (a) and τ_m (b) for a graded-index MMF at 1310 nm

length z becomes then,

$$\begin{aligned}\bar{E}_{out}(t,z) &= E_0 \sum_{m=1}^{N_M} A_m \cdot \bar{e}_m(x,y) \cdot \sqrt{1+y(t-\tau_m z)} \cdot \\ &\cdot \exp\left\{\jmath\left[2\pi f_0 t - \beta_m z + \phi_m(t,z) + \psi(t-\tau_m z)\right]\right\} \end{aligned} \quad (3.9)$$

The quantity $\phi_m(t)$ is a slow phase variation with respect to the theoretical phase shift, $\beta_m z$, of the optical carrier [75]. This phase variation is induced by fluctuations of environmental physical quantities, such as the ambient temperature or mechanical stress. The presence of this random phase variation is the cause of modal noise. From a statistical point of view it is possible to assume $\phi_m(t)$ of different modes uniformly distributed between $-\pi$ and $+\pi$ and uncorrelated as done in [75]. This assumption does not describe any physical relationship between phase variations of different modes. Indeed, the random phase variations described by $\phi_m(t)$ are related to the changes of the refractive index profile, i.e. value and/or shape, caused by temperature or stress variation. A thermo-optic coefficient around $10^{-5}\ /^{\circ}K$ and a pressure-optic coefficient around $10^{-5}\ /10^{6} Nm^{-2}$ have been reported for fused silica [76, 77]. Consequently, I assume that the effective index of refraction of every mode changes with temperature or pressure. Then, I define,

$$\phi_m(t,z) = \left(\beta_m - \frac{2\pi}{\lambda_0} n_{eff,m}(t)\right) z \quad (3.10)$$

where $n_{eff,m}(t)$ is the effective index of refraction of the m^{th} mode ($n_2 < n_{eff,m} < n_1$) [57].

Since $n_{eff,m}$ is related to the refractive indexes n_1 and n_2, it is reasonable to consider also its time variations related to the time variations of the same indexes. But, $n_{eff,m}$ referred to different modes will experience a different strength of slow variations. As a first approximation I consider $\phi_m(t)$ dependence from an external temperature variations $\Delta T(t)$ as,

$$\phi_m(t,z) = c_m \cdot \Delta T(t) + \phi_{0,m} \quad (3.11)$$

where c_m is a coefficient which takes into account the thermo-optic effects and $\phi_{0,m}$ is a random phase due to possible random imperfections of the fiber.

The initial phase $\phi_{0,m}$ can be chosen random between $-\pi$ and $+\pi$, while c_m can be chosen randomly between a minimum value and a maximum value with the same sign. These minimum and maximum values increase with fiber length, z, and can be simply estimated to fit experimental data since there is no simple direct relationship between refractive indexes and effective refractive indexes variations. With this model $\phi_m(t)$ is still uniformly distributed between $-\pi$ and $+\pi$, but phases related to different modes are no more uncorrelated. Considering two phase variations ϕ_m and ϕ_m related to mode m and n it is,

$$\mathrm{Cov}\left(\phi_m(t), \phi_n(t)\right) = \mathrm{E}\left[c_m c_n\right] \cdot \left\langle [\Delta T(t)]^2 \right\rangle + \mathrm{E}\left[\phi_{0,m}\phi_{0,n}\right] \tag{3.12}$$

where $\mathrm{Cov}\left(.,.\right)$ stands for statistical covariance, $\mathrm{E}\left[.\right]$ for statistical averaging, and $\langle . \rangle$ for time averaging. To obtain this result I took the hypothesis $\langle \Delta T(t) \rangle = 0$ which comes from the definition of temperature variation.

The result in (3.12) demonstrates that even if the statistical couples c_m, c_n and $\phi_{0,m}$, $\phi_{0,n}$ are uncorrelated the covariance of ϕ_m and ϕ_n is not zero since $E\left[c_m c_n\right]$ is always a positive number. This is due to the hypothesis of assuming c_m to be positive or negative for all modes. This assumption comes from the physical consideration that at a certain wavelength the index of refraction always decreases or increases for a positive temperature variation ΔT.

3.1.3 Receiver model

After the propagation in one span of MMF, the electrical field is detected by a photodiode. With respect to the SMF case of (2.28), it is crucial to consider the finite detecting area of the photodiode. Indeed, if in the SMF this means just a loss of optical power, in this case it also represents different attenuations for the MMF modes, and different mutual interference.

The received electrical current generated by the photodiode is,

$$\begin{aligned} i_{out}(t,z) &= \mathrm{R}\cdot\int_{S_{PD}}\frac{\left|\bar{E}_{out}(t,z)\right|^2}{2Z}dS = I_0\sum_{m=1}^{N_M}A_m^2 b_{mm}\left(1+y(t-\tau_m z)\right)+ \\ &+2I_0\cdot\Re\left\{\sum_{m=1}^{N_M-1}\sum_{n=m+1}^{N_M}A_m A_n b_{mn}\cdot\sqrt{1+y(t-\tau_m z)}\cdot\right. \\ &\cdot\sqrt{1+y(t-\tau_n z)}\cdot\exp\left\{\jmath\left[\psi(t-\tau_m z)-\psi(t-\tau_n z)\right]\right\}\cdot \\ &\left.\cdot\exp\left\{\jmath\left[\left(\phi_m(t,z)-\phi_n(t,z)\right)-\left(\beta_m-\beta_n\right)z\right]\right\}\right\} \end{aligned} \tag{3.13}$$

where $I_0 = \mathrm{R}E_0^2/2Z$ is the maximum possible direct current (DC) component, $\Re\{.\}$ stands for real part, and

$$b_{mn} = \int_{S_{PD}}\bar{e}_m(x,y)\bullet\bar{e}_n^*(x,y)\,dS \tag{3.14}$$

Note that b_{mn} given by (3.14) is the scalar product between the normalized electrical fields of MMF modes of numbers m and n computed over the detecting area of the photodiode, S_{PD}. Due to mode orthogonality, this quantity should ideally be equal to one for $m = n$ while it should be equal to zero for $m \neq n$. However, because of the finite detecting area of the photodiode neither condition is met. This non-ideal behavior is another factor which influences modal noise. Fig. 3.3 shows typical values of b_{mm} and b_{mn}. In this example I assumed that the photodiode surface was a square, with width 25 μm, misaligned of 2 μm with respect to the central axis of the MMF. From Fig. 3.3(a) it can be observed that b_{mm} values are mostly between 0.6 and 1 and tend to decrease for increasing m. This is due to the lower confinement of higher order modes in the core of the MMF. Fig. 3.3(b) shows $|b_{mn}|$ for $n = 20$. b_{m20} values are mainly between $1E-4$ and $1E-1$. Similar results can be presented for different values of n.

The phase differences present in the second summation in (3.13) need to be calculated,

$$\begin{aligned} \psi(t-\tau_m z)-\psi(t-\tau_n z) &= -\left[x_{mn,1}\cos\left(2\pi f_{c,1}\left(t-\bar{\tau}_{mn}-\nu_1\right)\right)+\right. \\ &\left.+\,x_{mn,2}\cos\left(2\pi f_{c,2}\left(t-\bar{\tau}_{mn}-\nu_2\right)\right)\right] \end{aligned} \tag{3.15}$$

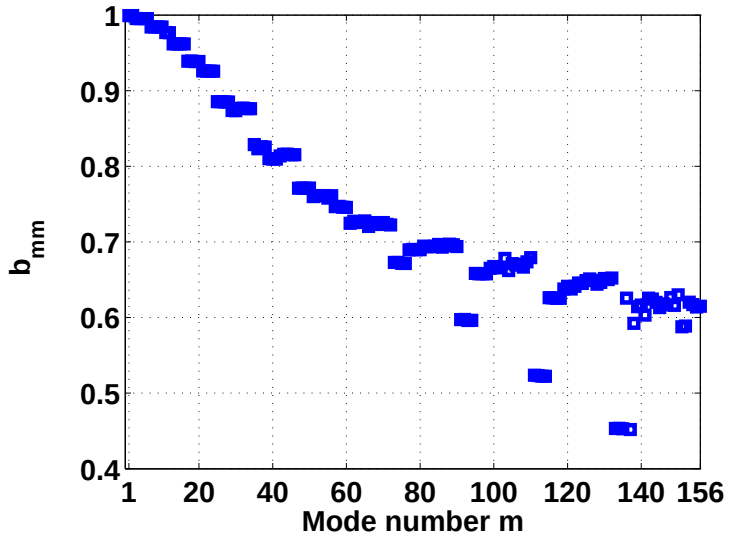

(a)

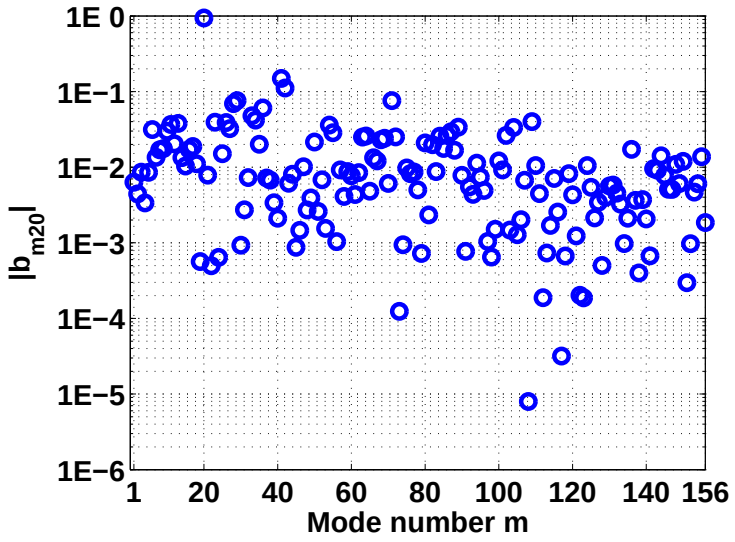

(b)

Figure 3.3: Example of typical values of b_{mm} (a) and b_{m20} (b) assuming the photodiode surface as a square with side 25 μm and a misalignment of 2 μm with respect to the central axis of the MMF

where

$$x_{mn,i} = 4\pi K_f I_{RF} \Delta\tau_{mn} \frac{\sin\left(2\pi f_{c,i} \Delta\tau_{mn}\right)}{2\pi f_{c,i} \Delta\tau_{mn}} \quad \text{for } i = 1, 2 \tag{3.16a}$$

$$\Delta\tau_{mn} = \frac{\tau_m - \tau_n}{2} z \tag{3.16b}$$

$$\bar{\tau}_{mn} = \frac{\tau_m + \tau_n}{2} z \tag{3.16c}$$

The quantity $x_{mn,i}$ in (3.16a) will be shown to be an important parameter which influences modal noise strength. It increases with the transmitter chirp factor, K_f, and with the amplitude current, I_{RF}. For the couples of modes with $|2\pi f_{c,i} \Delta\tau_{mn}| < \pi/2$, $x_{mn,i}$ also increases with fiber length z. This is the case of most of the couples of modes in short-range MMF link employing RF frequencies below 2–3 GHz.

The other part of the phase in (3.13) can be collected in,

$$\Delta\varphi_{mn}(t) = \left(\phi_m(t,z) - \phi_n(t,z)\right) - \left(\beta_m - \beta_n\right) z \tag{3.17}$$

Using (3.11) $\Delta\varphi_{mn}$ can be written in a form similar to ϕ_m,

$$\Delta\varphi_{mn}(t) = c_{mn} \cdot \Delta T(t) + \Delta\varphi_{0,mn} \tag{3.18}$$

where $c_{mn} = c_m - c_n$ and $\Delta\varphi_{0,mn} = (\phi_{0,m} - \phi_{0,n}) - (\beta_m - \beta_n) z$. Similarly to $\phi_{0,m}$ or $\phi_{0,n}$, $\Delta\varphi_{0,mn}$ can be chosen randomly between $-\pi$ and $+\pi$. On the other hand, contrary to c_m or c_n, c_{mn} referred to different couples of modes can have a different sign. This leads to take $\mathrm{E}[c_{mn}] = 0$. Consequently, $\mathrm{Cov}\left(\Delta\varphi_{mn}(t), \Delta\varphi_{kl}(t)\right)$ referred to different mode couples (m,n) and (k,l) can be zero if c_{mn}, c_{kl}, $\Delta\varphi_{mn}(t)$ and $\Delta\varphi_{kl}(t)$ are uncorrelated.

Using (3.15) and (3.17), (3.13) becomes,

$$\begin{aligned} i_{out}(t,z) \;=\; & I_0 \sum_{m=1}^{N_M} A_m^2 b_{mm} \left(1 + y(t - \tau_m z)\right) + 2I_0 \sum_{m=1}^{N_M - 1} \sum_{n=m+1}^{N_M} A_m A_n b_{mn} \cdot \\ & \cdot \sqrt{1 + y(t - \tau_m z) + y(t - \tau_n z) + y(t - \tau_m z) \cdot y(t - \tau_n z)} \cdot \\ & \cdot \left[\cos\left(\Delta\varphi_{mn}(t)\right) \cos\left(x_{mn,1} \cos\left(2\pi f_{c,1}\left(t - \bar{\tau}_{mn} - \nu_1\right)\right) + \right.\right. \\ & + \left. x_{mn,2} \cos\left(2\pi f_{c,2}\left(t - \bar{\tau}_{mn} - \nu_2\right)\right)\right) + \\ & + \sin\left(\Delta\varphi_{mn}(t)\right) \sin\left(x_{mn,1} \cos\left(2\pi f_{c,1}\left(t - \bar{\tau}_{mn} - \nu_1\right)\right) + \right. \\ & \left.\left. + \; x_{mn,2} \cos\left(2\pi f_{c,2}\left(t - \bar{\tau}_{mn} - \nu_2\right)\right)\right)\right] \end{aligned} \tag{3.19}$$

To determine the received current at each frequency all terms containing the time variable, t, in (3.19) were expanded with analytical series:

- the square root by using the Maclaurin series [59]:

$$\sqrt{1+x} = \sum_{k=0}^{\infty} \frac{(-1)^k (2k)!}{(1-2k)\,(k!)^2\,(4^k)} x^k \tag{3.20}$$

  where x is substitued by the content of the square root except from 1.

- the $\cos(x_{mn,1}... + x_{mn,1}...)$ and $\sin(x_{mn,1}... + x_{mn,1}...)$ by using the Jacobi-Anger expansion [59]:

$$e^{jx\cos\theta} = J_0(x) + 2\sum_{k=1}^{\infty} j^k J_k(x)\cos(k\theta) \tag{3.21}$$

  where J_k is a Bessel function of the k^{th} order [59].

Due to the initial assumption to consider laser non-linearities up to the third-order (see (3.2)), only power of m_I up to the third order should be taken into account. This means that the expansions in (3.20) and (3.21) should be considered for $k \leq 3$.

After a lengthy calculations the current can be determined at the following frequency components: DC, $f_{c,1}$, $f_{c,2}$, $2f_{c,1}$, $2f_{c,2}$, $f_{c,1}+f_{c,2}$, $3f_{c,1}$, $3f_{c,2}$, $2f_{c,1}-f_{c,2}$, and $2f_{c,2}-f_{c,1}$. The generic component at frequency $\bar{f}$ can be written as,

$$i_{out,\bar{f}}(t,z) = \left(\mathcal{A}_{c,\bar{f}} + \mathcal{B}_{c,\bar{f}}(t)\right)\cos\left(2\pi\bar{f}t\right) + \left(\mathcal{A}_{s,\bar{f}} + \mathcal{B}_{s,\bar{f}}(t)\right)\sin\left(2\pi\bar{f}t\right) \tag{3.22}$$

where

$$\mathcal{A}_{c,\bar{f}} = I_0 \cdot \mathrm{a}_{\bar{f}} \sum_{m=1}^{N_M} A_m^2 b_{mm} \cos\left(2\pi\bar{f}\tau_m z\right) \tag{3.23a}$$

$$\mathcal{A}_{s,\bar{f}} = I_0 \cdot \mathrm{a}_{\bar{f}} \sum_{m=1}^{N_M} A_m^2 b_{mm} \sin\left(2\pi\bar{f}\tau_m z\right) \tag{3.23b}$$

$$\mathcal{B}_{c,\bar{f}}(t) = 2I_0 \sum_{m=1}^{N_M-1} \sum_{n=m+1}^{N_M} A_m A_n b_{mn} D_{mn,\bar{f},c}(t) \tag{3.23c}$$

$$\mathcal{B}_{s,\bar{f}}(t) = 2I_0 \sum_{m=1}^{N_M-1} \sum_{n=m+1}^{N_M} A_m A_n b_{mn} D_{mn,\bar{f},s}(t) \tag{3.23d}$$

$$D_{mn,\bar{f},c}(t) = C_{mn,\bar{f},C,c} \cos\left(\Delta\varphi_{mn}(t)\right) + C_{mn,\bar{f},S,c} \sin\left(\Delta\varphi_{mn}(t)\right) \tag{3.23e}$$

$$D_{mn,\bar{f},s}(t) = C_{mn,\bar{f},C,s} \cos\left(\Delta\varphi_{mn}(t)\right) + C_{mn,\bar{f},S,s} \sin\left(\Delta\varphi_{mn}(t)\right) \tag{3.23f}$$

The value of $\mathrm{a}_{\bar{f}}$ in (3.23a) and (3.23b) comes from (3.2). In particular it is,

$$\mathrm{a}_{f_{c,1}} = \mathrm{a}_{f_{c,2}} = m_I \tag{3.24a}$$

$$\mathrm{a}_{2f_{c,1}} = \mathrm{a}_{2f_{c,2}} = \frac{1}{2} a_2 m_I^2 \tag{3.24b}$$

$$\mathrm{a}_{2f_{c,1}-f_{c,2}} = \mathrm{a}_{2f_{c,2}-f_{c,1}} = \frac{3}{4} a_3 m_I^3 \tag{3.24c}$$

The expressions of the terms $C_{mn,\bar{f},C,c}$ and $C_{mn,\bar{f},S,c}$ in (3.23e) and $C_{mn,\bar{f},C,s}$ and $C_{mn,\bar{f},S,s}$ in (3.23f) are reported in Tab. 3.2 for the component at DC and at $2f_{c,1}$, in Tab. 3.3 for the component at $f_{c,1}$, and in Tab. 3.4 for the component at $2f_{c,2} - f_{c,1}$. The expressions referred to other frequency components are not included in this thesis.

With all the terms in (3.22), the amplitude $I_{out,\bar{f}}$ of the component at frequency $\bar{f}$ can be determined,

$$I_{out,\bar{f}}(t) = \sqrt{\left(\mathcal{A}_{c,\bar{f}} + \mathcal{B}_{c,\bar{f}}(t)\right)^2 + \left(\mathcal{A}_{s,\bar{f}} + \mathcal{B}_{s,\bar{f}}(t)\right)^2} \tag{3.25}$$

From (3.25) it is possible to observe that the amplitude of the current at frequency $\bar{f}$ is ruled by non-fluctuating terms ($\mathcal{A}_{c,\bar{f}}$ and $\mathcal{A}_{s,\bar{f}}$) and time-fluctuating terms ($\mathcal{B}_{c,\bar{f}}(t)$ and $\mathcal{B}_{s,\bar{f}}(t)$). Indeed, these last terms depend from the difference of phases $\Delta\varphi_{mn}(t)$ and represent the modal noise contribution.

The characterization of the statistical distribution of $I_{out,\bar{f}}(t)$ is complex and in general possible only numerically. For this reason, I will only determine analytically the mean value of the received power at frequency $\bar{f}$ and the standard deviation for the components at DC and $f_{c,1}$. Other statistical quantities used in this work are determined numerically.

Table 3.2: Expression of $C_{mn,\bar{f},C,c}$, $C_{mn,\bar{f},S,c}$, $C_{mn,\bar{f},C,s}$ and $C_{mn,\bar{f},S,s}$ for DC and $2f_{c,1}$

DC
$C_{mn,DC,C,c} = J_0(x_{mn,1})J_0(x_{mn,2})\left\{1+\frac{m_I^2}{8}\left[\cos\left(2\pi 2 f_{c,1}\Delta\tau_{mn}\right)+\cos\left(2\pi 2 f_{c,2}\Delta\tau_{mn}\right)-2\right]\right\}$
$C_{mn,DC,S,c} = m_I\left[J_0(x_{mn,1})J_1(x_{mn,2})\cos\left(2\pi f_{c,2}\Delta\tau_{mn}\right)\cos\left(2\pi f_{c,1}\nu_1\right)+ J_0(x_{mn,2})J_1(x_{mn,1})\cos\left(2\pi f_{c,1}\Delta\tau_{mn}\right)\cos\left(2\pi f_{c,2}\nu_2\right)\right]$
$C_{mn,DC,C,s} = 0 \qquad C_{mn,DC,S,s} = 0$
$2f_{c,1}$
$C_{mn,2f_{c,1},C,c} = \frac{m_I^2}{8}J_0(x_{mn,1})J_0(x_{mn,2})\left[(4a_2-1)\cos\left(2\pi 2 f_{c,1}\Delta\tau_{mn}\right)+1\right]\underline{\cos}\left(2\pi(2f_{c,1})\bar{\tau}_{mn}\right) - 2J_0(x_{mn,2})J_2(x_{mn,1})\underline{\cos}\left(2\pi 2 f_{c,1}\left(\bar{\tau}_{mn}+\nu_1\right)\right)$
$C_{mn,2f_{c,1},S,c} = m_I J_0(x_{mn,2})J_1(x_{mn,1})\cos\left(2\pi f_{c,1}\Delta\tau_{mn}\right)\underline{\cos}\left(2\pi\left(2f_{c,1}\bar{\tau}_{mn}+f_{c,1}\nu_1\right)\right)$
$C_{mn,2f_{c,1},C,s}$ ($C_{mn,2f_{c,1},S,s}$) identical to $C_{mn,2f_{c,1},C,c}$ ($C_{mn,2f_{c,1},S,c}$) with $\underline{\cos}$ substituted with sin

Table 3.3: Expression of $C_{mn,f_{c,1},C,c}$, $C_{mn,c,1},S,c}$, $C_{mn,f_{c,1},C,s}$ and $C_{mn,f_{c,1},S,s}$

$f_{c,1}$
$C_{mn,f_{c,1},C,c} = J_0(x_{mn,1})J_0(x_{mn,2})\left\{m_I\cos(2\pi f_{c,1}\Delta\tau_{mn}) + \frac{m_I^3}{32}(4a_2-1)\left[(4\cos(2\pi 2 f_{c,2}\Delta\tau_{mn})-5)\cdot\right.\right.$ $\left.\left.\cos(2\pi f_{c,1}\Delta\tau_{mn}) + \cos(2\pi 3 f_{c,1}\Delta\tau_{mn})\right]\right\}\underline{\cos}(2\pi f_{c,1}\bar{\tau}_{mn}) -$ $m_I J_0(x_{mn,2})J_2(x_{mn,1})\cos(2\pi f_{c,1}\Delta\tau_{mn})\,\underline{\cos}(2\pi f_{c,1}(\bar{\tau}_{mn}+2\nu_1)) -$ $2m_I J_1(x_{mn,1})J_1(x_{mn,2})\cos(2\pi f_{c,2}\Delta\tau_{mn})\cos(2\pi f_{c2}\nu_2)\,\underline{\cos}(2\pi f_{c,1}(\bar{\tau}_{mn}+\nu_1))$
$C_{mn,f_{c,1},S,c} = J_0(x_{mn,2})J_1(x_{mn,1})\left\{2+\frac{m_I^2}{8}\left[4\cos(2\pi 2 f_{c,2}\Delta\tau_{mn})-3+(4a_2-1)\cos(2\pi 2 f_{c,1}\Delta\tau_{mn})\right]\right\}\cdot$ $\underline{\cos}(2\pi f_{c,1}(\bar{\tau}_{mn}+\nu_1)) + J_0(x_{mn,1})J_1(x_{mn,2})\frac{m_I^2}{4}\{[2a_2\cos(2\pi(f_{c,2}-f_{c,1})\Delta\tau_{mn}) -$ $\sin(2\pi f_{c,1}\Delta\tau_{mn})\sin(2\pi f_{c,2}\Delta\tau_{mn})]\,\underline{\cos}(2\pi(f_{c,1}\bar{\tau}_{mn}+f_{c,2}\nu_2)) +$ $[2a_2\cos(2\pi(f_{c,1}+f_{c,2})\Delta\tau_{mn}) - \sin(2\pi f_{c,1}\Delta\tau_{mn})\sin(2\pi f_{c,2}\Delta\tau_{mn})]\,\underline{\cos}(2\pi(f_{c,1}\bar{\tau}_{mn}-f_{c,2}\nu_2))\}$
$C_{mn,f_{c,1},C,s}$ ($C_{mn,f_{c,1},S,s}$) identical to $C_{mn,f_{c,1},C,c}$ ($C_{mn,f_{c,1},S,c}$) with $\underline{\cos}$ substituted with sin

Table 3.4: Expression of $C_{mn,2f_{c,2}-f_{c,1},C,c}$, $C_{mn,2f_{c,2}-f_{c,1},S,c}$, $C_{mn,2f_{c,2}-f_{c,1},C,s}$ and $C_{mn,2f_{c,2}-f_{c,1},S,s}$

$2f_{c,2} - f_{c,1}$
$C_{mn,2f_{c,2}-f_{c,1},C,c} = \frac{m_I^3}{32}\{J_0(x_{mn,1})J_0(x_{mn,2})[3(8a_3 - 4a_2 + 1)\cos(2\pi(2f_{c,2} - f_{c,1})\Delta\tau_{mn}) + (4a_2 - 1)\cdot (\cos(2\pi(2f_{c,2} + f_{c,1})\Delta\tau_{mn}) + 2\cos(2\pi f_{c,1}\Delta\tau_{mn}))]\}\,\underline{\cos}(2\pi(2f_{c,2} - f_{c,1})\bar{\tau}_{mn}) - m_I\{J_0(x_{mn,1})J_2(x_{mn,2})\cos(2\pi f_{c,1}\Delta\tau_{mn})\,\underline{\cos}(2\pi((2f_{c,2} - f_{c,1})\bar{\tau}_{mn} + 2f_{c,2}\nu_2)) - J_1(x_{mn,1})J_1(x_{mn,2})\cos(2\pi f_{c,2}\Delta\tau_{mn})\,\underline{\cos}(2\pi((2f_{c,2} - f_{c,1})\bar{\tau}_{mn} + f_{c,2}\nu_2 - f_{c,1}\nu_1))\}$
$C_{mn,2f_{c,2}-f_{c,1},S,c} = \frac{m_I^2}{8}\{2J_0(x_{mn,1})J_1(x_{mn,2})[(4a_2 - 1)\cos(2\pi(f_{c,2} - f_{c,1})\Delta\tau_{mn}) + \cos(2\pi(f_{c,2} + f_{c,1})\Delta\tau_{mn})]\cdot \underline{\cos}(2\pi((2f_{c,2} - f_{c,1})\bar{\tau}_{mn} + f_{c,2}\nu_2)) + J_0(x_{mnm,2})J_1(x_{mn,1})[(4a_2 - 1)\cos(2\pi 2f_{c,2}\Delta\tau_{mn}) + 1]\cdot \underline{\cos}(2\pi((2f_{c,2} - f_{c,1})\bar{\tau}_{mn} - f_{c,1}\nu_1))\} - 2J_1(x_{mn,1})J_2(x_{mn,2})\underline{\cos}(2\pi((2f_{c,2} - f_{c,1})\bar{\tau}_{mn} + 2f_{c,2}\nu_2 - f_{c,1}\nu_1))$
$C_{mn,2f_{c,2}-f_{c,1},C,s}$ ($C_{mn,2f_{c,2}-f_{c,1},S,s}$) identical to $C_{mn,2f_{c,2}-f_{c,1},C,c}$ ($C_{mn,2f_{c,2}-f_{c,1},S,c}$) with $\underline{\cos}$ substituted with sin

The received power at frequencies $\bar{f}$ is,

$$P_{out,\bar{f}}(t) = \frac{R_L}{2} I^2_{out,\bar{f}}(t) = \frac{R_L}{2}\left[\left(\mathcal{A}_{c,\bar{f}} + \mathcal{B}_{c,\bar{f}}(t)\right)^2 + \left(\mathcal{A}_{s,\bar{f}} + \mathcal{B}_{s,\bar{f}}(t)\right)^2\right] \quad (3.26)$$

where R_L is the load resistance (50Ω).

The mean electrical power at frequencies $\bar{f}$ is,

$$\begin{aligned}\langle P_{out,\bar{f}}(t)\rangle &= \frac{R_L}{2}\Big(\mathcal{A}^2_{c,\bar{f}} + \mathcal{A}^2_{s,\bar{f}} + \langle \mathcal{B}^2_{c,\bar{f}}(t)\rangle + \langle \mathcal{B}^2_{s,\bar{f}}(t)\rangle + \\ &+ 2\mathcal{A}_{c,\bar{f}}\langle \mathcal{B}_{c,\bar{f}}(t)\rangle + 2\mathcal{A}_{s,\bar{f}}\langle \mathcal{B}_{s,\bar{f}}(t)\rangle\Big) \end{aligned} \quad (3.27)$$

To determine $\langle P_{out,\bar{f}}(t)\rangle$ it is necessary to calculate the mean and the mean square value of $\mathcal{B}_{c,\bar{f}}(t)$ and $\mathcal{B}_{s,\bar{f}}(t)$. For the mean value it is,

$$\langle \mathcal{B}_{c,\bar{f}}(t)\rangle = 2I_0 \sum_{m=1}^{N_M-1}\sum_{n=m+1}^{N_M} A_m A_n b_{mn}\langle D_{mn,\bar{f},c}(t)\rangle = 0 \quad (3.28)$$

where I used the property of the mean value of $D_{mn,\bar{f},c}(t)$ to be equal to zero since $\Delta\varphi_{mn}(t)$, as ϕ_m, uniformly distributed between $-\pi$ and $+\pi$.

The mean square value is,

$$\langle \mathcal{B}^2_{c,\bar{f}}(t)\rangle = 4I_0^2 \sum_{m=1}^{N_M-1}\sum_{n=m+1}^{N_M}\sum_{k=1}^{N_M-1}\sum_{l=m+1}^{N_M} A_m A_n A_k A_l b_{mn} b_{kl}\langle D_{mn,\bar{f},c}(t) D_{kl,\bar{f},c}(t)\rangle \quad (3.29)$$

In (3.29) we need to determine $\langle D_{mn,\bar{f},c}(t) D_{kl,\bar{f},c}(t)\rangle$,

$$\begin{aligned}\langle D_{mn,\bar{f},c}(t) D_{kl,\bar{f},c}(t)\rangle &= C_{mn,\bar{f},C,c} C_{kl,\bar{f},C,c}\langle \cos\left(\Delta\varphi_{mn}(t)\right)\cos\left(\Delta\varphi_{kl}(t)\right)\rangle + \\ &+ C_{mn,\bar{f},C,c} C_{kl,\bar{f},S,c}\langle \cos\left(\Delta\varphi_{mn}(t)\right)\sin\left(\Delta\varphi_{kl}(t)\right)\rangle + \\ &+ C_{mn,\bar{f},S,c} C_{kl,\bar{f},C,c}\langle \sin\left(\Delta\varphi_{mn}(t)\right)\cos\left(\Delta\varphi_{kl}(t)\right)\rangle + \\ &+ C_{mn,\bar{f},S,c} C_{kl,\bar{f},S,c}\langle \sin\left(\Delta\varphi_{mn}(t)\right)\sin\left(\Delta\varphi_{kl}(t)\right)\rangle \end{aligned} \quad (3.30)$$

To simplify (3.30) I use the assumption described above that $\Delta\varphi_{mn}$ and $\Delta\varphi_{kl}$ are uncorrelated. This leads to,

$$\langle \cos\left(\Delta\varphi_{mn}(t)\right)\cos\left(\Delta\varphi_{kl}(t)\right)\rangle = \frac{1}{2}\left(\delta_{mk}\delta_{nl} + \delta_{ml}\delta_{nk}\right) \quad (3.31a)$$

$$\langle \sin(\Delta\varphi_{mn}(t)) \sin(\Delta\varphi_{kl}(t)) \rangle = \frac{1}{2}(\delta_{mk}\delta_{nl} - \delta_{ml}\delta_{nk}) \tag{3.31b}$$

$$\langle \cos(\Delta\varphi_{mn}(t)) \sin(\Delta\varphi_{kl}(t)) \rangle = 0 \tag{3.31c}$$

where δ_{mk} is the Kronecker delta function.

Substituting (3.31a), (3.31b) and (3.31c) in (3.30) it is,

$$\langle D_{mn,\bar{f},c}(t) D_{kl,\bar{f},c}(t) \rangle = \frac{C^2_{mn,\bar{f},C,c} + C^2_{mn,\bar{f},S,c}}{2} \cdot (\delta_{mk}\delta_{nl} + \delta_{ml}\delta_{nk}) \tag{3.32}$$

Substituting (3.32) in (3.29) we have,

$$\langle \mathcal{B}^2_{c,\bar{f}}(t) \rangle = 2I_0^2 \sum_{m=1}^{N_M-1} \sum_{n=m+1}^{N_M} A_m^2 A_n^2 b_{mn}^2 \cdot \left[C^2_{mn,\bar{f},C,c} + C^2_{mn,\bar{f},S,c} \right] \tag{3.33}$$

and similarly for $\mathcal{B}^2_{s,\bar{f}}(t)$.

Substituting (3.23a), (3.23b), (3.28) and (3.33) in (3.27) the mean value can be determined as,

$$\begin{aligned} \langle P_{out,\bar{f}}(t) \rangle = & \frac{R_L}{2} I_0^2 \left\{ \mathrm{a}_{\bar{f}}^2 \left[\sum_{m=1}^{N_M} A_m^4 b_{mm}^2 + 2 \sum_{m=1}^{N_M-1} \sum_{n=1}^{N_M} A_m^2 A_n^2 b_{mm} b_{nn} \cdot \right. \right. \\ & \left. \cdot \cos\left(2\pi \bar{f} 2\Delta\tau_{mn}\right) \right] + 2 \sum_{m=1}^{N_M-1} \sum_{n=1}^{N_M} A_m^2 A_n^2 b_{mn}^2 \cdot \\ & \left. \cdot \left(C^2_{mn,\bar{f},C,c} + C^2_{mn,\bar{f},S,c} + C^2_{mn,\bar{f},C,s} + C^2_{mn,\bar{f},S,s} \right) \right\} \end{aligned} \tag{3.34}$$

The variance of the electrical power at frequencies $\bar{f}$ is,

$$\begin{aligned} \mathrm{Var}\left(P_{out,\bar{f}}(t)\right) = & \mathrm{Var}\left(\mathcal{B}^2_{c,\bar{f}}(t) + \mathcal{B}^2_{s,\bar{f}}(t) \right) + 4 \cdot \mathrm{Var}\left(\mathcal{A}_{c,\bar{f}} \mathcal{B}_{c,\bar{f}}(t) + \mathcal{A}_{s,\bar{f}} \cdot \right. \\ & \left. \cdot \mathcal{B}_{s,\bar{f}}(t) \right) + 4 \cdot Cov\left(\mathcal{B}^2_{c,\bar{f}}(t) + \mathcal{B}^2_{s,\bar{f}}(t), \mathcal{A}_{s,\bar{f}} \mathcal{B}_{s,\bar{f}} + \mathcal{A}_{s,\bar{f}} \mathcal{B}_{s,\bar{f}} \right) \end{aligned} \tag{3.35}$$

To determine the variance in (3.35) it is necessary to calculate the mean value of powers of $\mathcal{B}_{c,\bar{f}}(t)$ and $\mathcal{B}_{s,\bar{f}}(t)$ up to the fourth order, which involves calculation even longer than the one reported for $\langle P_{out,\bar{f}}(t) \rangle$. For this reason

I report analytical results just for the cases where it is $\mathcal{B}^2_{c,\bar{f}}(t) + \mathcal{B}^2_{s,\bar{f}}(t) \ll \mathcal{A}^2_{c,\bar{f}} + \mathcal{A}^2_{s,\bar{f}}$. This leads to assume,

$$P_{out,\bar{f}}(t) \approx \frac{R_L}{2}\left(\mathcal{A}^2_{c,\bar{f}} + \mathcal{A}^2_{s,\bar{f}} + 2\mathcal{A}_{c,\bar{f}}\mathcal{B}_{c,\bar{f}}(t) + 2\mathcal{A}_{s,\bar{f}}\mathcal{B}_{s,\bar{f}}(t)\right) \tag{3.36}$$

Utilizing (3.36) the mean value and the variance of $P_{out,\bar{f}}(t)$ simplify to,

$$\langle P_{out,\bar{f}}(t)\rangle \approx \frac{R_L}{2}\left(\mathcal{A}^2_{c,\bar{f}} + \mathcal{A}^2_{s,\bar{f}}\right) \tag{3.37a}$$

$$\begin{aligned}\mathrm{Var}\left(P_{out,\bar{f}}(t)\right) &\approx R_L^2 \cdot \mathrm{Var}\left(\mathcal{A}_{c,\bar{f}}\mathcal{B}_{c,\bar{f}}(t) + \mathcal{A}_{s,\bar{f}}\mathcal{B}_{s,\bar{f}}(t)\right) = \\ &= R_L^2\left(\mathcal{A}^2_{c,\bar{f}}\langle\mathcal{B}_{c,\bar{f}}(t)^2\rangle + \mathcal{A}^2_{s,\bar{f}}\langle\mathcal{B}_{s,\bar{f}}(t)^2\rangle + \right. \\ &\quad \left. + 2\mathcal{A}_{c,\bar{f}}\mathcal{A}_{s,\bar{f}}\langle\mathcal{B}_{c,\bar{f}}(t)\cdot\mathcal{B}_{s,\bar{f}}(t)\rangle\right)\end{aligned} \tag{3.37b}$$

All the terms in (3.37b) have been already determined apart from $\langle\mathcal{B}_{c,\bar{f}}(t)\cdot\mathcal{B}_{s,\bar{f}}(t)\rangle$. Following the same approach used to obtain $\langle\mathcal{B}_{c,\bar{f}}(t)^2\rangle$ in (3.33), it is,

$$\begin{aligned}\langle\mathcal{B}_{c,\bar{f}}(t)\mathcal{B}_{s,\bar{f}}(t)\rangle =& 2I_0^2\sum_{m=1}^{N_M-1}\sum_{n=m+1}^{N_M} A_m^2A_n^2b_{mn}^2\cdot \\ &\cdot\left[C_{mn,\bar{f},C,c}C_{mn,\bar{f},C,s} + C_{mn,\bar{f},S,c}C_{mn,\bar{f},S,s}\right]\end{aligned} \tag{3.38}$$

Substituting (3.33) and (3.38) in (3.37b), we have finally,

$$\begin{aligned}\mathrm{Var}\left(P_{out,\bar{f}}(t)\right) \approx& R_L^2I_0^2\sum_{m=1}^{N_M-1}\sum_{n=m+1}^{N_M} A_m^2A_n^2b_{mn}^2\cdot \\ &\cdot\left[\left(\mathcal{A}_{c,\bar{f}}C_{mn,\bar{f},C,c} + \mathcal{A}_{s,\bar{f}}C_{mn,\bar{f},C,s}\right)^2 + \right. \\ &\left. + \left(\mathcal{A}_{c,\bar{f}}C_{mn,\bar{f},S,c} + \mathcal{A}_{s,\bar{f}}C_{mn,\bar{f},S,s}\right)^2\right]\end{aligned} \tag{3.39}$$

The formula in (3.39) is a good approximation of the variance of the received component at frequency $\bar{f}$ if the non-fluctuating term $\mathcal{A}^2_{c,\bar{f}} + \mathcal{A}^2_{s,\bar{f}}$ prevails on the fluctuating term $\mathcal{B}^2_{c,\bar{f}}(t) + \mathcal{B}^2_{s,\bar{f}}(t)$. This is the case for the DC component and the component at $f_{c,1}$ if not close to a minimum of the MMF transfer function. For the component at other frequencies this approximation is not valid since the received non-fluctuating term has typically very low values.

3.1.4 Extension to multi-wavelength sources

The model presented in the previous subsections refers to a single-wavelength laser, such as a DFB LD. However, in MMF systems also multi-wavelength lasers, such as FP LDs, are currently employed. For this reason, it is meaningful to extend the previous model to multi-wavelength sources.

The starting point is the electrical field $\bar{E}_{MW}(t)$ emitted from a multi-wavelength source,

$$\bar{E}_{MW}(t) = \sum_{k=1}^{N_W} E_0^{(k)} \cdot \bar{e}_{(k)}(x,y) \cdot \sqrt{1 + y_{(k)}(t)} \cdot \exp\left\{\jmath\left[2\pi f_k t + \psi^{(k)}(t)\right]\right\} \quad (3.40)$$

Referring to the generic wavelength k, f_k is the optical frequency, and all the other quantities have the same meaning of (3.1) with the superscript (k) which applies to all the implicit quantities in (3.40) which depend on the wavelength.

Since the different wavelengths can be considered completely uncorrelated, the electrical field can be written as,

$$\bar{E}_{MW}(t) = \sum_{k=1}^{N_W} \bar{E}_{in}^{(k)}(t) \quad (3.41)$$

where $\bar{E}_{in}^{(k)}(t)$ is the normalized electrical field produced by the k^{th} wavelength.

Since the MMF is a linear medium, also the output electrical field is a superposition of the electrical field generated by the propagation of the electrical field of each wavelength giving,

$$\bar{E}_{out,MW}(t,z) = \sum_{k=1}^{N_W} \bar{E}_{out}^{(k)}(t) \quad (3.42)$$

where $\bar{E}_{out}^{(k)}(t)$ is the normalized electrical field produced by the k^{th} wavelength. Its mathematical expression is the same in (3.9) with the superscript (k) applied to all the quantities which depend on the wavelength.

The electrical received current is,

$$i_{out,MW}(t,z) = \mathrm{R}\int_{S_{PD}} \frac{\left|\bar{E}_{out,MW}(t,z)\right|^2}{2Z} dS = \frac{\mathrm{R}}{2Z}\left[\sum_{k=1}^{N_W}\int_{S_{PD}}\left(\bar{E}_{out}^{(k)}(t)\right)^2 dS + \right.$$
$$\left. +2\sum_{k=1}^{N_W-1}\sum_{l=k+1}^{N_W}\int_{S_{PD}} \bar{E}_{out}^{(k)}(t)\bar{E}_{out}^{(l)}(t) dS\right] \tag{3.43}$$

Since in a multi-wavelength source the distance between two adjacent wavelengths is of the order of hundreds of GHz, the cross-product between two electrical fields referred to different wavelengths cannot be detected by a common photodiode. Hence, (3.43) simplifies to,

$$i_{out,MW}(t,z) = \sum_{k=1}^{N_W}\frac{\mathrm{R}}{2Z}\int_{S_{PD}}\left(\bar{E}_{out}^{(k)}(t)\right)^2 dS = \sum_{k=1}^{N_W} i_{out}^{(k)}(t,z) \tag{3.44}$$

Equation (3.44) states that the received current from a multi-wavelength source is the superposition of the received current of each wavelength taken separately. Since the component of the current at frequency $\bar{f}$ of each wavelength can be written as (3.22), the overall received current can also be written in a similar way,

$$i_{out,MW,\bar{f}}(t,z) = \left(\mathcal{A}_{c,MW,\bar{f}} + \mathcal{B}_{c,MW,\bar{f}}(t)\right)\cos\left(2\pi\bar{f}t\right) +$$
$$+ \left(\mathcal{A}_{s,MW,\bar{f}} + \mathcal{B}_{s,MW,\bar{f}}(t)\right)\sin\left(2\pi\bar{f}t\right) \tag{3.45}$$

where

$$\mathcal{A}_{c,MW,\bar{f}} = \sum_{k=1}^{N_W} I_0^{(k)}\cdot \mathrm{a}_{\bar{f}}^{(k)}\sum_{m=1}^{N_M}\left(A_m^{(k)}\right)^2 b_{mm}^{(k)}\cos\left(2\pi\bar{f}\tau_m^{(k)}z\right) \tag{3.46a}$$

$$\mathcal{A}_{s,MW,\bar{f}} = \sum_{k=1}^{N_W} I_0^{(k)}\cdot \mathrm{a}_{\bar{f}}^{(k)}\sum_{m=1}^{N_M}\left(A_m^{(k)}\right)^2 b_{mm}^{(k)}\sin\left(2\pi\bar{f}\tau_m^{(k)}z\right) \tag{3.46b}$$

$$\mathcal{B}_{c,MW,\bar{f}}(t) = 2\sum_{k=1}^{N_W} I_0^{(k)}\cdot \sum_{m=1}^{N_M-1}\sum_{n=m+1}^{N_M} A_m^{(k)}A_n^{(k)}b_{mn}^{(k)}D_{mn,\bar{f},c}^{(k)}(t) \tag{3.46c}$$

$$\mathcal{B}_{s,MW,\bar{f}}(t) = 2\sum_{k=1}^{N_W} I_0^{(k)} \cdot \sum_{m=1}^{N_M-1} \sum_{n=m+1}^{N_M} A_m^{(k)} A_n^{(k)} b_{mn}^{(k)} D_{mn,\bar{f},s}^{(k)}(t) \tag{3.46d}$$

$$D_{mn,MW,\bar{f},c}^{(k)}(t) = C_{mn,\bar{f},C,c}^{(k)} \cos\left(\Delta\varphi_{mn}^{(k)}(t)\right) + C_{mn,\bar{f},S,c}^{(k)} \sin\left(\Delta\varphi_{mn}^{(k)}(t)\right) \tag{3.46e}$$

$$D_{mn,MW,\bar{f},s}^{(k)}(t) = C_{mn,\bar{f},C,s}^{(k)} \cos\left(\Delta\varphi_{mn}^{(k)}(t)\right) + C_{mn,\bar{f},S,s}^{(k)} \sin\left(\Delta\varphi_{mn}^{(k)}(t)\right) \tag{3.46f}$$

The terms $C_{mn,\bar{f},C,c}^{(k)}$, $C_{mn,\bar{f},S,c}^{(k)}$, $C_{mn,\bar{f},C,s}^{(k)}$, and $C_{mn,\bar{f},S,s}^{(k)}$ in (3.46e) and (3.46f) have the same expression of $C_{mn,\bar{f},C,c}$, $C_{mn,\bar{f},S,c}$, $C_{mn,\bar{f},C,s}$, and $C_{mn,\bar{f},S,s}$ in (3.23e) and (3.23f) with the superscript (k) applied to all the quantities which depend on the wavelength.

In this work, when applying this model I will take the simplification of considering only the phase differences $\Delta\varphi_{mn}^{(k)}(t)$ as depending on the wavelength , while I will take all the other quantities as wavelength independent. This means to assume the laser modulation characteristics indicated by m_I, a_2, a_3, K_f, ν_1 and ν_2 to be similar for all the wavelengths emitted by the laser. Moreover, I will take all the quantities related to MMF launch and propagation independent from the wavelength as well. This assumption is supported by the consideration that all the presented results are reported around 1310 nm where the material dispersion is minimum. This means that the fiber index profile is almost constant for all the wavelength of the source and consequently the quantities $A_m^{(k)}$, $b_{mm}^{(k)}$, $b_{mn}^{(k)}$, $\tau_m^{(k)}$ can be considered wavelength independent. With this assumptions it follows that:

$$\mathcal{A}_{c,MW,\bar{f}} = I_0^{tot} \cdot \mathrm{a}_{\bar{f}} \sum_{m=1}^{N_M} A_m^2 b_{mm} \cos\left(2\pi\bar{f}\tau_m z\right) = I_0^{tot} \cdot \mathcal{A}_{c,SW,\bar{f}} \tag{3.47a}$$

$$\mathcal{A}_{s,MW,\bar{f}} = I_0^{tot} \cdot \mathrm{a}_{\bar{f}} \sum_{m=1}^{N_M} A_m^2 b_{mm} \sin\left(2\pi\bar{f}\tau_m z\right) = I_0^{tot} \cdot \mathcal{A}_{s,SW,\bar{f}} \tag{3.47b}$$

$$\mathcal{B}_{c,MW,\bar{f}}(t) = 2\sum_{m=1}^{N_M-1} \sum_{n=m+1}^{N_M} A_m A_n b_{mn} \sum_{k=1}^{N_W} I_0^{(k)} D_{mn,\bar{f},c}^{(k)}(t) \tag{3.47c}$$

$$\mathcal{B}_{s,MW,\bar{f}}(t) = 2\sum_{m=1}^{N_M-1} \sum_{n=m+1}^{N_M} A_m A_n b_{mn} \sum_{k=1}^{N_W} I_0^{(k)} D_{mn,\bar{f},s}^{(k)}(t) \tag{3.47d}$$

$$D^{(k)}_{mn,MW,\bar{f},c}(t) = C_{mn,\bar{f},C,c}\cos\left(\Delta\varphi^{(k)}_{mn}(t)\right) + C_{mn,\bar{f},S,c}\sin\left(\Delta\varphi^{(k)}_{mn}(t)\right) \quad (3.47e)$$

$$D^{(k)}_{mn,MW,\bar{f},s}(t) = C_{mn,\bar{f},C,s}\cos\left(\Delta\varphi^{(k)}_{mn}(t)\right) + C_{mn,\bar{f},S,s}\sin\left(\Delta\varphi^{(k)}_{mn}(t)\right) \quad (3.47f)$$

where $I_0^{tot} = \sum_{k=1}^{N_W} I_0^{(k)}$ is the maximum DC component received from the multi-wavelength source.

Assuming as uncorrelated the phase differences $\Delta\varphi^{(k)}_{mn}(t)$ related to different wavelengths, it is possible to determine, as it has been done for (3.34), the mean value of the received power at frequency $\bar{f}$,

$$\begin{aligned}\langle P_{out,MW,\bar{f}}(t)\rangle =& \frac{R_L}{2}\left\{\left(I_0^{tot}\right)^2\cdot \mathrm{a}^2_{\bar{f}}\left[\sum_{m=1}^{N_M} A_m^4 b_{mm}^2 + 2\sum_{m=1}^{N_M-1}\sum_{n=1}^{N_M} A_m^2 A_n^2 b_{mm} b_{nn}\cdot\right.\right.\\ &\left.\cdot\cos\left(2\pi\bar{f}2\Delta\tau_{mn}\right)\right] + 2\sum_{k=1}^{N_W}\left(I_0^{(k)}\right)^2\cdot\sum_{m=1}^{N_M-1}\sum_{n=1}^{N_M} A_m^2 A_n^2 b_{mn}^2\cdot\\ &\left.\cdot\left(C^2_{mn,\bar{f},C,c} + C^2_{mn,\bar{f},S,c} + C^2_{mn,\bar{f},C,s} + C^2_{mn,\bar{f},S,s}\right)\right\} \quad (3.48)\end{aligned}$$

The approximate expression for the mean value, $\langle P_{out,MW,\bar{f}}(t)\rangle$, and for the variance, $\mathrm{Var}\left(P_{out,MW,\bar{f}}(t)\right)$, in the case of small fluctuations are,

$$\langle P_{out,MW,\bar{f}}(t)\rangle \approx \frac{R_L}{2}\left(I_0^{tot}\right)^2\cdot\left(\mathcal{A}^2_{c,SW,\bar{f}} + \mathcal{A}^2_{s,SW,\bar{f}}\right) \quad (3.49a)$$

$$\begin{aligned}\mathrm{Var}\left(P_{out,MW,\bar{f}}(t)\right) \approx& R_L^2\left(I_0^{tot}\right)^2\cdot\sum_{k=1}^{N_W}\left(I_0^{(k)}\right)^2\cdot\sum_{m=1}^{N_M-1}\sum_{n=m+1}^{N_M} A_m^2 A_n^2 b_{mn}^2\cdot\\ &\cdot\left[\left(\mathcal{A}_{c,SW,\bar{f}}C_{mn,\bar{f},C,c} + \mathcal{A}_{s,SW,\bar{f}}C_{mn,\bar{f},C,s}\right)^2 +\right.\\ &\left.+\left(\mathcal{A}_{c,SW,\bar{f}}C_{mn,\bar{f},S,c} + \mathcal{A}_{s,SW,\bar{f}}C_{mn,\bar{f},S,s}\right)^2\right] \quad (3.49b)\end{aligned}$$

The mean power, $\langle P_{out,MW,\bar{f}}(t)\rangle$, and the variance, $\mathrm{Var}\left(P_{out,MW,\bar{f}}(t)\right)$, given by (3.49a) and (3.49b), respectively, are identical to the expression derived in (3.37a) and (3.39) for a single-wavelength source apart from the current I_0 substituted with I_0^{tot} in (3.49a), which is not due to a modal noise effect, and substituted with $\sum_{k=1}^{N_W}(I_0^{(k)})^2$ in (3.49b), which comes from modal noise. This term represents the benefit on modal noise due to the use of a

multi-wavelength source with respect to a single-wavelength source. Using the Cauchy's inequality [59] it is indeed possible to prove that,

$$\frac{\sum_{k=1}^{N_W}\left(I_0^{(k)}\right)^2}{\left(I_0^{tot}\right)^2}=\frac{\sum_{k=1}^{N_W}\left(I_0^{(k)}\right)^2}{\left(\sum_{k=1}^{N_W}I_0^{(k)}\right)^2}\geq\frac{1}{N_W} \tag{3.50}$$

where the equality holds when $I_0^{(k)}$ is identical for all wavelengths.

This means that a maximum reduction of the impact on modal noise of N_W times on $\langle P_{out,MW,\bar{f}}\rangle$ and Var $\left(P_{out,MW,\bar{f}}(t)\right)$ is theoretically possible. However, the number of wavelengths is not the only parameter which influences modal noise. A case by case study is therefore performed in the experimental section.

3.2 Experimental and theoretical results

In this section experimental results regarding the impact of modal noise on link gain, harmonic and intermodulation distortions will be presented and explained with the aid of simulation results obtained by the application of the model described in section 3.1.

3.2.1 Experimental setup

Fig. 3.4 shows the general setup used for the experimental activity on link gain and harmonic and intermodulation distortions. An Anritsu MS4624B three-port vector network analyzer (VNA) was used as RF source and receiver. In particular, two of the VNA ports were used as RF sources and one as receiver. The two source ports emitted two RF tones at different frequencies, $f_{c,1}$ and $f_{c,2}$. The two tones were multiplied together using a RF coupler and frequencies higher than $f_{c,1}$ and $f_{c,2}$ were removed with a low-pass filter. This filter prevented higher order harmonics of $f_{c,1}$ and $f_{c,2}$ coming from the VNA to modulate the RoF TX. The filtered combination of the two tones modulated a RoF TX, based on directly modulated DFB or FP LD at 1310 nm. All the RoF TXs had a single-mode pig-tail. Hence,

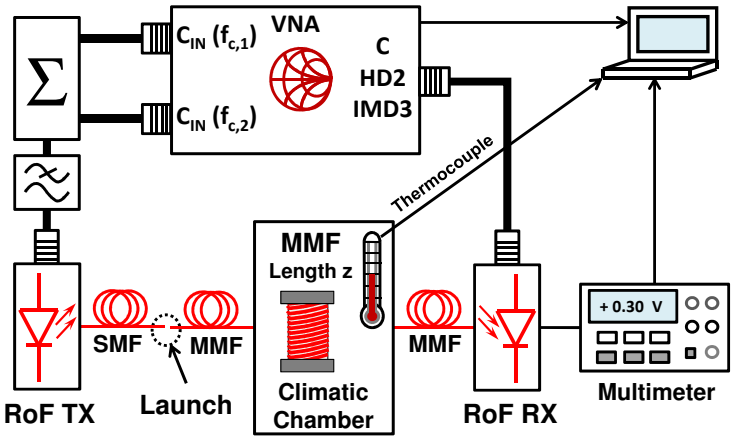

Figure 3.4: Experimental setup for the characterization of a RoMMF link

it was possible to apply a restricted launch condition to the MMF. In particular, three types of launch were investigated: central launch, offset launch and overfilled launch.

Several spans of OM2 MMF were employed obtaining a total length ranging from 75 to 525 m. The MMF spans were inserted in a climatic chamber and underwent a controlled temperature variation. In this way, they were forced to experience typical environmental temperature changes in a much shorter time giving stable results and a repeatable experimental condition. The received optical power was detected by a RoF RX based on InGaAs PIN photodiodes equipped with multi-mode pigtail. No electrical amplification stage was used in this kind of measurements since the purpose was to determine non-linear distortions induced by the optical part of the RoMMF link. Apart from the received power at the different frequencies, measured by the VNA, also the received DC component and the temperature of the climatic chamber were monitored. The DC component was measured with a HP 3478A digital multimeter connected to an output DC port of the RoF RX, while the temperature was measured by a thermocouple placed in the climatic chamber. All the measured quantities were collected by a computer.

The set of realized measurements were chosen to investigate the impact

on modal noise of the following aspects of the optical part of the RoMMF link:

- Launch condition
- Photodiode collecting area characteristics
- Laser modulation characteristics

The impact of these characteristics on modal noise will in general be described in terms of statistical quantities, such as mean value and variance. However, I also present the relationship between the time behavior of components at different frequencies and the variation of temperature. This is the first point I will deal with, because it allows to have a clearer physical insight on the characteristics of modal noise, allowing to understand what is behind the various statistical quantities that will be considered in the following.

3.2.2 Time behavior of received power

The simple way to describe the relationship between the time behavior of different frequency components of the received signal is to assume that all the received quantities vary in the same way with different peak-to-peak values. Hence, the time fluctuations normalized on the respective mean value is in this case the same. That was the reason to use the speckle contrast γ^2 as the modal noise parameter [78, 79]. The speckle contrast is the normalized variance of the intensity distribution at the output of the MMF. In our case we are not interested in the normalized variance of a single speckle but of all the intensity distribution received by the finite area of the photodiode. Thus, I define a quantity Γ^2_{DC} similar to the speckle contrast but referred to all the power received by the photodiode, which is proportional to the DC current,

$$\Gamma^2_{DC} = \frac{\mathrm{Var}(I_{out,DC})}{(\langle I_{out,DC} \rangle)^2} \tag{3.51}$$

where $I_{out,DC}$ is the received DC current as in (3.25) with $\bar{f} = 0$.

Since in the case of the DC component it is $A_{s,DC} = 0$ and $B_{s,DC}(t) = 0$, Γ^2_{DC} can be determined analytically by,

$$\Gamma^2_{DC} = \frac{\langle B^2_{c,DC}(t)\rangle}{A^2_{c,DC}} = \frac{\mathrm{Var}\left(P_{out,DC}(t)\right)}{4\left(\langle P_{out,DC}(t)\rangle\right)^2} \tag{3.52}$$

where the expressions of $\langle P_{out,\bar{f}}(t)\rangle$ and $\mathrm{Var}\left(P_{out,\bar{f}}(t)\right)$ in (3.37a) and (3.37b) need to be used.

The main attention of this work is to study the impact of modal noise on the RF linear and non-linear components. Similarly to the DC component, I define a normalized variance Γ^2_{RF} for the main frequency components at $f_{c,1}$ or $f_{c,2}$,

$$\Gamma^2_{RF} = \frac{\mathrm{Var}(I_{out,f_{c,1}})}{(\langle I_{out,f_{c,1}}\rangle)^2} \approx \frac{\mathrm{Var}\left(P_{out,f_{c,1}}(t)\right)}{4\left(\langle P_{out,f_{c,1}}(t)\rangle\right)^2} \tag{3.53}$$

where the last approximation holds when it is possible to employ the approximations in (3.37a) and (3.37b). This is typically acceptable for the components at $f_{c,1}$ or $f_{c,2}$.

The question to be solved is if Γ^2_{RF} and Γ^2_{DC} give similar values, or in other words if Γ^2_{DC} is sufficient to describe the modal noise impact. To answer this question I will graph in the next figures the normalized current $\gamma_{\bar{f}}(t)$ defined as follow,

$$\gamma_{\bar{f}}(t) = \frac{I_{out,f_{c,1}} - \langle I_{out,f_{c,1}}\rangle}{\langle I_{out,f_{c,1}}\rangle} \tag{3.54}$$

With the definition in (3.54) it is $\Gamma^2_{DC} = \langle \gamma^2_{DC}(t)\rangle$ and $\Gamma^2_{RF} = \langle \gamma^2_{f_{c,1}}(t)\rangle$. I consider two opposite cases: transmitter almost without frequency chirping and transmitter with a high frequency chirping.

Fig. 3.5 shows a comparison of experimentally measured $\gamma_{DC}(t)$ and $\gamma_{RF}(t) = \gamma_{f_{c,1}}(t)$ for a RoMMF link employing an external modulator, i.e. a transmitter with very low frequency chirping. Note that the $\gamma_{DC}(t)$ and $\gamma_{RF}(t)$ have a really similar behavior in time. This feature is described by the model presented in section 3.1. Indeed, in the case of a transmitter without frequency chirping we have that $x_{mn,i}$, defined in (3.16a), is zero. Consequently it is,

$$D_{mn,DC,c}(t) = \cos\left(\Delta\varphi_{mn}(t)\right) \tag{3.55a}$$

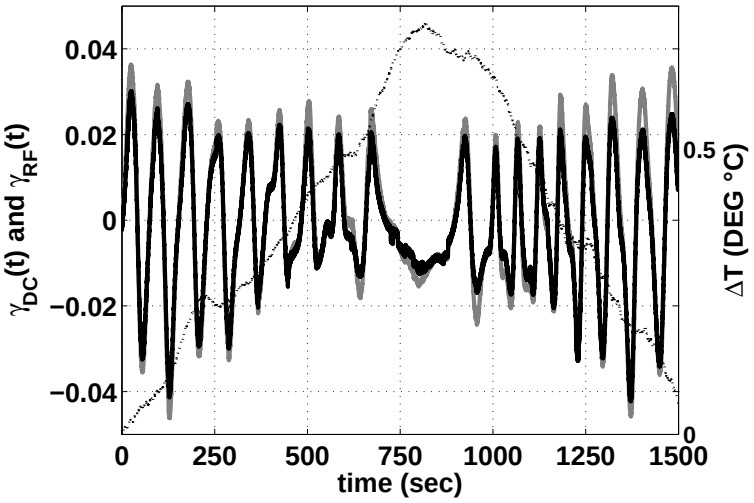

Figure 3.5: Behavior of experimentally measured $\gamma_{DC}(t)$ (black solid line) and $\gamma_{RF}(t) = \gamma_{f_{c,1}}(t)$ (gray solid line) in a RoMMF link employing external modulator. The temperature variation is also represented (dashed black line)

$$D_{mn,f_{c,1},c}(t) = m_I \cos\left(2\pi f_{c,1}\Delta\tau_{mn}\right)\cos\left(2\pi f_{c,1}\bar{\tau}_{mn}\right)\cos\left(\Delta\varphi_{mn}(t)\right) \quad (3.55b)$$

$$D_{mn,f_{c,1},s}(t) = m_I \cos\left(2\pi f_{c,1}\Delta\tau_{mn}\right)\sin\left(2\pi f_{c,1}\bar{\tau}_{mn}\right)\cos\left(\Delta\varphi_{mn}(t)\right) \quad (3.55c)$$

where I neglect all the terms which depends on powers of m_I greater than one.

From (3.55a), (3.55b), and (3.55c) it is clear that in the case of no transmitter frequency chirping both $D_{mn,DC,c}(t)$, $D_{mn,f_{c,1},c}(t)$ and $D_{mn,f_{c,1},s}(t)$ vary with the same phase fluctuation, $\cos\left(\Delta\varphi_{mn}(t)\right)$, related to the temperature variation $\Delta T(t)$. The received DC and RF current can be written as,

$$i_{out,DC}(t,z) = I_0\left[\sum_{m=1}^{N_M} A_m^2 b_{mm} + 2\sum_{m=1}^{N_M-1}\sum_{n=m+1}^{N_M} A_m A_n b_{mn}\cos\left(\Delta\varphi_{mn}(t)\right)\right] \quad (3.56a)$$

$$\begin{aligned} i_{out,f_{c,1}}(t,z) =& m_I I_0\left[\sum_{m=1}^{N_M} A_m^2 b_{mm}\cos\left(2\pi f_{c,1}(t-\tau_m)\right) + 2\sum_{m=1}^{N_M-1}\sum_{n=m+1}^{N_M} A_m A_n \cdot\right. \\ &\left.\cdot b_{mn}\cos\left(2\pi f_{c,1}\Delta\tau_{mn}\right)\cos\left(\Delta\varphi_{mn}(t)\right)\cos\left(2\pi f_{c,1}(t-\bar{\tau}_{mn})\right)\right] \end{aligned} \quad (3.56b)$$

To determine the relationship between the amplitude of $i_{out,DC}(t,z)$ and of $i_{out,f_{c,1}}(t,z)$ I take the simplification $\tau_m \approx \tau_n \approx \bar{\tau}_{mn}$, defined in (3.16a), implying that $\Delta\tau_{mn}$, defined in (3.16c), is an infinitesimal quantity. In other word I suppose to use a frequency $f_{c,1}$ which is below the 3 dB low-pass bandwidth. With this assumption the amplitude of the current $i_{out,f_{c,1}}(t,z)$ becomes,

$$i_{out,f_{c,1}}(t,z) \approx m_I \cdot i_{out,DC}(t,z) \quad (3.57)$$

From (3.57) it is,

$$\gamma_{RF}(t) \approx \gamma_{DC}(t) = 2\frac{\sum_{m=1}^{N_M-1}\sum_{n=m+1}^{N_M} A_m A_n b_{mn}\cos\left(\Delta\varphi_{mn}(t)\right)}{\sum_{m=1}^{N_M} A_m^2 b_{mm}} \quad (3.58)$$

This explains why in Fig. 3.5 $\gamma_{DC}(t)$ and $\gamma_{RF}(t)$ present very similar time behaviors. Consequently, it is $\Gamma_{DC}^2 = \Gamma_{RF}^2$ and it is possible to show that the same relationship is valid for different frequency components. Hence, in the

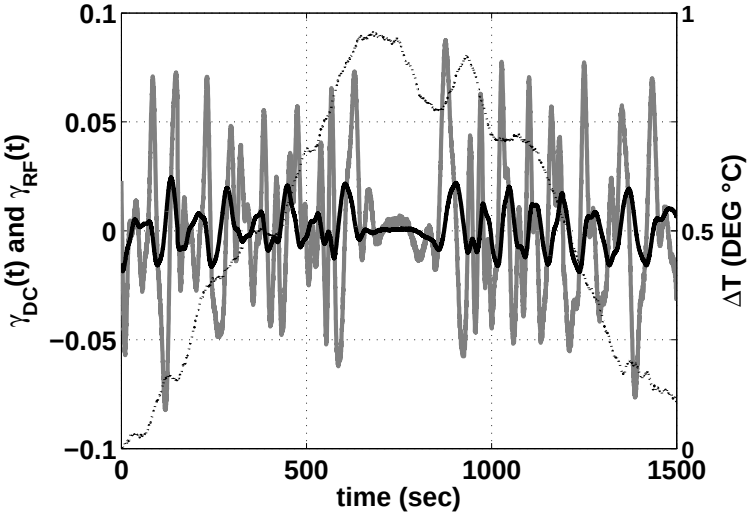

Figure 3.6: Behavior of experimentally measured $\gamma_{DC}(t)$ (black solid line) and $\gamma_{RF}(t) = \gamma_{f_{c,1}}(t)$ (gray solid line) in a RoMMF link employing directly modulated DFB LD with high frequency chirping. The temperature variation is also represented (dashed black line)

case of a transmitter almost without frequency chirping the quantity Γ^2_{DC}, or speckle contrast, is sufficient to describe the statistical behavior of all the received quantities.

Fig. 3.6 shows instead a comparison of experimentally measured $\gamma_{DC}(t)$ and $\gamma_{RF}(t) = \gamma_{f_{c,1}}(t)$ for a RoMMF link employing a RoF TX with a high chirp parameter, K_f. There are two major differences with respect to Fig. 3.5. First, the peak-to-peak value of $\gamma_{RF}(t)$ is much greater that the one of $\gamma_{DC}(t)$, meaning that the impact of modal noise on the component at $f_{c,1}$ is higher than on the DC component. Secondly, the time behavior of the two quantities is different. In particular, when one of the two is reaching a local maximum or minimum the other is almost zero and is changing with a local high derivative. This leads to presume that there is a kind of derivative relationship between the two γ values.

This feature is described by the model presented in section 3.1. Indeed,

in the case of a transmitter with a nonzero frequency chirping, $x_{mn,i}$, defined in (3.16a), is not anymore zeros. It is then,

$$D_{mn,DC,c}(t) = J_0(x_{mn,1})J_0(x_{mn,2})\cos\left(\Delta\varphi_{mn}(t)\right) \tag{3.59a}$$

$$\begin{aligned} D_{mn,f_{c,1},c}(t) = &[m_I J_0(x_{mn,1})J_0(x_{mn,2})\cos\left(2\pi f_{c,1}\Delta\tau_{mn}\right)\cos\left(\Delta\varphi_{mn}(t)\right) + \\ &+2J_0(x_{mn,2})J_1(x_{mn,1})\sin\left(\Delta\varphi_{mn}(t)\right)]\cos\left(2\pi f_{c,1}\bar{\tau}_{mn}\right) \end{aligned} \tag{3.59b}$$

$$\begin{aligned} D_{mn,f_{c,1},s}(t) = &[m_I J_0(x_{mn,1})J_0(x_{mn,2})\cos\left(2\pi f_{c,1}\Delta\tau_{mn}\right)\cos\left(\Delta\varphi_{mn}(t)\right) + \\ &+2J_0(x_{mn,2})J_1(x_{mn,1})\sin\left(\Delta\varphi_{mn}(t)\right)]\sin\left(2\pi f_{c,1}\bar{\tau}_{mn}\right) \end{aligned} \tag{3.59c}$$

where I assumed for simplicity $\nu_1 \approx 0$.

Comparing (3.55a) with (3.59a), there is no major difference apart from a coefficient reduction, compared to 1, performed by $J_0(x_{mn,1})J_0(x_{mn,2})$. Instead, comparing (3.59b) and (3.59c) with (3.55b) and (3.55c), we find now a new addend multiplying $\sin\left(\Delta\varphi_{mn}(t)\right)$ in addition to the one multiplying $\cos\left(\Delta\varphi_{mn}(t)\right)$. Assuming also in this case $\tau_m \approx \tau_n \approx \bar{\tau}_{mn}$, we have,

$$\begin{aligned} I_{out,f_{c,1}}(t,z) \approx &m_I \cdot i_{out,DC}(t,z) + 4I_0 \sum_{m=1}^{N_M-1}\sum_{n=m+1}^{N_M} A_m A_n b_{mn} \cdot \\ &\cdot J_0(x_{mn,2})J_1(x_{mn,1})\sin\left(\Delta\varphi_{mn}(t)\right) \end{aligned} \tag{3.60}$$

It is confirmed from (3.60) that the amplitude of the component at $f_{c,1}$ can be written as in (3.57) with the addition of a fluctuating component due to transmitter frequency chirping. Remembering the definition of $x_{mn,i}$ in (3.16a) and applying the approximation at the first order of the Bessel functions $J_0(x) \approx 1$, $J_1(x) \approx x/2$ for low values of x, it is,

$$\begin{aligned} I_{out,f_{c,1}}(t,z) \approx &m_I \cdot i_{out,DC}(t,z) + I_0 \cdot 4\pi K_f I_{RF} z \sum_{m=1}^{N_M-1}\sum_{n=m+1}^{N_M} A_m A_n b_{mn} \cdot \\ &\cdot (\tau_m - \tau_n)\sin\left(\Delta\varphi_{mn}(t)\right) \end{aligned} \tag{3.61}$$

Note that the second addend at the right-hand side of (3.61) is directly proportional to the adiabatic frequency chirp coefficient, K_f, and to the fiber length, z.

For a transmitter with high frequency chirping or when the distance increases, the second addend at the right-hand side of (3.61) becomes the prevalent fluctuating term. Therefore it is,

$$\gamma_{RF}(t) \approx 4\pi K_f z \frac{I_{RF}}{m_I} \frac{\sum_{m=1}^{N_M-1} \sum_{n=m+1}^{N_M} A_m A_n b_{mn} (\tau_m - \tau_n) \sin(\Delta\varphi_{mn}(t))}{\sum_{m=1}^{N_M} A_m^2 b_{mm}} \tag{3.62}$$

Comparing (3.62) with (3.58), it can be observed that, while for a transmitter almost without chirp $\gamma_{RF}(t)$ varies in time with the cosine of the phase difference $\Delta\varphi_{mn}(t)$, for a transmitter with high chirp $\gamma_{RF}(t)$ varies in time with the sine of $\Delta\varphi_{mn}(t)$. This is the reason that produces a different time behavior of $\gamma_{RF}(t)$ with respect to $\gamma_{DC}(t)$ as shown in Fig. 3.6. Moreover, since for a transmitter with high frequency chirping, K_f has a value of 200–300 MHz/mA, the peak-to-peak variation of $\gamma_{RF}(t)$ is higher with respect to $\gamma_{DC}(t)$. This leads to underline that for a general situation of a transmitter with nonzero frequency chirping, the quantity Γ^2_{DC}, or speckle contrast, is not sufficient to describe the statistical behavior of the RoMMF link, but each component needs to be studied and measured by itself. Indeed, Γ^2_{RF} is different from Γ^2_{DC} and the same is valid for the other frequency components.

3.2.3 Launch condition impact

As said in section 3.2.1, three types of launch were employed in the experimental activity: central launch, offset launch and overfilled launch. Central launch was obtained linking together the connectors of the laser single-mode pigtail and the MMF with an adapter. All the connectors used were angle-polished standard connectors (SC–APC) and all the adapters were the same used for SMF. Offset launch was obtained with a mode conditioning patch-cord connected to the RoF TX single-mode pigtail. This patch-cord provides a launch of the optical power out of the MMF center with an offset between 10 and 16 μm [80]. Overfilled launch was obtained by using a mode scrambler [81] on a short multi-mode patch-cord. The mode scrambling was obtained by inducing periodic microbendings on a short part of the multi-mode patch-cord.

The results presented in this subsection show the impact of the three different types of launch on modal noise. The quantities under study are:

- σ_G : the standard deviation of the link gain, i.e. the standard deviation in dB of the received power at $f_{c,1}$
- $\langle C/HD2 \rangle$: the mean value of the ratio in dB between the received power at $f_{c,1}$ and the received power at $2f_{c,1}$
- $\langle C/IMD3 \rangle$: the mean value of the ratio in dB between the received power at $f_{c,1}$ and the received power at $2f_{c,2} - f_{c,1}$ or $2f_{c,1} - f_{c,2}$

The mean value of the received power at $f_{c,1}$ is not reported because it is slightly dependent from modal noise as also reported in (3.37a). The experimental results are compared with the simulations results coming from the model described in section 3.1. The mean value of $C/HD2$ and $C/IMD3$ in dB were calculated numerically on a simulated time behavior of all the received components, while σ_G was calculated through analytical formulas applying the approximation that leads to (3.37a) and (3.37b). Indeed, in this case it is,

$$\sigma_G \approx \frac{20}{\ln(10)} \Gamma_{RF} \approx 20 \log_{10} (1 + \Gamma_{RF}) \tag{3.63}$$

where Γ_{RF}^2 is defined in (3.53).

Fig. 3.7 shows the standard deviation, σ_G, between 50 and 550 m. The theoretical and experimental curves were obtained using the RoF TX classified as TX1 in 3.2.5, and the RoF RX classified as RX1 in 3.2.4. However, the considerations on the different types of launch are the same for all TXs and RXs used. The input power was chosen to have an OMI per carrier of 0.2. The gray line and crosses refer to central launch, the black line and circles refer to offset launch, and the gray dashed line and triangles to overfilled launch. Lines refer to simulation results while markers refer to measurements. Note that theoretical and experimental results are in good agreement. Note that overfilled launch and offset launch have σ_G values higher than central launch. In particular, at 525 m the difference is of about 1.5 dB with offset launch and of about 2.5 dB with overfilled launch. The reason for this behavior can be explained with the help of the developed model.

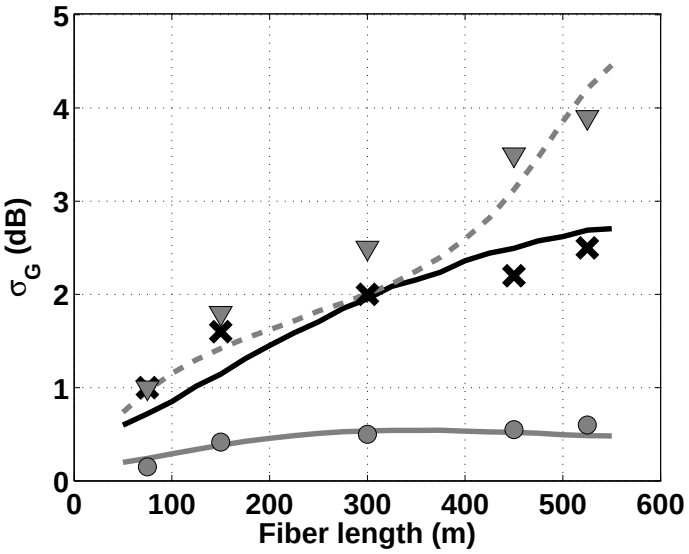

Figure 3.7: Comparison of measured (markers) and modeled (lines) values of σ_G for increasing fiber length using central launch (gray line and circle), offset launch (black line and cross) and overfilled launch (gray dashed line and triangle)

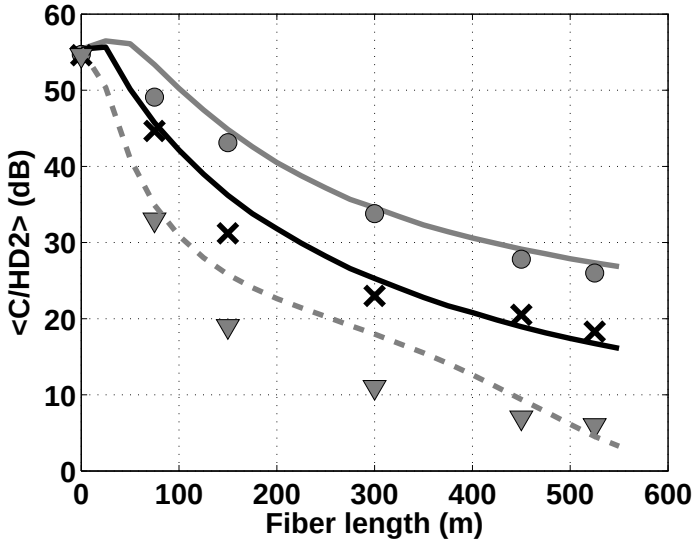

(a)

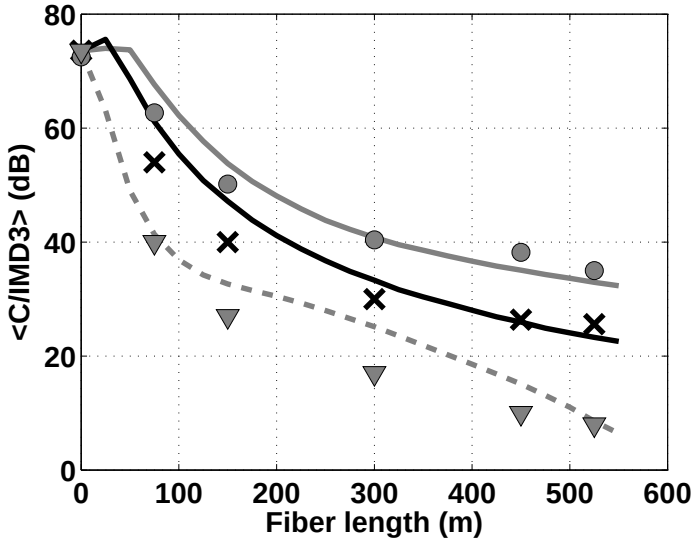

(b)

Figure 3.8: Comparison of measured (markers) and modeled (lines) values of $\langle C/HD2 \rangle$ (a) and $\langle C/IMD3 \rangle$ (b) using central launch (gray line and circles), offset launch (black line and crosses) and over-filled launch (gray dashed line and triangles)

All the three launches excite all the MMF modes, i.e. in (3.5) it is always $|A_m| > 0$ for all m. Hence, the difference between the three launches lies in the relative weights of the various A_m. All the other model parameters are the same since we are using the same RoF TX and RoF RX, and MMF. In the case of central launch, more than 99.9% of the optical power is distributed just among the eight modes LP01 to LP04, each one taken in its two degeneracies (LP stands for linearly polarized [3]). These modes are invariant azimuthally, and therefore the electrical field is mostly concentrated in the central part of the MMF core. It is therefore in high percentage detected, regardless of the finite value of the photodiode surface S_{PD}. This means that for these modes the scalar products b_{mn} in (3.14) become relatively close to zero, reducing the impact of the modal noise on the variance of the received power in (3.39). The same effect is true for a not perfect central launch. In this case not only the eight azimuthally invariant modes, LP01 to LP04, are excited. Anyway, the additionally excited modes are still lower order modes which are as well confined in the central part of the MMF core.

In the case of offset launch, the 99.9% of the total power results distributed among a set of more than 90 modes. Many pairs of modes (m, n) must now be considered in the evaluation of the variance of the received power in (3.39). Since most of these pairs refer to higher order modes the amplitudes of their electrical fields are not negligible in regions of the MMF core far from its center. This means that the correspondent scalar products b_{mn} are not close to zero, and thus the variance of the received power gives relatively high values.

In the case of overfilled launch, the 99.9% of the total power results distributed among all the set of 156 guided modes. Hence, most of the pairs of modes produces high b_{mn} values. Moreover, since both low and high order modes are present, for most of the couples (m, n) the quantity $\Delta\tau_{mn}$ can assume higher values compared to central and offset launch.

Fig. 3.8 presents the results for the mean value of $C/HD2$ and $C/IMD3$. Indeed, central launch gives rise to higher values of $\langle C/HD2\rangle$ and $\langle C/IMD3\rangle$ with respect to offset launch and overfilled launch. At 300 m a difference of about 10 dB in $\langle C/HD2\rangle$ and $\langle C/IMD3\rangle$ is reported between central

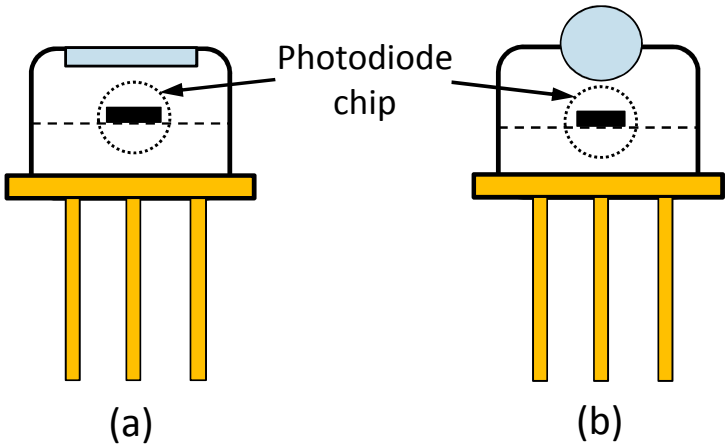

Figure 3.9: Schematic drawing showing the difference between TO-Can PDs with flat window (a) or ball lens (b)

launch and offset launch and of more than 20 dB between central launch and overfilled launch. The reason for this behavior is the same used to explain the difference in σ_G. I also underline that the previous results are valid in general also for different RoF TXs, RoF RXs and MMFs even if not reported here. This demonstrates the better performance of central launch with respect to offset launch and overfilled launch. Hence, in the following I will always consider central launch technique.

3.2.4 Receiver impact

Three different receivers were employed in the experimental study. All the three RoF RXs were based on coaxial InGaAs PIN photodiodes equipped with multi-mode pigtail. The difference between the photodiodes lies in the way the outgoing power from the pigtail is coupled with the photodiode chip. RoF RX1 employs a large area photodiode packaged in a TO-Can with a flat window as represented in Fig. 3.9(a). RoF RX2 and RX3 employ a large area photodiode packaged in a TO-Can with a built-in ball-lens as represented in Fig. 3.9(b).

The modeling of the different photodiodes is not trivial since the value of the illuminated collecting area and the exact coupling scheme between the pigtail and the photodiode, which is typically done sample by sample, are both unknown. Hence, a simple equivalent model was used to describe the reception of the power coming from the MMF. The photodiode was modeled as a square placed in front of the fiber. The center of the square and the fiber core center might not coincide, thus a misalignment could be present. The estimation of side width and misalignment was performed comparing the received power with central and offset launch with the different receivers and the values of Γ^2_{DC} at different lengths. Then, a least square estimation was done. The solution, i.e. the values of the pair side width and misalignment, resulted not uniquely defined. For this reason, the misalignment was set to 1 μm in all the three cases and the side width was consequently estimated. The side width for the three RoF RXs was: 23 μm for RX1, 26 μm for RX2, and 28 μm for RX3. As expected, the photodiodes equipped with ball lens had an equivalent detecting square larger than the photodiode with flat window. Anyway, the two photodiodes equipped with ball lens have not the same size of the equivalent square. In particular, RX3 had a larger size of the equivalent square with respect to RX2.

Fig. 3.10 shows σ_G between 50 and 550 m for the three different receivers. The theoretical and experimental curves were obtained using the RoF TX classified as TX1 in 3.2.5, and central launch. The input power was chosen to have a OMI per carrier of 0.2. Gray line and circles refer to RoF RX1, blue line and crosses to RoF RX2, and green line and triangles to RoF RX3. Lines refer to simulation results while markers refer to measurements. Note that RoF RX1 gives rise to higher values of σ_G with respect to RX2. Similarly, RX2 has higher values of σ_G with respect to RX3. In particular, at 300 m there is a difference of 0.25 dB between RX1 and RX2, and of 0.12 dB between RX2 and RX3.

The reason for this behavior is in the higher equivalent collecting area of RX3 compared to RX2 and of RX2 compared to RX1. In the numerical model the impact of the equivalent size of the photodiode is contained in b_{mn}, expressed in (3.14). Indeed, a larger photodiode area, S_{PD}, reduces the value

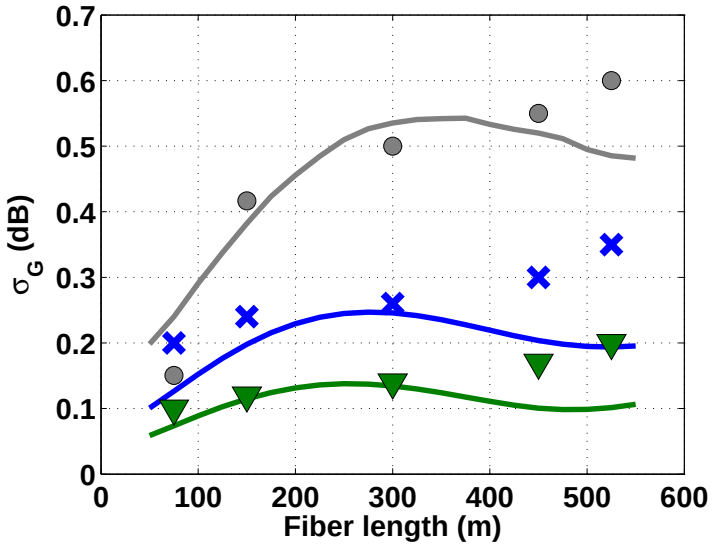

Figure 3.10: Comparison of measured (markers) and modeled (lines) values of σ_G for increasing fiber length using RoF RX1 (gray line and circles), RoF RX2 (blue line and crosses) and RX3 (green line and triangles)

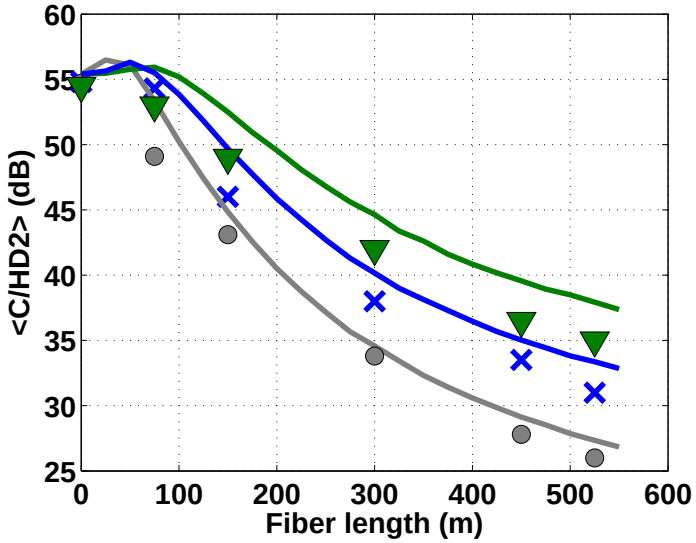

(a)

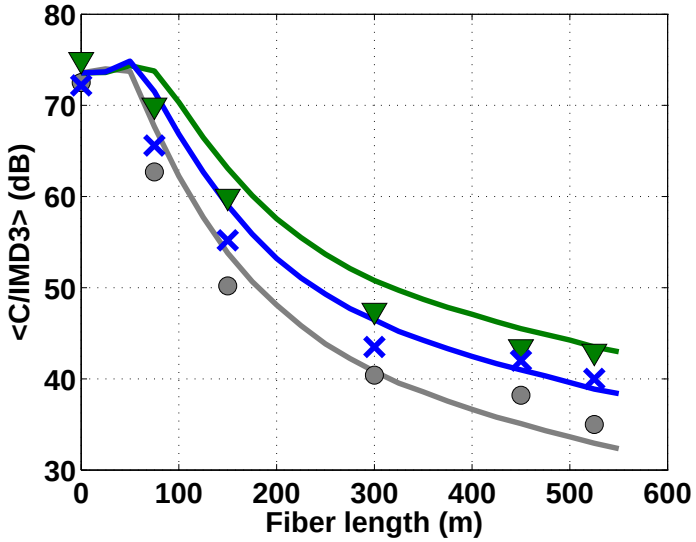

(b)

Figure 3.11: Comparison of measured (markers) and modeled (lines) values of $\langle C/HD2 \rangle$ (a) and $\langle C/IMD3 \rangle$ (b) for increasing fiber length using RoF RX1 (gray line and circles), RoF RX2 (blue line and crosses) and RX3 (green line and triangles)

of b_{mn} of all couples, (m, n), of different modes since it is approaching the ideal case of a large surface where b_{mn} is zero when $m \neq n$, i.e. orthogonality of the set of modes. In practice, this situation is not feasible since other causes of loss of orthogonality such as connector imperfections becomes important in the determination of modal noise. However, lower values of b_{mn} gives rise to lower values of the variance of the received power in (3.39).

Fig. 3.11 presents similar results for the mean value of $C/HD2$ and $C/IMD3$. Since the effect of a different photodiode surface impacts on all the received components in the same way through the coefficients b_{mn}, also in this case RoF RX1 gives rise to worst $\langle C/HD2 \rangle$ and $\langle C/IMD3 \rangle$ compared to RX2 and the same for RX2 compared to RX3. Since a larger equivalent area has an impact on all modes, the results presented are not dependent on the launch or on the transmitter, but are generally valid.

3.2.5 Transmitter impact

The impact on modal noise of the transmitter characteristics is the last one to be pointed out. I will compare transmitters based on directly modulated DFB LD and on directly modulated FP LD. In particular, I will comment on the main transmitter characteristics influencing modal noise.

3.2.5.1 Comparison of transmitters based on DFB laser

Two different RoF TXs based on directly modulated DFB LD were employed. The modeling parameters of the two TXs are listed in Tab. 3.5. To give an idea of the dependence of modal noise on these parameters, I will consider at first a particular condition where the approximation in (3.62) tends to hold. In this case, the relationship between σ_G and the transmitter parameters is,

$$\sigma_G \approx \frac{20}{\ln(10)} \Gamma_{RF} \propto \frac{K_f I_{RF}}{m_I} z = \frac{K_f}{\eta_{TX}/P_0} z \tag{3.64}$$

where (3.63) and (3.62) have been used.

Parameter	*TX1*	*TX2*
λ_0 (nm)	1313	1309
P_0 (mW)	4.6	3.2
η_{TX} (mW/mA)	0.06	0.07
IIP2 (dBm)	57.0	46.8
IIP3 (dBm)	44.5	34.8
a_2	1.71×10^{-2}	3.30×10^{-2}
a_3	6.95×10^{-3}	2.31×10^{-2}
α	4.2	3
κ (GHz/mW)	5.82	4.49
K_f (MHz/mA)	140	130

Table 3.5: Parameters of RoF TXs based on DFB LD used in the experimental activity

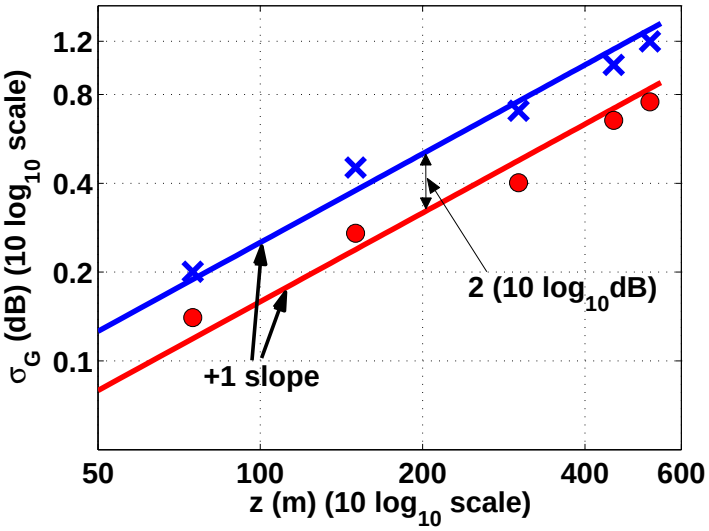

Figure 3.12: Asymptotic theoretical behaviors (lines) and measured values (markers) of σ_G in $10\log_{10}$ for varying values of fiber length in $10\log_{10}$ scale using TX1 (blue) or TX2 (red) and RX1

To evidence this relationship, Fig. 3.12 shows experimental values and asymptotic behaviors of σ_G in $10\log_{10}$ scale versus fiber length in $10\log_{10}$ scale for TX1 and TX2 in a practical situation where the linear proportionality in (3.64) can be taken with good accuracy. The input power was set to -4.3 dBm. It was $f_1 = 700$ MHz, $f_2 = 750$ MHz, and the RX1 was used. Both axes of the graph are in $10\log_{10}$ scale to evidence that the asymptotic curves referred to the two different TXs are parallel with slope $+1$ and with a distance of 2 $10\log_{10}$(dB). Since the only difference in the two cases is given by the transmitter parameters, this distance can be verified theoretically by,

$$10\log_{10}\left(\sigma_{G,TX1}/\sigma_{G,TX2}\right) = 10\log_{10}\left(\frac{K_{f,TX1}}{\eta_{TX1}/P_{0,TX1}}/\frac{K_{f,TX2}}{\eta_{TX2}/P_{0,TX2}}\right) \approx$$
$$\approx 2.57 \quad 10\log_{10}(\text{dB})$$

A similar behavior can be determined for the mean values of $\langle C/HD2\rangle$ and $\langle C/IMD3\rangle$. The theoretical expression of the mean value of the received power at each frequency in (3.34) can be approximated as follows for the components at $f_{c,1}$, $2f_{c,1}$ and $2f_{c,2} - f_{c,1}$,

$$\langle P_{out,f_{c,1}}(t)\rangle \approx \frac{R_L}{2} I_0^2 m_I^2 \left[\sum_{m=1}^{N_M} A_m^4 b_{mm}^2 + 2\sum_{m=1}^{N_M-1}\sum_{n=1}^{N_M} A_m^2 A_n^2 b_{mm} b_{nn} \cdot \right.$$
$$\left. \cdot \cos\left(2\pi f_{c,1} 2\Delta\tau_{mn}\right)\right] \tag{3.65a}$$

$$\langle P_{out,2f_{c,1}}(t)\rangle \approx \frac{R_L}{2} I_0^2 \left\{ \frac{a_2^2 m_I^4}{4} \left[\sum_{m=1}^{N_M} A_m^4 b_{mm}^2 + 2\sum_{m=1}^{N_M-1}\sum_{n=1}^{N_M} A_m^2 A_n^2 b_{mm} b_{nn} \cdot \right.\right.$$
$$\left.\left. \cdot \cos\left(2\pi 2 f_{c,1} 2\Delta\tau_{mn}\right)\right] + 8\sum_{m=1}^{N_M-1}\sum_{n=1}^{N_M} A_m^2 A_n^2 b_{mn}^2 J_0^2(x_{mn,2}) J_2^2(x_{mn,1}) \right\} \tag{3.65b}$$

$$\langle P_{out,2f_{c,2}-f_{c,1}}(t)\rangle \approx \frac{R_L}{2} I_0^2 \left\{ \frac{3}{4} a_3^2 m_I^6 \left[\sum_{m=1}^{N_M} A_m^4 b_{mm}^2 + 2 \sum_{m=1}^{N_M-1} \sum_{n=1}^{N_M} A_m^2 A_n^2 b_{mm} b_{nn} \cdot \right.\right. \\ \left. \cdot \cos\left(2\pi \left(2f_{c,2} - f_{c,1}\right) 2\Delta\tau_{mn}\right)\right] + \\ \left. +8 \sum_{m=1}^{N_M-1} \sum_{n=1}^{N_M} A_m^2 A_n^2 b_{mn}^2 J_1^2(x_{mn,1}) J_2^2(x_{mn,2}) \right\} \tag{3.65c}$$

where in (3.65a) the approximation in (3.37a) was used, while in (3.65b) and (3.65c) the prevailing terms among $C_{mn,\bar{f},C,c}$, $C_{mn,\bar{f},S,c}$, $C_{mn,\bar{f},C,s}$, and $C_{mn,\bar{f},S,s}$ have been taken, neglecting the others (see Tab. 3.2 and Tab. 3.4). These approximations are typically valid in the cases considered here.

The expression in (3.65a) shows that the power at $f_{c,1}$, indicated as $\langle C\rangle$, depends mainly from the OMI and slightly also on the distance through $\Delta\tau_{mn}$, at least for short-range links. The components at $2f_{c,1}$ and $2f_{c,2}-f_{c,1}$, indicated as $\langle HD2\rangle$ and $\langle IMD3\rangle$ respectively, are composed by two terms. The first one is similar to the expression of $\langle C\rangle$, and it mainly depends on the non linear coefficients a_2 and a_3 and on the OMI. The second term depends on $x_{mn,1}$ and $x_{mn,2}$ and increases consequently (see (3.16a)) with the chirp parameter K_f, the input current I_{RF} and the fiber length z. Hence, $\langle C/HD2\rangle$ and $\langle C/IMD3\rangle$ have two asymptotic behaviors. For very short fiber links the first terms in (3.65b) and (3.65c) prevail over the second ones giving,

$$\langle C/HD2\rangle \propto \left(a_2 \cdot \eta_{TX}/P_0\right)^{-2} \frac{1}{I_{RF}^2} \tag{3.66a}$$

$$\langle C/IM3\rangle \propto \left(a_3 \cdot \eta_{TX}/P_0\right)^{-2} \frac{1}{I_{RF}^2} \tag{3.66b}$$

On the contrary, for increasing fiber length the second terms in (3.65b) and (3.65c) prevail over the first ones. Remembering the definition of $x_{mn,i}$ in (3.16a) and applying the approximation of the Bessel functions $J_0(x) \approx 1$, $J_1(x) \approx x/2$ and $J_2(x) \approx x^2/8$, the following asymptotic behaviors tend then to hold,

$$\langle C/HD2\rangle \propto \left(\frac{K_f}{\sqrt{\eta_{TX}/P_0}}\right)^{-4} \frac{1}{I_{RF}^2 z^4} \tag{3.67a}$$

$$\langle C/IM3\rangle \propto \left(\frac{K_f}{\sqrt[3]{\eta_{TX}/P_0}}\right)^{-6} \frac{1}{I_{RF}^4 z^6} \tag{3.67b}$$

To prove the asymptotic behaviors in (3.66a), (3.66b), (3.67a), and (3.67b), Fig. 3.13 shows experimental values and asymptotic behaviors of $\langle C/HD2\rangle$ (a) and $\langle C/IMD3\rangle$ (b) versus fiber length in $10\log_{10}$ for TX1 and TX2. The experimental conditions are the same used to derive Fig. 3.12. Note that for a fiber length below 100 m the values of $\langle C/HD2\rangle$ and $\langle C/IMD3\rangle$ are constant at the back-to-back values. In particular there are more than 10 dB between the two transmitter initial values of $\langle C/HD2\rangle$ due to the different second order non-linear characteristics (see Tab. 3.5). The initial values of $\langle C/IMD3\rangle$ are instead the same for the two transmitters since in this experimental condition I took a low input power of -4.3 dBm which did not allow to appreciate any laser intrinsic IMD since it was below the noise level. The initial difference of the two transmitters will be underlined in another figure. For a fiber length above 150–200 m the values of $\langle C/HD2\rangle$ and $\langle C/IMD3\rangle$ decrease with linear asymptotic behavior which are well approximated by the theoretical slopes of -4 and -6, respectively, as described in (3.67a) and (3.67b). The difference between the asymptotic curves of the two TXs is 6 and 7 dB for $\langle C/HD2\rangle$ and $\langle C/IMD3\rangle$, respectively.

Since the only difference in the two cases is given by the transmitter parameters, this distance can be verified theoretically to be,

$$\begin{aligned}\langle C/HD2\rangle_{TX2} - \langle C/HD2\rangle_{TX1} =& 40\log_{10}\left(\frac{K_{f,TX1}}{\sqrt{\eta_{TX1}/P_{0,TX1}}}/\right.\\ &\left./\frac{K_{f,TX2}}{\sqrt{\eta_{TX2}/P_{0,TX2}}}\right) = 5.78 \quad \text{dB}\end{aligned}$$

$$\begin{aligned}\langle C/IMD3\rangle_{TX2} - \langle C/IMD3\rangle_{TX1} =& 60\log_{10}\left(\frac{K_{f,TX1}}{\sqrt[3]{\eta_{TX1}/P_{0,TX1}}}/\right.\\ &\left./\frac{K_{f,TX2}}{\sqrt[3]{\eta_{TX2}/P_{0,TX2}}}\right) = 6.42 \quad \text{dB}\end{aligned}$$

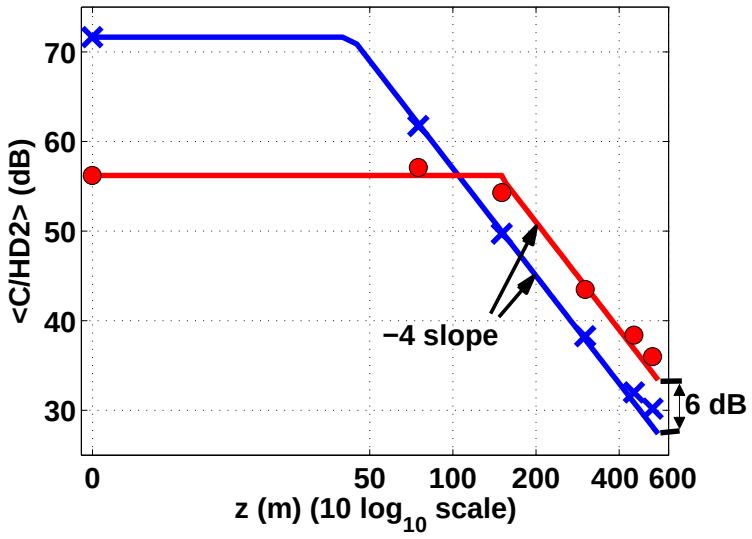

(a)

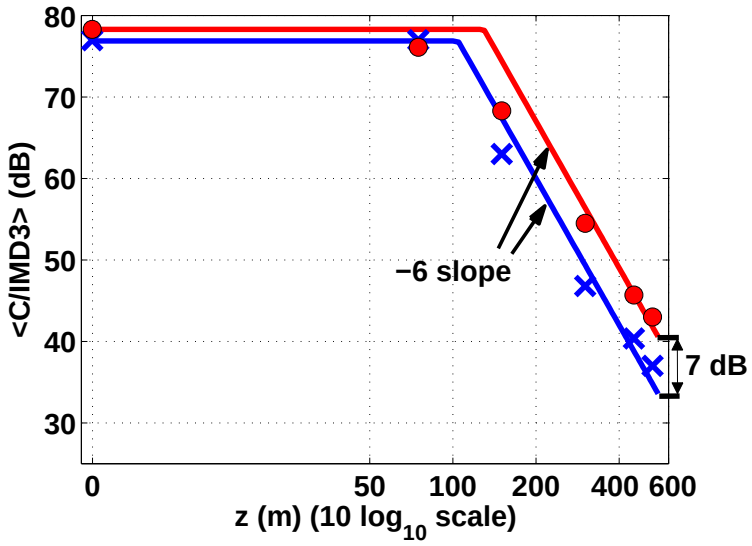

(b)

Figure 3.13: Asymptotic theoretical behaviors (lines) and measured values (markers) of $\langle C/HD2 \rangle$ (a) and $\langle C/IMD3 \rangle$ (b) for varying values of fiber length in $10\log_{10}$ scale using TX1 (blue) or TX2 (red). The receiver utilized was RX1 in both cases.

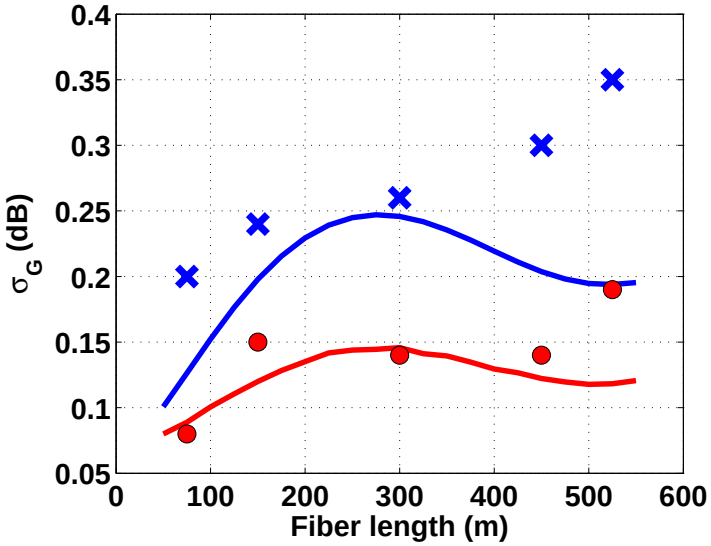

Figure 3.14: Comparison of measured (markers) and modeled (lines) values of σ_G for increasing fiber length using RoF TX1 (blue line and crosses) and RoF TX2 (red line and circles) and RX2

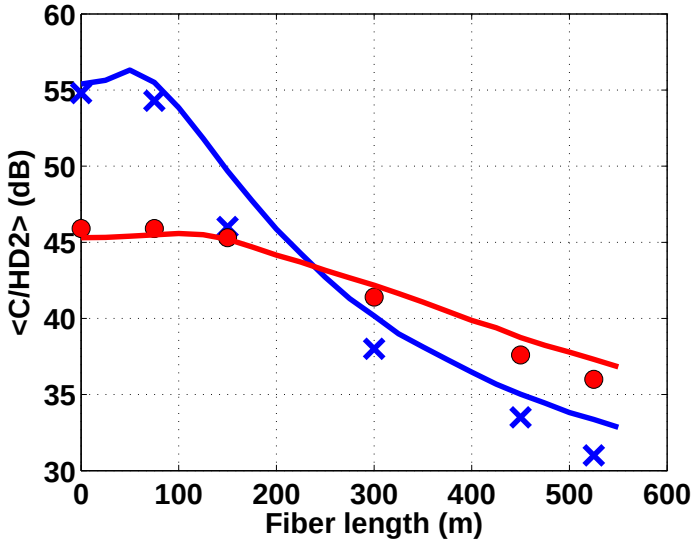

(a)

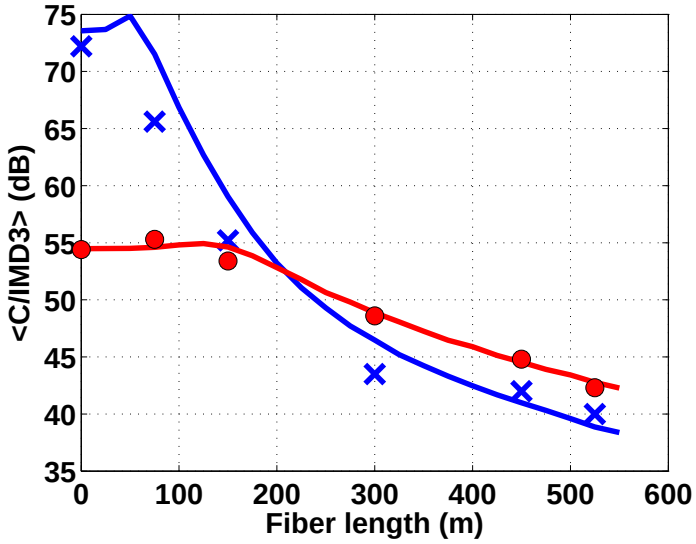

(b)

Figure 3.15: Comparison of measured (markers) and modeled (lines) values of $\langle C/HD2 \rangle$ (a) and $\langle C/IMD3 \rangle$ (b) for increasing fiber length using RoF TX1 (blue line and crosses) and RoF TX2 (red line and circles). The receiver utilized was RX2 in both cases.

The approximated relationships (3.64), (3.67a) and (3.67b) are not strictly applicable in all the possible operating conditions. Anyway, it is always confirmed:

- the decrease of σ_G with the increase of $K_f/(\eta_{TX}/P_0)$
- the decrease of $\langle C/HD2\rangle$ with the increase of $K_f/\sqrt{\eta_{TX}/P_0}$
- the decrease of $\langle C/IMD3\rangle$ with the increase of $K_f/\sqrt[3]{\eta_{TX}/P_0}$

Fig. 3.14 and 3.15 shows experimental and theoretical values of σ_G, and $\langle C/HD2\rangle$ and $\langle C/IMD3\rangle$, respectively, for TX1 (blue) and TX2 (red). In this case the input power was 7.7 dBm, $f_1 = 1000$ MHz and $f_2 = 1200$ MHz, and the receiver RX2 was used.

Fig. 3.14 demonstrates that σ_G tends to increase with fiber length and that TX2 performs better than TX1 of about 0.15 dB above 300 m. Fig. 3.15 shows that $\langle C/HD2\rangle$ and $\langle C/IMD3\rangle$ start from asymptotic initial values related to the non-linear characteristics of the TXs (see again Tab. 3.5). In particular, since TX1 has better non-linear characteristics, the initial values of $\langle C/HD2\rangle$ and $\langle C/IMD3\rangle$ are higher than TX2 of 10 dB for $\langle C/HD2\rangle$ and of 15 dB for $\langle C/IMD3\rangle$. However, for increasing fiber length the values of $\langle C/HD2\rangle$ and $\langle C/IMD3\rangle$ referred to TX1 sharply decrease and become lower than the respective values referred to TX2. This is due to the higher value of the parameters $K_f/\sqrt{\eta_{TX}/P_0}$ and $K_f/\sqrt[3]{\eta_{TX}/P_0}$ of TX1 compared to TX2. In particular, there is a difference of 4 dB in $\langle C/HD2\rangle$ and $\langle C/IMD3\rangle$ between the two TXs performance.

3.2.5.2 Comparison of transmitters based on Fabry-Perot laser

Two different RoF TXs based on directly modulated FP LDs were employed. The reason to use multi-wavelength sources in RoMMF link is that a lower coherent laser is expected to reduce the impact of modal noise. Anyway, to verify this expectation it is important to compare the experimental and theoretical results obtained for FP sources with the results obtained with DFB sources. The modeling of the FP RoMMF link was performed using

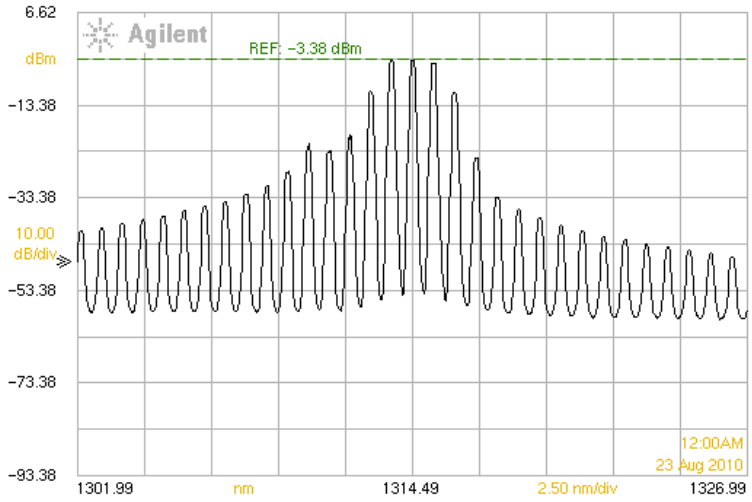

(a) FP-TX1

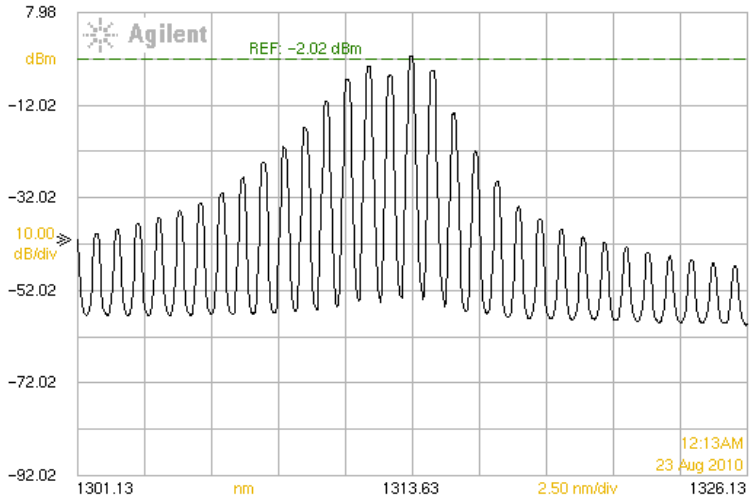

(b) FP-TX2

Figure 3.16: Optical spectrum of FP-TX1 (a) and FP-TX2 (b)

Parameter	*FP-TX1*	*FP-TX2*
Peak wavelength (nm)	1314.5	1313.6
Mode spacing (nm)	0.79	0.8
FWHM (nm)	2.4	3
P_0 (mW)	2.3	4.4
η_{TX} (mW/mA)	0.055	0.08
IIP2 (dBm)	37	45
IIP3 (dBm)	32	40
a_2	9.34×10^{-2}	4.92×10^{-2}
a_3	3.68×10^{-2}	1.01×10^{-2}
α	8.7	2.4
κ (GHz/mW)	2.25	6.68
K_f (MHz/mA)	120	110

Table 3.6: Parameters of RoF TXs based on DFB LD used in the experimental activity

the model described in subsection 3.1.4. The laser parameters are listed in Tab. 3.6. The optical spectrum of the two FP TXs is reported in Fig. 3.16. Note that the optical spectra are composed by many wavelengths, but only few of them hold the maior part of the power. Indeed, the parameter defined in (3.50) assumes the following values for the two TXs,

$$\left(\frac{\sum_{k=1}^{N_W} \left(I_0^{(k)} \right)^2}{\left(\sum_{k=1}^{N_W} I_0^{(k)} \right)^2} \right)_{FP-TX1} = 0.18 \quad , \quad \left(\frac{\sum_{k=1}^{N_W} \left(I_0^{(k)} \right)^2}{\left(\sum_{k=1}^{N_W} I_0^{(k)} \right)^2} \right)_{FP-TX2} = 0.15$$

Since the values of this parameter are between 0.15 and 0.18, this means that the two FP-TXs are similar to multi-wavelength sources with 5–7 wavelengths with identical power. The impact of this characteristic on σ_G is shown in Fig. 3.17. In this figure experimental and theoretical values of σ_G are shown for FP-TX1 (yellow), FP-TX2 (brown) and compared with TX2 (red) of the previous section. These results are obtained with an input power of 7.7 dBm, $f_1 = 1000$ MHz and $f_2 = 1200$ MHz. The receiver used was RX2.

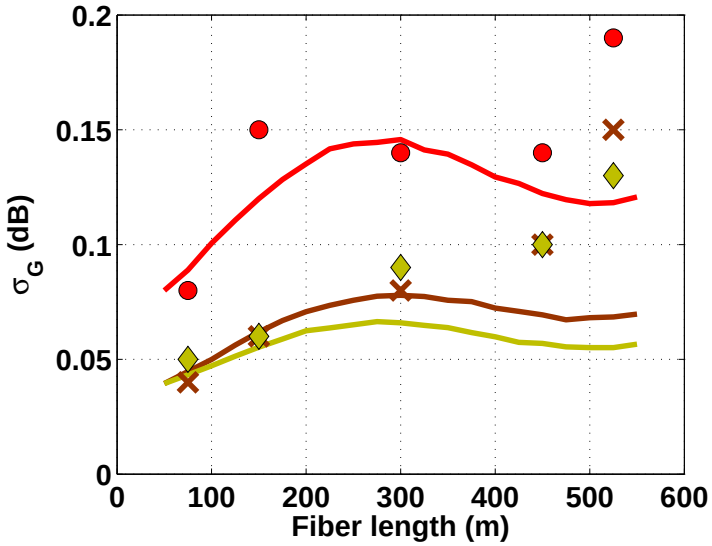

Figure 3.17: Comparison of measured (markers) and modeled (lines) values of σ_G for increasing fiber length using RoF FP-TX1 (yellow line and diamond), RoF FP-TX2 (brown line and cross), and TX2 (red line and circle)

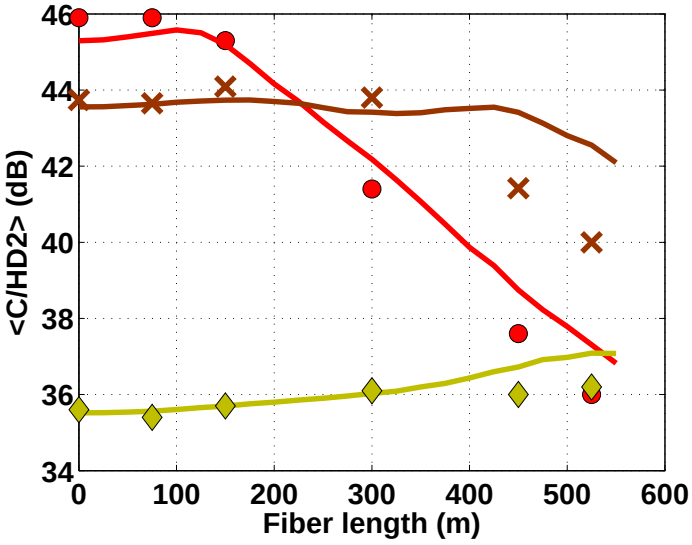

(a)

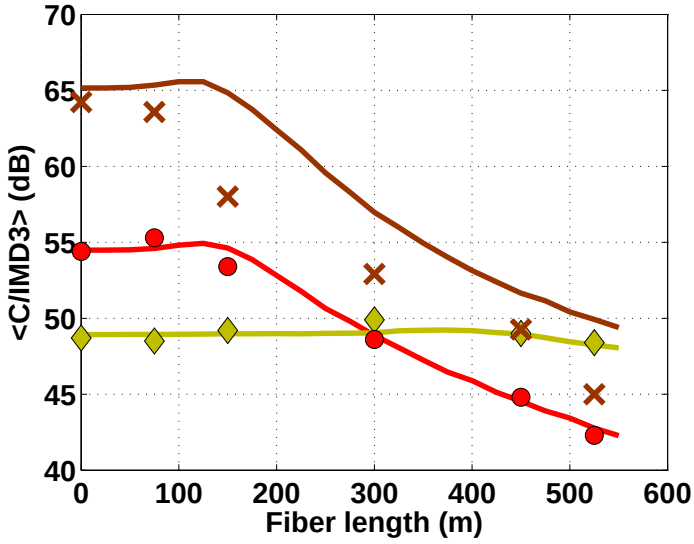

(b)

Figure 3.18: Comparison of measured (markers) and modeled (lines) values of $\langle C/HD2 \rangle$ (a) and $\langle C/IMD3 \rangle$ (b) for increasing fiber length using RoF FP-TX1 (yellow line and diamond), RoF FP-TX2 (brown line and cross), and TX2 (red line and circle)

From the figure it can be noted that the values of σ_G referred to FP-TX1 and FP-TX2 are approximately the same. But, they are about half of the one referred to TX2. This behavior is quite in agreement with theoretical results. Indeed for all the TXs considered the parameter $K_f/\left(\eta_{TX}/P_{0,TX}\right)$ is approximately the same, hence the difference between TX2 and the FP-TXs is due to the multi-wavelength characteristics. Indeed, using (3.63), (3.53), (3.48), and (3.49a) it is,

$$\sigma_G \approx \frac{20}{\ln(10)}\Gamma_{RF} \approx \frac{10}{\ln(10)}\sqrt{\frac{\mathrm{Var}\left(P_{out,f_{c,1}}(t)\right)}{\left(\langle P_{out,f_{c,1}}(t)\rangle\right)^2}} \propto \sqrt{\frac{\sum_{k=1}^{N_W}\left(I_0^{(k)}\right)^2}{\left(\sum_{k=1}^{N_W} I_0^{(k)}\right)^2}} \tag{3.69}$$

The result in (3.69) claims that σ_G is proportional to the square root of the introduced parameter of multi-wavelength sources. In the presented case this parameter is 0.18 for FP-TX1 and 0.15 for FP-TX2, which provides a decreasing factor around 0.4 in σ_G. This decreasing factor is confirmed with the experimental results shown in Fig. 3.17.

Similar behaviors could be presented for $\langle C/HD2\rangle$ and $\langle C/IMD3\rangle$. However, also the non-linear characteristics of the LDs need to be considered in this case. Fig. 3.18 shows experimental and theoretical values of $\langle C/HD2\rangle$ and $\langle C/IMD3\rangle$ for FP-TX1 (yellow), FP-TX2 (brown) and TX2 (red). Note that the curves and markers referred to FP-TX1 do not change with increasing length. This is due to the multi-wavelength nature of FP-TX1, but also to the poor non-linear performance of this transmitter as can be evinced comparing IIP2 and IIP3 values of different transmitters in Tab. 3.5 and Tab. 3.6. Hence, the non-linear characteristics of FP-TX1 prevail over modal noise effect. The results referred to FP-TX2 show instead a reduction of $\langle C/HD2\rangle$ and $\langle C/IMD3\rangle$ with increasing fiber length. FP-TX2 has good non-linear performance which allows to observe some effect of modal noise. On the other hand the multi-wavelength nature of FP-TX2 reduces the impact of modal noise compared to single-wavelength sources, such as TX2. This can be appreciated particularly in Fig. 3.18(a), where the value of $\langle C/HD2\rangle$ decreases slowly for FP-TX2 while it decreases more rapidly for TX2. I underline that this is possible due to the good behavior of FP-TX2 not only in terms of

non-linear characteristics but also linear characteristics, i.e. modulation efficiency, η_{TX}, and frequency chirping, K_f, which are, respectively, the higher and the lower among the presented DFB and FP transmitters. This suggests that FP-TX2 can be successfully applied to a complete RoMMF link.

3.3 LTE transmission experiments

The experimental and theoretical activity presented in the previous sections was performed to investigate the impact of different quantities of the link components on the RoMMF link linear and non-linear performances limited by modal noise. With the results coming from this study it was possible to develop a cost-effective RoMMF link with good performance. The RoF TX was based on the FP-TX2 reported in subsection 3.2.5.2 and the launching technique was central launch since it was proved in subsection 3.2.3 to provide the best performance. The RoF RX was then equipped by the photodiode with built-in ball lens, addressed as RX3 in subsection 3.2.4,which showed the best performances. The photodiode was followed by a TIA.

A general characterization of the properties of the designed link was performed in terms of the spurious free dynamic range (SFDR) [52]. SFDR is an important parameter for analog links which takes into account both the intermodulation distortion effects and the noise of the entire link. Therefore it accounts also for noise and intermodulation distortions of the TIA. SFDR is defined as the ratio between the received power and the noise level in a 1 Hz band when the third-order intermodulation distortions are at the noise level. It gives an idea of the maximum signal-to-noise ratio achievable by the link under test, therefore higher values correspond to better performances.

Fig. 3.19 depicts the SFDR of the RoMMF link for increasing fiber length. In particular, the markers refer to the mean value of SFDR at each distance and the bars represents the intervals between the 99% minimum and the 99% maximum values. The 99% minimum/maximum is the value which is exceeded/not exceeded for 99% of time. Note that the mean value of SFDR is practically invariant with increasing length while the minimum at 99% goes

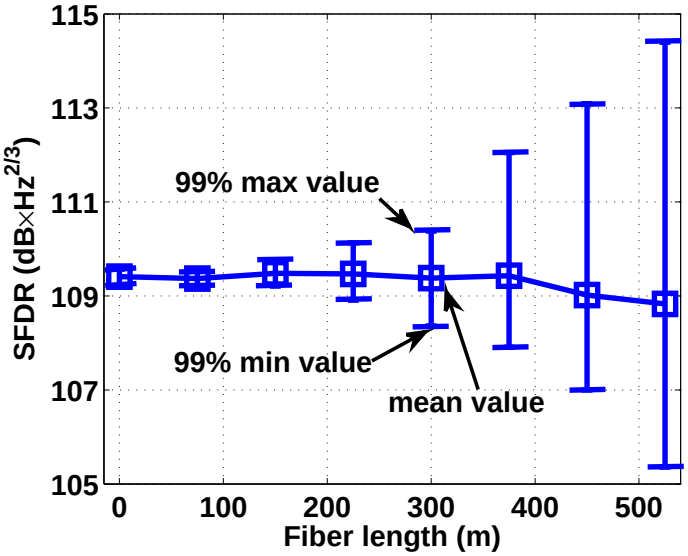

Figure 3.19: SFDR mean and 99% min/max values of the RoMMF link for increasing MMF fiber

from 110 dB × $Hz^{2/3}$ for a short fiber length to 105 dB × $Hz^{2/3}$ after 525 m MMF. Although there are 5 dB of degradation due to modal noise after 525 m, values of SFDR in excess of 100 dB × $Hz^{2/3}$ are considered good for RoMMF systems [35]. This is the result of the careful choice of components related to the experimental and theoretical activity of the previous sections.

In this section I will show the capability of this cost-effective RoMMF link to perform the transmission of LTE signals with high quality. The test of the transmission quality was performed evaluating the ACLR and the error vector magnitude (EVM) of the received signals. Fig. 3.20 shows the experimental setup. Two Agilent N9020A MXG VSGs were used to generate the LTE carriers: one for the downlink (DL) 750 MHz band and one for the DL 1950 MHz band. For the ACLR test two carriers per band were generated according to test-model 1.1 for LTE signals with channel bandwidth of 1.4 MHz [82]. The two carriers per band were spaced by 2.8 MHz and centered at 750 MHz and 1950 MHz. Thus, the two pairs of carrier frequencies were 748.6 MHz, 751.4 MHz and 1948.6 MHz, 1951.4 MHz, respectively. For

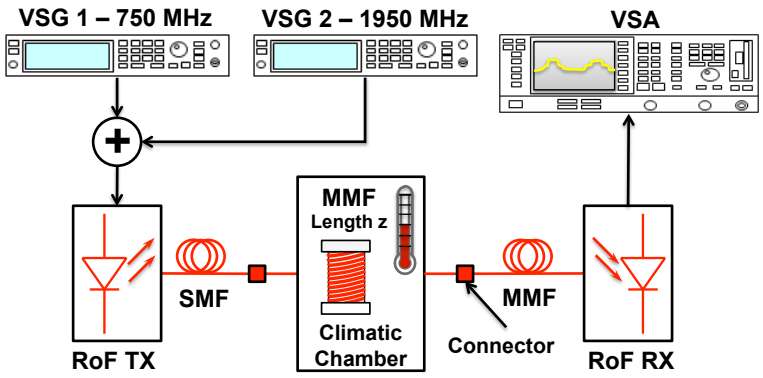

Figure 3.20: Experimental setup of dual band LTE transmission over the designed RoMMF link

the EVM test one carrier per band was generated according to test-model 3.1 for LTE signals with channel bandwidth of 20 MHz [82]. The carrier frequencies were 750 and 1950 MHz. The signals coming from the two VSGs were combined and applied to the RoF TX. The output power of the two VSGs was 0 dBm in both tests. At the receiver side an Agilent N5182A MXA VSA was used to perform the ACLR and the EVM tests.

As discussed regarding Fig. 3.19, the degradation increases with fiber length. Hence, the ACLR and EVM tests can focus just on the comparison between the performances in the back-to-back case and after 525 m of MMF. In the following table the mean value, the 99%maximum and the 99% minimum of ACLR are presented for back-to-back and 525 m fiber length for both bands.

	back-to-back		525 m MMF	
	750 MHz	1950 MHz	750 MHz	1950 MHz
ACLR mean (dBc)	-57.14	-60.31	-58.09	-56.64
ACLR 99% max (dBc)	-54.26	-57.65	-50.96	-48.14
ACLR 99% min (dBc)	-60.47	-63.27	-65.55	-63.87

As can be evinced from the table, the mean value at 750 MHz of the ACLR in the back-to-back case is comparable with the one after 525 m transmission.

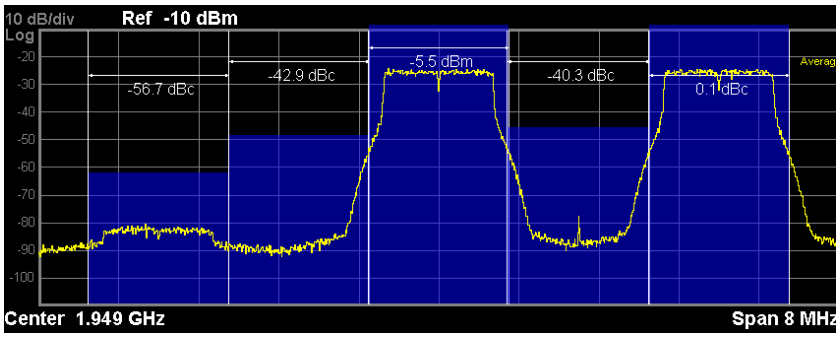

(a) Mean situation

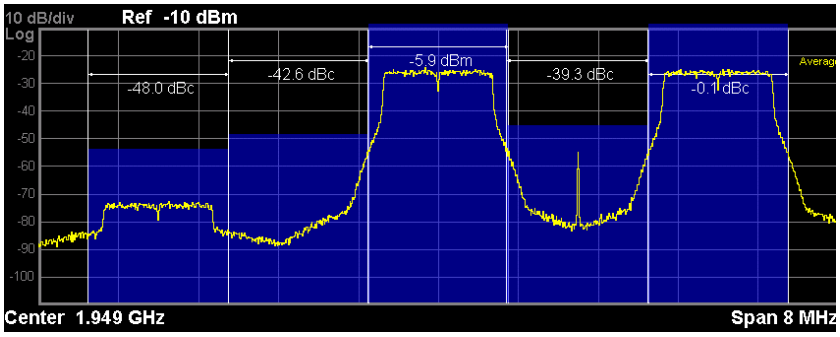

(b) Worst situation

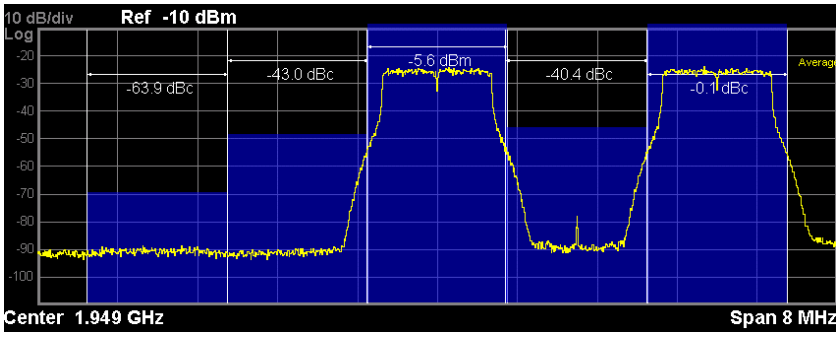

(c) Best situation

Figure 3.21: 525 m RoMMF link ACLR test with two 1.4 MHz LTE carriers in the 1950 MHz band

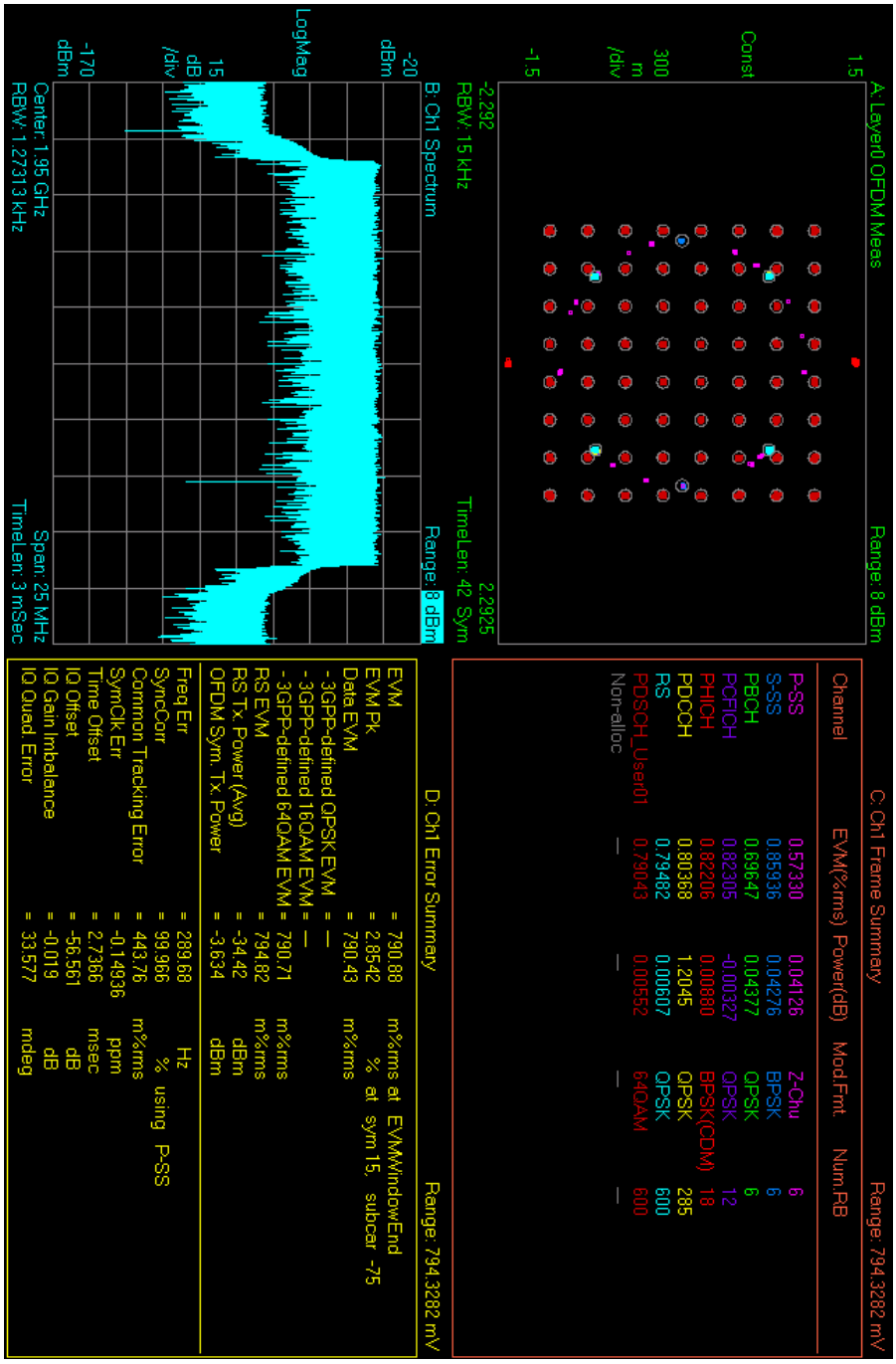

Figure 3.22: 525 m RoMMF link EVM test on a 20 MHz LTE carrier in the 1950 band

This is true also at 1950 MHz, because the reduction of approximately 4 dB in this case is mainly due to a reduced frequency response of the RoMMF link for increasing frequency more than modal noise. On the contrary, the difference between the mean value and the 99% max value of ACLR increases from 3 dB in the back-to-back case to 8–9 dB after 525 m. This increase of 5–6 dB in the difference between mean and 99% max value is due to modal noise. Fig. 3.21 explains graphically the meaning of the three different ACLR values for the 1950 MHz band in the previous table. In all sub-figures the two LTE carriers at 1948.6 and 1951.4 MHz can be noted in the center and on the right, respectively, and the adjacent channel at 1945.8 MHz on the left used for the determination of the ACLR. In sub-figure (a) a typical situation corresponding to the mean value of ACLR is shown. Sub-figures (b) and (c) depict experimental cases corresponding to the 99% max value, i.e. the worst case, and the 99% min value, i.e. the best case, respectively. Note that the difference between the three situations is represented practically by the spectral density contained in the adjacent channel since the power in the bands of the signals varies only by fraction of dB in the three cases. The best case, corresponding to the 99% min value, corresponds to the ACLR case limited only by noise, while the worst case, corresponding to the 99% max value, corresponds to the ACLR case limited by non-linear distortion. Note that, also in the worst case, the ACLR value is above the ACLR limit for DL of -45 dBc [22].

The other test to be performed on the received signal is the EVM test. As mentioned, for this test a LTE signal with a nominal band of 20 MHz is used. In the following table the mean, and the 99% max and 99% min values of the overall EVM and the peak EVM, EVM_{Peak}, for the back-to-back and the 525 m transmission are reported.

	back-to-back		525 m MMF	
	EVM (%)	EVM_{Peak} (%)	EVM (%)	EVM_{Peak} (%)
mean	0.561	2.187	0.622	2.350
99% max	0.617	2.831	0.773	2.961
99% min	0.496	1.736	0.543	1.969

As shown in the table, the impact of the MMF transmission on the EVM is negligible both on the overall EVM and the peak EVM. This is due to the good performance of the designed link and to the small sensitivity of the OFDMA format, used by a LTE signal, to impairments. Fig. 3.22 renders the typical EVM test corresponding to the max 99% value of the 525 m transmission. The close-to-ideal constellation diagram of the received 64–QAM can be evinced. The same figure contains also the spectrum of the received signal and more detailed information about the LTE signal reception. The presented result supports the designed RoMMF link as a viable cost-effective solutions for present and next-generation F–DAS systems based on MMF.

3.4 Summary

This chapter presented the modeling and experimental activity on RoMMF links employing directly modulated DFB and FP lasers. A theoretical model able to quantify the impact of modal noise on different received frequency components has been reported in section 3.1 and applied for the analytical calculation of the some meaningful statistical quantities, i.e. the mean received power at each frequency component and the standard deviation of the DC and the RF components. In section 3.2 an experimental activity for the determination of the impact of different characteristics of the link components on link gain, harmonic and intermodulation distortions due to modal noise has been presented. Some important design guidelines obtained from experimental results and supported by the developed theory have been reported. The major detrimental effects of modal noise has been proved to be adequately controllable with the appliance of central launch technique, a photodiode with a built-in ball lens, and a FP laser characterized by non-linear properties, modulation efficiency and frequency chirping competitive with DFB lasers. The designed RoMMF link was then described and characterized in section 3.3. This link proved to guarantee good performances in terms of ACLR and EVM up to 525 m when applied to a dual band radio

transmission of LTE signals.

Chapter 4

POF systems for home area networks

In this chapter, with the aim to illustrate the applicability of plastic optical fibers to a home area network (HAN), multi-gigabit transmission over 1 mm diameter POF IM–DD links employing a red VCSEL and Si photodiodes will be demonstrated. A model for the channel capacity of the POF link will be described in section 4.1. Experimental results using discrete multitone (DMT) modulation with 2^N–quadrature amplitude modulation (QAM) and bit-loading algorithm will be presented in section 4.2 and compared with the theoretical capacity. Finally, the positive addition of 3×2^N–QAM in the DMT bit-loading algorithm will be shown in section 4.3.

4.1 Model for the channel capacity of IM–DD POF links

Plastic optical fibers with a core diameter of approximately 1 mm are a kind of multimode fibers with more than one million of potentially excited modes [11]. This large amount of excitable modes together with the use of

This chapter is based on the results published in P6., P10., and P16.

low coherence sources, such as a LED or a VCSEL, reduces at the minimum level optical interferences effects described in section 3, such as modal noise. This leads to an initial simplification to the expansion of the detected current i_{out} with respect to the case of silica MMF.

Starting from (3.19), and neglecting the interference term, we can then write,

$$i_{out}(t,z) = I_0 \sum_{m=1}^{N_M} A_m^2 b_{mm} \left(1 + y(t - \tau_m z)\right) \tag{4.1}$$

In this section broadband digital transmission is considered. Hence, the modulating signal $y(t)$ in (4.1) can be expressed as,

$$y(t) = m_I \cdot s(t) \tag{4.2}$$

where $s(t)$ is the normalized signal with $\max|s(t)| = 1$. The last normalization is due to the fact that $s(t)$ is a baseband signal for digital transmission, thus the peak normalization of OMI is employed (see subsection 2.1.1.1).

Substituting (4.2) in (4.1) and considering the relationship in the Fourier domain, it is,

$$\begin{aligned} I_{out}(f,z) &= I_0 \sum_{m=1}^{N_M} A_m^2 b_{mm} \delta(f) + m_I I_0 \sum_{m=1}^{N_M} A_m^2 b_{mm} \exp\left(-j2\pi\tau_m z f\right) S(f) = \\ &= I_{out,0} \cdot \delta(f) + H(f)\, S(f) \end{aligned} \tag{4.3}$$

where $I_{out}(f,z)$ and $S(f)$ are the Fourier transform of $i_{out}(t,z)$ and $s(t)$, respectively, and $\delta(f)$ is the Dirac delta function.

Apart from the DC component, which can be disregarded using alternating current (AC) coupling between photodiode and electronics, in (4.3) the spectrum of the received current is linearly related with the normalized transmitted signal through the transfer function $H(f)$. Unfortunately, the huge number of modes present in large core POF causes the determination of the transfer function starting from an electromagnetic analysis to be very complex. It is then a common approach to describe $H(f)$ by a simplified model, such as a gaussian or a first order low-pass channel response or to recover it from measurements [11].

To determine the maximum capacity of the channel, C, with a known transfer function, $H(f)$, and a known noise density it is possible to use the result coming from the information theory [83, 84],

$$C \leq \int_{-\infty}^{+\infty} \frac{1}{2} \log_2 \left[1 + \frac{G_s(f) \left| H(f) \right|^2}{N(f)} \right] df \tag{4.4}$$

where $G_s(f)$ and $N(f)$ are the spectral densities of the transmitted signal and of the noise, respectively.

To calculate the capacity in (4.4) it is usually added the power constraint on the transmitted power P_s ,

$$P_s = \int_{-\infty}^{+\infty} G_s(f) df \tag{4.5}$$

In this derivation, to refer the performance to the received signal-to-noise ratio (SNR), I will instead force a constraint on the received power P_R ,

$$P_R = \int_{-\infty}^{+\infty} G_s(f) \left| H(f) \right|^2 df \tag{4.6}$$

The transmitted power spectral density $G_s(f)$ is the quantity to be optimized. The solution to this optimization problem is obtained with Lagrange multipliers and the so-called water-filling method. The solution is given by [83, 84],

$$G_s(f) = \left(\nu - \frac{N(f)}{\left| H(f) \right|^2} \right)^+ \tag{4.7}$$

where ν is the "water-level" to be determined applying the constraint in (4.6) and $(.)^+$ is the function giving the positive part of its argument,

$$(x)^+ = \begin{cases} x & if x \geq 0 \\ 0 & if x < 0 \end{cases} \tag{4.8}$$

In general there can be more than one interval of frequencies in which the "water-level" ν is above $N(f)/|H(f)|^2$, and thus $G_s(f)$ is not zeros. However, assuming that $N(f)/|H(f)|^2$ has an high-pass characteristic, i.e. it increases

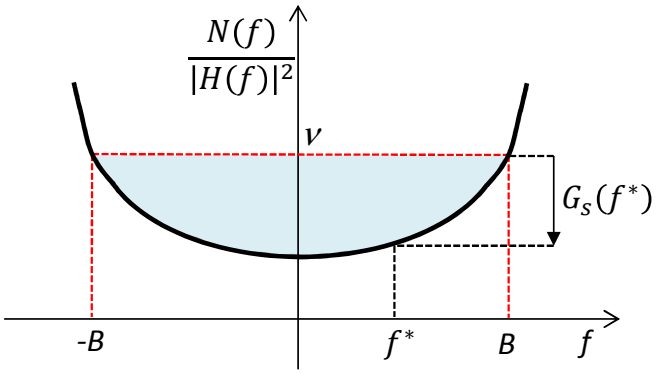

Figure 4.1: Water-filling method applied to $N(f)/|H(f)|^2$ with high-pass characteristic

with increasing frequency, there is only one interval starting from zero and ending in an unknown maximum bandwidth B in which $N(f)/|H(f)|^2$ is below the "water-level" ν as depicted in Fig. 4.1. This assumption corresponds to consider $H(f)$ a low-pass transfer function and $N(f)$ increasing with frequency or decreasing less than $|H(f)|^2$. Both assumptions can be taken since the transfer function of a large core POF has a low-pass characteristics and the noise spectral density typically increases with frequency. Substituting (4.7) in (4.6) and applying the previous assumption it is,

$$P_R = \int_{-\infty}^{+\infty} \left(\nu - \frac{N(f)}{|H(f)|^2}\right)^+ |H(f)|^2 \, df = 2\int_{0^+}^{B} \left(\nu - \frac{N(f)}{|H(f)|^2}\right) |H(f)|^2 \, df =$$
$$= 2\nu \int_{0^+}^{B} |H(f)|^2 \, df - 2\int_{0^+}^{B} N(f) df \tag{4.9}$$

where the starting point of the integral 0^+ denotes that the frequency 0 cannot be used for transmission.

From (4.9) the "water-level" can be determined,

$$\nu = \frac{\frac{1}{B}\int_{0^+}^{B} N(f) df}{\frac{1}{B}\int_{0^+}^{B} |H(f)|^2 \, df} \left(1 + \frac{P_R}{2\int_{0^+}^{B} N(f) df}\right) = \frac{\frac{1}{B}\int_{0^+}^{B} N(f) df}{\frac{1}{B}\int_{0^+}^{B} |H(f)|^2 \, df} (1 + SNR) \tag{4.10}$$

where SNR is the signal-to-noise ratio at the receiver.

Substituting (4.10) and (4.7) in (4.4), it is,

$$\begin{aligned} C \;\leq\; & \int_{0^+}^{B} \log_2 \left[\frac{\frac{1}{B}\int_{0^+}^{B} N(f)df}{\frac{1}{B}\int_{0^+}^{B} |H(f)|^2 \, df} \left(1+SNR\right) \frac{|H(f)|^2}{N(f)} \right] df = \\ = \; & B\log_2\left(1+SNR\right) + B\log_2\left(\frac{1}{B}\int_{0^+}^{B}\frac{N(f)}{N(B)}df\right) - \int_{0^+}^{B}\log_2\left(\frac{N(f)}{N(B)}\right)df - \\ & -B\log_2\left(\frac{1}{B}\int_{0^+}^{B}|H(f)|^2\,df\right) + \int_{0^+}^{B}\log_2\left(|H(f)|^2\right)df \end{aligned} \tag{4.11}$$

It is important to underline that the bandwidth B in (4.11) depends from the SNR value. To compare correctly this result with the classical one and with different channels it is necessary to consider the spectral efficiency instead of the capacity,

$$\begin{aligned} \frac{C}{B} \leq & \log_2\left(1+SNR\right) + \log_2\left(\frac{1}{B}\int_{0^+}^{B}\frac{N(f)}{N(B)}df\right) - \frac{1}{B}\int_{0^+}^{B}\log_2\left(\frac{N(f)}{N(B)}\right)df - \\ & - \log_2\left(\frac{1}{B}\int_{0^+}^{B}|H(f)|^2\,df\right) + \frac{1}{B}\int_{0^+}^{B}\log_2\left(|H(f)|^2\right)df \end{aligned} \tag{4.12}$$

The first term at the right hand of (4.12) is identical to the Shannon limit for a non-frequency selective additive white gaussian noise (AWGN) channel. The other terms represent the amount of difference from the classical limit. As it is reasonable to suppose, the spectral efficiency of the non-frequency selective AWGN channel is higher compared to the spectral efficiency of a low-pass frequency selective AWGN channel, as the one considered here. To prove this assumption, it is necessary to use the Jensen's inequality on the convex function $-\log_2(.)$ [84],

$$\log_2\left(\frac{1}{B}\int_{0^+}^{B}\frac{N(f)}{N(B)}df\right) - \frac{1}{B}\int_{0^+}^{B}\log_2\left(\frac{N(f)}{N(B)}\right)df \geq 0 \tag{4.13a}$$

$$- \log_2\left(\frac{1}{B}\int_{0^+}^{B}|H(f)|^2\,df\right) + \frac{1}{B}\int_{0^+}^{B}\log_2\left(|H(f)|^2\right)df \leq 0 \tag{4.13b}$$

where the equality holds when $N(f)$ or $|H(f)|^2$ are constant, i.e. white spectrum over the bandwidth B.

For frequency selective AWGN channels the power density $N(f)$ is constant, thus in (4.13a) the equality holds, while in (4.13b) the strict inequality holds. This means that the spectral efficiency of a frequency selective AWGN channel is lower than the one of a non-frequency selective AWGN channel. For an IM–DD POF system, although the noise is not rigourously white, the spectral efficiency is still lower than the one of a non-frequency selective AWGN channel due to the low-pass characteristics of the channel response.

To calculate (4.11) and (4.12) it is necessary to determine the value of the bandwidth B for every SNR value. Noting that with the assumption taken to derive (4.9) no power is allocated outside the bandwidth B, the "water-level", ν, corresponds to the value of $N(f)/|H(f)|^2$ for $f = B$. This consideration leads us to rewrite (4.10) to depend only on B,

$$\frac{\frac{1}{B}\int_{0^+}^{B}\frac{|H(f)|^2}{|H(B)|^2}df}{\frac{1}{B}\int_{0^+}^{B}\frac{N(f)}{N(B)}df} = (1+SNR) \tag{4.14}$$

Solving (4.14) for every SNR it is possible to derive the value of B to be substituted in (4.11) and (4.12). Noting that the term $1+SNR$ in (4.14) is also present in (4.12), it is possible to express C/B only as a function of the noise density and the transfer function,

$$\frac{C}{B} \leq \frac{1}{B}\int_{0^+}^{B}\log_2\left(\frac{|H(f)|^2}{|H(B)|^2}\right)df - \frac{1}{B}\int_{0^+}^{B}\log_2\left(\frac{N(f)}{N(B)}\right)df \tag{4.15}$$

I will show the application of this model to a super-Gaussian family of low-pass channel responses with white noise [85]. Indeed, a gaussian low-pass characteristic is often assumed to well describe an IM–DD optical link based on POF, in particular the step-index one [86].

The transfer function of a super-gaussian low-pass channel and the noise density are respectively,

$$|H(f)| = H_0 \cdot e^{-\frac{\ln(2)}{2}\left(\frac{f}{f_{3dB}}\right)^{2n}} \tag{4.16a}$$

$$N(f) = N_0 \tag{4.16b}$$

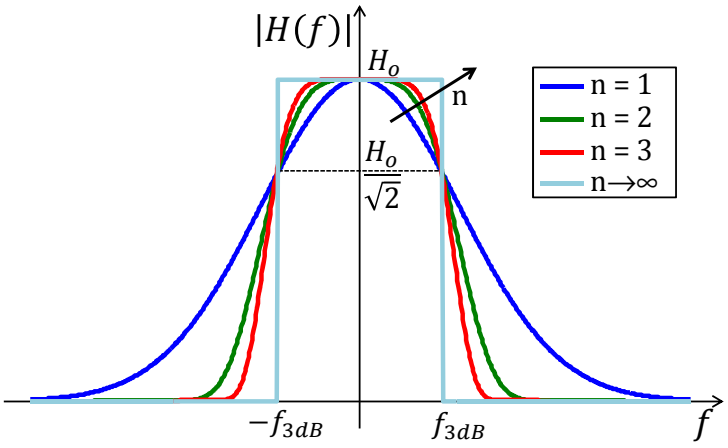

Figure 4.2: Example of a super-Gaussian shape of the channel response

where H_0 is an amplitude factor, f_{3dB} is the single-sided 3 dB bandwidth of the channel and n is an integer channel parameter. N_0 is the noise density. In Fig. 4.2 an example of the super-gaussian shape of the channel response with increasing values of n is represented.

Substituting (4.16a) and (4.16b) in (4.15), it is,

$$\frac{C}{B} \leq \frac{1}{B}\int_{0^+}^{B} \log_2\left(\frac{e^{-\ln(2)\left(\frac{f}{f_{3dB}}\right)^{2n}}}{e^{-\ln(2)\left(\frac{B}{f_{3dB}}\right)^{2n}}}\right) df = \frac{2n}{2n+1}\left(\frac{B}{f_{3dB}}\right)^{2n} \tag{4.17}$$

Substituting (4.16a) and (4.16b) in (4.14), we have,

$$\begin{aligned} 1 + SNR &= \frac{1}{B}\int_{0^+}^{B} \frac{e^{-\ln(2)\left(\frac{f}{f_{3dB}}\right)^{2n}}}{e^{-\ln(2)\left(\frac{B}{f_{3dB}}\right)^{2n}}} df = \\ &= 2^{\left(\frac{B}{f_{3dB}}\right)^{2}} \frac{f_{3dB}}{(\ln(2))^{1/2n} B} \cdot \int_{0^+}^{(\ln(2))^{1/2n}\frac{B}{f_{3dB}}} e^{-t^{2n}} dt \end{aligned} \tag{4.18}$$

The integral in (4.18) does not have a representation by elementary functions. Anyway, it can be solved by using a special function, in particular a confluent hypergeometric function of the first kind, often represented by the

symbol ${}_1\mathrm{F}_1(a;b;z)$ [59]. Indeed, the following integral representation holds,

$$ {}_1\mathrm{F}_1(a;b;z) = \frac{\Gamma(b)}{\Gamma(b-a)\Gamma(a)} \int_0^1 e^{tz} t^{a-1} (1-t)^{b-a-1} dt \tag{4.19} $$

where $\Gamma(.)$ is the Gamma function [59].

After some calculation, using (4.19) it is possible to show that,

$$ \int_0^z e^{-t^{2n}} dt = z e^{-z^{2n}} {}_1\mathrm{F}_1 \left(1; \frac{2n+1}{2n}; z^{2n} \right) \tag{4.20} $$

Substituting (4.20) in (4.18), it gives us,

$$ 1 + SNR = {}_1\mathrm{F}_1 \left(1; \frac{2n+1}{2n}; \ln(2) \cdot \left(\frac{B}{f_{3dB}} \right)^{2n} \right) \tag{4.21} $$

From (4.21) it is not possible to derive a closed-form relationship of B to insert in (4.17). However, it is possible to do the reverse operation. Obtaining B/f_{3dB} from (4.17) and substituting in (4.21) it is,

$$ SNR \geq {}_1\mathrm{F}_1 \left(1; \frac{2n+1}{2n}; \ln(2) \cdot \frac{2n+1}{2n} \cdot \frac{C}{B} \right) - 1 \tag{4.22} $$

I underline that (4.22) states that there is a relationship between SNR and C/B which does not depend on the channel bandwidth f_{3dB}, but only on its shape. This does not mean that two gaussian channels with different 3 dB bandwidth give rise to the same capacity, but that for the same SNR the ratio between the capacity and the used bandwidth for transmission is the same. This property is generally derivable from (4.12) and (4.14) assuming a scaling factor in the frequency domain.

Fig. 4.3(a) shows the spectral efficiency of super-gaussian low-pass AWGN channels with the integer parameter n ranging from 1 to 4, compared with a flat AWGN channel. As expected, the spectral efficiency of all the super-gaussian low-pass channels is lower than the spectral efficiency of an AWGN channel and similar for low SNR value. For increasing values of the integer parameter n the channel spectral efficiency approaches the flat AWGN channel limit. This is related to the fact that for increasing values of n the channel becomes similar to a flat channel with bandwidth $B = f_{3dB}$.

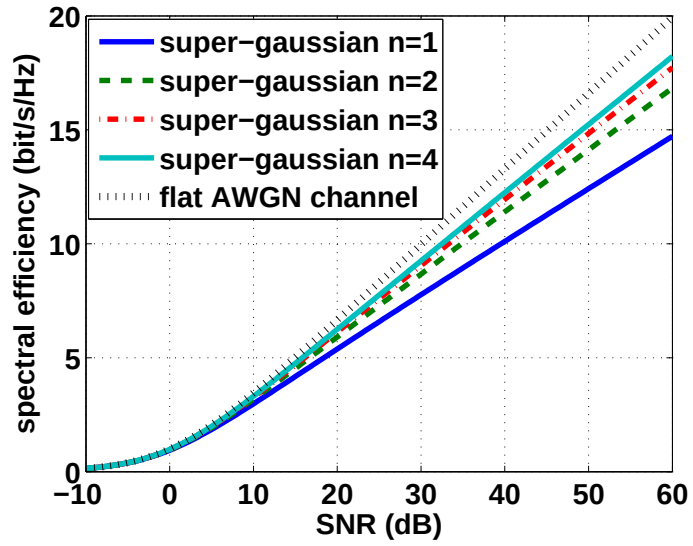

(a)

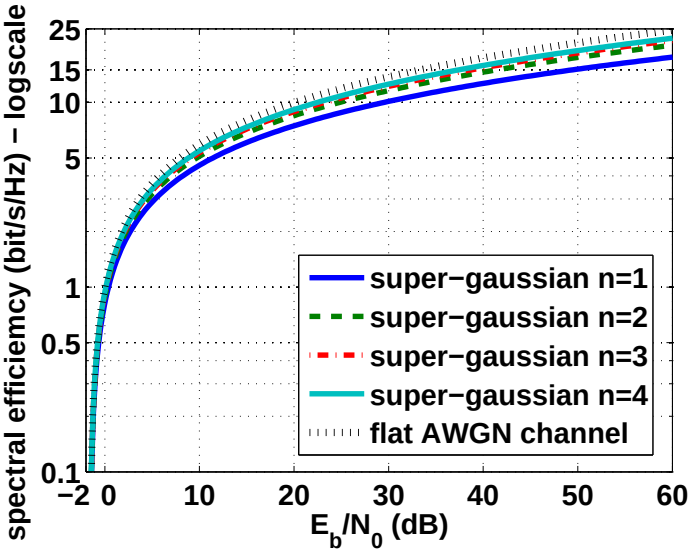

(b)

Figure 4.3: Comparison of spectral efficiencies of different super-gaussian low-pass AWGN channels and of a flat AWGN channel versus the received SNR (a) and the received E_b/N_0 (b)

From (4.22) it is also possible to determine the relationship between the capacity and the received energy per bit to noise ratio, E_b/N_0 [84], which in the case of white noise it is simply related to SNR with,

$$\frac{E_b}{N_0} = SNR \cdot \frac{B}{R_b} \tag{4.23}$$

where R_b is the bit-rate.

Substituting (4.23) in (4.22) when the bit-rate, R_b, approaches the capacity, C, we obtain,

$$\frac{E_b}{N_0} \geq \frac{{}_1\mathrm{F}_1\left(1; \frac{2n+1}{2n}; \ln(2)\frac{2n+1}{2n}\frac{C}{B}\right) - 1}{\frac{C}{B}} \tag{4.24}$$

Fig. 4.3(b) compares the spectral efficiency of super-gaussian low-pass AWGN channels with the integer parameter n ranging from 1 to 4, and a flat AWGN channel. For the flat AWGN channel the relationship between E_b/N_0 and C/B is the following [84],

$$\frac{E_b}{N_0} \geq \frac{2^{\frac{C}{B}} - 1}{\frac{C}{B}} \tag{4.25}$$

From Fig. 4.3(b) it is evidenced that the spectral efficiency of the super-gaussian low-pass channels is always lower than the spectral efficiency of the flat AWGN channel. Again the spectral efficiency of the super-gaussian channels approaches the flat AWGN channel limit for increasing n. Note also that all the curves start from the minimum allowable E_b/N_0 value for data transmission around -1.59 dB [84].

Even if the spectral efficiency increases with the integer parameter n, this does not mean that for a fixed SNR a super-gaussian channel with higher n gives rise to a theoretical capacity higher with respect to a super-gaussian channel with lower n. To prove this statement it is possible to determine the absolute capacity normalized by the 3 dB bandwidth of the channel, f_{3dB}, instead that the used bandwidth, B, which depends from the SNR. From (4.17) it is,

$$\frac{C}{f_{3dB}} \leq \frac{2n}{2n+1}\left(\frac{B}{f_{3dB}}\right)^{2n+1} \tag{4.26}$$

Obtaining B/f_{3dB} from (4.26) and substituting in (4.21) it results,

$$SNR \geq {}_1\mathrm{F}_1\left(1; \frac{2n+1}{2n}; \ln(2)\left(\frac{2n+1}{2n}\frac{C}{f_{3dB}}\right)^{\frac{2n}{2n+1}}\right) - 1 \tag{4.27}$$

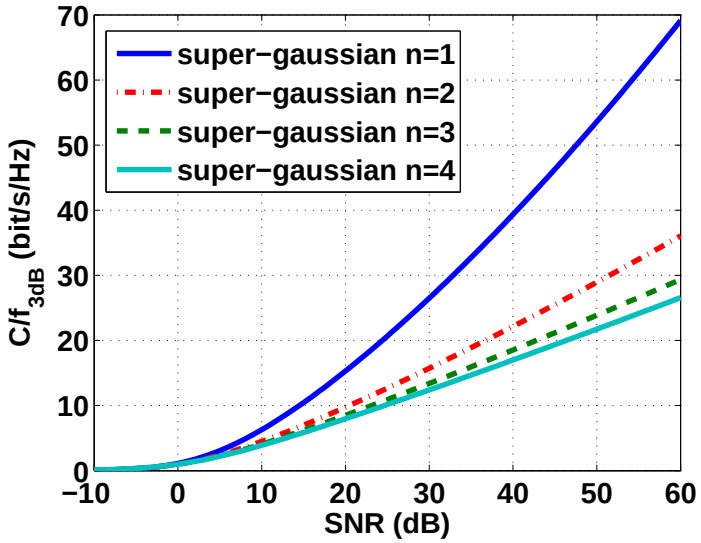

Figure 4.4: Comparison of normalized capacity C/f_{3dB} of super-gaussian low-pass AWGN channels with increasing n versus SNR

Fig. 4.4 reports the capacity normalized to the 3 dB bandwidth for super-gaussian channels with integer parameter n ranging from 1 to 4. The curve corresponding to $n = 1$ gives rise to the highest normalized capacity and in general the normalized capacity decreases with increasing n. For example for a SNR around 20 dB there is a factor of 2 between the curve corresponding to $n = 1$ and the curve corresponding to $n = 4$. This is due to the fact that in the super-gaussian channel with $n = 1$ the information can be allocated in a larger bandwidth compared to the super-gaussian channel with $n > 1$. This leads to a lower spectral efficiency, but a higher capacity.

The result obtained for the super-gaussian low-pass channel will be used as a reference for the capacity of IM–DD POF links used in the experimental activity. In that case, the spectral efficiency and capacity will be determined

also numerically. I underline that with the described model it is possible to obtain an upper bound of the real capacity of the channel. Indeed, an IM–DD POF is not only limited in power, but also in dynamic range. This means that if the transmitted signal, $s(t)$, with spectral density $G_s(f)$, has a crest factor, i.e. the ratio of the peak to the root-mean-square amplitude value of the signal, exceeding the maximum dynamic range, clipping occurs. However, for POF transmission equal or longer than 50 m the received SNR with a broadband transmission is typically below 20 dB. For low received signal power and SNR values the system is much more SNR-limited than dynamic-range limited, hence the theoretical results maintain a practical meaning.

4.2 High capacity transmission over GI–POF employing DMT

In this section I will present IM–DD POF links employing graded-index POF and two different types of receiver. In subsection 4.2.1 I will shortly introduce DMT and the used bit-loading algorithm. Then, in subsection 4.2.2 I will present the experimental setup and the theoretical maximum performance of this links with the model described in section 4.1. In subsection 4.2.3 and 4.2.4 I will show experimental results related to the application of DMT modulation with power and bit-loading to obtain multi-gigabit transmission. Finally, I will depict the influence on the main DMT and optical parameters on the link performance in subsection 4.2.5.

4.2.1 Bit and power loading in DMT

DMT modulation is the baseband version of orthogonal frequency division multiplexing (OFDM) [87]. It has been widely used in digital subscriber copper lines for the DSL techniques. The application of this technique to optical technologies derives from the widespread availability of digital signal processing (DSP) electronics at affordable prices. The key point to consider

DMT modulation as a candidate for high-capacity transmission over POF is the possibility to use a bit and power-loading algorithm which adapts to the channel. The subcarriers are treated as separate narrowband channels whose power and modulation can be optimized to fit better the channel characteristics at the subcarrier frequency. Since the optimization is always subject to a constraint on the total power, the rate-adaptive bit-loading problem is a discrete reformulation of the problem expressed by (4.4) and (4.5). Indicating as N the number of subcarriers, b_n and E_n, respectively, the number of bits and the energy allocated for the n^{th} subcarrier, it is [88],

$$\max_{E_n}(b) = \max_{E_n}\left(\sum_{n=1}^{N} b_n\right) = \max_{E_n}\left(\sum_{n=1}^{N} \log_2\left(1+\frac{E_n g_n}{\Gamma}\right)\right) \tag{4.28}$$

subject to

$$\sum_{n=1}^{N} E_n = E_{tot} \tag{4.29}$$

where b is the total numer of bits, g_n is the SNR of the n^{th} subcarrier when unit energy is applied, and E_{tot} is the total available energy.

Γ is the SNR gap, also reported as normalized SNR, which is the difference in SNR required to achieve maximum capacity as defined by the Shannon limit at a given error probability.

For M–QAM modulation, the SNR gap, Γ, can be related to the probability of (two-dimensional) symbol error, P_e, by the following tight upper bound [89, 90],

$$P_e \leq 2 \cdot \mathrm{erfc}\left(\sqrt{\frac{3}{2}\Gamma}\right) \tag{4.30}$$

where erfc is the complementary error function [59].

In this work the probability of symbol error is fixed to be 10^{-3}, hence from the inversion of (4.30) it can be determined $\Gamma \approx 6$ dB. This means that with M–QAM and probability of symbol error of 10^{-3}, the maximum achievable capacity is shifted of 6 dB in SNR with respect to the Shannon limit of the channel.

The bit error rate (BER) related to the symbol error probability of 10^{-3} depends on the exact modulation and mapping employed, but in any case it is always less than the symbol error probability, since a symbol error typically corresponds to a number of bit errors lower than the number of bits transported by the symbol. However, for real implementation BER of the order of 10^{-4} or 10^{-3} is too high. A forward error correction (FEC) code is then required to reduced the BER. Focusing on error-free operation, defined as BER less than 10^{-12}, an enhanced forward error correction (EFEC) code can be employed to reduce an input BER of up to $3 - 4 \times 10^{-3}$ to an output BER below 10^{-12} at the cost of a 7% redundancy ratio [91].

In the experimental activity I have not implemented the EFEC but I have considered uncoded performance giving a BER below 10^{-3} to guarantee error-free operation when EFEC is inserted.

The solution to the bit-rate maximization problem in (4.28) and (4.29) is similar to the water-filling method described in section 4.1, and thus it could be solved with the same technique. However, in this case the optimization variables E_n should be choose in order to achieve integer values of bits, b_n, allocated per subcarrier. Among the different algorithm to solve the problem in (4.28) and (4.29) with finite bit granularity, in this work the Chow's rate-adaptive algorithm was employed [92]. The algorithm works as follow [93]:

1. Sort g_n in decreasing order, so that g_1 is the largest
2. Set $b_{temp}(N+1) = 0$ and $i = N$ ($b_{temp}(i)$ and i are the tentative total bits per subcarrier and number of used subcarriers, respectively)
3. Set equal energy on used tones: $E_n = E_{tot}/i$ for $n = 1, ..., i$
4. Compute $b_{temp}(i) = \sum_{n=1}^{i} \log_2 (1 + E_n g_n/\Gamma)$
5. If $b_{temp}(i) < b_{temp}(i+1)$, then $i \leftarrow i + 1$ and go to step 6; otherwise $i \leftarrow i - 1$ and go to step 3
6. Compute $E_n = E_{tot}/i$ and $b_n = \log_2 (1 + E_n g_n/\Gamma)$ for $n = 1, ..., i$, $E_n = 0$ and $b_n = 0$ for $n = i + 1, ..., N$

7. Scale E_n by the factor $\left(2^{\text{Round}(b_n)} - 1\right) / \left(2^{b_n} - 1\right)$ for $n = 1, ..., i$ (Round(x) is the function giving the nearest integer to x)

8. Compute $b_n = \text{Round}(b_n)$ for $n = 1, ..., i$

9. Scale E_n by the factor $E_{tot} / \left(\sum_{n=1}^{i} E_n\right)$ for $n = 1, ..., i$

The Chow's algorithm does not obtain the exact solution of the optimization problem in (4.28) and (4.29), but it achieves a near-optimum solution [93, 92].

Once the number of bits, b_n, allocated to the n^{th} subcarrier has been determined by Chow's algorithm, the proper modulation scheme can be assigned to each subcarrier. Using M–QAM modulation, the n^{th} subcarrier is allocated with a M_n–QAM modulation where $M_n = 2^{b_n}$. The value E_n is used as a pre-emphasis.

4.2.2 Experimental setup

Fig. 4.5 depicts the experimental setup used in this work. The DMT modulation and demodulation were performed off-line starting from a software developed in a previous thesis [88]. The transmitted DMT signal was physically generated by a Tektronix AWG7122B arbitrary waveform generator (AWG) with 10-bit resolution. The received DMT signal was digitally converted by a real-time Tektronix DPO72004 digital phosphor oscilloscope (DPO) with 8-bit resolution. The AWG and the DPO were substantially used as the digital-to-analog converter (DAC) and the analog-to-digital converter (ADC) elements, respectively. More details on the DMT signal will be reported in the next sections. The IM–DD POF link was composed by a VCSEL, a graded-index POF and a receiver based on two different PDs. The VCSEL was a Firecomms red VCSEL, represented in Fig. 4.6(a), emitting at the wavelength of 667 nm, with a peak power of 1 mW, a beam divergence of 14° and more than 3 GHz of modulation bandwidth [94]. Due to the large beam divergence and the peak power of 1 mW, the VCSEL was compliant with eye-safety regulations [95]. The emitted light from the VCSEL was coupled directly in free space with the GI-POF. I employed different lengths

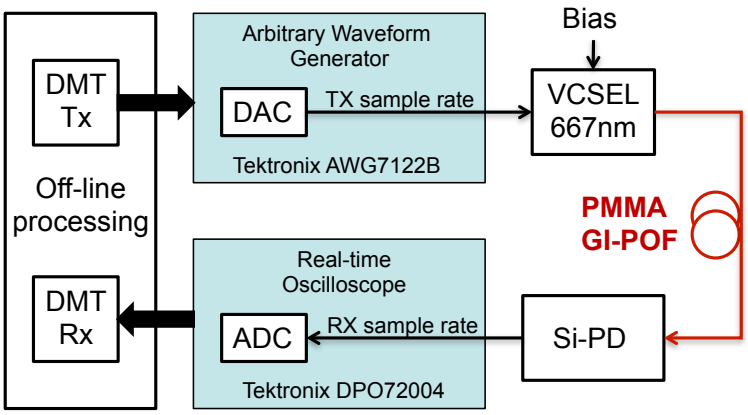

Figure 4.5: Experimental setup

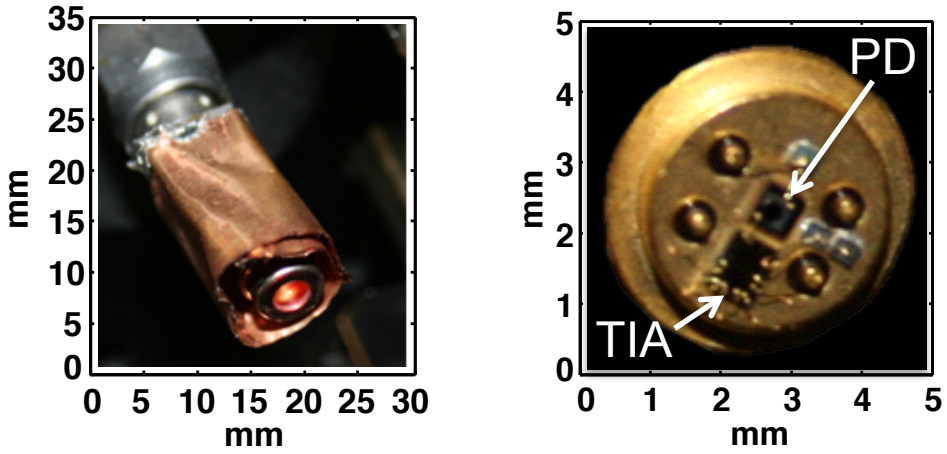

(a) VCSEL

(b) Si-PIN PD

Figure 4.6: Photos of the red VCSEL (a) and the receiver based on the Si-PIN PD (b) used in the experimental setup

of fiber ranging from a few meters to a maximum distance of 50 m, which was the main target of this work. All the GI-POF samples were Optimedia OM-GIGA fibers with a diameter of 1 mm, a loss of 0.3 dB/m at 665 nm, and a nominal bandwidth of more than 3 Gbit/s at 50 m [96]. The output power of the POF was coupled in free space with the receiver. Two receivers were employed, one based on a silicon (Si) avalanche photodetector (APD) and one based on a Si-PIN PD. The APD had an active area with a diameter of 230 μm and was followed by a two-stage electrical amplifier with 40 dB of gain. The PIN PD had an active area with a diameter of 400 μm and was followed by a TIA with a trans-impedance gain of 10 $k\Omega$ placed close to the PD as shown in Fig. 4.6(b).

The design of the optical link is critical with respect to the performance of the system. The main parameter to be optimized is the VCSEL bias current which influences the transmitted power, the link gain and the non-linearities. Fig. 4.7(a) shows the static Light-Current characteristics of the VCSEL at the ambient temperature of 21°C. As can be noted from Fig. 4.7(a), the optical power is close to zero below the threshold current of around 0.5 mA, it increases up to 1 mW for a bias current around 4 mA, and then it decreases for higher bias currents. Fig. 4.7(a) suggests to apply a bias current of 2-3 mA to obtain both a high gain and a linear operation due to the saturation effect of the power for higher currents. Fig. 4.7(b) presents the small signal gain variation for a bias current between 2 and 6 mA. The figure confirms that the bias current of 2-3 mA presents higher small signal gain values. However there is just a decrease of 1 dB for 4 mA which does not exclude this value. To take a decision, Fig. 4.7(c) shows the IIP2 and IIP3 for increasing bias current. These values are obtained with a two tone test at 365 and 375 MHz. As shown in Fig. 4.7(c), the bias current of 4 mA corresponds to the maximum IIP2 and close to maximum IIP3. Due to this better non-linear performance, to the small loss of gain, and to the possibility to modulate the VCSEL with higher peak-to-peak currents, the bias current of 4 mA was used in this experimental activity. However, the performances obtained with different values of bias current will be also addressed with reference to DMT transmission.

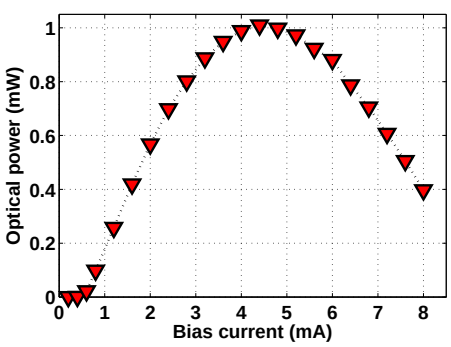

(a) Optical power

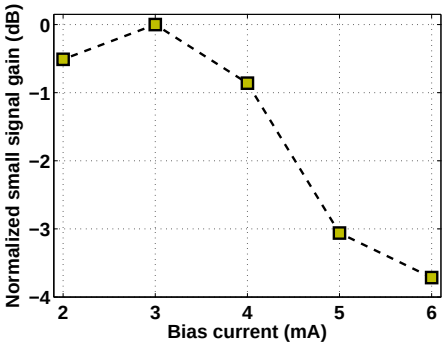

(b) Normalized small signal gain

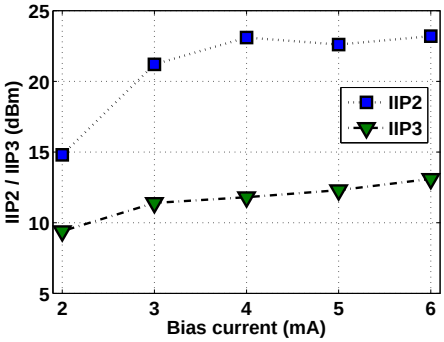

(c) IIP2 / IIP3

Figure 4.7: Optical emitted power (a), normalized small signal gain (b), and IIP2 / IIP3 (dBm) versus VCSEL bias current

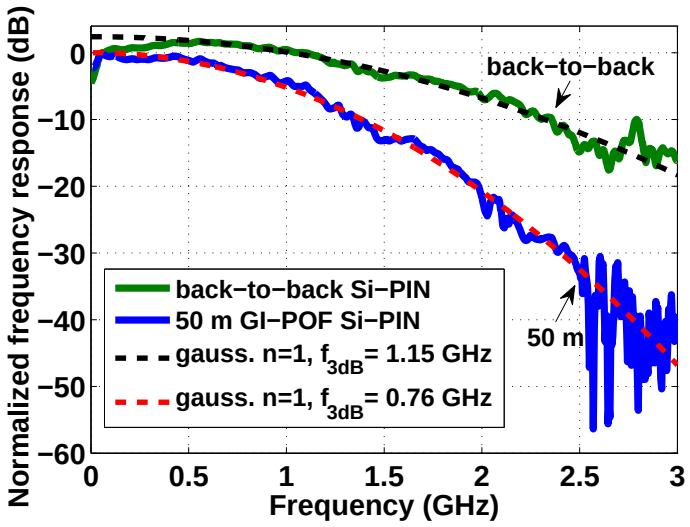

(a) PIN-PD

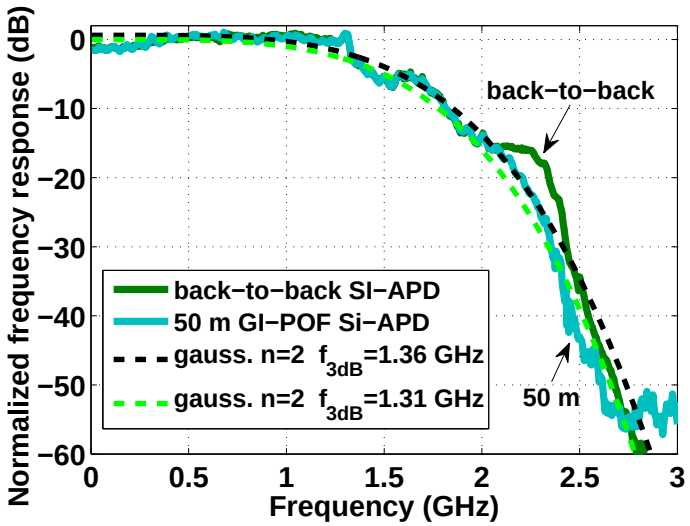

(b) APD

Figure 4.8: Normalized frequency response of the POF link using PIN-PD (a) or APD (b) for back-to-back and 50 m transmission, and best super-gaussian interpolating functions

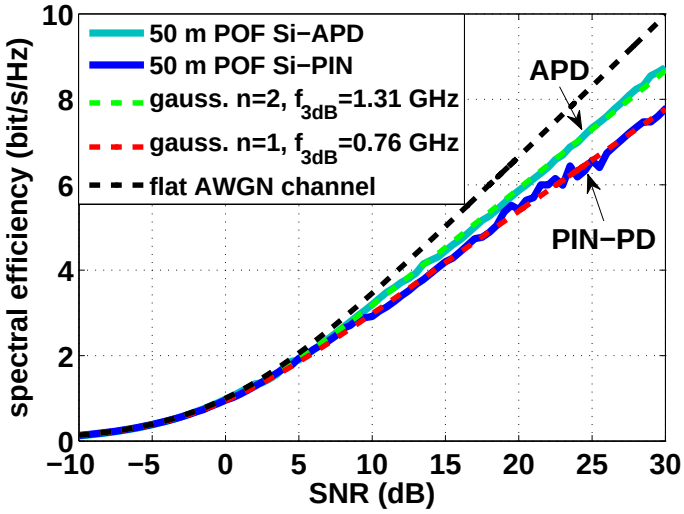

(a)

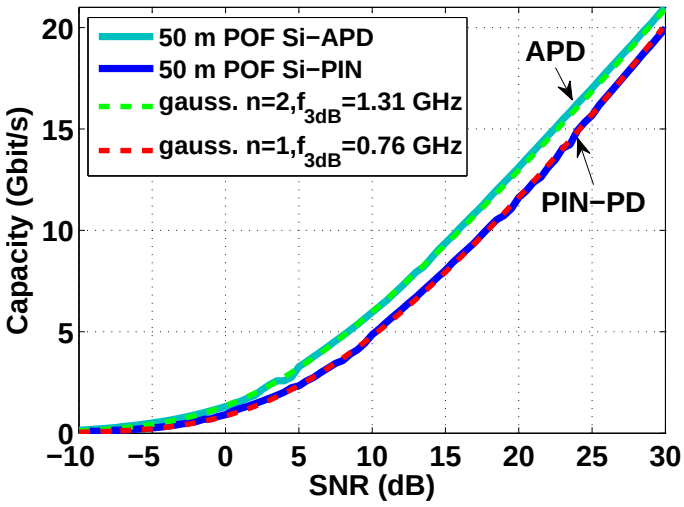

(b)

Figure 4.9: Comparison of spectral efficiency (a) and capacity (b) of the 50 m POF link employing PIN-PD orAPD, and of the best super-gaussian interpolating functions

Once the bias current of the VCSEL is set, the two other factors which limits the systems are the finite bandwidth of the receiver, and the finite bandwidth and loss of the POF. Fig. 4.8 shows the frequency responses of the POF link employing the PIN–PD (a) and the APD (b) after 2 m of POF transmission, denoted as back-to-back case, and after 50 m of POF transmission. Since the transmitter has a modulation bandwidth of 3 GHz, from Fig. 4.8 it can be evinced that the PIN-PD (a) and the APD (b) have different frequency responses. In particular, the PIN-PD has a frequency response that above 300 MHz has a gaussian shape, i.e. super-gaussian with $n = 1$, with a 3 dB bandwidth of 1.15 GHz. The APD has instead a flat response up to 1.25 GHz and then decreases sharply due to reduction of the avalanche effect for higher frequencies. This frequency response can be described by a super-gaussian function with $n = 2$ and 3 dB bandwidth equal to 1.36 GHz. When a 50 m long fiber is inserted between transmitter and receiver, apart from a reduction of 30 dB in the electrical response, due to the optical attenuation of 15 dB, there is also a reduction of the system bandwidth which can be evinced from fig. 4.8(a) and fig. 4.8(b) comparing the 50 m case with the back-to-back case. The 50 m transmission with PIN-PD has a frequency response that has again a gaussian shape but with a 3 dB bandwidth of 0.76 GHz. This is due to the bandwidth reduction operated by the POF transmission. The 50 m transmission with APD has instead a frequency response which is similar to the back-to-back case. It can still be represented by a super-gaussian function with $n = 2$ and with a slightly lower 3 dB bandwidth of 1.31 GHz. The different effect of 50 m POF on the systems employing APD and PIN-PD is due for high frequencies to the sharply reduction of the response of the APD, while for medium frequency this is maybe due to the lower collecting area of the APD which could avoid some higher order modes to be detected.

The APD seems to be the better solution for transmission. However, there are two points to be underlined. First, the APD receiver guarantees a considerable gain, but also a much higher noise compared to the PIN-PD. In second place, as reported in Fig. 4.4 the theoretical capacity normalized to the 3 dB bandwidth is lower for super-gaussian channels with higher n

parameter. Fig. 4.9 shows the numerical evaluation of the spectral efficiency (a) and the capacity (b) of the 50 m long POF link employing PIN–PD and APD. The theoretical evaluation of the same quantities is also performed with the super-gaussian interpolating functions reported in Fig. 4.8. From Fig. 4.9(a), it can be noted that the evaluated spectral efficiency of the POF link is below the theoretical spectral efficiency of the flat AWGN channel. Moreover, there is a good agreement between the spectral efficiency obtained from the measured frequency responses and the ones of the super-gaussian interpolating functions. Fig. 4.9(b) shows the absolute capacity in Gbit/s of the two different 50 m long POF links. As expected, the APD guarantees a larger theoretical capacity due to the higher 3 dB bandwidth. However, since the link employing the PIN–PD has a frequency response close to a super-gaussian with a lower parameter n its theoretical capacity is competitive with the link employing the APD even if the 3 dB bandwidth is lower. For example, for a target capacity of 10 Gbit/s a minimum SNR of 16 dB and 18 dB is necessary for the link employing APD and PIN–PD, respectively. This difference of 2 dB can be considered negligible due to the lower noise level of the receiver employing PIN–PD and TIA with respect to the receiver with APD and two-stage electrical amplifier.

4.2.3 50 m PMMA GI–POF transmission with APD

To achieve an optimized transmission over 50 m POF with APD or PIN–PD, the DMT modulation parameters were optimized separately in both cases. For the system employing APD the DMT parameters listed in Tab. 4.1 were utilized. In particular, the DMT signal used 256 subcarriers spaced by 6.25 MHz within a bandwidth of 1.6 GHz. To this purpose, the sampling rate of the AWG was fixed at 3.2 Gsample/s. The sampling rate of the DPO was instead fixed to the maximum of 50 Gsample/s. This high sampling speed is due to the lack of a physical clock recovery to be used as trigger by the DPO. Hence, the sampling rate reconstruction was performed off-line by digital filter suppression and resampling. Indeed, oversampling was necessary to reduce inter-carrier interference [97]. For cost-effective real implementation,

Number of subcarriers	256
Cyclic prefix length	8
Number of Schimdl blocks	4 every 200 DMT symbols
Digital clipping	Clipping factor $\mu = 9$ dB
Receiver equalizer	one-tap channel equalizer
Transmitter sampling rate	3.2 Gsample/s
Receiver sampling rate	50 Gsample/s

Table 4.1: DMT signal parameter for 50 m transmission with APD

the use of such high sampling speed can be avoided performing TX–RX synchronization with Schimdl & Cox approach [98], and/or training symbols [69].

An important DMT parameter is the clipping factor, μ, i.e. the ratio between the maximum permissible amplitude of an envelope limiter and the root-mean-square amplitude value of the DMT signal before clipping [99]. Due to its multitone nature, DMT signal presents a high peak-to-average power ratio (PAPR). As deeply studied in [88], to increase the received average power and therefore the transmission rate, digital clipping is required. With digital clipping the DMT crest factor is reduced to a value close to the clipping factor , μ, (the crest factor does not become equal to μ since the root-mean-square amplitude value is also slightly reduced by clipping). In [100] it was demonstrated that a clipping factor $\mu = 10$ dB is typically optimum. Starting from that value I determined experimentally that for the system employing APD the optimum value for maximizing the bit-rate was $\mu = 9$ dB.

With these DMT parameters, a DMT signal with the same number of bits and power levels in all subcarriers was sent into the channel to test it. Using 4 Schimdl blocks every 200 DMT symbols for symbol synchronization and channel estimation, it was possible to estimate the SNR characteristics of the channel. Fig. 4.10(a) shows the estimated SNR. From these values the bit-loading algorithm described in subsection 4.2.1 can determine the optimum bit and power to be allocated to each subcarrier. Fig. 4.10(c)

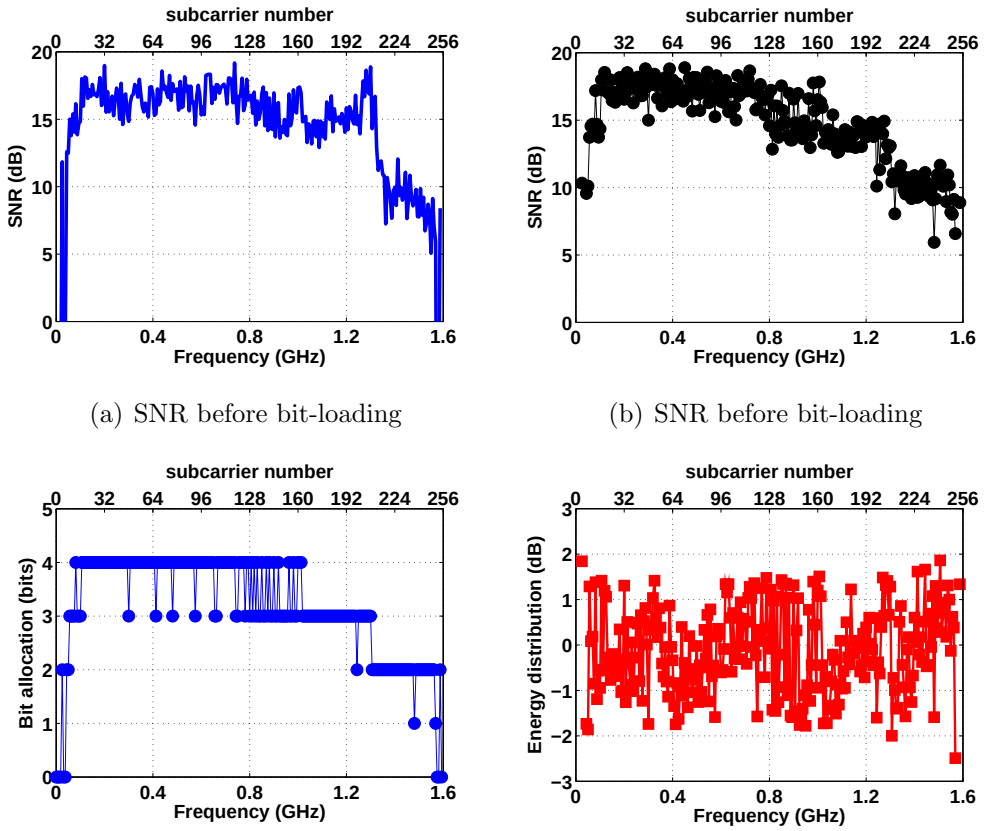

(a) SNR before bit-loading

(b) SNR before bit-loading

(c) Bit allocation

(d) Power allocation

Figure 4.10: Bit loading application on 50 m POF transmission with APD: estimated SNR before bit-loading (a), estimated SNR after bit-loading (b), bit (c) and power (d) allocation

shows the optimum bit allocation for a symbol error target below 10^{-3} ($\Gamma =$ 6 dB). The bit allocation has a stair-like shape from a maximum number of bits equal to 4, corresponding to 16–QAM modulation, to a minimum of 1 bit, corresponding to binary phase shift keying (BPSK) modulation. Note that there are also some unused subcarriers. The energy distribution corresponding to this bit allocation is shown in Fig. 4.10(d). With this power allocation the estimated SNR after bit-loading is presented in Fig. 4.10(b). Note that the estimated SNR after bit-loading remembers the bit-allocation of Fig. 4.10(c). This is due to the pre-emphasis performed by the power allocation.

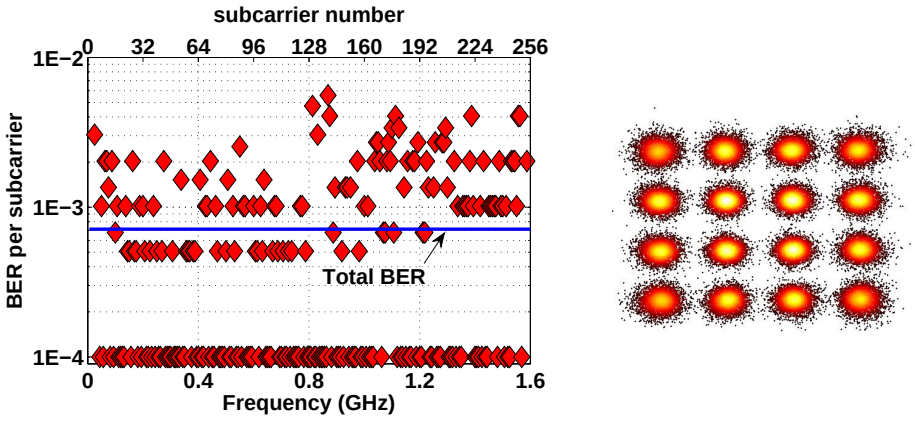

(a) (b)

Figure 4.11: BER performance per subcarrier (a), constellation diagram of the demodulated signal for the subcarriers with 16–QAM (b)

With the presented bit and power allocation a gross bit-rate of 5 Gbit/s was achieved with a BER of 7.1×10^{-4}, which is below the target of 10^{-3}. Fig. 4.11(a) shows the measured BER per subcarrier. The measured BER ranges from 10^{-4} to 10^{-2}. In many of the subcarriers in Fig. 4.11(a) no errors where found. To these subcarriers a BER of 10^{-4} was associated, which was a value immediately below the minimum detectable BER per subcarrier. Note that there are subcarriers with BER larger than the total BER of 7.1×10^{-4} and the BER target of 10^{-3}. This is due to the bit-rounding

in the bit-loading algorithm. However, DMT modulation provides the benefit to achieve a total average BER below the target BER even in presence of some subcarriers above that limit. Fig. 4.11(b) shows the superimposed equalized constellation diagram of all the subcarriers with 16–QAM, corresponding to 4 allocated bits. The clearly distinguishable constellation points indicate that the received signal quality is high enough to guarantee sufficient performance also with a simple one-tap channel equalizer.

The previous bit-rate value of 5 Gbit/s must be intended as gross because it considers as useful information also the Schimdl blocks and the cyclic prefix. Accounting correctly for cyclic prefix and Schimdl blocks, an overhead of 3.6% needs to be removed from the gross bit-rate. This leads to a uncoded net bit-rate of 4.85 Gbit/s, corresponding to a spectral efficiency of 3 bit/s/Hz. Accounting also for a 6.7% EFEC overhead, the net bit-rate for error-free operation becomes 4.55 Gbit/s.

It is possible to compare the obtained bit-rate with the theoretical capacity of the system presented in Fig. 4.9(b).To this purpose, we should compare the uncoded net bit-rate with the theoretical capacity corresponding to the measured SNR reduced by the SNR gap, Γ, of 6 dB. Since the overall measured SNR is 15.5 dB, the capacity corresponding to 9.5 dB should be taken. From Fig. 4.9(b) this capacity is 5.6 Gbit/s. Therefore, the obtained bit-rate is 0.75 Gbit/s far from the theoretical capacity achievable by M–QAM.

4.2.4 50 m PMMA GI–POF transmission with PIN PD

For the system employing PIN–PD the parameters listed in Tab. 4.2 were utilized. The DMT signal used 256 subcarriers spaced by 8.79 MHz within a bandwidth of 2.25 GHz. The sampling rate of the AWG and the DPO were fixed at 4.5 and 50 Gsample/s, respectively. For this system the optimum clipping factor was found to be $\mu = 8$ dB.

Fig. 4.12(a) and 4.12(b) show the estimated SNR before and after bit-loading, respectively. Note that the SNR of the system employing PIN–PD is slightly higher than the corresponding SNR of the system employing APD. This is due to the larger area of the PD and to a lower noise level. Due

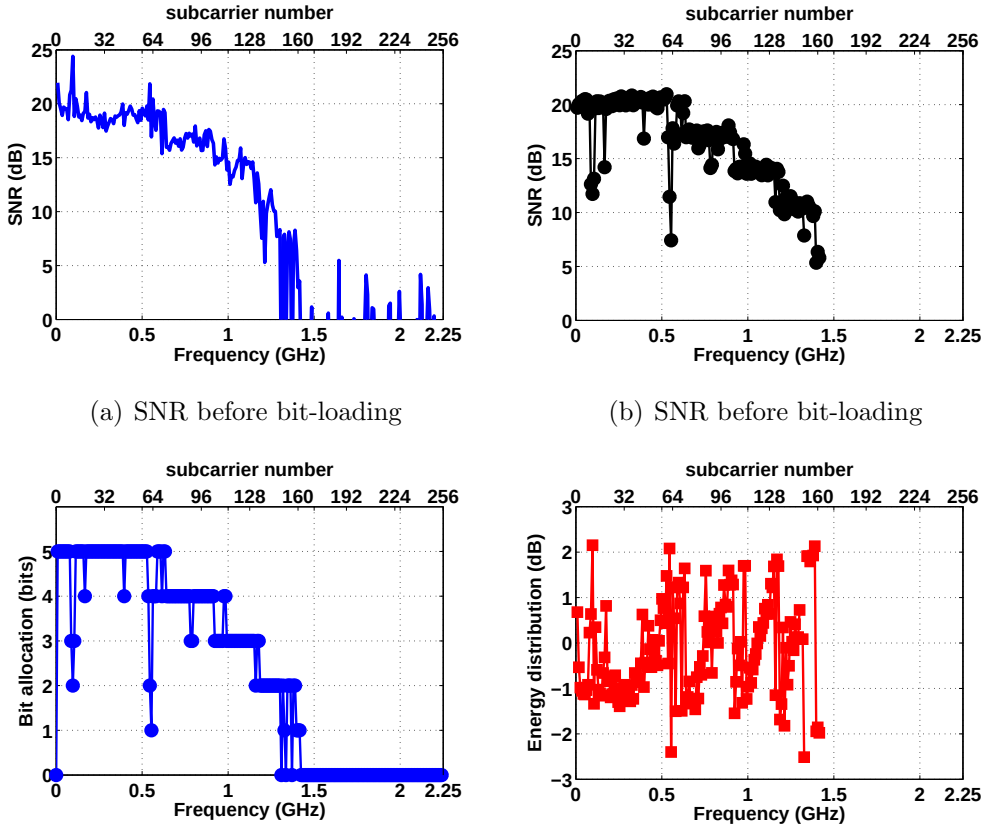

(a) SNR before bit-loading

(b) SNR before bit-loading

(c) Bit allocation

(d) Power allocation

Figure 4.12: Bit loading application on 50 m POF transmission with PIN–PD: estimated SNR before bit-loading (a), estimated SNR after bit-loading (b), bit (c) and power (d) allocation

Number of subcarriers	256
Cyclic prefix length	8
Number of Schimdl blocks	2 every 200 DMT symbols
Digital clipping	Clipping factor $\mu = 8$ dB
Receiver equalizer	one-tap channel equalizer
Transmitter sampling rate	4.5 Gsample/s
Receiver sampling rate	50 Gsample/s

Table 4.2: DMT modulator and demodulator parameter for 50 m transmission with PIN–PD

to the higher SNR, up to 5 bits, corresponding to 32–QAM modulation, are allocated. Note that after 1.42 GHz (subcarrier number 162) no bits are allocated due to low SNR values. For this reason in Fig. 4.12(b) the SNR after bit-loading can only be evaluated up to 1.42 GHz. The energy distribution corresponding to the bit allocation is shown in Fig. 4.12(d).

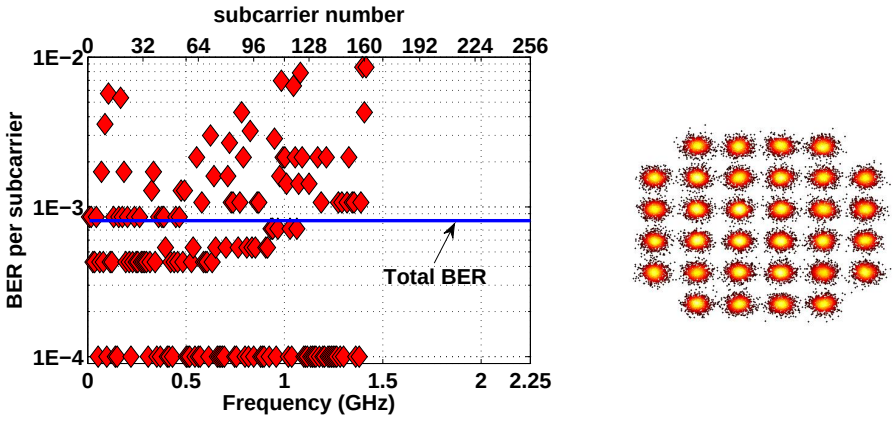

(a) (b)

Figure 4.13: BER performance per subcarrier (a), constellation diagram of the demodulated signal for the subcarriers with 32–QAM (b)

With the optimum bit and power allocation a gross bit-rate of 5.3 Gbit/s was achieved with a BER of 8.5×10^{-4}, which is below the target of 10^{-3}.

Fig. 4.13(a) shows the measured BER per subcarrier. As for the APD system, the BER per subcarrier ranges from 10^{-4} to 10^{-2}, where the value 10^{-4} is associated to the subcarrier where no errors were found. Also in this case, there are subcarriers with BER larger than the target BER of 10^{-3} mitigated by the DMT signal averaging property. Fig. 4.13(b) shows the superimposed equalized constellation diagram of all the subcarriers with 32–QAM, corresponding to 5 allocated bits.

Accounting for cyclic prefix and Schimdl blocks within the gross bit-rate of 5.3 Gbit/s, the uncoded net bit-rate is 5.15 Gbit/s, corresponding to a spectral efficiency of 3.6 bit/s/Hz. Accounting also for a 6.7% EFEC overhead, the net bit-rate for error-free operation becomes 4.85 Gbit/s.

The overall SNR is 17 dB. Hence, to compare the uncoded net bit-rate with the theoretical capacity of the system the capacity corresponding to a SNR of 11 dB should be taken. From Fig. 4.9(b) this capacity is 5.4 Gbit/s, meaning that the obtained net bit-rate is only 0.25 Gbit/s far from the maximum capacity achievable with M–QAM.

Summarizing, even if the the 3 dB bandwidth of the system employing PIN–PD is lower than the 3 dB bandwidth of the system employing APD, the resulting data-rate is higher. This is due to the use of a matched PD–TIA receiver which guarantees a high sensitivity and a receiver bandwidth competitive with the APD solution.

4.2.5 Evaluation of DMT and optical link parameters

The results shown in subsections 4.2.3 and 4.2.4 refer to the transmission over 50 m GI-POF with all parameters optimized. To prove that the chosen parameters are optimum and to determine the impact of a not optimum choice, in this section I will show the effect on the link performance of deviation of these parameters from their optimal values. In particular, I will show the dependencies of the total bit-rate on different values of the number of subcarriers, the clipping level, the laser bias current, fiber length and bending loss. The link performance is expressed by the bit-rate deviation from

the reference bit-rate, indicated as $\Delta Bitrate$, and defined as follows,

$$\Delta Bitrate = \frac{Bitrate - Bitrate_{ref}}{Bitrate_{ref}} \cdot 100 \quad (\%) \tag{4.31}$$

where $Bitrate$ is the achieved bit-rate for the applied parameter values, while $Bitrate_{ref}$ is the reference bit-rate.

The following results are obtained using the system with PIN–PD described in section 4.2.4, but similar behaviors can be observed for the system employing APD. Hence, $Bitrate_{ref} = 5.3$ Gbit/s and $Bitrate$ is the gross maximum bit-rate with BER below 1×10^{-3} obtained applying the bit-loading algorithm with the deviated parameter values.

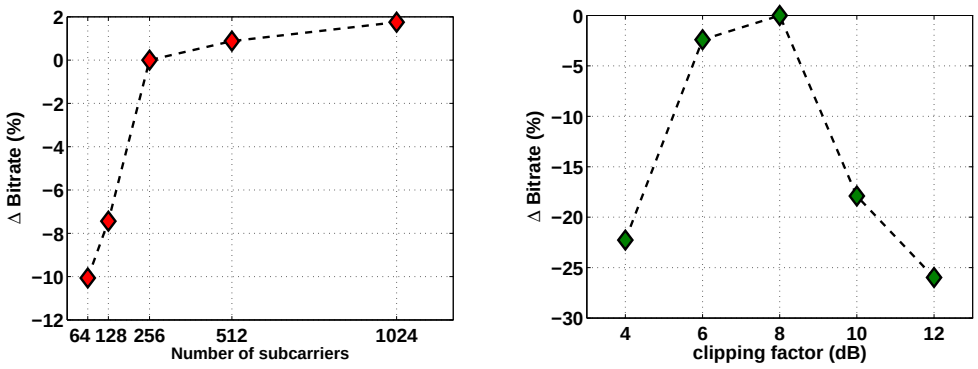

(a) (b)

Figure 4.14: Percentage bit-rate variation versus number of subcarriers (a) and clipping factor (b) of the DMT signal

Fig. 4.14 depicts the impact of the main DMT parameters, namely the number of subcarriers and the digital clipping factor. From Fig. 4.14(a) it can be evinced that increasing the number of subcarriers the total bit-rate tends to increase, since the available bandwidth is better used. However, while up to 256 subcarriers the performance increases considerably, thereafter the performance becomes saturated increasing of less than 2% for 1024 subcarries. Hence, since an increase of the number of subcarriers determines

higher complexity and latency, a compromise is required. For this reason, choosing 256 subcarriers is the optimum compromise for the case considered.

Fig. 4.14(b) shows $\Delta Bitrate$ against the clipping factor. For the 50 m transmission described in subsections 4.2.4 a clipping factor of 8 dB was used, which from Fig. 4.14(b) is demonstrated to be optimum. But, note that a clipping factor between 6 and 8 dB gives close to optimum results. For lower values of clipping factor the clipping noise increases substantially providing a reduction of the bit-rate [101]. For higher values of clipping factor, due to a fixed peak-to-peak amplitude of the modulating current to avoid laser clipping, the average received power decreases resulting in a reduction of the SNR and hence of the bit-rate. I remark that the crest factor of the DMT signal without digital clipping would be around 14–15 dB which results in more than 30% reduction in bit-rate.

Besides number of subcarriers and clipping factor, which are the main parameters of the DMT signal and can be controlled in the DSP, I analyze the impact of some other parameters of the optical link. In particular, the driving bias current of the VCSEL, the POF length and the bending loss of the POF are examined.

I showed in subsection 4.2.2 that the VCSEL bias current was set to 4 mA based on considerations on the transmitted power, the link gain and the non-linearities. For further clarification, Fig. 4.15(a) depicts $\Delta Bitrate$ versus the bias current of the VCSEL. The optimum bias current value of 4 mA is confirmed. For low bias currents, the link performance is dominated by laser clipping leading to asymmetric clipping noise on the received DMT signal which reduces the achievable bit-rate. For high bias currents the SNR reduction due to a lower system gain and optical power reduces as well the achievable bit-rate.

Fig. 4.15(b) presents $\Delta Bitrate$ variation with POF link ranging from 10 to 50 m. Since the reference bit-rate is the one at the longest length of 50 m, $\Delta Bitrate$ is always positive. At 10 m a relative increase around 43% is obtained with respect to the 50 m case. Note that Fig. 4.15(b) shows a linear relationship between $\Delta Bitrate$ and fiber length with a negative slope of -1.1 $\%/m$. This linear relationship is due to the high loss (0.3 dB/m) of

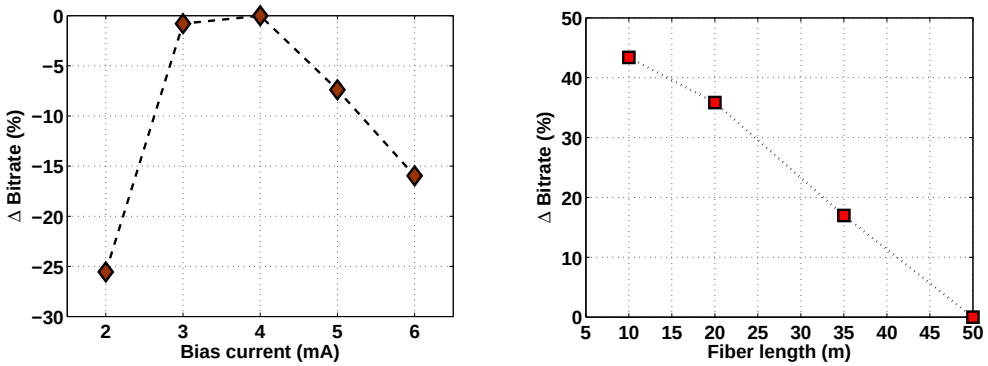

(a) (b)

Figure 4.15: Percentage bit-rate variation versus laser bias current (a) and POF length (b)

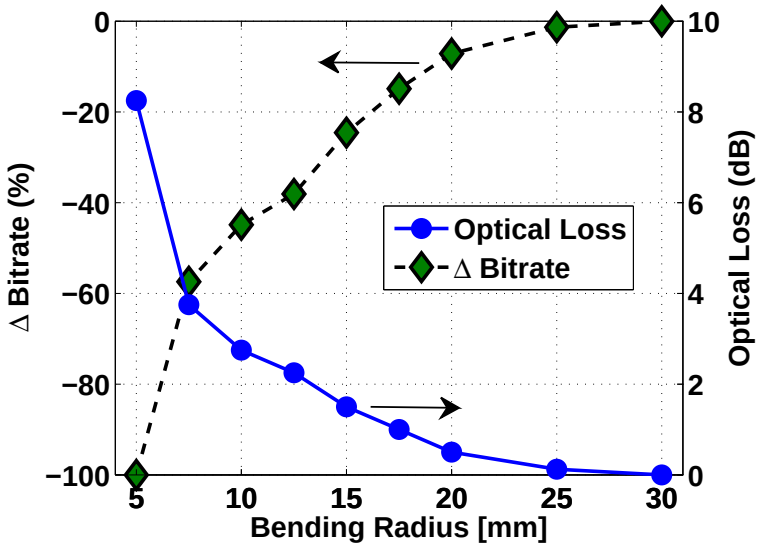

Figure 4.16: Percentage bit-rate varation and optical loss versus the bending radius of a 180° bend

the GI-POF which limits the system by SNR beyond 10 m.

Another important parametric evaluation related to in-field installation is the bending loss sensitivity of the system. Indeed, GI–POF is today the large core plastic optical fiber with the highest available bandwidth, but at the same time it is more sensitive to bending loss with respect to standard SI–POF [11]. For this reason, Fig. 4.16 presents $\Delta Bitrate$ variation due to decreasing bending radius. The experimental values are obtained using a half bend (180° bend). The optical loss associated to each bending radius is also reported in Fig. 4.16. No penalty is observed above a bending radius of 25 mm, which is the nominal allowable bending radius reported for the sample of GI–POF [96]. A penalty of more than 7% can be observed below a bending radius of 20 mm. $\Delta Bitrate$ decreases linearly coming from 20 to 7.5 mm and then asymptotically decreases below 7.5 mm. Note that $\Delta Bitrate$ decrease follows perfectly the increase of the optical bending loss.

4.3 3×2^N–QAM constellations for DMT

The results presented in the previous section where obtained using QAM constellations with a number of points which is a power of 2 (2^N). Using these constellations it is possible to transport an integer number of bits per subcarrier. In particular, on the n^{th} subcarrier it is possible to transport a number of bits b_n which satisfy the relation,

$$b_n = \log_2\left(1 + \frac{E_n g_n}{\Gamma}\right) \tag{4.32}$$

which was implicit in (4.28).

In (4.32), $E_n g_n$ is the SNR produced by the energy E_n, and can be indicated by SNR_n. Hence, from (4.28) it is possible to derive the minimum SNR_n to be able to transport b_n bits on the n^{th} subcarrier,

$$SNR_n \geq \left(2^{b_n} - 1\right) \cdot \Gamma \tag{4.33}$$

For standard M–QAM it is $b = log_2(M)$, and for symbol error fixed to 10^{-3} it is $\Gamma = 6$ dB. From (4.33) the minimum SNR necessary to support a M–QAM modulation is reported in the following table.

Number of bits	Constellation	Minimum SNR (dB)
2	4–QAM	10.8
3	8–QAM	14.5
4	16–QAM	17.8
5	32–QAM	20.9
6	64–QAM	24

From the previous table it can be noticed that in order to increase by 1 bit the number of transported bits it is necessary to increase the SNR by about 3 dB. However, this increase is not always feasible on all the DMT subcarriers due to the constraint on total power.

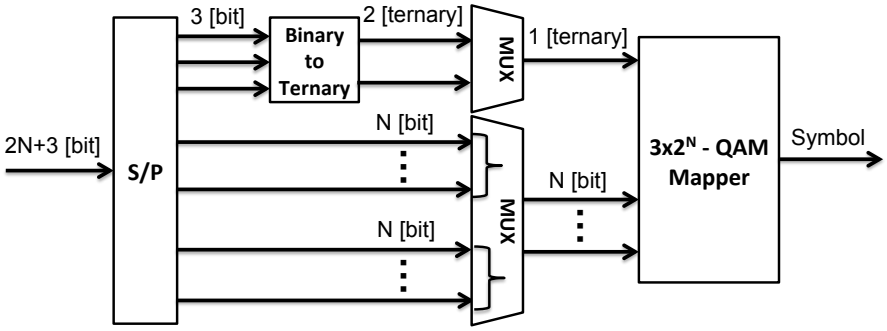

Figure 4.17: 3×2^N–QAM modulator

To allow a higher adaptability of the DMT signal to the channel, a finer granularity in SNR is needed. Referring to (4.33), this can be done by the introduction of constellations transporting a non-integer number of bits. For radio communication systems, novel adaptive constellation formats have been proposed in recent years, transporting a fractional number of bits [102]. In particular, the family of 3×2^N–QAM constellations have been studied [102, 103]. With a 3×2^N–QAM constellation it is possible to transport $N+1.5$ bits per symbol. Fig. 4.17 shows how to obtain this feature. For a 3×2^N–QAM constellation $2N+3$ bits are parallelized and then divided into three groups: one group of 3 bits and two groups of N bits. The 3 bits are converted from binary to ternary format. One of the ternary values and one group of N bits

are selected for each symbol time to be mapped. Therefore, the modulator generates two symbols from $2N + 3$ bits, leading to an average number of $N + 1.5$ bits per symbol.

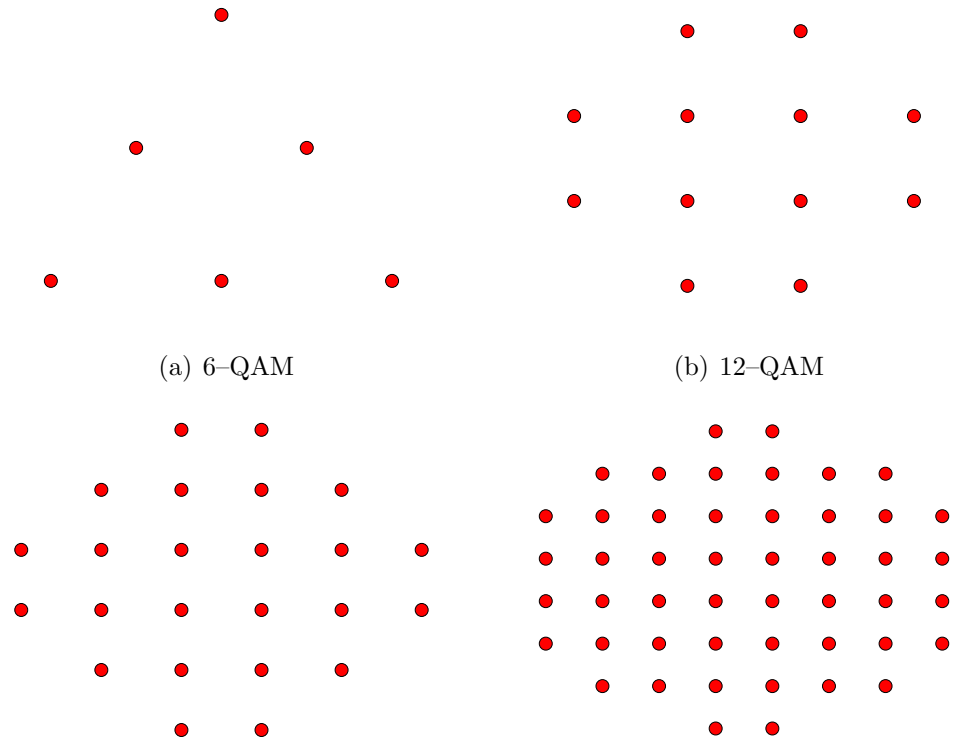

(a) 6–QAM (b) 12–QAM

(c) 24–QAM (d) 48–QAM

Figure 4.18: Example of 3×2^N–QAM constellation diagrams

Since a ternary value can assume the three values 0, 1 and 2, and N bits give rise to 2^N combinations, 3×2^N different symbols are needed. A detailed explanation of optimal constellation construction and mapping is given in [102, 103] and not reported here. As an example, Fig. 4.18 shows the constellation diagram of 3×2^N–QAM constellations with N ranging from 1 to 4, i.e. from 6–QAM to 48–QAM. Apart from the triangle constellation corresponding to 6–QAM, all the other constellations can be obtained from a rectangular 2^{N+2}–QAM in which the points with higher power are removed

to obtain 3×2^N symbols. Since the upper bound of (4.30) can be applied also to these constellations, for a symbol error probability of 10^{-3} the Γ value of 6 dB can be taken. Hence, the minimum SNR to support a M–QAM modulation can be completed according to the following table.

Number of bit	Constellation	Minimum SNR (dB)
2	4–QAM	10.8
2.5	6–QAM	12.7
3	8–QAM	14.5
3.5	12–QAM	16.1
4	16–QAM	17.8
4.5	24–QAM	19.4
5	32–QAM	20.9
5.5	48–QAM	22.5
6	64–QAM	24

From the table it can be evinced that now the SNR granularity has reduced to about 1.5 dB due to the half bit granularity. This allows a solution of the bit-loading algorithm presented in subsection 4.2.1 closer to the water-filling solution. To support both 2^N–QAM and 3×2^N–QAM, steps 7. and 8. of the bit-loading algorithm described in subsection 4.2.1 need to be substituted by the following,

7. Scale E_n by the factor $\left(2^{\text{Round}(2 \cdot b_n)/2} - 1\right) / \left(2^{b_n} - 1\right)$ for $n = 1, ..., i$

8. Compute $b_n = \text{Round}(2 \cdot b_n)/2$ for $n = 1, ..., i$

4.3.1 Application to 50 m PMMA GI–POF link with APD

The application of 3×2^N–QAM constellation formats on DMT was tested on the system employing APD, because, as was stated in the end of section 4.2.3, this system has more margin of improvement with respect to the

system employing PIN–PD. Indeed, the systems employing PIN–PD and APD were close 0.25 Gbit/s and 0.75 Gbit/s, respectively, to the maximum capacity achievable with M–QAM. The DMT parameters for this experimental study were the same reported in Tab. 4.1.

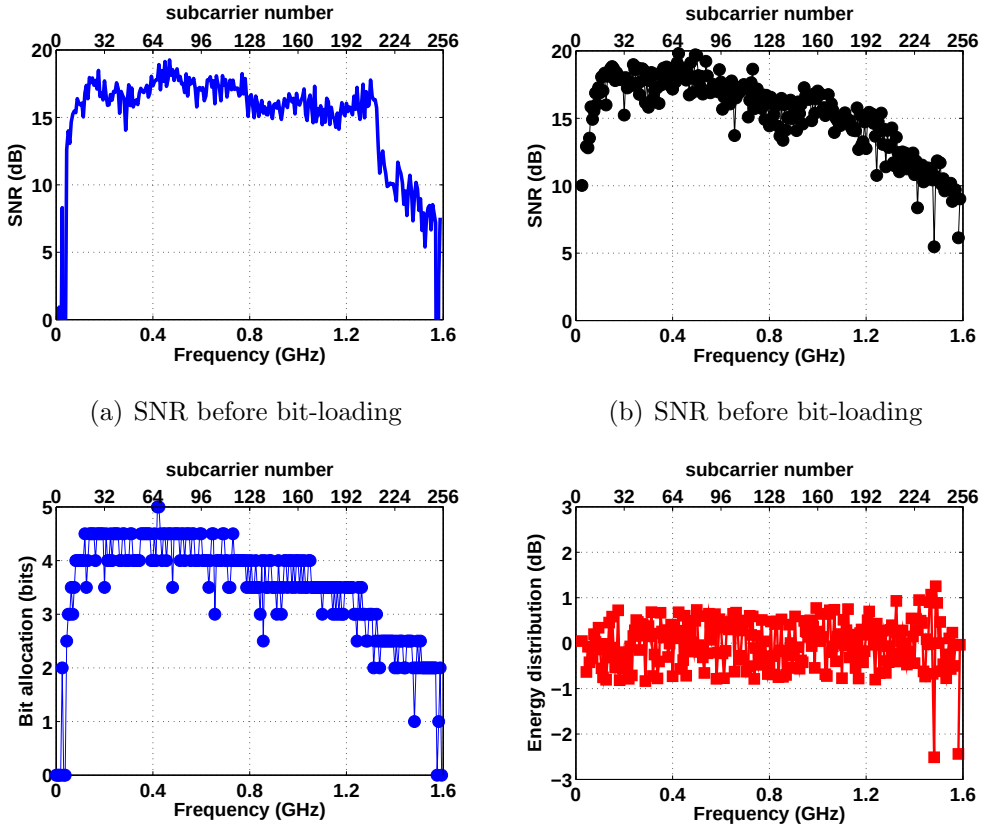

(a) SNR before bit-loading

(b) SNR before bit-loading

(c) Bit allocation

(d) Power allocation

Figure 4.19: Bit loading application over 50 m POF transmission with APD and 3×2^N constellation formats: estimated SNR before bit-loading (a), estimated SNR after bit-loading (b), bit (c) and power (d) allocation

Fig. 4.19(a) shows the estimated SNR, which is in-line with the one reported in Fig. 4.10(a). From this SNR estimation the modified bit-loading

algorithm determined the optimum number of bits and the energy level to be allocated to each subcarrier with half-bit granularity. Fig. 4.19(c) shows the optimum bit allocation for a BER target below 10^{-3} employing 3×2^N constellation formats. Note that there are many subcarriers with 4.5, 3.5 and 2.5 bits allocated, corresponding to 24–QAM, 12–QAM and 6–QAM, respectively. Compared to Fig. 4.10(c), the bit allocation in Fig. 4.19(c) follows better the SNR estimation in Fig. 4.19(a) leading to a more continuous shape. The energy distribution corresponding to this bit allocation is shown in Fig. 4.19(d). Note that in the frequency range where 3×2^N–QAM are employed, the energy is now distributed in a range of no more than 2 dB, which is half of the range of 4 dB in Fig. 4.10(d), where only 2^N–QAM constellation formats were used. Indeed, a finer granularity in the bit allocation leads to a more uniform power distribution among the subcarriers. Fig. 4.19(b) presents the SNR per used subcarrier resulting from the energy distribution of Fig. 4.19(d).

Employing 3×2^N–QAM constellations it was possible to achieve a gross bit-rate of 5.6 Gbit/s with a BER of 9.2×10^{-4}. Fig. 4.20(a) shows the measured BER per subcarrier, which ranges from 10^{-4} to 10^{-2}. As for the previous experimental results, there are many subcarriers with a BER above the total BER, equal to 9.2×10^{-4}, whose detrimental effect is limited by DMT modulation. Fig. 4.20(b) shows the superimposed equalized constellation diagram of all the subcarriers with 24–QAM, corresponding to 4.5 allocated bits. The constellation points are well distinguishable indicating correct operation of the receiver also for 3×2^N–QAM constellation formats.

Accounting for cyclic prefix and Schimdl blocks, an overall overhead of 3.6% needs to be removed from the gross bit-rate. This leads to a uncoded net bit-rate of 5.4 Gbit/s, corresponding to a spectral efficiency of 3.4 bit/s/Hz. Accounting also for a 6.7% EFEC overhead, the net bit-rate for error-free operation becomes 5 Gbit/s. With respect to the result reported in subsection 4.2.3 there is a percentage gain of 12% in the achievable bit-rate.

Fig. 4.21 shows the comparison between the uncoded net bit-rate of DMT with (w/) and without (w/o) 3×2^N constellations with the theoretical channel capacity of Fig. 4.9(b). In particular, the comparison is made at different

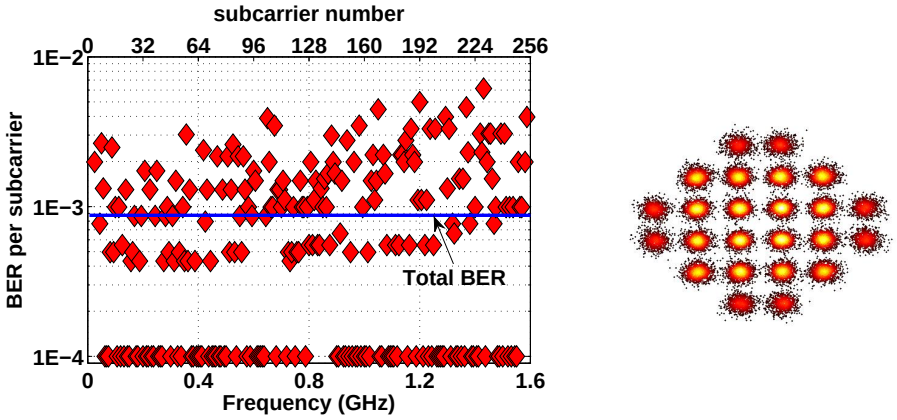

(a) (b)

Figure 4.20: BER performance per subcarrier (a), constellation diagram of the demodulated signal for the subcarriers with 24–QAM (b)

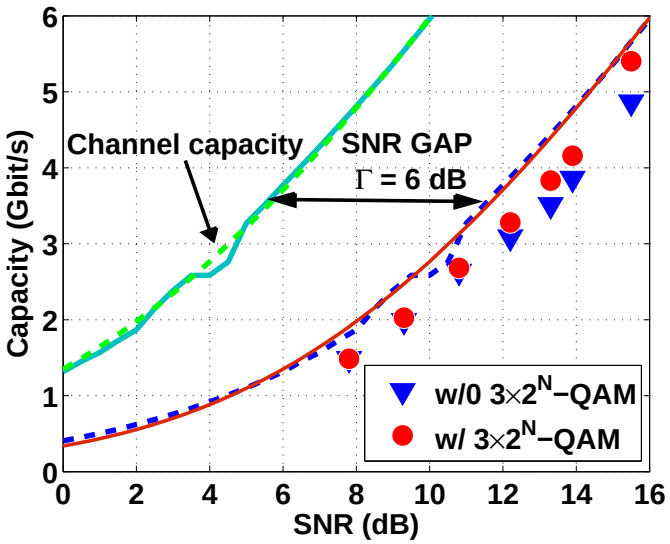

Figure 4.21: Comparison of DMT achieved data rate with (red circle) or without (blue triangle) 3×2^N–QAM with the theoretical channel capacity

received SNR obtained by decreasing the received optical power always after 50 m of POF transmission. From the figure it can be evinced that for SNR below 10 dB the two types of DMT signal give similar values since none or few subcarriers are allocated with 3×2^N–QAM constellations. Then, for increasing values of SNR 3×2^N–QAM constellation formats begin to be allocated to a larger number of subcarriers, leading to an over-performance of the DMT signal employing 3×2^N–QAM constellations with respect to the DMT signal employing only 2^N–QAM constellations.

The obtained results are also compared with the theoretical capacity shifted by the SNR gap $\Gamma = 6$ dB. For the SNR of 15.5 dB, corresponding to the results presented in this section, a difference of only 0.2 Gbit/s from the theoretical capacity shifted by the SNR gap is observed in Fig. 4.21 for the DMT with 3×2^N–QAM constellations. This means that with DMT modulation employing 3×2^N–QAM constellations, in addition to 2^N–QAM, it is possible to be practically at a distance equal to the SNR gap from the theoretical channel capacity, which is the minimum distance achievable with M–QAM.

4.4 Summary

A solution based on plastic optical fiber for the realization of home area networks has been studied in detail. In this framework, a theoretical and experimental analysis on the application of DMT to IM–DD GI–POF links has been presented. Closed-form equations for the capacity of POF links simplified as super-gaussian AWGN channels were reported in section 4.1 and applied for the description of POF links employing APD and PIN–PD in subsection 4.2.2.

To use efficiently the non-flat channel response of the POF link, DMT modulation was employed together with a bit and power loading algorithm which was described in subsection 4.2.1. The achieved uncoded net bit-rates were 4.85 and 5.15 Gbit/s for the system employing APD and PIN–PD, respectively, with optimum parameters. The achieved data-rate are distant

0.75 and 0.25 Gbit/s, respectively, from the maximum achievable capacity with M–QAM. To define the effect of non-optimum parameters choice or real installation conditions, a detailed parametric evaluation was performed determining also the impact of small bending radii on the POF link.

Finally, 3×2^N constellation formats were studied to approach even closer the maximum achievable capacity with the only limitation of the SNR gap. Indeed, the half-bit granularity of the bit-loading algorithm exploits at the best the non-flat channel response. With this scheme the uncoded net bit-rate of the system employing APD becomes 5.4 Gbit/s which is only 0.2 Gbit/s from the maximum achievable capacity with M–QAM.

These results demonstrate that DMT can provide close to optimum performance in POF links even with a simple one-tap equalizer and a humble number of subcarriers such as the 256 employed in this work. Scalability of these results towards 10 Gbit/s after 50 m POF transmission is feasible provided that an increase of SNR of at least 6 dB or a receiver based on APD or PIN–PD with at least double 3 dB bandwidth is realized.

Chapter 5

POF systems for converged home networks

As an example of the possibility to use plastic optical fibers for a converged home area network, in this chapter a combined transmission of a multi-gigabit baseband data stream, based on DMT, and a radio frequency signal, based on UWB technology, over 1 mm core diameter POF is shown. After a short introduction on the employed UWB technology in section 5.1, a detailed experimental study on the performance of the two types of signals in the combined transmission is carried out in section 5.2.

5.1 Ultra wideband technologies

As already described in section 1.3.2, the near-future indoor scenario is expected to be full of devices able to transmit with each other. These devices can use different wireless technologies and some UWB technologies are expected to be employed especially where reduced energy consumption, device co-existence and positioning are requested. While narrowband radio technologies in the ISM band of 2.4 GHz are typically able to transmit up to tens of meter, UWB technologies are intended to be used below ten meter.

This chapter is based on the results published in P5. and P22.

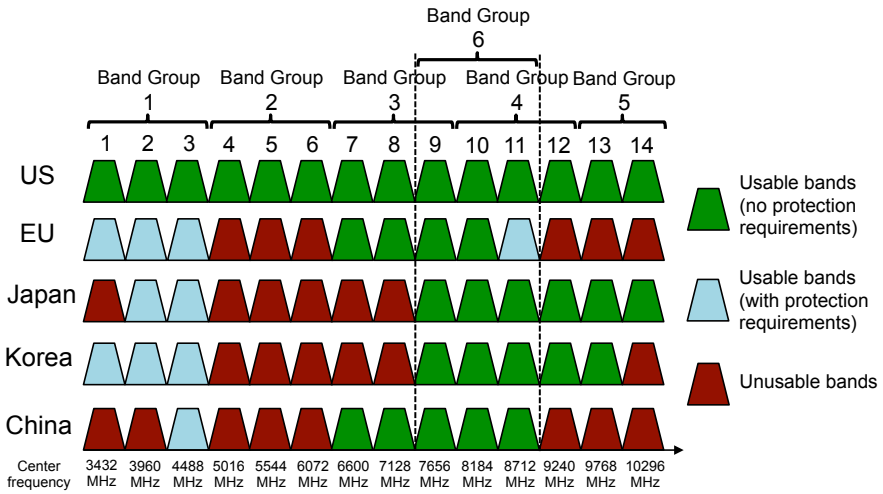

Figure 5.1: WiMedia Alliance regulatory frequency bands chart

Hence, full speed UWB transmission could be not completely feasible inside a house. For this reason, the possibility to use also the wired infrastructure to extend the maximum reachable distance can be of interest. Nevertheless, the impact of the introduction of the wireless service in the broadband wireline infrastructure should be minimized.

The challenge related to the pursuit of this scope for UWB signals is the wideband feature of UWB technologies. The Federal Communications Commission (FCC) stated that UWB technology should use a minimum bandwidth of 500 MHz and operate in the frequency range between 3.1 and 10.6 GHz, where other services are licensed. For this reason, the power spectral density measured in 1 MHz bandwidth must not exceed -41.3 dBm [104].

UWB systems support two kinds of modulation techniques: the direct sequence technique and the multi-band OFDM (MB–OFDM) UWB technology [105]. MB–OFDM is preferred for indoor data communication over other UWB implementations, like impulse-radio UWB, or proprietary UWB solution, due to the widely commercial availability of low-cost OFDM-based solutions. According to the WiMedia Alliance [106], the available spectrum for MB–OFDM UWB technology is divided in 14 bands, each with a band-

width of 528 MHz as summarized in Fig 5.1. The first 12 bands are grouped into 4 band groups counting 3 frequency bands each. The last two bands are grouped in a fifth group. A sixth band group intended for worldwide usage is also defined within the spectrum of the first four group bands.

The radio signal is based on an OFDM modulation format with 128 subcarriers, spaced by 4.125 MHz. A total of 110 subcarriers (100 data carriers and 10 guard carriers) are used per band to transmit the information. Other 12 pilot subcarriers allow for coherent detection, while other 6 subcarriers, including the one corresponding to the central frequency, are null. Hence, 122 subcarriers are used in total for each band. Frequency-domain spreading, time-domain spreading, and FEC coding are provided for optimum performance under a variety of channel conditions. The supported data rate ranges from 53.3 to 480 Mbit/s [107]. For use within wireless USB technology the support of transmitting and receiving data rate of 53.3, 106.7 and 200 Mbit/s are mandatory within a maximum distance of 10 m, while the remaining data rates up to 480 Mbit/s are optional [108].

5.2 Converged transmission of baseband DMT and UWB signals

5.2.1 Experimental setup

The experimental setup used in our study is depicted in Fig. 5.2. A Tektronix AWG7122 was used to generate the DMT signal in the same way described in section 4.2.2. The real-time MB–OFDM UWB signal was generated by a Wisair development kit DV9110M. The UWB signal was centered at 3.96 MHz and had a bandwidth of 528 MHz transporting 200 Mbit/s. This bit-rate was imposed by the limitation of the particular UWB device, but the concept is scalable to the full UWB data rate of 480 Mbit/s.

The POF link was the same described in section 4.2.2. The transmitter was a red VCSEL with a peak optical power of 1 mW. The fiber was a 50 m GI–POF with a core diameter of 1 mm. The receiver based on APD was

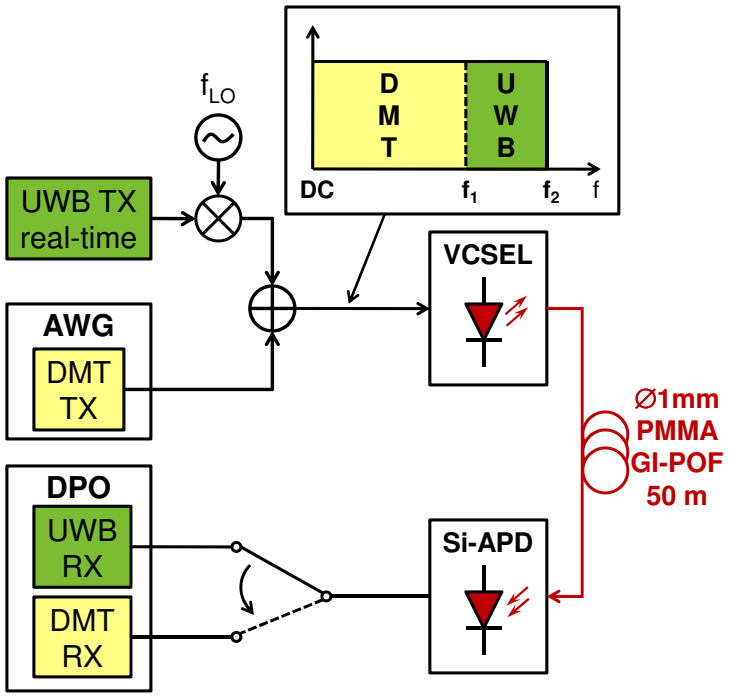

Figure 5.2: Experimental setup

Number of subcarriers	128
Cyclic prefix length	8
Number of Schimdl blocks	10 every 200 DMT symbols
Digital clipping	Clipping factor $\mu = 10$ dB
Receiver equalizer	one-tap channel equalizer
Transmitter sampling rate	1.6 Gsample/s
Receiver sampling rate	50 Gsample/s

Table 5.1: DMT signal parameters for the combined transmission with a MB–OFDM UWB signal over a 50 m POF link

employed. The choice of the APD receiver is based on two considerations. First, the 3 dB bandwidth of the link employing APD is higher than the 3 dB bandwidth of the link employing PIN–PD. In second place, the frequency response of the link employing APD is very flat within the 3 dB bandwidth. Both features can be verified from Fig. 4.8 of chapter 4.

Due to the high center frequency of the UWB signal compared to the 3 dB bandwidth of the POF link, i.e. 1.31 GHz, the UWB signal was down-converted to an intermediate frequency (IF). The DMT and UWB signals were transported over the POF link splitting the available bandwidth into two parts, DC to f_1 for DMT and f_1 to f_2 for UWB, as summarized in the inset in Fig. 5.2. In particular, the UWB signal was down-converted to a center frequency of 1.1 GHz using an electrical mixer. Then, it was combined with a low-pass DMT signal occupying the bandwidth below 0.8 GHz.

The DMT signal parameters are listed in Tab. 5.1. In particular, 128 subcarriers spaced by 6.25 MHz within the fixed bandwidth of 0.8 GHz were used. To this purpose, the sampling rate of the AWG was fixed at 1.6 Gsample/s.

The electrical combination of DMT and down-converted UWB signals were transmitted on the POF link. At the receiver side a real-time Tektronix DPO72004 DPO was used to separately analyze the DMT and the UWB performance. The quality of the UWB signal will be presented in terms of EVM of the received quadrature phase shift keying (QPSK) constellation, while for the DMT signal the maximum bit-rate achievable with a bit-error rate below 10^{-3} will be considered, as done also for the experimental results of chapter 4.

5.2.2 Experimental results and discussion

In Fig. 5.3 the power spectral density (PSD) of the transmitted (a) and received (b) electrical combination of DMT and UWB signals is depicted. As can be evinced from the figure, the DMT signal occupies the bandwidth below 0.8 GHz, while the UWB signal is allocated between 0.8 GHz and 1.4 GHz. Note that both signals are not particularly distorted by the POF link, but

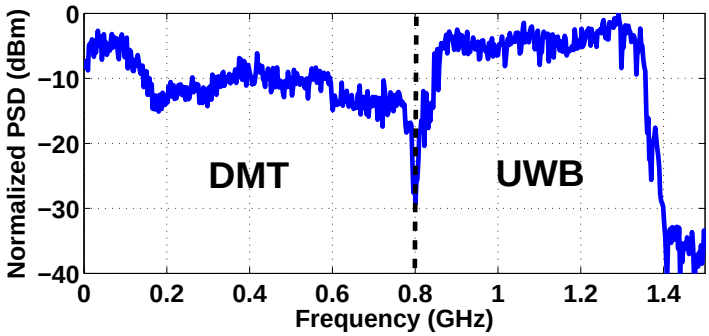

(a) Transmitted PSD

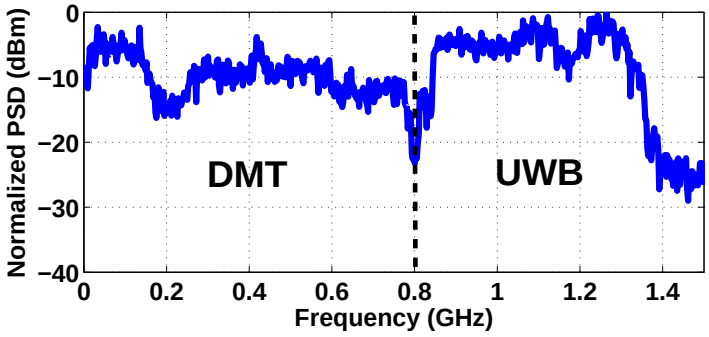

(b) Received PSD

Figure 5.3: Transmitted (a) and received (b) PSD for the combined transmission of DMT and UWB signals

only a relative increase of the noise level of about 10 dB can be evinced. Therefore, apart from noise, the main limiting factor of our system is not the frequency selectiveness of the channel, but the non linear distortion and the consequent cross-talk between the two signals induced by the VCSEL, which is directly modulated by the combination of the two signals.

To study this non-linear effect, I show the impact of different transmitted power levels of the two signals on EVM and maximum data rate for UWB and DMT signals, respectively. Fig. 5.4 shows the variation of the UWB EVM and the DMT bit-rate with respect to the transmitted power of the DMT signal (a) and the UWB signal (b). In Fig. 5.4(a), the UWB power is fixed to -1 dBm, and the DMT power varies from -7.2 to $+2.8$ dBm. For values of the DMT power below 0.8 dBm, the UWB EVM performance is compliant with the EVM limit of 15.5% defined for transmission in the standard [107]. Note that at 0.8 dBm the maximum data rate of DMT starts to decrease. The recommended operating region is where the difference between the two curves is the largest, i.e. between -4 and 0 dBm. In this study, the value of -3.2 dBm was selected as the optimum DMT input power in order to achieve more than 2 Gbit/s of DMT transmission while maintaining an UWB EVM below 13%.

In Fig. 5.4(b) the opposite case is presented. DMT power is set at the constant level of -3.2 dBm, while UWB power varies between -7.4 and $+2.6$ dBm. Note that the minimum UWB EVM value can be achieved with a UWB power of -1dBm. The recommended region of operation is between the UWB input power of -5 and 0 dBm. In the following figures more details about the performance of two signals are shown for the DMT input power of -3.2 dBm and the UWB input power of 1 dBm, meaning that the VCSEL is modulated with an overall power of 2.4 dBm.

First of all, the results for the DMT transmission are presented in Fig. 5.5. Fig. 5.5(a) and 5.5(b) show the estimated SNR before and after bit-loading, respectively. Note that the SNR is quite constant below 0.55 GHz while it decreases approaching 0.8 GHz. This effect is due to the presence of a filter used at the transmitter to isolate the two signals. As shown in Fig. 5.5(c), three bits, corresponding to 8–QAM, are mainly allocated below 0.55 GHz,

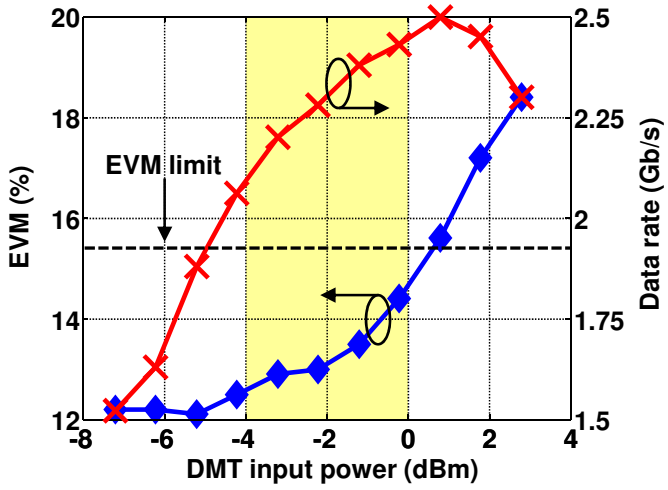

(a) Link performance (DMT and UWB) versus DMT input power

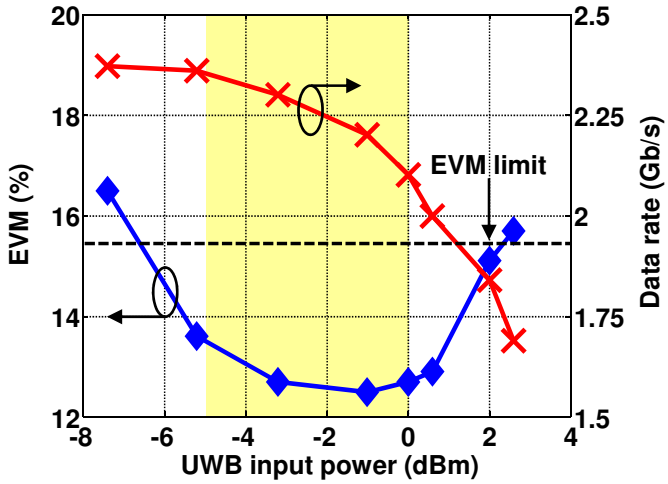

(b) Link performance (DMT and UWB) versus UWB input power

Figure 5.4: DMT maximum bit-rate (red line and cross) and UWB EVM (blue line and diamond) versus input power of the DMT signal (a) or of the UWB signal (b)

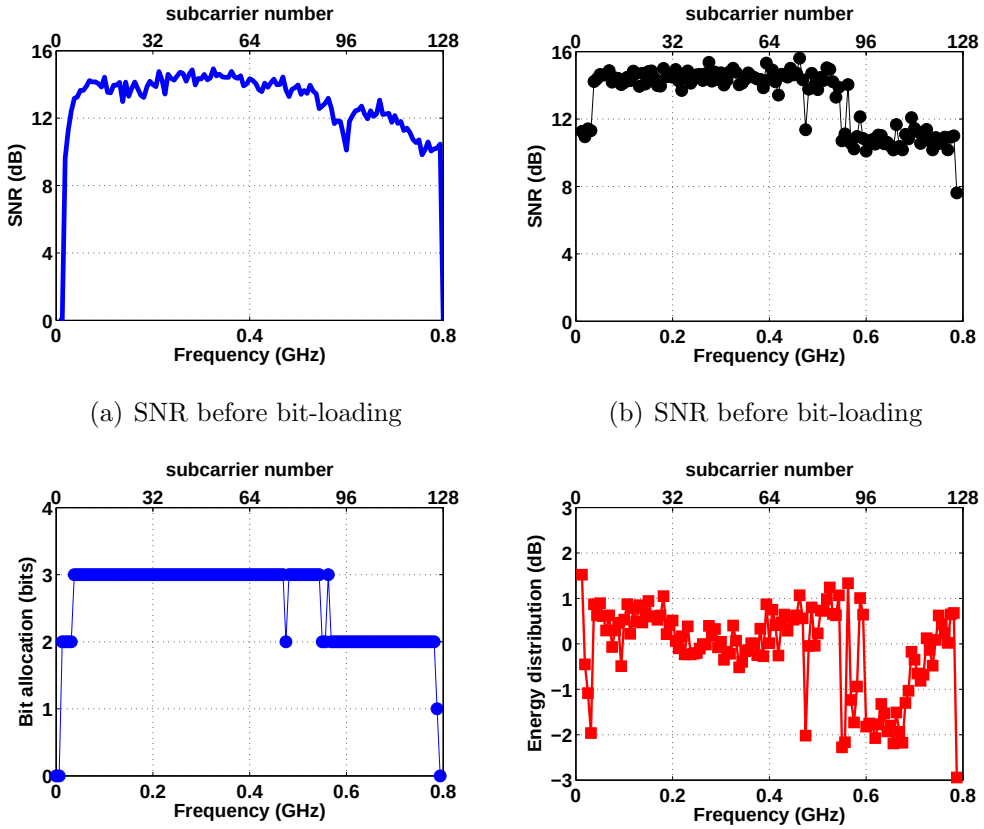

(a) SNR before bit-loading

(b) SNR before bit-loading

(c) Bit allocation

(d) Power allocation

Figure 5.5: DMT bit loading application on the simultaneous transmission of DMT and UWB signals over 50 m GI–POF : estimated SNR before bit-loading (a), estimated SNR after bit-loading (b), bit (c) and power (d) allocation

while two bits, corresponding to 4–QAM, are allocated above. The related energy distribution is shown in Fig. 5.5(d). An almost constant value of energy per subcarrier is allocated below 0.55 GHz, while increasing amounts of energy per subcarrier are allocated between 0.55 and 0.8 GHz. In this way the SNR after bit-loading assumes mainly two values corresponding to the allocated bits as depicted in Fig. 5.5(b).

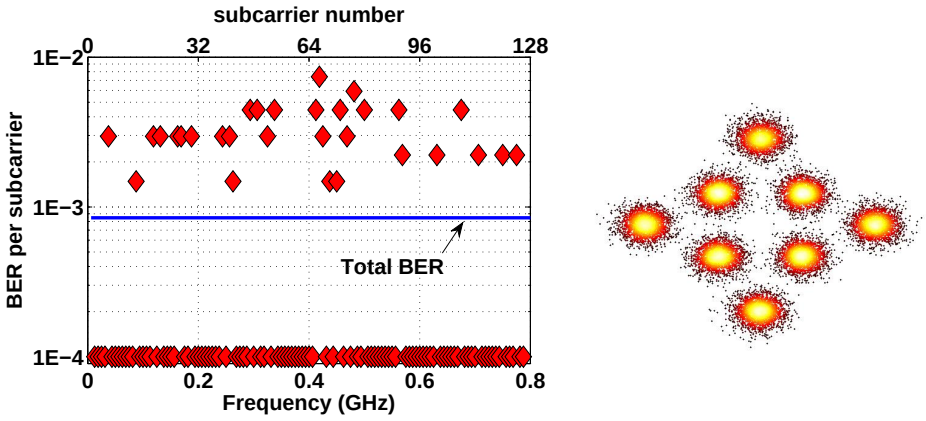

(a) (b)

Figure 5.6: DMT BER performance per subcarrier (a) and constellation diagram of the demodulated signal for the subcarriers with 8–QAM (b)

With the optimum bit and power allocation a gross bit-rate of 2.2 Gbit/s was achieved with a BER of 8.5×10^{-4}, which is below the target of 10^{-3}. Fig. 5.6(a) shows the measured BER per subcarrier. The BER of the subcarriers is mainly below the overall BER, and just few subcarriers are above the target BER of 10^{-3}. Fig. 5.6(b) shows the superimposed equalized constellation diagram of all the subcarriers with 8–QAM, corresponding to three allocated bits.

Accounting for cyclic prefix and Schimdl blocks within the gross bit-rate of 2.2 Gbit/s, the uncoded net bit-rate is 2 Gbit/s, corresponding to a spectral efficiency of 2.5 bit/s/Hz. Accounting also for a 6.7% EFEC overhead, the net bit-rate for error-free operation becomes 1.9 Gbit/s. Hence, gigabit

transmission is well supported with this scheme.

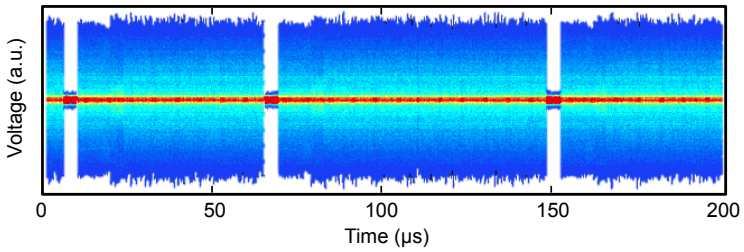

(a)

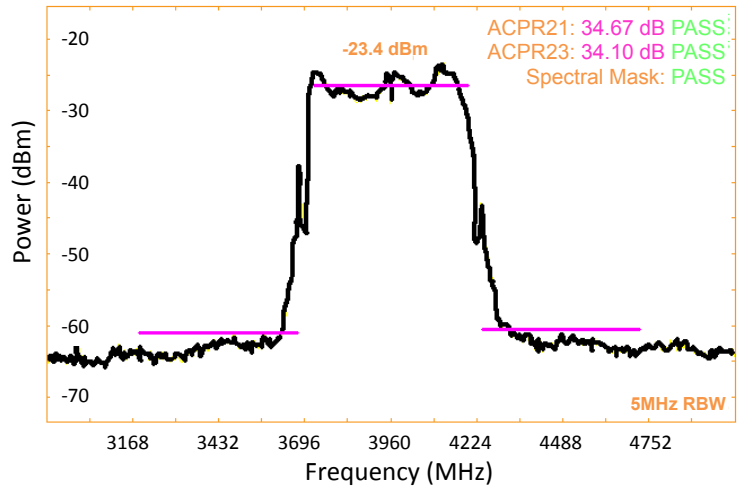

(b)

Figure 5.7: Time (a) and spectrum (b) behaviors of the received up-converted UWB signal

I show now the results related to UWB transmission. These results are determined on the off-line up-converted UWB signal. Indeed, the received UWB signal at the IF of 1.1 GHz was at first digitally converted by the DPO. Then, to analyze this signal with a Tektronix proprietary MB–OFDM analysis software, an off-line filtering and up-conversion was performed. Fig. 5.7(a) shows the time behavior of the received MB–OFDM signal, where the frame structure can be observed. Fig. 5.7(b) shows instead the spectral mask anal-

ysis of the same signal from which the original center frequency of 3.96 GHz can be evinced. The spectrum emission complies with the requirements of the standard [107], and consequently the received signal can be radiated into air. Note also that the spectrum is not distorted meaning that the signal quality has been preserved.

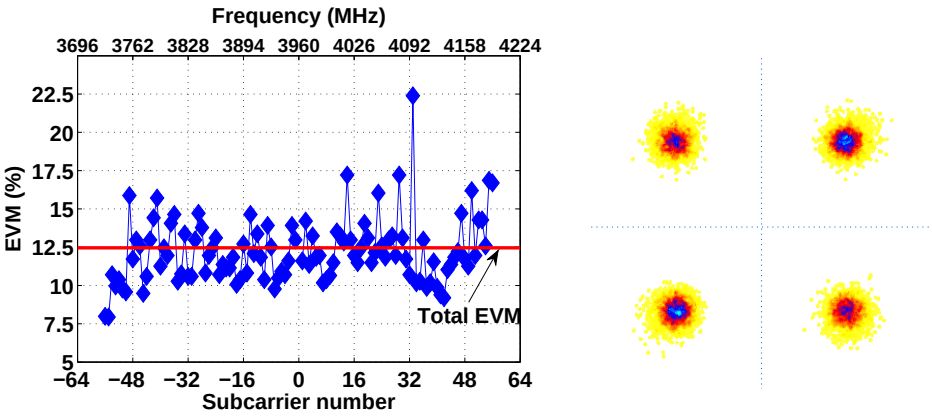

(a) (b)

Figure 5.8: EVM performance per subcarrier (a) and constellation diagram (b) of the demodulated UWB signal

Fig. 5.8(a) shows the EVM value for each one of the used subcarriers of the MB–OFDM signal. There are some subcarriers that are above the overall EVM value of 12.5% whose impact is reduced by the averaging property of the OFDM format. No region of the spectrum with particularly high EVM values compared to the average are observed in Fig. 5.8(a), meaning that the transmission over the POF link is not frequency dependent. Finally, Fig. 5.8(b) shows the received QPSK constellation diagrams of the MB–OFDM UWB signal. Note that the EVM of 12.5% corresponds to clear constellation points.

5.3 Summary

The experimental verification of a converged infrastructure based on large core PMMA POF for the transmission of broadband wired and wireless services has been presented in this chapter. After a short introduction on the MB–OFDM UWB wireless technology used in this activity in section 5.1, the simultaneous transmission over 50 m GI-POF of DMT and UWB signals has been investigated in section 5.2.

An experimental study on the impact of the non-linearity of the laser source was performed to determine the optimum signal power values for transmission. An uncoded net bit-rate of 2 Gbit/s with BER$< 10^{-3}$ was obtained with DMT transmission and bit-loading. A 528 MHz WiMedia-compliant UWB signal transporting 200 Mbit/s was successfully demonstrated on the link guaranteing an EVM of 12.5% on the received QPSK constellation.

Conclusions

This thesis dealt with fiber-optic technologies enabling an efficient distribution of broadband wireline and wireless communication services for in-building networks. An overview of silica fibers and 1 mm core diameter PMMA plastic optical fibers has been addressed in chapter 1. Silica fiber is recognized as the more appropriate fiber medium for large and medium in-building networks. At present, OM laser-optimized multimode fibers can guarantee 10 Gbit/s transmission up to 550 m, and 40 or 100 Gbit/s up to 150 m. If distance or data rate increases, singlemode fiber becomes the most appropriate medium. In accordance with these considerations, fiber distributed antenna systems based on single and multimode fibers were introduced as an enabling technology to provide wireless coverage and high data rate with current and emerging wireless technologies in large and medium buildings. Radio over fiber systems employing intensity modulated - direct detection were considered as cost-effective solutions to realize F–DASs in an in-building scenario.

The major cost-sensitivity of small building networks with respect to large and medium building networks was pointed out. For this scenario, PMMA plastic optical fibers with a core diameter of approximately 1 mm were discussed as an alternative to copper solutions, such as Cat-5. The feasibility of an in-building optical backbone employing plastic optical fibers has been related to the possibility of multi-gigabit transmission and the capability to transport wireless services.

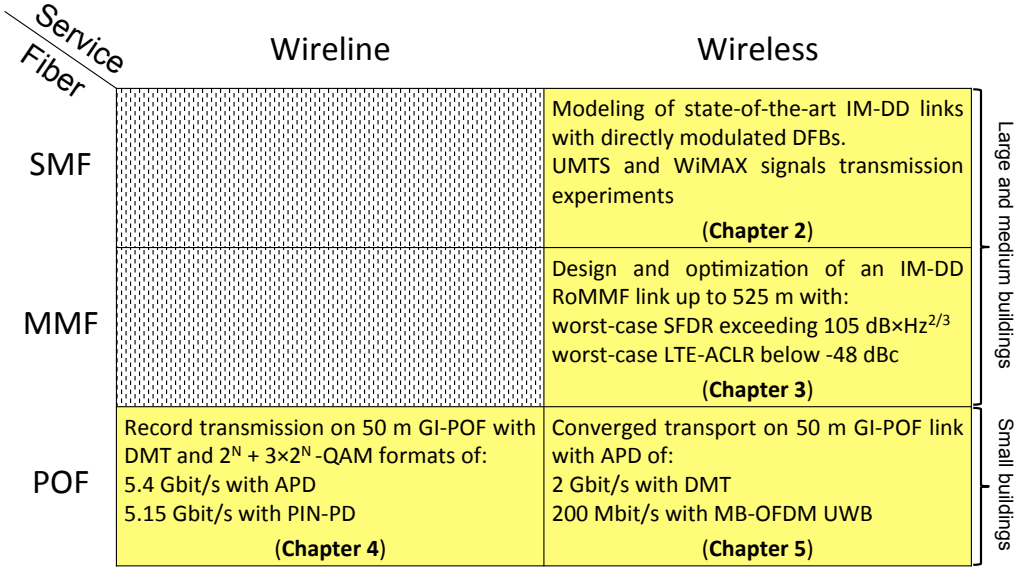

Figure 1: Summary of the main technical achievements of this thesis

Fig. 1 summarizes the main technical achievements of this work.

Chapter 2 dealt with IM–DD RoF links with directly modulated DFBs for wireless signal distribution on singlemode fiber. A modeling tool was developed to describe in an accurate and efficient way the simultaneous transmission of radio signals. The experimental activity pointed out the interactions between two modulating RF signals compliant with UMTS and WiMAX standards. A good agreement between experimental and simulation results has been reported. The wide feasibility of IM–DD RoF links over few kilometers of single mode fibers has been verified, while some criticalities have been underlined for longer links due to identified linear and non-linear characteristics of the laser.

Chapter 3 reported my research activity on IM–DD RoF links with directly modulated lasers for wireless signal distribution on multimode fiber. The comprehensive theoretical and experimental research has clarified the physical mechanisms of the main transmission impairments of IM–DD RoMMF systems, and allowed to develop design guidelines for enhancing the performance. The main detrimental effect in short-range RoMMF links

is modal noise which leads to a time fluctuation of the link gain and to an increment of distortion effects. These undesired effects have been proved to be strictly related to the launching condition, the photodiode structure and the source characteristics, such as frequency chirping and non-linearity. The impact of modal noise can be adequately controlled when a central launch, as opposed to offset and overfilled launches, is applied, a photodiode with a built-in ball lens is used, and a Fabry-Perot laser with low frequency chirping, high modulation efficiency, and non-linearity properties comparable with DFBs is employed. With the designed link a worst-case SFDR exceeding 105 dB $\times$ Hz$^{2/3}$ up to 525 m was obtained. Hence, a successful transmission of LTE signals in a dual-band configuration was verified giving worst-case ACLR performance below -48 dBc at 525 m.

Chapter 4 showed my activity on 1 mm core diameter POF systems for high-speed wireline transmission in small buildings and home networks. Closed-form equations for the modeling of the channel capacity of POF links has been derived describing the complete transmission chain with super-gaussian functions. Multi-gigabit transmission experiments over 1 mm core diameter PMMA GI–POF were performed employing simple and eye–safety compliant VCSEL transmitter and two photoreceivers, one based on a 230 μm active-area diameter Si–APD and another based on a 400 μm active-area diameter Si–PIN PD. It has been shown that by using these simple components in combination with DMT modulation and bit-loading, uncoded net bit-rates of 4.85 and 5.15 Gbit/s with BER$< 10^{-3}$ over 50 m POF are achievable with APD and PIN–PD, respectively. These bit-rates are distant 0.75 and 0.25 Gbit/s, respectively, from the maximum achievable channel capacity employing M–QAM. To approach even closely the channel capacity, 3×2^N–QAM constellations, corresponding to a fractional number of bits per symbol, were added to the constellation set used for the data rate optimization within the DMT bit-loading algorithm. This led to an half-bit granularity in the bit-loading algorithm, enabling a potential higher spectral efficiency in the use of the channel. With this new scheme the uncoded net bit-rate of the system employing APD becomes 5.4 Gbit/s keeping a distance of only 0.2 Gbit/s from the maximum achievable capacity with M–QAM.

Chapter 5 depicted my work on wireless and wireline signal distribution on 1 mm core diameter POF systems intended for short-range communications inside a small building and a home network. An experimental feasibility study of a simultaneous transmission on a single 1 mm core diameter POF of a UWB radio signal and a baseband data stream was performed. An uncoded net bit-rate of 2 Gbit/s with BER$< 10^{-3}$ was achieved after 50 m transmission employing DMT modulation with bit-loading. A 528 MHz WiMedia-compliant UWB signal transporting 200 Mbit/s was successfully transported on the link leading to an EVM of 12.5% on the received QPSK constellation, which is better than the maximum required EVM.

As mentioned in the Introduction, the aim of this thesis was to investigate the convenience and necessity of fiber-optic technologies for in-building networks now that wireless technologies are driving the market. Some answers can be found in the work presented in this thesis:

- Different fiber-optic technologies (SMF, MMF and POF) are convenient for different in-building scenarios (large, medium and small buildings)
- Intensity modulation and direct detection systems are the most attractive solutions for present and near-future short-range fiber-optic systems
- Advanced digital modulation formats can counterpoise the intrinsic limitations of fiber-optic technologies different from SMF (in this thesis it was shown for POF systems)
- A positive mutual cooperation is possible between fiber-optic and wireless technologies. For large and medium buildings a dedicated fiber distributed antenna system on SMF and/or MMF can answer for the multi-operator, multi-service needs. For small buildings, including home scenarios, a converged wireline and wireless optical backbone has to be considered (in this thesis it was shown with a POF system)

Further research activities are needed to study the ultimate capacity limits of fiber-optic solutions different from SMF. Moreover, this thesis dealt

with point-to-point links, while also the impact of a complete network architecture needs to be considered. More generally, in a strategic future perspective, an appropriate converged wireline and wireless optical infrastructure appears to be the solution to transport and manage all the potential in-building services also in large and medium buildings. This will be a direction to which research bodies and private industries will have to direct their investigation activities.

Bibliography

[1] B. Skutnik and C. Smith, "Multimode, Large-Core and Plastic Clad (PCS) Fibers," in *Specialty Optical Fibers Handbook*, A. Mendez and T. Morse, Eds. Oxford: Academic Press, 2007.

[2] A. Bjarklev, A. Bjarklev, and J. Broeng, *Photonic crystal fibers.* New York: Springer, 2003.

[3] G. Agrawal, *Fiber-Optic Communication Systems*, 3rd ed. New York: Wiley, 2002.

[4] *Characteristics of a single-mode optical fiber cable*, ITU-T Recommendation G.652, 2009.

[5] "Corning SMF-28e+ optical fiber with nexcor technology product information," Corning Incorporated, Corning, NY.

[6] B. Saleh and M. Teich, *Fundamentals of Photonics,.* New York: Wiley, 1991,.

[7] *Characteristics of a 50/125 μm multimode graded index optical fibre cable for the optical access network*, ITU-T Recommendation G.651.1, 2007.

[8] *Information technology - Generic cabling for customer premises*, ISO/IEC Std. 11 801, 2009.

[9] P. Kish. (2010, Jan.) Next generation fibers arrive. [Online]. Available: http://www.cnsmagazine.com/news/next-generation-fiber-arrives/1000355010/

[10] J. Zubia and J. Arrue, "Plastic optical fibers: An introduction to their technological processes and applications," *Optical Fiber Technology*, vol. 7, no. 2, pp. 101–140, Apr. 2001.

[11] O. Ziemann, J. Krauser, P. E. Zamzow, and W. Daum, *POF Handbook: Optical Short Range Transmission Systems*, 2nd ed. Berlin: Springer-Verlag, 2008.

[12] *Optical fibre cables - Part 2-40: Indoor optical fibre cables - Family specification for A4 fibre cables*, IEC Std. 60 794-2-40, 2008.

[13] *IEEE Standard for Information Technology - Telecommunications and Information Exchange Between Systems - Local and Metropolitan Area Networks - Specific Requirements. Part 3: Carrier Sense Multiple Access With Collision Detection (CSMA/CD) Access Method and Physical Layer Specifications*, IEEE Std. 802.3, 1998.

[14] *IEEE Standard for Information Technology - Telecommunications and Information Exchange Between Systems - Local and Metropolitan Area Networks - Specific Requirements. Supplement to Carrier Sense Multiple Access With Collision Detection (CSMA/CD) Access Method and Physical Layer Specifications - Physical Layer Parameters and Specifications for 1000 Mb/s Operation Over 4-Pair of Category 5 Balanced Copper Cabling, Type 1000BASE-T*, IEEE Std. 802.3ab, 1999.

[15] *IEEE Standard for Information Technology-Telecommunications and Information Exchange Between Systems-Local and Metropolitan Area Networks-Specific Requirements Part 3: Carrier Sense Multiple Access With Collision Detection (CSMA/CD) Access Method and Physical Layer Specifications*, IEEE Std. 802.3an, 2006.

[16] A. Nespola, S. Straullu, P. Savio, D. Zeolla, S. Abrate, D. Cardenas, J. Ramirez, N. Campione, and R. Gaudino, "First demonstration of real-time LED-based gigabit ethernet transmission on 50m of A4a.2 SI-POF with significant system margin," in *36th European Conference on Optical Communication (ECOC) 2010*, Torino, Italy, 19–23 Sep. 2010, p. PD3.1.

[17] A. Antonino, S. Straullu, S. Abrate, A. Nespola, P. Savio, D. Zeolla, J. R. Molina, R. Gaudino, S. Loquai, and J. Vinogradov, "Real-time gigabit ethernet bidirectional transmission over a single SI-POF up to 75 meters," in *Conference on Optical Fiber Communication/National Fiber Optic Engineers Conference (OFC/NFOEC) 2011*, Los Angeles, CA, 6–10 Mar. 2011, p. OWA2.

[18] H. Yang, E. Tangdiongga, S. C. J. Lee, C. M. Okonkwo, H. P. A. van den Boom, S. Randel, and A. M. J. Koonen, "4.7 Gbit/s transmission over 50m long 1mm diameter multi-core plastic optical fiber," in *Conference on Optical Fiber Communication/National Fiber Optic Engineers Conference (OFC/NFOEC) 2010*, San Diego, CA, 21–25 Mar. 2010, p. OWA4.

[19] D. O'Brien, L. Zeng, H. Le-Minh, G. Faulkner, O. Bouchet, S. Randel, J. Walewski, J. Rabadan Borges, K.-D. Langer, J. Grubor, K. Lee, and E. Tae Won, "Visible light communications," in *Short-Range Wireless Communications: Emerging Technologies and Applications*, R. Kraemer and M. Katz, Eds. Chichester: Wiley, 2009.

[20] J. Kahn and J. Barry, "Wireless infrared communications," *Proceedings of the IEEE*, vol. 85, no. 2, pp. 265–298, Feb. 1997.

[21] IEEE 802.11™WIRELESS LOCAL AREA NETWORKS; the working group for wlan standards. [Online]. Available: http://www.ieee802.org/11/

[22] *Evolved Universal Terrestrial Radio Access (E-UTRA); Base Station (BS) radio transmission and reception*, 3GPP Technical Specification 36.141 Release 8, V8.12.0, 2011.

[23] (2010, Oct.) ITU paves way for next-generation 4G mobile technologies. [Online]. Available: http://www.itu.int/net/pressoffice/press_releases/2010/40.aspx/

[24] M. Fabbri and P. Faccin, "Radio over fiber technologies and systems: New opportunities," in *9th International Conference on Transparent Optical Networks (ICTON) 2007*, Rome, Italy, 1–5 Jul. 2007, p. We.C3.1.

[25] J. Capmany and D. Novak, "Microwave photonics combines two worlds," *Nature Photonics*, vol. 1, no. 6, pp. 319–330, Jun. 2007.

[26] I. Cox, C.H., E. Ackerman, G. Betts, and J. Prince, "Limits on the performance of RF-over-fiber links and their impact on device design," *IEEE Transactions on Microwave Theory and Techniques*, vol. 54, no. 2, pp. 906–920, Feb. 2006.

[27] T. Kurniawan, A. Nirmalathas, C. Lim, D. Novak, and R. Waterhouse, "Performance analysis of optimized millimiter-wave fiber radio lilnks," *IEEE/OSA Journal of Lightwave Technology*, vol. 54, no. 2, pp. 921–928, Feb. 2006.

[28] M. Beltran, J. Jensen, R. Llorente, and I. Tafur Monroy, "Experimental analysis of 60-GHz VCSEL and ECL photonic generation and transmission of impulse-radio ultra-wideband signals," *IEEE Photonics Technology Letters*, vol. 23, no. 15, pp. 1055–1057, Aug. 2011.

[29] C.-S. Choi, J.-H. Seo, W.-Y. Choi, H. Kamitsuna, M. Ida, and K. Kurishima, "60-GHz bidirectional radio-on-fiber links based on InP-InGaAs HPT optoelectronic mixers," *IEEE Photonics Technology Letters*, vol. 17, no. 12, pp. 2721–2723, Dec. 2005.

[30] D. Zibar, R. Sambaraju, A. Caballero, J. Herrera, U. Westergren, A. Walber, J. Jensen, J. Marti, and I. Monroy, "High-capacity wireless signal generation and demodulation in 75- to 110-GHz band employing all-optical OFDM," *IEEE Photonics Technology Letters*, vol. 23, no. 12, pp. 810–812, Jun. 2011.

[31] P. Gamage, A. Nirmalathas, C. Lim, D. Novak, and R. Waterhouse, "Design and analysis of digitized RF-over-fiber links," *IEEE/OSA Journal of Lightwave Technology*, vol. 27, no. 12, pp. 2052–2061, Jun. 2009.

[32] D. Wake, A. Nkansah, and N. J. Gomes, "Radio over fiber link design for next generation wireless systems," *IEEE/OSA Journal of Lightwave Technology*, vol. 28, no. 16, pp. 2456–2464, Aug. 2010.

[33] I. Cox, C.H., G. Betts, and L. Johnson, "An analytic and experimental comparison of direct and external modulation in analog fiber-optic links," *IEEE Transactions on Microwave Theory and Techniques*, vol. 38, no. 5, pp. 501–509, May 1990.

[34] I. Cox, C., E. Ackerman, R. Helkey, and G. Betts, "Direct-detection analog optical links," *IEEE Transactions on Microwave Theory and Techniques*, vol. 45, no. 8, pp. 1375–1383, Aug. 1997.

[35] N. J. Gomes, A. Nkansah, and D. Wake, "Radio-over-MMF techniques - part I: RF to microwave frequency systems," *IEEE/OSA Journal of Lightwave Technology*, vol. 26, no. 15, pp. 2388–2395, Aug. 2008.

[36] H. Al-Raweshidy and S. Komaki, *Radio Over Fiber Technologies for Mobile Communication Networks*. Boston: Artech House, 2002.

[37] A. Nkansah and N. J. Gomes, "Characterization of radio over multimode fiber links using coherence bandwidth," *IEEE Photonics Technology Letters*, vol. 17, no. 12, pp. 2694–2696, Dec. 2005.

[38] G. Tartarini and P. Faccin, "Efficient characterization of harmonic and intermodulation distortion effects in dispersive radio over fiber systems

with direct laser modulation," *Microwave and Optical Technology Letters*, vol. 46, no. 2, pp. 114–117, Jul. 2005.

[39] R. Kalman, J. Fan, and L. Kazovsky, "Dynamic range of coherent analog fiber-optic links," *IEEE/OSA Journal of Lightwave Technology*, vol. 12, no. 7, pp. 1263–1277, Jul. 1994.

[40] R. Taylor and S. Forrest, "Optically coherent direct modulated FM analog link with phase noise canceling circuit," *IEEE/OSA Journal of Lightwave Technology*, vol. 17, no. 4, pp. 556–563, apr 1999.

[41] N. Walker, D. Wake, and I. Smith, "Efficient millimetre-wave signal generation through FM-IM conversion in dispersive optical fibre links," *Electronics Letters*, vol. 28, no. 21, pp. 2027–2028, Oct. 1992.

[42] T. Darcie, J. Zhang, P. Driessen, and J.-J. Eun, "Class-B microwave-photonic link using optical frequency modulation and linear frequency discriminators," *IEEE/OSA Journal of Lightwave Technology*, vol. 25, no. 1, pp. 157–164, Jan. 2007.

[43] G. Chen, J. Kang, and J. Khurgin, "Frequency discriminator based on ring-assisted fiber sagnac filter," *IEEE Photonics Technology Letters*, vol. 17, no. 1, pp. 109–111, Jan. 2005.

[44] V. Urick, F. Bucholtz, J. McKinney, P. Devgan, A. Campillo, J. Dexter, and K. Williams, "Long-haul analog photonics," *IEEE/OSA Journal of Lightwave Technology*, vol. 29, no. 8, pp. 1182–1205, Apr. 2011.

[45] M. LaGasse and S. Thaniyavaru, "Bias-free high-dynamic-range phase-modulated fiber-optic link," *IEEE Photonics Technology Letters*, vol. 9, no. 5, pp. 681–683, May 1997.

[46] B. Davies and J. Conradi, "Hybrid modulator structures for subcarrier and harmonic subcarrier optical single sideband," *IEEE Photonics Technology Letters*, vol. 10, no. 4, pp. 600–602, Apr. 1998.

[47] H. Kim, "Integrated transmitter with amplitude and phase modulations," in *IEEE PhotonicsGlobal@Singapore (IPGC) 2008*, Singapore, 8–11 Dec. 2008.

[48] U.-S. Lee, H.-D. Jung, and S.-K. Han, "Optical single sideband signal generation using phase modulation of semiconductor optical amplifier," *IEEE Photonics Technology Letters*, vol. 16, no. 5, pp. 1373–1375, May 2004.

[49] The nano3G^{TM}access points. [Online]. Available: http://www.ipaccess.com/en/nano3G-access-point/

[50] H. Yang, Y. Shi, W. Wang, C. M. Okonkwo, H. P. A. van den Boom, A. M. J. Koonen, and E. Tangdiongga, "Wimedia-compliant UWB transmission over 1 mm core diameter plastic optical fibre," *IET Electronics Letters*, vol. 46, no. 6, pp. 434–436, Mar. 2010.

[51] T. D. Michaelis, "Laser diode evaluation for optical analog link," *IEEE Transactions on Cable Television*, vol. CATV-4, no. 1, pp. 30–42, Jan. 1979.

[52] J. L. Prince, E. I. Ackerman, and I. Cox, C. H., "Analog fiber-optic link technology," in *Digest of the LEOS Summer Topical Meetings on Biophotonics/Optical Interconnects and VLSI Photonics/WBM Microcavities 2004*, Jun. 2004.

[53] A. Villafranca, J. Lasobras, and I. Garces, "Precise characterization of the frequency chirp in directly modulated DFB lasers," in *Spanish Conference on Electron Devices (CDE) 2007*, Madrid, Spain, Jan. 31-Feb. 2 2007, pp. 173–176.

[54] R. Chan and J. Liu, "Time-domain wave propagation in optical structures," *IEEE Photonics Technology Letters*, vol. 6, no. 8, pp. 1001–1003, Aug. 1994.

[55] S. Ryu and S. Yamamoto, "Measurement of direct frequency modulation characteristics of DFB-LD by delayed self-homodyne technique," *IET Electronics Letters*, vol. 22, no. 20, pp. 1052–1054, Sep. 1986.

[56] U. Krüger and K. Krüger, "Simultaneous measurement of the linewidth, linewidth enhancement factor α, and FM and AM response of a semiconductor laser," *IEEE/OSA Journal of Lightwave Technology*, vol. 13, no. 4, pp. 529–597, Apr. 1995.

[57] A. Yariv and P. Yeh, *Photonics: Optical Electronics in Modern Communications*, 6th ed. New York, Oxford: Oxford Universirt Press, 2006.

[58] *Telecommunications: Glossary of Telecommunication Terms*, General Services Administration Federal Standard 1037C, 1996.

[59] M. Abramowitz and I. Stegun, *Handbook of Mathematical Functions with Formulas, Graphs, and Mathematical Tables*, 10th ed. Washington: National Bureau of Standardds, 1972.

[60] *Universal Mobile Telecommunications System (UMTS); Base Station (BS) radio transmission and reception (FDD)*, 3GPP Technical Specification 25.104 Release 8, V8.13.0, 2011.

[61] *WiMAX Forum® Air Interface Specifications; WiMAX Forum® Mobile Radio Specification*, WiMAX Forum Technical Specification T23-005-R015v04, 2010.

[62] *Universal Mobile Telecommunications System (UMTS); User Equipment (UE) radio transmission and reception (FDD)*, 3GPP Technical Specification 25.101 Release 8, V8.15.0, 2011.

[63] S. Bottacchi, *Multi-gigabit Transmission Over Multimode Optical Fibre: Theory and Design Methods for 10GbE Systems.* New York: Wiley, 2006.

[64] J. Fleming, "Dispersion in GeO_2–SiO_2 glasses," *OSA Appled Optics*, vol. 23, no. 24, pp. 4486–4493, Dec. 1984.

[65] D. Donlagic, "Opportunities to enhance multimode fiber links by application of overfilled launch," *IEEE/OSA Journal of Lightwave Technology*, vol. 23, no. 11, pp. 3526–3540, Nov. 2005.

[66] G. Tartarini and H. Renner, "Efficient finite-element analysis of tilted open anisotropic optical channel waveguides," *IEEE Microwave and Guided Wave Letters*, vol. 9, no. 10, pp. 389–391, Oct. 1999.

[67] "RF module," Model Library, COMSOL AB, Stockholm, Sweden, Nov. 2008.

[68] M. Ohashi, K. Kitayama, Y. Ishida, and Y. Negishi, "Simple approximations for chromatic dispersion in single-mode fibers with various index profiles," *IEEE/OSA Journal of Lightwave Technology*, vol. 3, no. 1, pp. 110–115, Feb. 1985.

[69] L. Raddatz, I. H. White, D. G. Cunningham, and M. C. Nowell, "An experimental and theoretical study of the offset launch technique for the enhancement of the bandwidth of multimode fiber links," *IEEE/OSA Journal of Lightwave Technology*, vol. 16, no. 3, pp. 324–331, Mar. 1998.

[70] L. Raddatz and I. H. White, "Overcoming the modal bandwidth limitation of multimode fiber by using passband modulation," *IEEE Photonics Technology Letters*, vol. 11, no. 2, pp. 266–268, Feb. 1999.

[71] L. Geng, C. Kwok, S. Lee, J. Ingham, R. Penty, I. White, and D. Cunningham, "Efficient line launch for bandwidth improvement of 10 Gbit/s multimode fibre links using elliptical gaussian beam," in *36th European Conference on Optical Communication (ECOC) 2009*, Torino, Italy, 19–23 Sep. 2010, p. We.6.B.5.

[72] D. H. Sim, Y. Takushima, and Y. C. Chung, "High-speed multimode fiber transmission by using mode-field matched center-launching technique," *IEEE/OSA Journal of Lightwave Technology*, vol. 27, no. 8, pp. 1018–1026, Apr. 2009.

[73] I. Gasulla and J. Capmany, "Transfer function of multimode fiber links using an electric field propagation model: Application to radio over fibre systems," *OSA Optics Express*, vol. 14, no. 20, pp. 9051–9070, Oct. 2006.

[74] J. Capmany and I. Gasulla, "Transfer function of radio over fiber multimode fiber optic links considering third-order dispersion," *OSA Optics Express*, vol. 15, no. 17, pp. 10 591–10 596, Aug. 2007.

[75] B. Crosignani and A. Yariv, "Statistical properties of modal noise in fiber-laser systems," *OSA Journal of Optical Society of America*, vol. 73, no. 8, pp. 1022–1027, Aug. 1983.

[76] G. Ghosh, M. Endo, and T. Iwasaki, "Temperature-dependent Sellmeier coefficients and chromatic dispersions for some optical fiber glasses," *IEEE/OSA Journal of Lightwave Technology*, vol. 12, no. 8, pp. 1338–1342, Aug. 1994.

[77] G. Ghosh and H. Yajima, "Pressure-dependent sellmeier coefficients and material dispersions for silica fiber glass," *IEEE/OSA Journal of Lightwave Technology*, vol. 16, no. 11, pp. 2002–2005, Nov. 1998.

[78] R. Dandliker, A. Bertholds, and F. Maystre, "How modal noise in multimode fibers depends on source spectrum and fiber dispersion," *IEEE/OSA Journal of Lightwave Technology*, vol. 3, no. 1, pp. 7–12, Feb. 1985.

[79] I. Gasulla and J. Capmany, "Modal noise impact in radio over fiber multimode fiber links," *OSA Optics Express*, vol. 16, no. 1, pp. 121–126, Jan. 2008.

[80] "Mode conditiong patchcord IEC 61300," Diamond SA, Losone, Switzerland.

[81] "FM-1 mode scrambler," Newport Corporation, Irvine, CA.

[82] *Evolved Universal Terrestrial Radio Access (E-UTRA); Base Station (BS) conformance testing*, 3GPP Technical Specification 36.141 Release 8, V8.11.0, 2011.

[83] C. Shannon, "Communication in the presence of noise," *Proceedings of the IRE*, vol. 37, no. 1, pp. 10–21, Jan. 1949.

[84] T. M. Cover and J. A. Thomas, *Elements of lnformation Theory*, 2nd ed. New York: Wiley, 2006.

[85] G. Agrawal, *Nonlinear Fiber Optics*, 3rd ed. San Diego: Academic Press, 2001.

[86] D. Cardenas, A. Nespola, P. Spalla, S. Abrate, and R. Gaudino, "A media converter prototype for 10-Mb/s Etherent transmission over 425 m of large-core step-index polymer optical fiber," *IEEE/OSA Journal of Lightwave Technology*, vol. 24, no. 12, pp. 4946–4952, Dec. 2006.

[87] J. Bingham, "Multicarrier modulation for data transmission: an idea whose time has come," *IEEE Communications Magazine*, vol. 28, no. 5, pp. 5–14, May 1990.

[88] S. Lee, "Discrete multitone modulation for short-range optical communcations," Ph.D. dissertation, Eindhoven University of Technology, Dec. 2009.

[89] J. Cioffi. (2008) A multicarrier primer. [Online]. Available: http://www.stanford.edu/group/cioffi/documents/multicarrier.pdf

[90] D. Forney. (Spring 2005) Principles of digital communication II (lecture notes). [Online]. Available: http://ocw.mit.edu/courses/electrical-engineering-and-computer-science/6-451-principles-of-digital-communication-ii-spring-2005/

[91] *Forward error correction for high-bit rate DWDM submarine systems*, ITU-T Recommendation G.975.1, 2004.

[92] P. S. Chow, J. M. Cioffi, and J. A. C. Bingham, "A practical discrete multitone transceiver loading algorithm for data transmission over spectrally shaped channels," *IEEE Transactions on Communications*, vol. 43, no. 234, pp. 773–775, Feb./Mar./Apr. 1995.

[93] J. Cioffi. (Spring Quarter 2007-2008) Advanced digital communication (course handouts). [Online]. Available: http://www.stanford.edu/class/ee379c/

[94] "665 nm multimode VCSEL (RVM665T) preliminary product specification," Firecomms Ltd., Cork, Ireland.

[95] *Safety of laser products - Part 1: Equipment classification and requirements*, IEC Std. 60 825-1, 2007.

[96] "OM-GIGA product specification," Optimedia, Inc., Korea.

[97] T. Pollet, P. Spruyt, and M. Moeneclaey, "The BER performance of OFDM systems using non-synchronized sampling," in *IEEE Global Telecommunications Conference (GLOBECOM) 1994*, vol. 1, Dec. 1994, pp. 253–257.

[98] T. Schmidl and D. Cox, "Robust frequency and timing synchronization for OFDM," *IEEE Transactions on Communications*, vol. 45, no. 12, pp. 1613–1621, Dec. 1997.

[99] H. Ochiai and H. Imai, "Performance analysis of deliberately clipped OFDM signals," *IEEE Transactions on Communication Technology*, vol. 50, no. 1, pp. 89–101, Jan. 2002.

[100] H. Yang, S. C. J. Lee, E. Tangdiongga, C. M. Okonkwo, H. P. A. van den Boom, F. Breyer, S. Randel, and A. M. J. Koonen, "47.4 Gb/s transmission over 100 m graded-index plastic optical fiber based on

rate-adaptive discrete multitone modulation," *IEEE/OSA Journal of Lightwave Technology*, vol. 28, no. 4, pp. 352–359, Feb. 2010.

[101] S. Randel, F. Breyer, S. C. J. Lee, and J. W. Walewski, "Advanced modulation schemes for short-range optical communications," *IEEE Journal of Selected Topics in Quantum Electronics*, vol. 16, no. 5, pp. 1280–1289, Sep.-Oct. 2010.

[102] S. Noda, Y. Saito, and T. Yoshida, "Configuration and error ratio performance of M-QAM whose number of signal points is not a power of 2," *Electronics and Communications in Japan*, vol. 90, no. 2, pp. 46–57, Feb. 2007.

[103] A. T. Le and K. Araki, "A group of modulation schemes for adaptive modulation," in *11th IEEE Singapore International Conference on Communication Systems (ICCS) 2008*, Nov. 2008, pp. 864–869.

[104] L. Yang and G. Giannakis, "Ultra-wideband communications: an idea whose time has come," *IEEE Signal Processing Magazine*, vol. 21, no. 6, pp. 26–54, Nov. 2004.

[105] M. Ghavami, L. Michael, and R. Kohno, *Ultra Wideband Signals and Systems in Communication Engineering*, 2nd ed. Chichester: Wiley, 2007.

[106] *Multiband OFDM Physical Layer Specification*, WiMedia Alliance PHY Specification Final Deliverable 1.5, 2009.

[107] *High Rate Ultra Wideband PHY and MAC Standard*, ECMA Std. 368, 2008.

[108] *Wireless Universal Serial Bus*, Wireless USB Promoter Group Specification 1.1, 2010.

List of acronyms

3G third generation

4G fourth generation

AC alternating current

ACLR adjacent channel leakage ratio

ADC analog-to-digital converter

APD avalanche photodetector

AWG arbitrary waveform generator

AWGN additive white gaussian noise

BER bit error rate

BPSK binary phase shift keying

BW bandwidth

Cat-5 Category 5

DAC digital-to-analog converter

DAS distributed antenna system

DC direct current

DFB distributed feed-back

DL downlink

DMT discrete multitone

DPO digital phosphor oscilloscope

DSL digital subscriber line

DSP digital signal processing

EFEC enhanced forward error correction

EMB effective modal bandwidth

EMI electromagnetic immunity

EVM error vector magnitude

FCC Federal Communications Commission

F–DAS fiber DAS

FEC forward error correction

FIR finite impulse response

FP fabry-perot

FTTH fiber-to-the-home

GI graded-index

GOF glass optical fiber

GSM Global System for Mobile communications

HAN home area network

HSPA high speed packet access

ICT information and communications technology

IF intermediate frequency

IIP2 input intercept point of the second order

IIP3 input intercept point of the third order

IMD intermodulation distorsion

IM–DD intensity modulation – direct detection

IMT International Mobile Telecommunications

ISM industrial, scientific and medical

ITU International Telecommunication Union

MB–OFDM multi-band OFDM

LAN local area network

LD laser diode

LED light emitting diode

LTE Long Term Evolution

MC multi-core

MMF multi-mode fiber

NA numerical aperture

OFDM orthogonal frequency division multiplexing

OFL overfilled launch

OMI optical modulation index

PA power amplifier

PAPR peak-to-average power ratio

PD photodiode

PIN positive-intrinsic-negative

PMMA Poly(methyl methacrylate)

POF plastic optical fiber

PSD power spectral density

QAM quadrature amplitude modulation

QPSK quadrature phase shift keying

RC resonant cavity

RF radio frequency

RoF radio over fiber

RoMMF radio over multi-mode fiber

RX receiver

SC–APC standard connector - angle-polished connector

SFDR spurious free dynamic range

SI step-index

SNR signal-to-noise ratio

SMF single-mode fiber

SSB single sideband

TIA trans-impedance amplifier

TX transmitter

UMTS Universal Mobile Telecommunications System

UWB ultra wideband

VCSEL vertical cavity surface emitting laser

VNA vector network analyzer

VSA vector signal analyzer

VSG vector signal generator

WiFi Wireless Fidelity

WiMAX Worldwide Interoperability for Microwave Access

WBAN wireless body area network

WHAN wireless home area network

WLAN wireless local area network

WMAN wireless metropolitan area network

WPAN wireless personal area network

WWAN wireless wide area network

List of publications

Journal Papers

P1. D. Visani, G. Tartarini, L. Tarlazzi, and P. Faccin, "Transmission of UMTS and WIMAX Signals Over Cost-Effective Radio Over Fiber Systems," *IEEE Microwave and Wireless Components Letters*, vol. 19, no. 12, pp. 831–833, Dec. 2009.

P2. D. Visani, G. Tartarini, M.N. Petersen, P. Faccin, and L. Tarlazzi, "Effects of laser frequency chirp on modal noise in short-range radio over multimode fiber links," *OSA Applied Optics*, vol. 49, no. 6, pp. 1032–1040, Feb. 2010.

P3. D. Visani, G. Tartarini, M.N. Petersen, L. Tarlazzi, and P. Faccin, "Link Design Rules for Cost-Effective Short-Range Radio Over Multimode Fiber Systems," IEEE Transactions on Microwave Theory and Techniques, vol. 58, no. 11, pp. 3144–3153, Nov. 2010.

P4. C.M. Okonkwo, E. Tangdiongga, H. Yang, D. Visani, S. Loquai, R. Kruglov, B. Charbonnier, M. Ouzzif, I. Greiss, O. Ziemann, R. Gaudino, and A.M.J. Koonen, "Recent Results From the EU POF-PLUS Project: Multi-Gigabit Transmission Over 1 mm Core Diameter Plastic Optical Fibers," *IEEE/OSA Journal of Lightwave Technology*, vol. 29, no. 2, pp. 186–193, Jan. 2011.

P5. D. Visani, Y. Shi, C.M. Okonkwo, H. Yang, H.P.A. van den Boom, G. Tartarini, E. Tangdiongga, and A.M.J. Koonen, "Wired and wireless multi-service transmission over 1mm-core GI-POF for in-home networks," *IET Electronics Letters*, vol. 47, no. 3, pp. 203–205, Feb. 2011.

P6. D. Visani, C.M. Okonkwo, S. Loquai, H. Yang, Y. Shi, H.P.A. van den Boom, T. Ditewig, G. Tartarini, S.C.J. Lee, A.M.J. Koonen, and E. Tangdiongga, "Beyond 1 Gbit/s Transmission Over 1 mm Diameter Plastic Optical Fiber Employing DMT for In-Home Communication Systems," *IEEE/OSA Journal of Lightwave Technology*, vol. 29, no. 4, pp. 622–628, Feb. 2011.

P7. M.N. Petersen, G. Tartarini, D. Visani, P. Faccin, and L. Tarlazzi, "Influence of transmitter chirp and receiver imperfections on RF gain in short-range ROMMF systems," *Microwave and Optical Technology Letters*, vol. 53, no. 4, pp. 822–824, Apr. 2011.

P8. S.T. Abraha, C.M. Okonkwo, H. Yang, D. Visani, Y. Shi, H. -D. Jung, E. Tangdiongga, and A.M.J. Koonen, "Performance Evaluation of IR-UWB in Short-Range Fiber Communication Using Linear Combination of Monocycles," *IEEE/OSA Journal of Lightwave Technology*, vol. 29, no. 8, pp. 1143–1151, Apr. 2011.

P9. D. Visani, G. Tartarini, P. Faccin, and L. Tarlazzi, "Cost-effective radio over fiber system for multi service wireless signal," *Optics Communications*, vol. 284, no. 12, pp. 2751–2754, June 2011.

P10. D. Visani, C.M. Okonkwo, Y. Shi, H. Yang, H.P.A. van den Boom, G. Tartarini, E. Tangdiongga, and A.M.J. Koonen, "3×2^N-QAM Constellation Formats for DMT Over 1-mm Core Diameter Plastic Optical Fiber," *IEEE Photonics Technology Letters*, vol. 23, no. 12, pp. 768–770, June 2011.

P11. G. Alcaro, D. Visani, L. Tarlazzi, P. Faccin, and G. Tartarini, "Distortion Mechanisms Originating from Modal Noise in Radio over Multimode

Fiber Links," *IEEE Transactions on Microwave Theory and Techniques*, vol. 60, no. 1, pp. 185–194, Jan. 2012.

P12. Y. Shi, C.M. Okonkwo, D. Visani, H. Yang, H.P.A. van den Boom, G. Tartarini, E. Tangdiongga, and A.M.J. Koonen, "Ultra-Wideband Signal Distribution over Large-Core POF for In-Home Networks," submitted to *IEEE/OSA Journal of Lightwave Technology*.

P13. D. Visani, M.N. Petersen, F. Sorci, L. Tarlazzi, P. Faccin, and G. Tartarini, "In-Building Wireless Distribution in legacy Multimode Fiber with an improved RoMMF system," submitted to *IEEE Microwave and Wireless Components Letters*.

International Conferences

P14. D. Visani, G. Tartarini, L. Tarlazzi, and P. Faccin, "Accurate and efficient transmission evaluation of wireless signals on radio over fiber links," *IEEE International Topical Meeting on Microwave Photonics (MWP) 2009*, Valencia, Spain, 14–16 Sep. 2010, p. Th4.17.

P15. D. Visani, G. Tartarini, M.N. Petersen, L. Tarlazzi, and P. Faccin, "Reducing Modal Noise in Short-Range Radio over Multimode Fibre Links," *Conference on Optical Fiber Communication/National Fiber Optic Engineers Conference (OFC/NFOEC) 2010*, San Diego, CA, 21-15 Mar. 2010, p. JWA56.

P16. D. Visani, C.M. Okonkwo, S. Loquai, H. Yang, Y. Shi, H.P.A. van den Boom, T. Ditewig, G. Tartarini, B. Schmauss, S. Randel, T. Koonen, and E. Tangdiongga, "Record 5.3 Gbit/s Transmission over 50m 1mm Core Diameter Graded-Index Plastic Optical Fiber," *Conference on Optical Fiber Communication/National Fiber Optic Engineers Conference (OFC/NFOEC) 2010*, San Diego, CA, 21-15 Mar. 2010, p. PDPA3.

P17. C. Raffaelli, M. Savi, G. Tartarini, and D. Visani, "Physical path analysis in photonic switches with shared wavelength converters," *12th International Conference on Transparent Optical Networks (ICTON) 2010*, Munich, Germany, June 27–July 1 2010, p. Mo.C1.5.

P18. G. Alcaro, D. Visani, G. Tartarini, L. Tarlazzi, and P. Faccin, "Controlling the impact of Modal Noise on Harmonic and Intermodulation distortions in Radio over Multimode Fiber links," *36th European Conference and Exhibition on Optical Communication (ECOC) 2010*, Torino, Italy, 19–23 Sep. 2010, p. We.7.B.5.

P19. Y. Shi, H. Yang, D. Visani, C.M. Okonkwo, H.P.A. van den Boom, H. Kragl, G. Tartarini, S. Randel, E. Tangdiongga, and A.M.J. Koonen, "First demonstration of broadcasting high capacity data in large-core POF-based in-home networks," *36th European Conference and Exhibition on Optical Communication (ECOC) 2010*, Torino, Italy, 19–23 Sep. 2010, p. We.6.B.2.

P20. H. Yang, D. Visani, C.M. Okonkwo, Y. Shi, G. Tartarini, E. Tangdiongga, and A.M.J. Koonen, "Multi-standard transmission of converged wired and wireless services over 100m plastic optical fibre," *36th European Conference and Exhibition on Optical Communication (ECOC) 2010*, Torino, Italy, 19–23 Sep. 2010, p. We.7.B.3.

P21. Y. Shi, H. Yang, C.M. Okonkwo, D. Visani, G. Tartarini, E. Tangdiongga, and A.M.J. Koonen, "Multimode fiber transmission of up-converted MB-OFDM UWB employing optical frequency multiplication," *IEEE International Topical Meeting on Microwave Photonics (MWP) 2010*, Montreal, Canada, 5–9 Oct. 2010, p. Th4.32.

P22. D. Visani, G. Tartarini, Y. Shi, H. Yang, C.M. Okonkwo, E. Tangdiongga, and A.M.J. Koonen, "Towards converged broadband wired and wireless in-home optical networks," *15th International Conference on Optical Network Design and Modeling (ONDM) 2011*, Bologna, Italy, 8–10 Feb. 2011, p. S4.2.

P23. Y. Shi, D. Visani, C.M. Okonkwo, H. Yang, H.P.A. van den Boom, G. Tartarini, E. Tangdiongga, and A.M.J. Koonen, "First demonstration of HD video distribution over large-core POF employing UWB for in-home networks," *Conference on Optical Fiber Communication/National Fiber Optic Engineers Conference (OFC/NFOEC) 2011*, Los Angeles, CA, 6–10 Mar. 2011, p. OWB5.

P24. E. Tangdiongga, C.M. Okonkwo, Y. Shi, D. Visani, H. Yang, H.P.A. van den Boom, and A.M.J. Koonen, "High-Speed Short-Range Transmission over POF," *Conference on Optical Fiber Communication/ National Fiber Optic Engineers Conference (OFC/NFOEC) 2011*, Los Angeles, CA, 6–10 Mar. 2011, p. OWS5.

P25. E. Tangdiongga, D. Visani, H. Yang, Y. Shi, C.M. Okonkwo, H.P.A. van den Boom, G. Tartarini, and A.M.J. Koonen, "Converged In-home Networks using 1-mm Core Size Plastic Optical Fiber," *OSA Access Networks and In-house Communications (ANIC) 2011*, Toronto, Canada, 12–14 June 2011,p. ATuC2.

P26. Y. Shi, D. Visani, C.M. Okonkwo, H.P.A. van den Boom, G. Tartarini, E. Tangdiongga, and A.M.J. Koonen, "Simultaneous Transmission of Wired and Wireless Services over Large Core POF for In-Home Networks," *367th European Conference and Exhibition on Optical Communication (ECOC) 2011*, Geneva, Switzerland, 18–22 Sep. 2011, p. Tu.3.C.5.

Acknowledgments

At the end of this dissertation I want to thank all the people who I met on the "journey" of these three years.

Firstly, I would like to thank Professor Paolo Bassi for allowing me to pursue doctoral studies within the Dipartimento di Elettronica, Informatica e Sistemistica (DEIS) of the University of Bologna. Then, I am deeply grateful to my supervisor Professor Giovanni Tartarini who supported me in all the moments of these three years with long and helpful discussions about our research topics and about life in general and with actual actions. Furthermore, I want to thank Gianpiero Alcaro e Francesca Sorci with whom I had the pleasure to work. Then, I want to thank my Ph.D. companion Luisa De Marco, with whom I shared all the moments and gossips of these three years, Dr. Giovanni Battista Montanari for always willing to help me, and Flavia Martelli, Ramona Rosini, Flavio Fabbri, Silvia Zampese and Cengiz Gezer of the Radio Networks group who often "adopted" me for lunch.

Part of this thesis has been carried out in collaboration with Commscope Italy S.r.l. In particular, I want to thank Eng. Pier Faccin and Eng. Luigi Tarlazzi for sharing their positive attitude and ideas. Moreover, I want to thank Dr. Martin Nordal Petersen, which spent more than one year in Italy and applied his experimental knowledge to the problems we were struggling with.

Part of this thesis has been carried out at the ECO group of the COBRA research institute at the Eindhoven University of Technology (TU/e). I want

to thank Professor Ton Koonen to have hosted me for 11 months in his group. Then, I want to express my gratitude to Professor Eduward Tangdiongga who was my supervisor during my stay in The Netherlands giving me the opportunity to increase strongly my research experience. He also actively participated to the revision process of this dissertation. Moreover, this work would not have been possible without the help of Dr. Hejie Yang, Dr. Chigo Okonkwo and Yan Shi with whom I had frequent discussions and shared some nights in the lab. Then, I want to thank my officemates Solomon Tesfay Abraha, Dr. Karen Solis, my almost-officemate Abnihav Rohit, and all the current and past ECO group components which made many moments during lunches, coffee breaks and evenings unforgettable. Finally, I want to thank Ariel Vargas for having been a very good friend during and after my stay in Eindhoven. I wish him all the best for his career either in Brazil or in Europe.

Even though not directly involved in this Ph.D. program, I want to thank my old Italian friends, and last but not least my family: “mamma” Stefania, “babbo” Giancarlo, and “nonna” Angela. You gave me your unconditional support even knowing that to pursue my goals I could get far away from you.